INFORMATION TO USERS

This manuscript has been reproduced from the microfilm master. UMI films the text directly from the original or copy submitted. Thus, some thesis and dissertation copies are in typewriter face, while others may be from any type of computer printer.

The quality of this reproduction is dependent upon the quality of the copy submitted. Broken or indistinct print, colored or poor quality illustrations and photographs, print bleedthrough, substandard margins, and improper alignment can adversely affect reproduction.

In the unlikely event that the author did not send UMI a complete manuscript and there are missing pages, these will be noted. Also, if unauthorized copyright material had to be removed, a note will indicate the deletion.

Oversize materials (e.g., maps, drawings, charts) are reproduced by sectioning the original, beginning at the upper left-hand corner and continuing from left to right in equal sections with small overlaps.

ProQuest Information and Learning
300 North Zeeb Road, Ann Arbor, MI 48106-1346 USA
800-521-0600

Multiband Models of High Temperature Superconductors

by

CHRIS O'DONOVAN

B.Sc. (Waterloo) 1992
M.Sc. (McMaster) 1994

A Thesis
Submitted to the School of Graduate Studies
in Partial Fulfilment of the Requirements
for the Degree
Doctor of Philosophy

McMaster University

Multiband Models of High Temperature Superconductors

DOCTOR OF PHILOSOPHY (2000)
(Physics)

McMaster University
Hamilton, Ontario

TITLE: Multiband Models of High Temperature Superconductors

AUTHOR: Chris O'Donovan

SUPERVISOR: Dr. J. P. Carbotte

NUMBER OF PAGES: ix, 135

Abstract

In order to understand the complex electromagnetic properties of high temperature superconductors the details of the electronic band structure must be included. In this thesis we go beyond the simple free electron model in which the electromagnetic properties are determined by a single, spherical, Fermi surface (which is adequate for most conventional superconductors) to more realistic models containing multiple, anisotropic tight binding bands. Using these models we are able to calculate several electromagnetic properties, including the magnetic penetration depth, Josephson tunneling currents, the density of states and the optical conductivity, we find our results are in good agreement with experimental observations.

One of the banes of the field of high temperature superconductivity is that many experiments are carried out on materials that are less than ideal. Often the presence of impurities or less than ideal stoichiometries can have a large impact upon the measured properties. We are able to calculate the effect of impurities upon the above mentioned electromagnetic properties in both the unitary and Born scattering limits and find significant differences between them. We find that the presence of impurities in the chain band has little effect upon the critical temperature which is consistent with the experimental observations that Ni impurities (which go into the chains) and overdoped materials (in which the excess oxygen also goes in the chains) have little effect upon the critical temperature, while Zn impurities (which go into both the chains and planes) and underdoped materials (in which both the chains and planes are oxygen deficient) have a significantly lower critical temperature.

Another of the difficulties with the experimental results is caused by the presence of twin domains in the orthorhombic materials. The presence of twins in a material can mask some of the significant anisotropies that are observed in untwinned materials such as the magnetic penetration depth in the a and b directions and the c direction Josephson tunneling into a conventional superconductor. We calculate these properties in models that take into account the large anisotropies that are present in these materials. We find that the c direction Josephson tunneling can not only be non-zero, but can actually be quite large in a pure d wave superconductor if the band is anisotropic (*i.e.*orthorhombic). This result helps explain one of the few experiments that was considered inconsistent with d wave superconductivity.

Acknowledgements

I don't know where to start. There are so many people to thank that this page could become a chapter in itself. For all that I have learned about superconductivity while at McMaster I have Jules Carbotte to thank the most but others also contributed significantly to my education, including Peter Arberg, Bill Atkinson, Dwayne Branch, David Feder, Catherine Kallin, Mark Kvale, Bill Minor, Pekka Soininen, and Tom Timusk. I would also like to thank those that made the various summer schools so worthwhile: Andy Beardsall, Mona Berciu, Chris Bidinosti, Erica Bird, May Chiao, Patricia Dolez, Benoit Dumoulin, Walter Hardy, Christian Lupien, Ian McDonald, Roger Miller, Puangratana Pairor, Jeff Sonier, Tanya Startseva, and Ilya Vekhter. There are too many others that have contributed scholasticly to my time at McMaster in smaller but still significant ways to list here but I want to thank them all.

The circle of friends that have contributed to my almost entirely enjoyable experience at McMaster is even larger and, in addition to those mentioned above, includes Abdalla[2], Nicola Ally, Maggie Austen, Roby Austin, Karen Bakker, Gordon Chan, Steve Cool, Charles Curry, Jennifer Dai, Spiro Daoussis, Randy Dumont, Mike Dunlavy, Rob Gojmerac, Cheryl Johnston, Hamish Johnston, Fuyuko Kataoka, Tim Lampman, Marcy Lumsden, Wendy Malarek, Rebeccah Marsh, Peter Mason, Rosemary McNeice, Patricia Monger, John Nieminen, Joanne O'Meara, Rachid Ouyed, Kelvin Prosyk, Jamal Sakhr, Bryan Schaly, Vicky Smallman, Ann-Marie Westlake, Jon Wilson and the entire SCD baseball team.

Finally and most importantly, I would like to thank my family for all of their love and support.

Preface

The main body of research in this thesis is contained in three papers that have been published in Physical Review B. All three papers have myself and Jules Carbotte as authors and the third has Mark Lumsden and Bruce Gaulin as additional authors. In the third paper Bruce and Mark provided the experimental results and the accompanying commentary. The rest of the work in the three papers was a cooperative effort of Jules and myself.

The ideas and the text of the papers (excluding those related to the experimental results in the third paper) were the result of many conversations and of passing the manuscripts back and forth between Jules and myself. The text and the actual calculations and results presented in the "formalism" and "results" sections of each paper were written or performed by myself with comments and observations being made by Jules throughout. The computer codes used to calculate the results presented were solely my effort. The "introduction" and "conclusion" sections of each paper, which place the work in the "formalism" and "results" sections in historical and current research contexts, were, in the large part, written by Jules.

Contents

List of Figures

Chapter 1

Introduction

1.1 Superconductors – Old and New

Superconductivity is the property of some materials which are able, below a certain temperature called the critical temperature, to conduct electricity without resistance. Without resistance means exactly that: once a current is set up in a loop of superconducting material it will continue indefinitely so long as the temperature of the loop is kept below the critical temperature of that material. This property has obvious uses in any application that requires large magnetic fields (fixed magnets have an upper limit of approximately two Tesla and a conventional electromagnet uses large quantities of electricity), and fields of several Tesla are used in the MRI machines of major hospitals and research institutions.

The only other common application of superconductors other than creating large magnetic fields is the sensitive measurement of variations in magnetic fields with SQUID[1] magnetometers. These magnetometers are used by mining and oil exploration teams to detect small changes in the earth's magnetic field which are caused by ore or oil deposits and by the medical community in imaging applications. They are also used in research labs, often in the study of superconductivity itself.

Other applications of superconductors, such as maglev trains, have proven too expensive or impractical for widespread use. The expense of these applications was almost entirely due to the extremely low critical temperatures of the available materials which required costly cryogenics and liquid helium as a coolant.

These restrictions have recently been somewhat removed by the discovery of materials with much higher critical temperatures, allowing the use of liquid nitrogen instead of liquid helium for the cryogenics. These new materials, however, have new restrictions and costs which will require much research and development in order to reduce them. Many new material processing methods have

[1] SQUID - Superconducting QUantum Interference Devices

been developed in order to meet the requirements of these new materials and, while there has been significant progress, this is an ongoing effort. Sadly, the progress of research into a fundamental understanding of these materials seems to be much more limited, with nothing close to consensus being reached after over ten years of research (with the one important exception being the fundamental symmetry of the superconducting state).

The reason for this difficulty is that, with the possible exception of the heavy Fermion superconductors, these materials are so unlike "conventional superconductors" (ie, those understood in the BCS framework): These materials exhibit magnetism as well as superconductivity and the presence of magnetism usually prevents superconductivity.

This thesis presents one particular model (out of many) which may account for the superconductivity in these materials and calculates some properties which are unique to superconductors that are a consequence of this model. However, many of these calculated properties are not unique to this model but are ramifications of the symmetry of the superconducting state which is a result of this model (and which is also a consequence of other possible models) and so the agreement with some of the experimental results is not as significant as it would be if they were unique to this model.

1.2 A Brief History of Superconductivity

The breakthrough discovery of superconductivity by Onnes in 1911[1] and the subsequent discovery of the eponymous Meissner effect in 1927[2] started a new field of research. With the exception of the Londons' phenomenological theory[3] and Ginsburg-Landau theory,[4] theoretical progress had to wait until Bardeen, Cooper and Schrieffer came up with what is now referred to as the BCS theory in 1957.[5] This theory, which used phonons (the quanta of lattice vibrations) as the mechanism which causes superconductivity, was so successful in explaining many of the physical properties of superconductors that it is, without doubt, correct.

However, with critical temperatures (ie, the temperature at which a material starts to superconduct) ranging only as high as 23K (ie, −250C) the uses of these materials were restricted to applications where the high cost of liquid helium cooling was justified. These applications were restricted to those which required either large magnetic fields (such as MRI machines in hospitals and bending magnets in particle accelerators) or the ability to measure magnetic fields very precisely using SQUIDs[2] (which make use of the Josephson effect).

With the addition of retarded effects by Eliashberg[6, 7] in 1960 the theory was substantially complete. By use of a method called "tunnelling inversion" to extract the phonon spectra of superconducting materials even the details of the superconducting properties became calculable and were so much in accord with the experimental results that any question of the correctness of the theory was put to rest.[8] There were only a few details, such as those relating to the heavy Fermion materials, to be tidied up before the field could be said to be complete.

[2]SQUID: Superconducting QUantum Interference Device

Complete, that is, until the spectacular discovery in 1986 by Bednorz and Müller[9] of high temperature superconductors (HTS). Initially discovered with a critical temperature of ~32K in $La_{2-x}Sr_xCuO_4$ (LSCO), soon materials, such as $YBa_2Cu_3O_{7-\delta}$ (YBCO), had critical temperatures in excess of 90K.

This was an important threshold since it is above the temperature of liquid nitrogen and liquid nitrogen is far less expensive than liquid helium. This, combined with the ease with which YBCO could be made, enabled the study of superconductivity to expand dramatically.

In this explosion of experiments there were many contradictory results and it was some time before it was widely accepted that the quality of the materials studied could have a dramatic effect upon the results. This is a consequence of the complexity of the new HTS materials: Not only did they not behave much like normal metals above their critical temperature but they were brittle ceramics instead of ductile metals!

This lack of ductility can limit the possible applications of these new materials. Superconducting magnets are made of coils of wire and it is extremely difficult to make wire out of a ceramic material (although it is not impossible and some progress has been made). It also turns out that the sensitivity of SQUIDs is limited by the thermal noise and so even SQUIDs made from HTS materials often require liquid helium as a coolant.

There are, however, new applications that the higher critical temperature make economical. These applications tend to be concentrated in high frequency electronics (ie, microwaves, $\sim 10^9$Hz) and signal processing and are waiting for progress in an unrelated field (reliable solid state cooling devices able to reach the critical temperatures required by these materials) before they are widely deployed – this sort of technological leap-frog is common, with progress in one field awaiting progress in an unrelated one. Since these high frequency electronics are used by communication satellites and cellular telephone networks, the use of both of which is growing, research and development in both cooling devices and high frequency electronics is continuing and substantial progress is being made. Since the clock speed of computers are approaching the microwave regime a possible future application of these materials is in the wires interconnecting the devices within these computers.

Alas, progress in the fundamental understanding of these materials has remained elusive. This elusiveness is in large part caused by the complexity of these new materials which display a complex array of properties, including but not limited to magnetism and superconductivity, as well as a complex crystalline structure. Although there are many competing theories that attempt to explain the presence of superconductivity in these materials the one explored in this thesis explores the likely link between the magnetism and superconductivity in these materials.

1.3 Thesis Outline

In the next chapter the BCS theory of superconductivity is briefly presented along with the simple but astounding modification that allows a repulsive instead of attractive interaction to

cause the electron pairing that is fundamental to superconductivity; how this repulsive interaction changes the symmetry of the superconducting state is also briefly discussed.

The two subsequent chapters give details of the model electron states and pairing interactions that are explored in this thesis. The ramifications of this model are explored somewhat in depth in these two chapters and the effect of one upon the other is calculated in a self-consistent manner.

The following two chapters investigate some of the properties unique to superconductors which are calculated within the model outlined in the preceding chapters and which are compared to the experimental results. These properties include the magnetic susceptibility, the magnetic penetration depth, Josephson tunnelling, the superconducting density of states and the optical conductivity.

The final chapter reports some of the conclusions that can be drawn from the research reported in this thesis.

There is also an appendix which presents some of the computer algorithms used to perform the calculations reported in this thesis.

Chapter 2

The BCS Theory

The BCS theory has ramifications in more areas of physics than just condensed matter. It has applications in nuclear theory in the binding of nucleons in even-even nuclei, the dynamics of degenerate stars (neutron stars and white dwarfs - called "degenerate" because they are supported by the Pauli exclusion principle) and the superfluidity of ^{3}He.

There are two main pieces of evidence that finally led to the theory of superconductivity. The first, the fact that superconductivity was observed in many different metals and alloys, meant that the details of the Fermi surface (and hence the underlying crystal lattice) was not an essential feature. The second piece of evidence was the isotope effect - the critical temperature of a superconductor was proportional to the reciprocal square root of the isotopic mass. The fact that this was the identical mass dependence of the phonons implies that the electron-phonon interaction was crucial to understanding the superconducting state.

2.1 The Frölich Hamiltonian

H. Frölich[10] proposed the following Hamiltonian (in second quantization notation) as a reasonable starting point for the study of a system containing interacting electrons and phonons

$$\mathcal{H} = \mathcal{H}_0 + \lambda \mathcal{H}_1 \tag{2.1}$$

where

$$\mathcal{H}_0 = \sum_{k\sigma} \varepsilon_k c^\dagger_{k\sigma} c_{k\sigma} + \sum_q \hbar\omega_q a^\dagger_q a_q$$

is the total energy of the electrons and phonons without any interactions and

$$\mathcal{H}_1 = \sum_{k\sigma,q} \left(M_q c^\dagger_{k\sigma+q} c_{k\sigma} a_q + M^\dagger_q c^\dagger_{k\sigma-q} c_{k\sigma} a^\dagger_q \right) \tag{2.2}$$

Figure 2.1: The adsorption and emission of phonons is depicted by their Feynmann diagrams. On the left is depicted the adsorption of a phonon of momentum q (wavy line) by an electron of initial momentum k and final momentum $k+q$. On the right is the inverse process – an electron of initial momentum k emits a phonon of momentum q and the electron has a final momentum $k-q$.

is the interaction or perturbation term with electron-phonon matrix element M_q. The λ in Eq. 2.1 is used for counting the order of the perturbation in the following analysis. In these sums the k and q are reciprocal lattice vectors in units of the reciprocal lattice constant, $\sigma = (\uparrow, \downarrow)$ represents the electron spin, $c_k^\dagger$ (c_k) and $a_q^\dagger$ (a_q) are the electron and phonon creation (annihilation) operators, respectively, and ε_k and $\hbar\omega_q$ are the electron and phonon dispersion relations.

While this Hamiltonian was formulated for the electron-phonon interaction there is no reason that it can not be extended to other electron-boson interactions. For high temperature superconducting materials other bosons have been proposed as the cause of superconductivity, such as spin fluctuations (discussed at length in the next chapter). In fact, in liquid ^{3}He the superfluidity is caused by the exchange of ferromagnetic paramagnons.

The first term on the right in Eq. 2.2 is depicted on the left in Fig. 2.1 and corresponds to the adsorption of a phonon of momentum q (wavy line) by an electron of initial momentum k and final momentum $k+q$ (straight lines). The second term on the right in Eq. 2.2 is depicted on the right in Fig. 2.1 and corresponds to the inverse process – an electron of initial momentum k emits a phonon of momentum q and the electron has a final momentum $k-q$. In both diagrams the M_q corresponds to the vertex where the three lines meet.

2.1.1 Virtual Phonons

By performing the canonical transformation

$$\mathcal{H}' = e^{-\lambda S}\mathcal{H}e^{\lambda S}$$

which is defined by the Baker-Hausdorff theorem,

$$e^A B e^{-A} = B + [A,B] + \tfrac{1}{2!}[A,[A,B]] + \tfrac{1}{3!}[A,[A,[A,B]]] + \ldots$$

and in which the operator S is defined by

$$S = \sum_{k\sigma,q} M_q c^\dagger_{k\sigma+q} c_{k\sigma} \left(\alpha a_{-q} + \beta a_q\right)$$

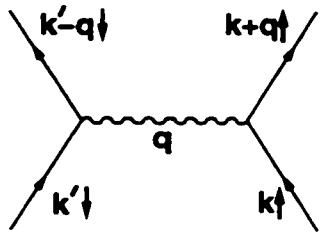

Figure 2.2: This Feynmann diagram corresponds to two electrons of momenta k' and k exchanging a virtual phonon of momentum q an ending up with momenta $k'-q$ and $k+q$ respectively.

on the Frölich Hamiltonian, Eq. 2.1, and choosing the α and β so that the first order term in λ disappears we get

$$\mathcal{H}' = \mathcal{H}_0 + \tfrac{1}{2}\lambda^2 \sum_{k\sigma,k'\sigma',q} |M_q|^2 \frac{2\hbar\omega_q}{(\varepsilon_{k+q}-\varepsilon_k)^2 - (\hbar\omega_q)^2} c^\dagger_{k\sigma+q} c^\dagger_{k'\sigma'-q} c_{k'\sigma'} c_{k\sigma} + O(\lambda^3) \quad (2.3)$$

which has two electrons connected by a virtual phonon (*i.e.*, there are no phonon operators, $a^\dagger_q$ or a_q, left in the interaction term). This process is depicted in Fig. 2.2 and corresponds to two electrons of momenta k' and k exchanging a virtual phonon of momentum q an ending up with momenta $k'-q$ and $k+q$ respectively. The factor $|M_q|^2$ corresponds to the two vertices where the wavy and straight lines meet.

For electrons near the Fermi surface $\varepsilon_{k+q} \approx \varepsilon_k$ and the denominator is negative, *i.e.* the interaction is attractive. This important result is a consequence of the Fermion nature of the electrons (*i.e.* only electrons near the Fermi level are involved in low energy processes).

Frölich next assumed that the most important interactions were those with zero centre of mass momentum, *i.e.* $k + k' = 0$, and zero spin, *i.e.* $\sigma + \sigma' = 0$. By performing this substitution and shifting the sum over q by k (*i.e.*, adding $-k$ to q everywhere in Eq. 2.3) we get from Eq. 2.3

$$\mathcal{H}' = \mathcal{H}_0 + \tfrac{1}{2}\lambda^2 \sum_{k,q} |M_{q-k}|^2 \frac{2\hbar\omega_{q-k}}{(\varepsilon_q-\varepsilon_k)^2 - (\hbar\omega_{q-k})^2} c^\dagger_{q\uparrow} c^\dagger_{-q\downarrow} c_{-k\downarrow} c_{k\uparrow} + O(\lambda^3).$$

This can be written as

$$\mathcal{H}_{\rm red} = \sum_{k\sigma} \varepsilon_k c^\dagger_{k\sigma} c_{k\sigma} + \sum_{k,k'} V_{k,k'} c^\dagger_{k'\uparrow} c^\dagger_{-k'\downarrow} c_{-k\downarrow} c_{k\uparrow} \quad (2.4)$$

where we have dropped all reference to phonons from $\mathcal{H}_o$, and in which

$$V_{k,k'} \equiv \tfrac{1}{2}\lambda^2 |M_{k'-k}|^2 \frac{2\hbar\omega_{k'-k}}{(\varepsilon_{k'}-\varepsilon_k)^2 - (\hbar\omega_{k'-k})^2}$$

is the resulting interaction and we have replaced q with k'. This Hamiltonian, $\mathcal{H}_{\rm red}$, is know as the "reduced Hamiltonian." In the interaction term the four Fermionic operators destroy a pair of electrons with momenta $(k\uparrow, -k\downarrow)$ and create a pair of electrons with momenta $(k'\uparrow, -k'\downarrow)$ with amplitude $V_{k,k'}$.

2.2 Cooper Pairs

Starting with Frölich's Hamiltonian, L.N. Cooper [11] examined the consequence of adding two electrons of opposite spin and momenta to a filled Fermi sea at $T = 0$. The energy of the two electrons, measured with respect to the Fermi level is given by Schrödinger's equation

$$\left(\frac{\hbar^2}{2m}\left(\nabla_r^2 + \nabla_{r'}^2\right) + V_{r-r'}\right)\Psi_{r,r'} = (E - 2\mu)\Psi_{r,r'}$$

where μ is the chemical potential which set the Fermi energy (or the number of electrons). Treating the interaction as a perturbation, the $\Psi_{r,r'}$ are expanded as plane waves of opposite momenta

$$\begin{aligned}\Psi_{r,r'} &= \sum_{k,k'} g_{k,k'} e^{ik\cdot r} e^{ik'\cdot r'} \delta_{k+k'} \\ &= \sum_{k} g_k e^{ik\cdot(r-r')} \end{aligned} \tag{2.5}$$

where $\delta_{k+k'}$ is a Kronecker delta function. Substitution of this wave function into the Schrödinger equation and Fourier transforming yields

$$g_k(E - 2\varepsilon_k) = \sum_{k'} g_{k'} V_{k-k'} \tag{2.6}$$

where $V_{k-k'}$ is the Fourier transform of $V_{r-r'}$ and $\varepsilon_k \equiv \hbar^2 k^2/2m - \mu$ is the unperturbed electron energy.

2.2.1 Isotropic Phonon Interaction

Restricting the interaction to be attractive for electrons within $\hbar\omega_D$ of the Fermi surface (due to the cutoff in the phonon dispersion at the Debye energy, ω_D) we get for the interaction

$$V_{k-k'} = -V_o\theta(|\varepsilon_k| - \hbar\omega_D)\theta(|\varepsilon'_k| - \hbar\omega_D)$$

where $\theta(x)$ is a Heavyside or step function (*i.e.*, zero for a negative argument and one for a positive argument), and defining

$$\begin{aligned} C &\equiv \sum_k g_k V_{k-k'} \\ &= -V_o \sum_k{}' g_k \end{aligned}$$

where the primed sum indicates that it is a sum only over those states within $\hbar\omega_D$ of the Fermi surface. Rearranging Eq. 2.6 and performing a primed sum on both sides yields

$$\sum_k{}' \frac{V_o C}{E - 2\varepsilon_k} = \sum_k{}' g_k = C$$

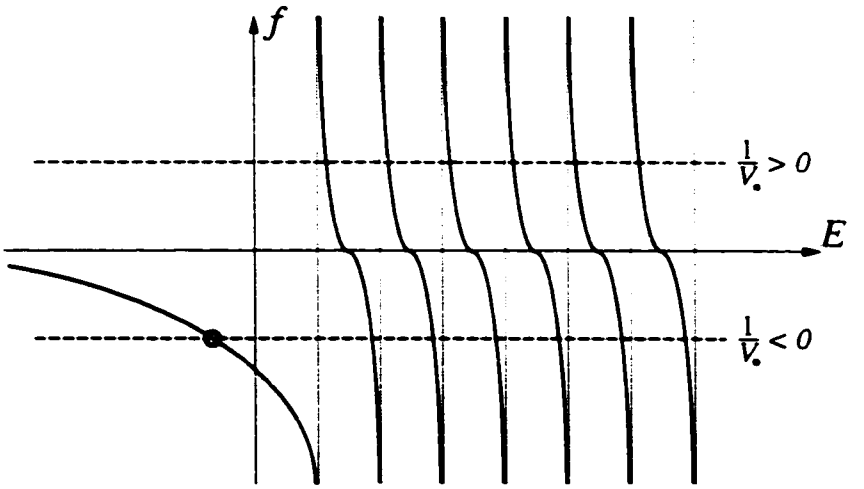

Figure 2.3: The Cooper pair problem (Eq. 2.7) must be solved graphically. The dotted lines are the normal state energies, ε_k and the solid curves represent schematically how f varies with E. The value of f for E between two ε_k approaches $\pm\infty$ except for E below the lowest ε_k, which approaches $f = 0$. When $f = 1/V_o$ is plotted on the same graph (dashed lines) the intersections with the solid curves are the solutions to Eq. 2.7.

and so our equation for the energy of the two electrons added to the filled Fermi sea is, after canceling the C's,

$$\frac{1}{V_o} = \sum_k{}' \frac{1}{E - 2\varepsilon_k} \equiv f. \tag{2.7}$$

This equation can be solved graphically if we note that as $E \to 2\varepsilon_k + 0^+$ only one term in the sum contributes and $f \to +\infty$, while if $E \to 2\varepsilon_k - 0^+$ again only the same term in the sum contributes and $f \to -\infty$. The value of f for E between two ε_k's varies from $+\infty$ to $-\infty$ except for E below the lowest ε_k, which approaches $f = 0$. In Fig. 2.3 f as a function of E is plotted. The dotted lines are the normal state energies, ε_k, and the solid curves represent schematically how f varies with E. When $f = 1/V_o$ is plotted on the same graph (dashed lines) the intersections with the solid curves are the solutions to Eq. 2.7.

For $1/V_o > 0$ and large the eigen energies are very close to those of the unperturbed system (dotted lines), but are shifted up in energy as $1/V_o$ decreases (*i.e.* V_o increases) as would be expected for a repulsive interaction. However, when $1/V_o < 0$ and large the energies are shifted down from the unperturbed system but stay between two unperturbed energy levels (again, as would be expected), except for the lowest energy (circled) which can be shifted down significantly more and, since the first unperturbed state is at zero energy, becomes negative. This is the significant result of the Cooper problem: two electrons of opposite spin and momenta added to the Fermi sea at $T = 0$ can have a lower energy than the top of the Fermi sea and so the Fermi sea is unstable since all of the electrons at the Fermi level can lower their energy by entering a paired state.

The binding energy, E, can be estimated by approximating the primed sum by an integral over a thin energy shell of thickness $\hbar\omega_D$ at the Fermi energy and assuming that the density of states, $N(\varepsilon_k)$, is a constant, $N(0)$, within this shell

$$\begin{aligned}\frac{1}{V_\circ} &= \sum_{k\sigma}{}' \frac{1}{E-2\varepsilon_k} \\ &= 2N(0)\int_{-\hbar\omega_D}^{\hbar\omega_D} \frac{d\varepsilon}{E-2\varepsilon} \\ &= -2N(0)\ln\left(\frac{E-2\hbar\omega_D}{E}\right),\end{aligned}$$

and for $E \ll \hbar\omega_D$

$$E = -2\hbar\omega_D e^{-2/N(0)V_\circ}. \tag{2.8}$$

This expression for the binding energy of a Cooper pair can not be expanded as a convergent series in $V_\circ$ for small $V_\circ$ and is the reason that this solution is not obtainable via perturbation theory.

2.2.2 Spatial Extent of a Cooper Pair

The spatial extent of the Cooper Pair wave function, also known as the coherence length, is given by $\sqrt{\langle R^2\rangle}$, with

$$\langle R^2\rangle = \frac{\int d\boldsymbol{R}\Psi_{\boldsymbol{R}}^\dagger R^2 \Psi_{\boldsymbol{R}}}{\int d\boldsymbol{R}\Psi_{\boldsymbol{R}}^\dagger \Psi_{\boldsymbol{R}}}$$

It is easy to show using Eq. 2.5 that this is equal to

$$\langle R^2\rangle = \frac{\sum_k |\nabla_k g_k|^2}{\sum_k |g_k|^2}.$$

If the isotropic phonon interaction is used this equation can be evaluated as

$$\begin{aligned}\langle R^2\rangle &= \frac{\int_0^{\hbar\omega_D} \frac{d\varepsilon}{(2\varepsilon-E)^4}\frac{2\hbar^2}{m}\varepsilon_F}{\int_0^{\hbar\omega_D}\frac{d\varepsilon}{(2\varepsilon-E)^2}} \\ &= \frac{8\hbar^2\varepsilon_F}{3mE^2}\end{aligned}$$

where ε_F is the Fermi energy. Which gives for the spatial extent of a Cooper pair in conventional superconductors

$$\begin{aligned}\sqrt{\langle R^2\rangle} &= \frac{2}{\sqrt{3}}\frac{\hbar v_F}{|E|} \\ &\approx 10^4 \text{Å}\end{aligned}$$

where v_F is the Fermi velocity given by $\varepsilon_F = mv_F^2/2$. Since the average distance between electrons in a metal is of the order of the lattice spacing, 1Å, this is very large.

For high temperature superconductors, since the condensation energy, E, is much larger and the Fermi velocity, v_F, is much smaller the spatial extent of the Cooper pairs is much smaller, on the order of 20Å in the CuO_2 plane and 3.5Å perpendicular to the CuO_2 plane, and is comparable to the lattice spacing. This introduces the possibility that the Cooper pairs may form at a temperature above T_c and only become coherent at T_c - what is known as "preformed pairs."

2.3 The BCS Wave Function

The next important step in the development of a theory of superconductivity was finding the many body ground state wave function. It was not until J. Bardeen and L.N. Cooper and J.R. Schrieffer[5] proposed what has now become known as the BCS theory that the full physics of conventional superconductors was understood.

One way of creating a wave function with $N/2$ Cooper pairs is to act on the vacuum with

$$\left(\sum_{\boldsymbol{k}} \alpha_{\boldsymbol{k}} c^{\dagger}_{\boldsymbol{k}\uparrow} c^{\dagger}_{-\boldsymbol{k}\downarrow}\right)^{N/2} |0\rangle \tag{2.9}$$

where the sum is over all $\boldsymbol{k}$, the $\alpha_{\boldsymbol{k}}$ are determined by a variational principle, and $|0\rangle$ is the vacuum. Each term in the expansion will have N creation operators, although there will be many terms with duplicate creation operators that will not contribute due to the anticommutation of the Fermionic operators, $c_{\boldsymbol{k}\sigma}$.

BCS assumed that each Cooper pair had amplitude $v_{\boldsymbol{k}_i}$ to be included in the wave function and $u_{\boldsymbol{k}_i}$ not to be included in the wave function (with $|u_{\boldsymbol{k}_i}|^2 + |v_{\boldsymbol{k}_i}|^2 = 1$)

$$\begin{aligned} |G\rangle &= \left(u_{\boldsymbol{k}_1} + v_{\boldsymbol{k}_1} c^{\dagger}_{\boldsymbol{k}_1\uparrow} c^{\dagger}_{-\boldsymbol{k}_1\downarrow}\right)\left(u_{\boldsymbol{k}_2} + v_{\boldsymbol{k}_2} c^{\dagger}_{\boldsymbol{k}_2\uparrow} c^{\dagger}_{-\boldsymbol{k}_2\downarrow}\right)\cdots|0\rangle \\ &= \prod_{\boldsymbol{k}_i}\left(u_{\boldsymbol{k}_i} + v_{\boldsymbol{k}_i} c^{\dagger}_{\boldsymbol{k}_i\uparrow} c^{\dagger}_{-\boldsymbol{k}_i\downarrow}\right)|0\rangle \end{aligned}$$

in which $|G\rangle$ represents the ground state BCS wave function. The number of electrons present in this wave function is not fixed but will be sharply peaked around the number set by the chemical potential. That this wave function contains Eq. 2.9 as its projection onto the N-particle manifold can be easily demonstrated by manipulating it as follows to obtain the projection onto the N-particle

manifold given by Eq. 2.9:

$$
\begin{aligned}
|G\rangle &= \prod_{k_i'} u_{k_i'} \prod_{k_i} \left(1 + \frac{v_{k_i}}{u_{k_i}} c^\dagger_{k_i,\uparrow} c^\dagger_{-k_i,\downarrow}\right)|0\rangle \\
&= \prod_{k_i'} u_{k_i'} \prod_{k_i} \left(1 + \frac{v_{k_i}}{u_{k_i}} c^\dagger_{k_i,\uparrow} c^\dagger_{-k_i,\downarrow} + \frac{1}{2!}\left(\frac{v_{k_i}}{u_{k_i}} c^\dagger_{k_i,\uparrow} c^\dagger_{-k_i,\downarrow}\right)^2 + \frac{1}{3!}\left(\frac{v_{k_i}}{u_{k_i}} c^\dagger_{k_i,\uparrow} c^\dagger_{-k_i,\downarrow}\right)^3 + \dots\right)|0\rangle \\
&= \prod_{k_i'} u_{k_i'} e^{\sum_{k_i} \frac{v_{k_i}}{u_{k_i}} c^\dagger_{k_i,\uparrow} c^\dagger_{-k_i,\downarrow}}|0\rangle \\
&= \prod_{k_i'} u_{k_i'} \left(1 + \left(\sum_{k_i} \frac{v_{k_i}}{u_{k_i}} c^\dagger_{k_i,\uparrow} c^\dagger_{-k_i,\downarrow}\right) + \dots + \frac{1}{(N/2)!}\left(\sum_{k_i} \frac{v_{k_i}}{u_{k_i}} c^\dagger_{k_{iN/2}\uparrow} c^\dagger_{-k_{iN/2}\downarrow}\right)^{N/2} + \dots\right)|0\rangle
\end{aligned}
$$

where in the third line use has been made of the relation $\prod_k e^{x_k} = e^{\sum_k x_k}$.

Once the wave function of a system is known one can calculate expectation values, such as $\langle E\rangle$, in order to compare with physical observables. However, for the purposes of this thesis the quantities of interest can be calculated in a more straightforward manner from the reduced Hamiltonian, Eq. 2.4.

2.4 The BCS Equation

By taking the mean field approximation of the interaction term in the reduced Hamiltonian, Eq. 2.4,

$$
\begin{aligned}
c_{k\uparrow} c_{-k\downarrow} &= \chi^p_k + (c_{k\uparrow} c_{-k\downarrow} - \chi^p_k) \\
c^\dagger_{k\uparrow} c^\dagger_{-k\downarrow} &= \chi^{p\dagger}_k + \left(c^\dagger_{k\uparrow} c^\dagger_{-k\downarrow} - \chi^{p\dagger}_k\right)
\end{aligned}
$$

where the pair susceptibility, $\chi^p_k \equiv \langle c_{k\uparrow} c_{-k\downarrow}\rangle$, is the thermal average of the pair annihilation operator, $c_{k\uparrow} c_{-k\downarrow}$. By neglecting the fluctuations (*i.e.* the term bilinear in the fluctuation, $(c_{k\uparrow} c_{-k\downarrow} - \chi^p_k)$) the reduced Hamiltonian, Eq. 2.4, can be rewritten as

$$
\mathcal{H}_{\rm red} = \sum_k \varepsilon_k \left(c^\dagger_{k\uparrow} c_{k\uparrow} + c^\dagger_{k\downarrow} c_{k\downarrow}\right) - \sum_k \left(\Delta_k c^\dagger_{k\uparrow} c^\dagger_{-k\downarrow} + \Delta^\dagger_k c_{k\uparrow} c_{-k\downarrow}\right) + C, \tag{2.10}
$$

where we have explicitly performed the sum over the spins, C is a constant, and

$$
\Delta_k \equiv -\sum_{k'} V_{k,k'} \chi^p_{k'} \tag{2.11}
$$

is, as we shall see, the BCS gap equation.

This mean field Hamiltonian can be diagonalized by a Bogolyubov canonical transformation[12, 13], defined by

$$
\begin{aligned}
c_{k\uparrow} &= u^\dagger_k \gamma_{k,0} + v_k \gamma^\dagger_{k,1} \\
c^\dagger_{-k\downarrow} &= -v^\dagger_k \gamma_{k,0} + u_k \gamma^\dagger_{k,1}
\end{aligned} \tag{2.12}
$$

with the normalization condition, $|u_k|^2 + |v_k|^2 = 1$. By substituting Eq. 2.12 into the reduced Hamiltonian, Eq. 2.10, the coefficient for the off-diagonal terms is

$$2\varepsilon_k u_k v_k + \Delta_k^\dagger |v_k|^2 - \Delta_k |u_k|^2$$

which is set equal to zero to diagonalize the Hamiltonian. Combining this with the normalization condition and solving for the u_k and v_k yields

$$|v_k|^2 = 1 - |u_k|^2 = \tfrac{1}{2}\left(1 - \frac{\varepsilon_k}{E_k}\right) \tag{2.13}$$

where $E_k^2 \equiv \varepsilon_k^2 + |\Delta_k|^2$ is the energy of the $\gamma_{k,s}$ quasiparticles defined by Eq. 2.12 (*i.e.*, they are the eigen values of the diagonalized Hamiltonian).

Inverting the Bogolyubov canonical transformation, Eq. 2.12, we get

$$\begin{aligned} \gamma_{k,0} &= u_k c_{k\uparrow} - v_k c_{-k\downarrow}^\dagger \\ \gamma_{k,1} &= u_k c_{-k\downarrow} + v_k c_{k\uparrow}^\dagger \end{aligned} \tag{2.14}$$

Examining equations 2.13 and 2.14 we can see that as $\Delta \to 0$, $E_k \to |\varepsilon_k|$, $v_k \to 0$ and $u_k \to 1$ and the $\gamma_{k,s}$ quasiparticle operators become the electron operators. As Δ_k becomes non-zero the quasiparticle excitations are particle-hole pairs with opposite spin and momenta, *i.e.*, the BCS ground state wave function plays the rôle of vacuum for the $\gamma_{k,s}$

$$\gamma_{k,s}|G\rangle = 0$$

Since the reduced Hamiltonian is diagonal in the Fermionic quasiparticles, $\gamma_{k,s}$, we can, from elementary statistical mechanics, write the expectation value of their number operators as

$$\left\langle \gamma_{k,s}^\dagger \gamma_{k,s} \right\rangle = f(\beta E_k)$$

where $f(x) \equiv (1 + e^x)^{-1}$ is the Fermi-Dirac distribution (with β the reciprocal temperature, $\beta \equiv 1/k_B T$, with k_B Boltzmann's constant[1]), and, using Eq. 2.12, we can solve for the pair susceptibility

$$\begin{aligned} \chi_k^p &\equiv \langle c_{k\uparrow} c_{-k\downarrow} \rangle \\ &= u_k^\dagger v_k \left(1 - \left\langle \gamma_{k,0}^\dagger \gamma_{k,0} \right\rangle - \left\langle \gamma_{k,1}^\dagger \gamma_{k,1} \right\rangle\right) \\ &= u_k^\dagger v_k \left(1 - 2f(\beta E_k)\right) \\ &= \frac{\Delta_k}{2E_k} \tanh\left(\tfrac{1}{2}\beta E_k\right). \end{aligned} \tag{2.15}$$

Combining this expression with the Eq. 2.11 gives the BCS equation

$$\Delta_k \equiv -\sum_{k'} V_{k,k'} \frac{\Delta_{k'}}{2E_{k'}} \tanh\left(\tfrac{1}{2}\beta E_{k'}\right). \tag{2.16}$$

[1] Temperature is an energy unit which is related to more conventional energy units by Boltzmann's constant, $k_B = 0.086\text{eV/K}$

Note that Δ_k is completely determined by the self-consistent solution to this equation and that the only inputs to this equation are the temperature, T, the dispersion, ε_k, and the interaction, $V_{k,k'}$.

The quantity Δ_k is the order parameter for the superconducting phase transition. Below a certain temperature, T_c, which depends upon ε_k and $V_{k,k'}$, Δ_k becomes non-zero. This phase transition, like all phase transitions, has a corresponding broken symmetry. In the case of superconductivity the broken syymmetry is global gauge symmetry: Above T_c we can replace the creation and annihilation operators, $c_k^\dagger$ and c_k, with $c_k^\dagger e^{i\phi}$ and $c_k e^{-i\phi}$ without effecting the electron system: this is not the case below T_c and so the gauge symmetry is broken.

2.5 Interactions

2.5.1 Isotropic Phonon Interaction

The BCS gap equation, Eq. 2.16, depends upon two functions (the interaction, $V_{k,k'}$, and the dispersion, ε_k) and the temperature, T. In order to make further progress in the analysis of this equation we must make some assumptions about the two functions. By making similar assumptions as were made for the Cooper pair problem (namely, $V_{k-k'} = -V_o\theta(|\varepsilon_k| - \hbar\omega_D)\theta(|\varepsilon'_k| - \hbar\omega_D)$ and $\varepsilon_k = \hbar^2k^2/2m - \mu$ with $N(\varepsilon_k)$ constant within $\hbar\omega_D$ of the Fermi surface) we see that the gap, $\Delta_k \equiv \Delta_o$, has no k-dependence and the gap equation becomes

$$\Delta_o = N(0)\int_{-\hbar\omega_D}^{\hbar\omega_D} V_o \frac{\Delta_o}{2E_k}\tanh\left(\frac{E_k}{2k_BT}\right)dE. \tag{2.17}$$

We can solve this equation in two limits in a straight forward manner. First in the limit $T \to 0$,

$$\Delta_o = \hbar\omega_D e^{-2/N(0)V_o}$$

which is the same as Eq. 2.8 so we see that Δ_o is the binding energy of a Cooper pair (*i.e.* the gap), and second, in the limit $T \to T_c$, $\Delta_o \to 0$ we get

$$k_BT_c = 1.13\hbar\omega_D e^{-1/N(0)V_o}.$$

By taking the ratio of these two equations we get

$$\frac{2\Delta_o}{k_BT_c} = 3.53$$

which is one of the famous results of the BCS theory.

For $0 < T < T_c$ the isotropic BCS equation can be solved numerically. In Fig. 2.4 the temperature dependence of the gap normalized to its zero temperature value is plotted as a function of the temperature normalized to T_c (solid curve). This temperature dependence is the same as for any second order transition in the mean field approximation and accurately reflects the observed behaviour of conventional superconductors. That the mean field approximation is accurate is a consequence of the large coherence length of the Cooper pairs (see §2.2.2).

2.5.2 Anisotropic Interactions

While an isotropic interaction is a good first approximation for conventional superconductors an implicit assumption of this choice of interaction is that the order parameter is also isotropic. It is the interaction that determines the possible $\boldsymbol{k}$-space dependence of the order parameter - choosing an isotropic interaction, as seen in §2.5.1, results in an isotropic order parameter.

We can, instead, choose any periodic function of the the difference $\boldsymbol{k}-\boldsymbol{k}'$ (This restriction is so that the interaction conserves momentum.). Any function of the difference $\boldsymbol{k}-\boldsymbol{k}'$ can be written as a sum of products of periodic basis functions of $\boldsymbol{k}$ and $\boldsymbol{k}'$ (*i.e.* a separable potential) [14, 15]

$$V_{\boldsymbol{k}-\boldsymbol{k}'} = \sum_j V_j \eta^j_{\boldsymbol{k}} \eta^j_{\boldsymbol{k}'}. \tag{2.18}$$

That this is so can be seen by replacing each $\cos(jk_x - jk'_x)$ in the Fourier expansion of $V_{\boldsymbol{k}-\boldsymbol{k}'}$ with $\cos(jk_x)\cos(jk'_x)$ (the $\sin(jk_x)\sin(jk'_x)$ terms will not contribute since they are odd in k'_x) with j enumerating the terms in the Fourier expansion (which will only contain cosine terms due to the periodicity of the Brillouin zone).

Upon substituting this separated potential, Eq. 2.18, into the BCS gap equation, Eq. 2.16, we get

$$\begin{aligned} \Delta_{\boldsymbol{k}} &= \sum_i \left\{ V_i \sum_{\boldsymbol{k}'} \eta^i_{\boldsymbol{k}'} \frac{\Delta_{\boldsymbol{k}'}}{2E_{\boldsymbol{k}'}} \right\} \eta^i_{\boldsymbol{k}} \\ &= \sum_i A_i \eta^i_{\boldsymbol{k}} \end{aligned} \tag{2.19}$$

where the A_i, defined as the quantities in the braces, are just c-numbers. We can see that the order parameter, $\Delta_{\boldsymbol{k}}$, can be written as a sum over the same set of basis functions as were used when writing $V_{\boldsymbol{k}-\boldsymbol{k}'}$ as a separable potential, and so it can not contain any basis functions that were not present in the separated potential and is likely to contain only those for which the corresponding V_i are relatively large. As a consequence the gap, $\Delta_{\boldsymbol{k}}$, can, as seen in Eq. 2.19, also have a more complicated $\boldsymbol{k}$-dependence - can in fact belong to irreducible representations[2] with a different symmetry from that in the above discussion for isotropic interactions (which belong to the identity representation).

2.5.3 Interaction Independent Properties

Many superconducting properties are dependent only upon the order parameter and the dispersion and are explicitly independent of the interaction. In light of this it is desirable not to use an explicit interaction when calculating these properties and instead to use only the dispersions detailed in Ch. 3 and an order parameter whose temperature dependence is given by a function that

[2]The irreducible representations (irreps) are the possible symmetries that are allowed by the crystal symmetry. For tetragonal systems the crystal symmetry is D_4 and there are four one dimensional irreps. In this thesis we only examine two of these, the identity ($s_{x^2+y^2}$) and d-wave ($d_{x^2-y^2}$) representations.

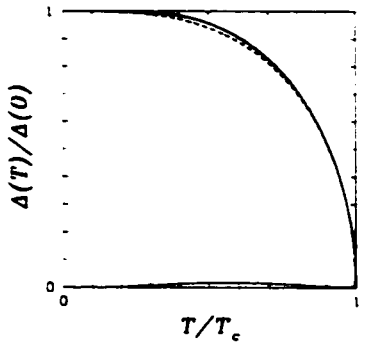

Figure 2.4: The temperature dependence of the order parameter as found by solving the BCS equation with an isotropic interaction (solid curve) and that given by $h(T)$, Eq. 2.21, (dashed curve). The agreement between the two curves is quite good except near $T/T_c \sim 0.5$ and $T/T_c \sim 0.5$ where, $h(T)$ deviates from the BCS solution; the dotted curve is the absolute value of the difference of the solid and dashed curves. This deviation is acceptable with the caveat that calculations of properties that rely upon the temperature derivative of the order parameter, such as the specific heat, will be incorrect if they use this function.

approximates that given by the BCS equation and whose momentum dependence is given by some set of basis functions which can be written as

$$\Delta_{\hat{k}}(T) = h(T) \sum_i A_i \eta^i_{\hat{k}} \tag{2.20}$$

with $h(T)$ giving the temperature dependence and, in a manner similar to the separable potential described in Eq. 2.19, the momentum dependence given by a set of basis functions, $\eta^i_{\hat{k}}$.

A good choice for the temperature dependence is

$$h(T) = \tanh\left(1.74\sqrt{T_c/T - 1}\right) \tag{2.21}$$

which agrees very well with the temperature dependence of the BCS equation. Shown in Fig. 2.4 is the temperature dependence of the order parameter as found by solving the BCS equation (solid curve) and that given by $h(T)$ (dashed curve). The agreement between the two curves is quite good except near $T/T_c \sim 0.5$ where, $h(T)$ deviates from the BCS solution; the dotted curve is the absolute value of the difference of the solid and dashed curves. This deviation is acceptable with the caveat that calculations of properties that rely upon the temperature derivative of the order parameter, such as the specific heat, will be incorrect if they use this function.

The momentum dependent functions must preserve the symmetry properties of the crystal; for high temperature superconductors (HTS), with D_4 or D_2 symmetry, the interesting choices are

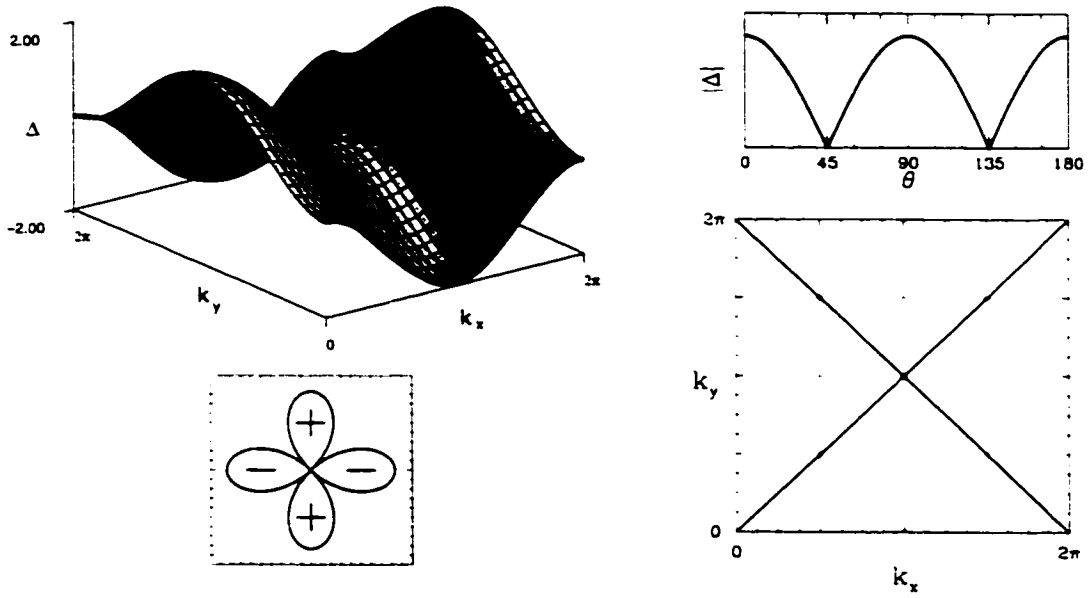

Figure 2.5: Four different representations of a d-wave order parameter, Δ_k. At the top left is a stereographic projection of a d-wave order parameter; the dark line is the node where $\Delta_k = 0$. On the top right is the magnitude of the gap as a function of angle along the Fermi surface and on the bottom left is the same quantity on a radial plot. Below on the right is the position of the gap nodes in the first Brillouin zone.

limited to combinations of the set

$$\begin{aligned} \eta_{\mathbf{k}}^{\circ} &\equiv 1 \\ \eta_{\mathbf{k}}^{s,j} &\equiv \cos(jk_x) + \cos(jk_y) \\ \eta_{\mathbf{k}}^{d,j} &\equiv \cos(jk_x) - \cos(jk_y) \end{aligned} \tag{2.22}$$

with j a positive integer. In general only $\eta_{\mathbf{k}}^{\circ}$ and the $j = 1$ case of the other basis functions will be needed; cases in which the j subscripts are omitted will be assumed to represent the $j = 1$ case. There are other allowed irreducible representations for the order parameter but only these two (*i.e.* s and d-waves) are considered in this thesis. For D_4 symmetry the $\eta_{\mathbf{k}}^{s,j}$ and $\eta_{\mathbf{k}}^{\circ}$ basis functions belong to the same irreducible representation (referred to as s-wave) but $\eta_{\mathbf{k}}^{d,j}$ belongs to a different irreducible representation (referred to as d-wave). For D_2 symmetry they all belong to the same representation but, since the D_4 symmetry is only slightly broken, the distinction is kept and the resulting order parameters are said to have "$d \pm \delta s$" symmetry if $\eta_{\mathbf{k}}^{d,j}$ is the dominant component.

Of particular interest for HTS are order parameters with the d-wave symmetry, $\eta_{\mathbf{k}}^{d}$, which is odd with respect to rotations by 90°. Shown in Fig. 2.5 are four different representations of a d-wave order parameter, $\Delta_{\mathbf{k}} = \eta_{\mathbf{k}}^{\mathrm{d}}$. At the top left is a stereographic projection of $\eta_{\mathbf{k}}^{\mathrm{d}}$; the dark line is the node where $\eta_{\mathbf{k}}^{\mathrm{d}}$ equals zero. On the top right is the magnitude of the $\eta_{\mathbf{k}}^{\mathrm{d}}$ as a function of angle

along the Fermi surface (The Fermi surfaces of HTS materials are discussed in detail in the next chapter.) and on the bottom left is the same quantity on a radial plot, note how the sign changes under 90° rotations. Below on the right is the position of the gap nodes in the first Brillouin zone.

2.5.4 Sample Anisotropic Interactions

Nearest Neighbour Interaction

As an example of a separable interaction a nearest neighbour interaction, $V^{\rm nn}_{\boldsymbol{r}-\boldsymbol{r}'} = -U^{\rm nn}\delta_{|\boldsymbol{r}-\boldsymbol{r}'|,1}$, is investigated. Note that since $V^{\rm nn}_{\boldsymbol{r}-\boldsymbol{r}'}$ is negative it is an attractive interaction. It has, in reciprocal space, the form

$$\begin{aligned} V^{\rm nn}_{\boldsymbol{k}-\boldsymbol{k}'} &= -U^{\rm nn}\left(\cos(k_x - k'_x) + \cos(k_y - k'_y)\right) \\ &= -U^{\rm nn}\sum_{i=1}^{4}\eta^i_{\boldsymbol{k}}\eta^i_{\boldsymbol{k}'} \end{aligned}$$

where

$$\begin{aligned} \eta^1_{\boldsymbol{k}} &\equiv \cos(k_x) + \cos(k_y) \\ \eta^2_{\boldsymbol{k}} &\equiv \cos(k_x) - \cos(k_y) \\ \eta^3_{\boldsymbol{k}} &\equiv \sin(k_x) + \sin(k_y) \\ \eta^4_{\boldsymbol{k}} &\equiv \sin(k_x) - \sin(k_y) \end{aligned}$$

are the basis functions which contribute to this interaction.

Upon substitution of the above into the BCS equation, Eq. 2.19, we get

$$\begin{aligned} \Delta_{\boldsymbol{k}} &= \sum_{i=1}^{4}\left\{U^{\rm nn}\sum_{\boldsymbol{k}'}\eta^i_{\boldsymbol{k}'}\frac{\Delta_{\boldsymbol{k}'}}{2E_{\boldsymbol{k}'}}\right\}\eta^i_{\boldsymbol{k}} \\ &= A_1\eta^1_{\boldsymbol{k}} + A_2\eta^2_{\boldsymbol{k}}, \end{aligned}$$

in which the A_i are c-numbers defined as the terms in the braces. Note that the sums containing $\eta^{3,4}_{\boldsymbol{k}}$ do not contribute to $\Delta_{\boldsymbol{k}}$ since they are odd in $k'_{x,y}$. The strength of the interaction, $U^{\rm nn}$, is, in this model, an adjustable parameter that is varied to yield a desired T_c when the BCS equation is solved.

This sort of interaction could arise in a system in which there are unusual phonons (*e.g.* "breathing" modes). Note that the A_i are not required to have the same complex phases [14] and that a system with different phases of the A_i would break time reversal symmetry. [16]

Repulsive Interaction

A very interesting result of the $\boldsymbol{k}$-space anisotropy of the interaction is that superconductivity can result from a repulsive interaction if it is peaked at (or near) $\boldsymbol{Q} \equiv (\pi, \pi)$. This

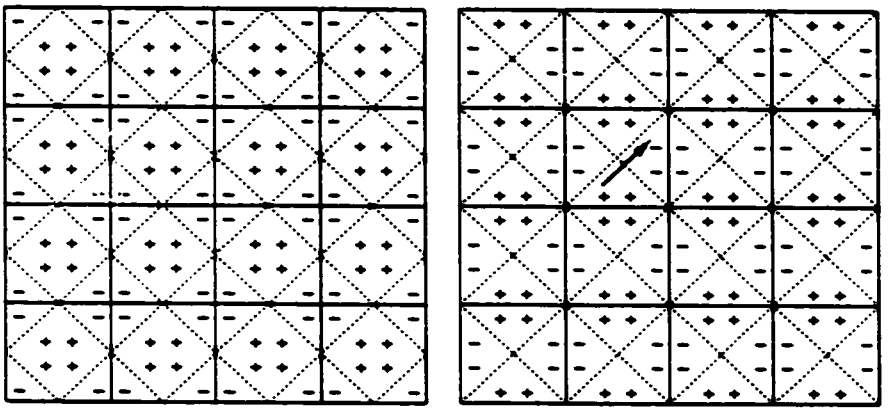

Figure 2.6: Shown in an extended Brillouin zone scheme (the solid lines depict the zone boundaries) is the order parameter that when connected to itself by $\boldsymbol{Q} \equiv (\pi, \pi)$ (gray arrow) has the opposite sign (the dotted lines depict the order parameter nodes). There are two ways that the gap nodes (dotted lines) can be placed in the Brillouin zone (solid lines) that preserve the crystal symmetry. The first way, on the left, has s-wave symmetry and the second way, on the right, has d-wave symmetry. However, since all possible d-wave functions have the gap nodes depicted on the right while only special s-wave functions have the gap nodes depicted on the left the d-wave symmetry is more stable.

superconductivity has an order parameter with d-wave symmetry, Fig. 2.5, which has the property $\eta^{\rm d}_{\boldsymbol{k}+\boldsymbol{Q}} = -\eta^{\rm d}_{\boldsymbol{k}}$.

That a repulsive interaction peaked at $\boldsymbol{Q} \equiv (\pi, \pi)$ can produce d-wave superconductivity can be elucidated by making the substitution $V_{\boldsymbol{k},\boldsymbol{k}'} = V_{\rm o}\delta_{|\boldsymbol{k}-\boldsymbol{k}'-\boldsymbol{Q}|}$ into the BCS equation, Eq. 2.16, to give

$$\begin{aligned} \Delta_{\boldsymbol{k}} &= -V_{\rm o}\sum_{\boldsymbol{k}'}\delta_{|\boldsymbol{k}-\boldsymbol{k}'-\boldsymbol{Q}|}\Delta_{\boldsymbol{k}'}\frac{\tanh\left(\frac{1}{2}\beta E_{\boldsymbol{k}'}\right)}{2E_{\boldsymbol{k}'}} \\ &= -V_{\rm o}\Delta_{\boldsymbol{k}-\boldsymbol{Q}}\left\{\frac{\tanh\left(\frac{1}{2}\beta E_{\boldsymbol{k}-\boldsymbol{Q}}\right)}{2E_{\boldsymbol{k}-\boldsymbol{Q}}}\right\}, \end{aligned}$$

and noting that since the term in the braces is positive definite and $V_{\rm o}$ is positive by definition, $\Delta_{\boldsymbol{k}-\boldsymbol{Q}}$ must have the opposite sign of $\Delta_{\boldsymbol{k}}$.

Shown in Fig. 2.6 is an extended Brillouin zone scheme (the solid lines depict the zone boundaries) of the two possible nodal structures of the order parameter (dotted lines) that when connected to itself by $\boldsymbol{Q} \equiv (\pi, \pi)$ (gray arrow) has the opposite sign (the dotted lines depict the order parameter nodes) that can be placed in the Brillouin zone (solid lines) and preserve the crystal symmetry. The first way, on the left, has s-wave symmetry (given by $\eta^{s}_{\boldsymbol{k}}$ in Eq. 2.22) and the second way, on the right, has d-wave symmetry (given by $\eta^{d}_{\boldsymbol{k}}$ in Eq. 2.22 and shown in Fig. 2.5). However, since all possible d-wave functions have the gap nodes depicted on the right while only special s-wave functions have the gap nodes depicted on the left the d-wave symmetry is more stable. Note that the two basis functions, $\eta^{s,d}_{\boldsymbol{k}}$, discussed in §2.5.4 on p. 18 have exactly this nodal form and that the

order parameter found upon solution of the BCS equation can, depending upon the dispersion used, have either or both (in an $s + id$ combination) of these symmetries.[14, 15]

In §4.2 the MMP model interaction [17] is introduced and discussed. This model interaction is repulsive and peaked at $\boldsymbol{Q} \equiv (\pi, \pi)$ and the solution of the BCS equation yields d-wave solutions.

2.6 Beyond BCS – The Eliashberg Equations

In 1960 Eliashberg introduced his eponymous equations [6, 7] which extended the BCS equations to allow for a frequency dependent interaction. The formalism used, Thermal Green's functions, appears initially quite different from that used above but in fact the pair susceptibility, $\chi^{\mathrm{p}}_{\boldsymbol{k}}$, is a Green's function.[3]

The Eliashberg equations are given by

$$\widehat{G}^{-1}_{\boldsymbol{k},n} = \widehat{G^{\circ}}^{-1}_{\boldsymbol{k},n} - \widehat{\Sigma}_{\boldsymbol{k},n} \tag{2.23}$$

where

$$\widehat{G^{\circ}}^{-1}_{\boldsymbol{k},n} = \imath\omega_n\widehat{\tau}_0 - \varepsilon_{\boldsymbol{k}}\widehat{\tau}_3 \tag{2.24}$$

bs the non-interacting Green's functions,

$$\widehat{\Sigma}_{\boldsymbol{k},n} \equiv \imath\omega_n(1 - Z_{\boldsymbol{k},n})\widehat{\tau}_0 + \xi_{\boldsymbol{k},n}\widehat{\tau}_3 + \phi_{\boldsymbol{k},n}\widehat{\tau}_1 \tag{2.25}$$

is the self-energy and

$$\widehat{G}^{-1}_{\boldsymbol{k},n} = \imath\tilde{\omega}_{\boldsymbol{k},n}\widehat{\tau}_0 - \tilde{\varepsilon}_{\boldsymbol{k},n}\widehat{\tau}_3 - \phi_{\boldsymbol{k},n}\widehat{\tau}_1 \tag{2.26}$$

is the inverse of the interacting (or dressed) Green's function where the renormalized dispersion and Matsubara frequencies have been defined as

$$\tilde{\varepsilon}_{\boldsymbol{k},n} \equiv \varepsilon_{\boldsymbol{k}} + \xi_{\boldsymbol{k},n} \tag{2.27}$$

$$\tilde{\omega}_{\boldsymbol{k},n} \equiv \omega_n Z_{\boldsymbol{k},n}, \tag{2.28}$$

and the $\widehat{\tau}_i$ are the Pauli matrices defined by

$$\widehat{\tau}_1 \equiv \begin{bmatrix} 0 & 1 \\ 1 & 0 \end{bmatrix}, \widehat{\tau}_2 \equiv \begin{bmatrix} 0 & -\imath \\ \imath & 0 \end{bmatrix}, \widehat{\tau}_3 \equiv \begin{bmatrix} 1 & 0 \\ 0 & -1 \end{bmatrix}, \tag{2.29}$$

[3]Green's functions, invented by a nineteenth century miller named George Green [18] for the analysis of Maxwell's equations (and, incidentally, introduced the concept of a "potential") have found uses in almost every area of physics that involves the solution of differential equations. Often these functions go by other names, for example, the ubiquitous propagators it QED are nothing but Green's functions. An even more frequently encountered example is George Green's original application of his eponymous function: The solution of Laplace's equation, $\nabla^2_r\phi_r = \rho_r$ (the $1/|r - r'|$ in $\phi_r = \int dr' \rho_{r'}/|r - r'|$ is the original Green's function).

with $\hat{\tau}_0 \equiv \hat{1}$ by convention. The BCS equation is, essentially, the zero frequency part of the off diagonal term of the self energy (in the BCS approximation the diagonal terms of the self energy are assumed negligible). The quantities $\phi_{k,n}$, $\xi_{k,n}$ and $Z_{k,n}$ are discussed in more detail in §4.1.1: $\phi_{k,n}$ is the Eliashberg analogue of the BCS order parameter, Δ_k.

By putting in the Pauli matrices the expression for the self-energy, $\hat{\Sigma}_{k,n}$, and the Green's function, $\hat{G}_{k,n}$ are 2×2 matricies

$$\hat{\Sigma}_{k,n} = \begin{bmatrix} i\omega_n(1 - Z_{k,n}) + \xi_{k,n} & \phi_{k,n} \\ \phi^{\dagger}_{k,n} & i\omega_n(1 - Z_{k,n}) - \xi_{k,n} \end{bmatrix} \tag{2.30}$$

$$\hat{G}^{-1}_{k,n} = \begin{bmatrix} -\tilde{\varepsilon}_{k,n} + i\tilde{\omega}_{k,n} & -\phi_{k,n} \\ -\phi^{\dagger}_{k,n} & \tilde{\varepsilon}_{k,n} + i\tilde{\omega}_{k,n} \end{bmatrix}, \tag{2.31}$$

At a certain critical temperature, called T_c, $\phi_{k,n}$ becomes non-zero and the system enters the superconducting state. In the normal state (*i.e.* $\phi_{k,n} = 0$ or $T > T_c$) the interacting Green's function, $\hat{G}^{-1}_{k,n}$, has the same form as the non-interacting Green's function, $\hat{G^{\circ}}^{-1}_{k,n}$, but with the energies and Matsubara frequencies having their renormalized values. As the temperature is decreased below the critical temperature the off-diagonal terms in the Green's function, Eq. 2.31, (sometimes called the "anomalous Green's function") become larger until they saturate at a value a few times larger that T_c.

Inverting $\hat{G}^{-1}_{k,n}$ to form $\hat{G}_{k,n}$ results in

$$\hat{G}_{k,n} = \frac{1}{\left|\hat{G}^{-1}_{k,n}\right|} \begin{bmatrix} \tilde{\varepsilon}_{k,n} + i\tilde{\omega}_{k,n} & \phi_{k,n} \\ \phi^{\dagger}_{k,n} & -\tilde{\varepsilon}_{k,n} + i\tilde{\omega}_{k,n} \end{bmatrix} \tag{2.32}$$

where

$$\left|\hat{G}^{-1}_{k,n}\right| = -\tilde{\varepsilon}^2_{k,n} - \tilde{\omega}^2_{k,n} - |\phi_{k,n}|^2 \tag{2.33}$$

is the determinant of the inverse of the Green's function, $\hat{G}^{-1}_{k,n}$.

In order to solve this coupled set of non-linear equations for $\hat{\Sigma}_{k,n}$, the self energy, (and, hence, the Green's function, $\hat{G}_{k,n}$) another expression for $\hat{\Sigma}_{k,n}$ is required. This expression comes from the effective electron-electron interaction.

2.6.1 Conventional Superconductors

In conventional superconductors the electron-phonon interaction is responsible for the phase transition to the superconducting state. In this model the self-energy is a convolution of the Green's function for the phonons, $D_{k,n}$, (multiplied by an electron-phonon matrix element, $g_{k,n}$) and the electron's Green's function

$$\hat{\Sigma}_{k,n} = -T \sum_{q} \sum_{m} |g_{k-q}|^2 D_{k-q,n-m} \hat{G}_{q,m}. \tag{2.34}$$

By equating this expression for the self-energy with that given by Eq. 2.30 we can obtain equations for $\tilde{\varepsilon}_{k,n}$, $\tilde{\omega}_{k,n}$ and $\phi_{k,n}$ which must then be solved self-consistently (*i.e.*, they form a set of coupled, non-linear integral equations). In practice,[19] the phonon's Green's function is replaced with by a function know as $\alpha^2 F_k(\Omega)$, which can be derived from tunneling experiments by a process know as "tunneling inversion."[20, 19] This function is related to the spectral representation of the phonon's Green's function, $B_k(\Omega)$, by

$$\alpha^2 F_k(\Omega) \equiv N(0)\,|g_k|^2\, B_k(\Omega)$$

which, in turn, is related to the phonon's Green's function by

$$D_{k,n} = \int_0^\infty d\Omega \left(\frac{1}{i\omega_n - \Omega} - \frac{1}{i\omega_n + \Omega} \right) B_k(\Omega).$$

In the above $N(0)$ is the density of states at the Fermi level. This process yields for the self-energy

$$\widehat{\Sigma}_{k,n} = -T \sum_q \sum_m V^{\rm ep}_{k-q,n-m} \widehat{G}_{q,m}$$

where the electron-phonon interaction, $V^{\rm ep}_{k,n}$, is given by

$$V^{\rm ep}_{k,n} \equiv \int_0^\infty d\Omega \left(\frac{-2\Omega}{\omega_n^2 + \Omega^2} \right) \frac{\alpha^2 F_k(\Omega)}{N(0)}.$$

This process yields the set of coupled, non-linear integral equations

$$\begin{aligned}
\tilde{\varepsilon}_{k,n} &= \varepsilon_k - T \sum_q \sum_m V^{\rm ep}_{k-q,n-m} \frac{\tilde{\varepsilon}_{q,m}}{\left| \widehat{G}^{-1}_{q,m} \right|} \\
\tilde{\omega}_{k,n} &= \omega_n + T \sum_q \sum_m V^{\rm ep}_{k-q,n-m} \frac{\tilde{\omega}_{q,m}}{\left| \widehat{G}^{-1}_{q,m} \right|} \\
\phi_{k,n} &= -T \sum_q \sum_m V^{\rm ep}_{k-q,n-m} \frac{\phi_{q,m}}{\left| \widehat{G}^{-1}_{q,m} \right|}.
\end{aligned} \tag{2.35}$$

which are coupled via Eq. 2.33 for $\left| \widehat{G}^{-1}_{q,m} \right|$. These equations are know as the Eliashberg equations and their self consistent solution characterizes the superconductivity of a system in which the only input to the theory is the electron dispersion, ε_k, which comes from band structure calculations and the electron-phonon interaction, $\alpha^2 F_k(\Omega)$, which is derived through the process of tunneling inversion.[20, 19]

This procedure has been followed to great success for many conventional superconductors [8] with many calculated superconducting properties, based upon only these two inputs, agreeing surprisingly well with experimental results. However, this thesis is concerned with unconventional superconductors in which this process does not appear to work – perhaps because the interaction is not due to phonons but has some other source. In the next section a possible source of this different interaction is investigated.

The physical significance of each of these three functions are discussed in detail in §4.1.1. Briefly, $\phi_{k,n}$ is related to the order parameter, Δ_k, of the BCS theory, $\tilde{\varepsilon}_{k,n}$ is the renormalized electron dispersion, and $\tilde{\omega}_{k,n}$ is a renormalization for the frequency.

2.7 High Temperature Superconductors (HTS)

The assumptions made in §2.5.1 (*i.e.* a spherical Fermi surface with an isotropic interaction) in order to solve the BCS equation are quite reasonable for many conventional superconductors such as Aluminum but are not so reasonable for high temperature superconductors[4] because firstly, they are highly anisotropic materials consisting of layers of CuO_2 sheets with layers of other atoms in between (some materials have adjacent CuO_2 layers and, interestingly, these materials tend to have higher critical temperatures) and secondly, they are doped materials with the parent compounds being antiferromagnetic insulators.

The ramifications of this are that the dispersion and the interaction, the two functions that are the inputs to the gap equation (either the BCS equation, Eq. 2.16, or the off-diagonal part of the Eliashberg equation, Eq. 2.35), can have (much) more complicated $\boldsymbol{k}$-dependences as was discussed in §2.5.2.

In Ch. 3 dispersion relations pertinent to HTS are discussed in detail with several specific models presented. In Ch. 4 a specific model interaction, the spin-fluctuation model, is discussed in several approximations and, combined with the dispersions of Ch. 3, the BCS and Eliashberg equations are solved to obtain the order parameter (and in the case of the Eliashberg equations, the renormalization functions are also obtained). In subsequent chapters the ramifications of these results upon several experimentally measurable quantities are discussed.

[4]These assumptions also do not appear to hold for the heavy Fermion or organic superconductors either.

Chapter 3

Electron States in HTS

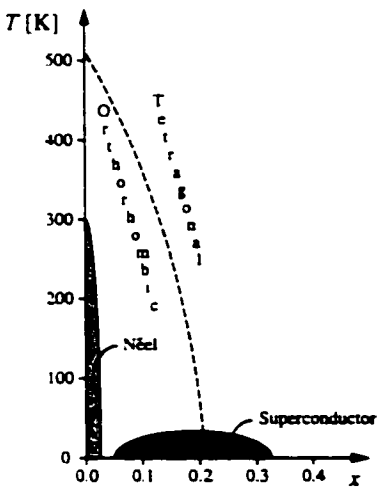

Figure 3.1: The phase diagram for $La_{2-x}Sr_xCuO_4$ as a function of doping, x, and temperature, T, containing orthorhombic and tetragonal phases (separated by a dashed line), a Néel state (lightly shaded region) and a superconducting state (darkly shaded region).

The HTS materials have complicated structures as well as vastly different properties as a function of doping. In Fig. 3.1 the phase diagram for $La_{2-x}Sr_xCuO_4$ as a function of doping, x, and temperature, T, is shown schematically. It contains orthorhombic and tetragonal phases (separated by a dashed line), a Néel state (lightly shaded region) and a superconducting state (darkly shaded region).

In order to understand the superconducting state in HTS materials the normal state must first be understood. Unfortunately, the normal state is complicated by both the crystal structure of the materials and the fact that superconductivity only appears when the compounds are doped. These two factors have contributed to the controversy about whether the materials can be treated as Fermi liquids or whether they have to be treated as strongly correlated electron systems.[21] The reason for this dichotomy is that successful formalisms have been developed to deal with electrons in the two limits, localized electrons (insulators) and free electrons (metals), but the region in between, where the electrons are mobile but highly correlated, does not yet have a formalism that is satisfactory.

There are two ways that attempt to deal with this region between localized and free electrons. The first starts from a localized electron picture and adds mobility to the electrons; this method is usually numerical and relies upon exact diagonalization[22] or quantum Monte-Carlo techniques.[23, 24] The second starts from the free electron model and adds correlations through

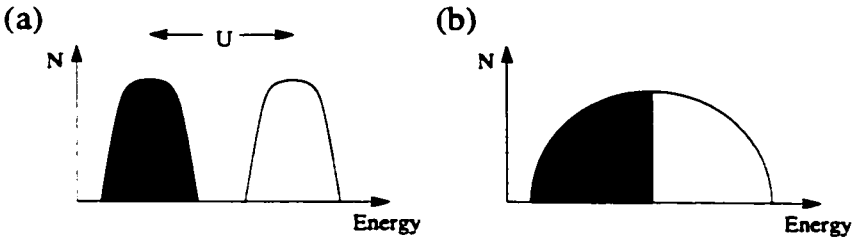

Figure 3.2: On the left (a) is shown schematically the density of states, N, for the Hubbard model in the $U \gg t$ limit; there are two bands, referred to as the upper and lower Hubbard bands, separated by a band gap, U. On the right (b) is shown schematically the density of states, N, for the Hubbard model in the $U \ll t$ limit; there is only one band in this limit. The shaded areas represent the occupied electron states.

perturbation theory. In this thesis the latter view is taken: that the doped materials can be treated as Fermi liquids with an interaction which adds some aspects of the correlations that are expected to be present in the HTS materials.

3.1 The HTS Parent Materials

The fact that the parent, or undoped, compounds of the HTS are antiferromagnetic insulators is highly unusual since superconductors and insulators are about as different, electronically, as two compounds can be. The parent compounds are believed to be Mott-Hubbard insulators which means that there is an electron on each lattice site and that the potential energy required for an electron to move to an adjacent site (thereby creating both a doubly occupied site and an unoccupied site) is much larger than the kinetic energy gained.

In most of the doped HTS materials the carriers are holes. A simple model that is widely believed to represent the HTS materials is the Mott-Hubbard model which is described by the Hamiltonian

$$\mathcal{H} = -t \sum_{\langle \mathbf{r}, \mathbf{r}' \rangle} (c^{\dagger}_{\mathbf{r}\uparrow} c_{\mathbf{r}'\uparrow} + c^{\dagger}_{\mathbf{r}\downarrow} c_{\mathbf{r}'\downarrow}) + U \sum_{\mathbf{r}} n_{\mathbf{r}\uparrow} n_{\mathbf{r}\downarrow} - \mu \sum_{\mathbf{r}} (n_{\mathbf{r}\uparrow} + n_{\mathbf{r}\downarrow}) \tag{3.1}$$

where $c^{\dagger}_{\mathbf{r}\sigma}$ is the electron creation operator, $n_{\mathbf{r}\sigma} \equiv c^{\dagger}_{\mathbf{r}\sigma} c_{\mathbf{r}\sigma}$ is the electron number operator, the sum on $\langle \mathbf{r}, \mathbf{r}' \rangle$ is restricted to nearest neighbour sites with hopping integral t, U is the on-site repulsion and μ is the chemical potential which sets the electronic filling.

For $U \gg t$ there are two bands, referred to as the upper and lower Hubbard bands, separated by a band gap, U. In Fig. 3.2.a the DOS is shown schematically for the half filled case (*i.e.*, $\mu = 2$) for $U \gg t$. In the figure the shaded region is occupied by electrons and the unshaded region is unoccupied; these two bands are separated by an energy gap, U.[1]

[1] For $U \ll t$ we are in the independent electron limit and there is only one tight binding band which for $\mu = 2$ is half filled. In Fig. 3.2.b the DOS is shown schematically for the half filled case (i.e., $\mu = 2$) for $U \ll t$.

This state can be understood intuitively from the Hubbard model: electrons can be added until there is one electron per site, after which it takes an additional energy, U, to create doubly occupied sites.

For the half filled case in the limit $U \gg t$ the Hubbard model can, by second order perturbation theory[21], be transformed to the t-J model which is given by the Hamiltonian

$$\mathcal{H} = -t \sum_{\langle r,r' \rangle} (c^{\dagger}_{r\uparrow} c_{r'\uparrow} + c^{\dagger}_{r\downarrow} c_{r'\downarrow}) + J \sum_{\langle r,r' \rangle} \vec{S}_r \cdot \vec{S}_{r'} - \mu \sum_r (n_{r\uparrow} + n_{r\downarrow}) \tag{3.2}$$

where the formalism is the same as for the Hubbard model, Eq. 3.1, and $\vec{S}_r$ is the spin of the electron on site r. The energy in this model can be lowered by having the electrons on adjacent sites have opposite spins which leads directly to the antiferromagnetic state.

3.2 The Doped HTS Materials

The above is highly satisfactory since it supports the view that the Hubbard model is a good starting point for HTS materials. However, away from half filling (*i.e.*, less than one electron per site) there is no exact solution for the Hubbard model and, if we are not in the $U \gg t$ limit, the perturbation theory is less valid. There are, however, two methods that can be brought to bear on this problem: exact diagonalizations of small systems can be performed[22], and quantum Monte-Carlo calculations can be performed on both the Hubbard model and the t-J model for certain fillings.[23, 24] These simulations indicate that while the long range antiferromagnetic order is no longer present, there are a significant amount of antiferromagnetic fluctuations (these fluctuations are discussed in more detail in §4.1.2 and are incorporated in the FLEX approximation which is discussed in §4.1).

As mentioned above, in this thesis the electrons are assumed to behave as Fermi liquids. The reasonableness of this assumption is supported by some experiments (particularly for the optimally or overdoped cases), although this support is not conclusive. In the Angle Resolved Photo Emission Spectroscopy (ARPES) experiments[25, 26, 27, 28, 29, 30] a Fermi surfaces consistent with LDA calculations[31, 32, 33, 34, 35] (as well as simple tight binding calculations) are observed, albeit indirectly. The same experiments sometimes, but not always, also show quasiparticle peaks; generally for the overdoped but not the underdoped case.

High temperature superconductors are highly anisotropic materials, having properties that can vary by several orders of magnitude in different directions. This anisotropy is caused by their crystal structure which is made up of CuO_2 layers separated by layers of different atoms. Above the superconducting temperature these materials conduct electricity in the plane of the CuO_2 layers and quite poorly in the direction perpendicular to them. Due to this large anisotropy many models of these materials are two dimensional and consider only the CuO_2 layers, sometimes coupling them to each other via a hopping integral, $t_\perp$, that is small compared to the in-plane hopping integrals. These

materials are three dimensional (not only is there an interlayer hopping integral, $t_\perp$, but the actual CuO_2 planes are buckled) but, for many properties, can be investigated using a two dimensional approximation. See §5.1.3, p.49, for a comparison of the 2D approximation to 3D results.

3.2.1 Tight Binding Bands

The unit cell of $La_{2-x}Sr_xCuO_4$ is depicted in Fig. 3.3. The lightly coloured spheres occupy the La and Sr sites and the darker spheres occupy the Cu (lighter) and O (darker) sites. It is the CuO_2 layers that are common to all HTS materials and it is widely believed that it is these layers that provide the conduction electrons and, below the critical temperature, the superconductivity. Each CuO_2 layer is separated from its nearest CuO_2 layer by two $La_{2-x}Sr_xO$ layers and it is this separation that accounts for the large difference of the conductuctivity within the plane from that perpendicular to it. A consequence of this large anisotropy is that for many properties the electrons can be considered to be confined to the two dimensional CuO_2 plane and it is only for those properties which specifically refer to the properties perpendicular to the plane that we need to account for it explicitly (see §5.1.3), for example the c-axis penetration depth (see §5.5.4).

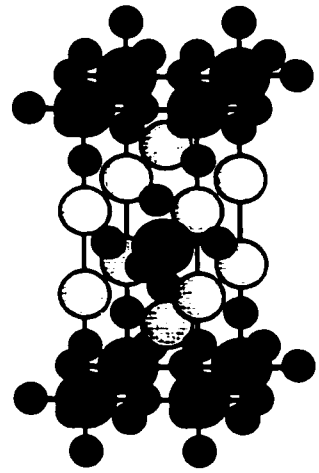

Figure 3.3: The unit cell of $La_{2-x}Sr_xCuO_4$ is depicted. The lightly coloured spheres occupy the La and Sr sites and the darker spheres occupy the Cu (lighter) and O (darker) site. Each CuO_2 layer is separated from its nearest CuO_2 layer by two $La_{2-x}Sr_xO$ layers.

The assumption that an infinite band, free electron model is a good starting point for the electron dispersion is at odds with the fact that the materials seem to be closer to their insulating parent compounds than a free electron system. This leads one to consider that a tight binding approximation would be a better starting point for the electron system with the electrons, instead of being completely delocalized as in the free electron model, are hopping from site to site in real space. This system is described by the following Hamiltonian in second quantization notation

$$\mathcal{H} = -\sum_{\boldsymbol{r},\boldsymbol{r}'} t_{\boldsymbol{r}-\boldsymbol{r}'} \left(c^\dagger_{\boldsymbol{r}\uparrow} c_{\boldsymbol{r}'\uparrow} + c^\dagger_{\boldsymbol{r}\downarrow} c_{\boldsymbol{r}'\downarrow} \right)$$

where $c^\dagger_{\boldsymbol{r}\sigma}$ is the electron creation operator, the hopping integral from site $\boldsymbol{r}$ to $\boldsymbol{r}'$ is $t_{\boldsymbol{r}-\boldsymbol{r}'}$ and t_0 (*i.e.* $\boldsymbol{r} = \boldsymbol{r}'$) corresponds to the chemical potential, μ, which sets the electronic filling.

By introducing the Fourier transform of the creation and annihilation operators

$$c^\dagger_{\boldsymbol{r}\sigma} = \sum_{\boldsymbol{k}} c^\dagger_{\boldsymbol{k}\sigma} e^{-i\boldsymbol{r}\cdot\boldsymbol{k}} \quad , \quad c_{\boldsymbol{r}\sigma} = \sum_{\boldsymbol{k}} c_{\boldsymbol{k}\sigma} e^{i\boldsymbol{r}\cdot\boldsymbol{k}}$$

we can rewrite the Hamiltonian as

$$\mathcal{H} = \sum_{\boldsymbol{k}} \varepsilon_{\boldsymbol{k}} \left(c^{\dagger}_{\boldsymbol{k}\uparrow} c_{\boldsymbol{k}\uparrow} + c^{\dagger}_{\boldsymbol{k}\downarrow} c_{\boldsymbol{k}\downarrow} \right) \tag{3.3}$$

where

$$\varepsilon_{\boldsymbol{k}-\boldsymbol{k}'} \equiv -\sum_{\boldsymbol{r},\boldsymbol{r}'} t_{\boldsymbol{r}-\boldsymbol{r}'} e^{i\boldsymbol{k}\cdot\boldsymbol{r}} e^{-i\boldsymbol{k}'\cdot\boldsymbol{r}'} \tag{3.4}$$

is the resulting dispersion relation (one of the sums over $\boldsymbol{r}$ is eliminated by the Kronecker delta that appears in each term of $t_{\boldsymbol{r}-\boldsymbol{r}'}$) which is periodic in $k_{x,y} = [-\pi, \pi]$, a region known as the Brillouin zone.

For a system with only nearest neighbour hopping, $t_{\boldsymbol{r}-\boldsymbol{r}'} = t\delta_{|\boldsymbol{r}-\boldsymbol{r}'|,1} + \mu\delta_{|\boldsymbol{r}-\boldsymbol{r}'|,0}$, the dispersion is

$$\varepsilon_{\boldsymbol{k}} = -2t\left(\cos(k_x) + \cos(k_y)\right) - \mu \tag{3.5}$$

with $\boldsymbol{k} = (k_x, k_y)$ in units of the lattice spacing. This dispersion is referred to as the Hubbard dispersion due to its presence in the Hubbard model. For a system with a next nearest neighbour hopping as well, $t_{\boldsymbol{r}-\boldsymbol{r}'} = t\delta_{|\boldsymbol{r}-\boldsymbol{r}'|,1} + t'\delta_{|\boldsymbol{r}-\boldsymbol{r}'|,\sqrt{2}} + \mu\delta_{|\boldsymbol{r}-\boldsymbol{r}'|,0}$, and the resulting dispersion is

$$\varepsilon_{\boldsymbol{k}} = -2t\left(\cos(k_x) + \cos(k_y)\right) + 4t'\cos(k_x)\cos(k_y) - \mu$$

with, again, $\boldsymbol{k} = (k_x, k_y)$ in units of the lattice spacing.

The bandwidth of these two bands, Eqs. 3.5 & 3.6, is $8t$ so long as $t' < 0.5t$. It is convenient for comparison purposes to express t' and μ in units of t and to define a shifted chemical potential, $\tilde{\mu} \equiv 2 - 2t' - \frac{1}{2}\mu$, yielding the dispersion

$$\varepsilon_{\boldsymbol{k}} = -2t\left(\cos(k_x) + \cos(k_y) + 4t'\cos(k_x)\cos(k_y) - (2 - 2t' - \tilde{\mu})\right) \tag{3.6}$$

so that the dispersions have the top and bottom of the bands defined by $\tilde{\mu} = 4, 0$, respectively.

In Fig. 3.4 is a dispersion with $t' = 0.00$ and $\tilde{\mu} = 0.1$ which is appropriate to the dispersion relation given by Eq. 3.5 with an electron filling consistent with optimal doping (ie, the maximum critical temperature) in HTS materials. On the top is a stereographic projection of $\varepsilon_{\boldsymbol{k}}$ for the two dimensional Brillouin zone; the solid curve is the Fermi surface. Below on the left is the Fermi surface in the first Brillouin zone; the dotted lines are guides to the eye (the diagonal lines would be the Fermi surface at half filling). On the right is $\varepsilon_{\boldsymbol{k}}$ along the $\Gamma X M \Gamma$ triangle in the Brillouin zone (inset). Note that the dispersion has a maximum at the M point, $\boldsymbol{k} = (\pi, \pi)$, a minimum at the Γ point, $\boldsymbol{k} = (0.0)$ and saddle points at the X and Y points, $\boldsymbol{k} = (\pm\pi, 0), (0, \pm\pi)$ (the saddle point appears as an inflection point at X on the lower right graph). This dispersion is often used by theorists because it contains a minimal number of parameters (t and μ are the only parameters in the model, both of which are set by experimental observations). The fact that this Fermi surface is not appropriate for any of the high temperature superconductors is often overlooked.

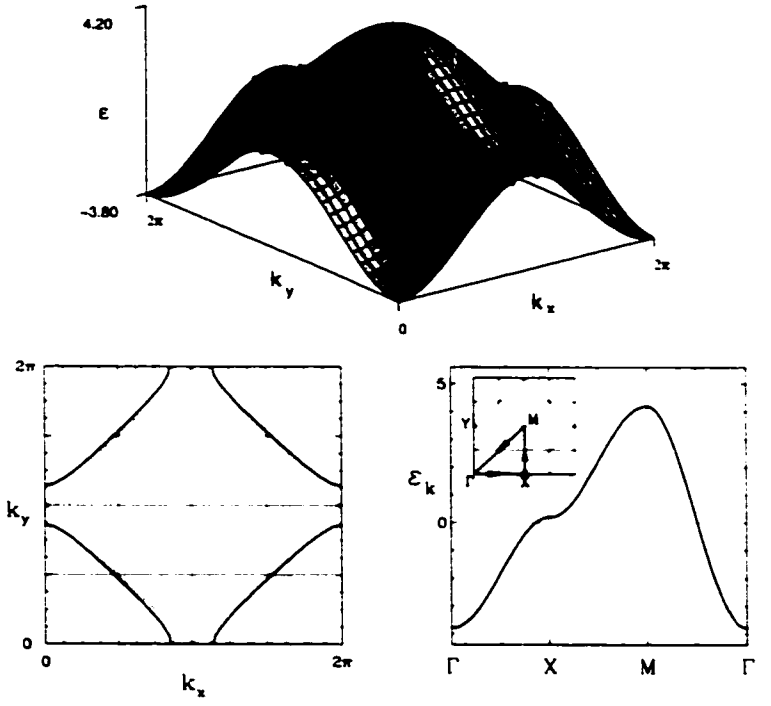

Figure 3.4: The dispersion relation for the Hubbard model is modeled by Eq. 3.4 with $t' = 0$ and $\bar{\mu} = 1.90$. On the top is a stereographic projection of $\varepsilon_{\vec{k}}$ for the two dimensional Brillouin zone; the solid curve is the Fermi surface. Below on the left is the Fermi surface in the first Brillouin zone and on the right is $\varepsilon_{\vec{k}}$ along a triangle in the Brillouin zone (inset).

3.2.2 Nesting and Magnetism

This dispersion, however, does display an interesting property, namely at half filling, $\langle n \rangle = 1$, (*i.e.* $\bar{\mu} = 2$) the Fermi surface is a perfect square (*i.e.* the diagonal dotted lines in the lower left diagram in Fig. 3.4). An important ramification of this situation is perfect "nesting"[2] of the Fermi surface which causes an antiferromagnetic (AFM) instability. This instability causes a gap to form at the Fermi surface (*i.e.* the system becomes insulating) and is responsible for the doubling of the unit cell (and, hence, the Brillouin zone halves). For $\bar{\mu} \neq 2$ the gap may or may not develop and may only partially coincide with the Fermi surface.

How nesting causes an AMF instability was first suggested by Overhauser[36] and this mechanism was used by Lomer[37] to explain the incommensurate AFM in Chromium. In Chromium there are two Fermi surfaces for which large parts are connected by an incommensurate vector close to $(\pi, 0)$. Since this form of AFM is caused by the itinerant electrons it is termed "itinerant AFM" and the stability of different forms of magnetism is explored in detail using mean field theory by Penn.[38] The main thrust of the argument is that if many pieces of Fermi surface are connected by

[2]Nesting is when many parts of the Fermi surface can be connected by a single wave vector.

the same wave vector, $\boldsymbol{Q}$, then the Hamiltonian will contain a term of the form

$$\mathcal{H}' = \sum_{k,k'} U c^\dagger_{k+Q\uparrow} c_{k\downarrow} c^\dagger_{k'-Q\downarrow} c_{k'\uparrow}, \tag{3.7}$$

where U is the Coulomb interaction, which represents two electrons exchanging momentum $\boldsymbol{Q}$ and spin one and corresponds to the Feynmann diagram in Fig. 3.5.

This interaction term, Eq. 3.7, can be analysed in exactly the same manner as the BCS reduced Hamiltonian, Eq. 2.4, with the following two changes: first, the mean field approximation uses $\chi^{\boldsymbol{Q}}_{\boldsymbol{k}} \equiv \left\langle c^\dagger_{k+Q\uparrow} c_{k\downarrow} \right\rangle$, and second, the Bogolyubov canonical transformation has quasiparticles given by $\gamma^\dagger_{\boldsymbol{k}} = u_{\boldsymbol{k}} c_{k\uparrow} - v_{\boldsymbol{k}} c^\dagger_{k+Q\downarrow}$. This analysis yields the gap equation

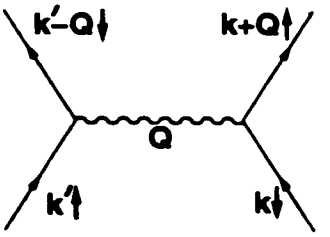

Figure 3.5: This Feynmann diagram corresponds to two electrons exchanging momentum $\boldsymbol{Q}$ and spin one. If there are many parts of the Fermi surface connected by the same $\boldsymbol{Q}$ vector then this scattering process can create an instability.

$$M^{\boldsymbol{Q}} \equiv \sum_{\boldsymbol{k}} U \chi^{\boldsymbol{Q}}_{\boldsymbol{k}}, \tag{3.8}$$

many properties of which are the same as those of the BCS theory (*e.g.* the ratio $2M^{\boldsymbol{Q}}/k_B T_N = 3.5$).

If this gap exists over all of the Fermi surface the system will become an insulator, otherwise the system remains a conductor with only part of the Fermi surface gapped. This latter system has been investigated for the case of a subsequent superconducting transition by Kato[39] in an analysis of heavy Fermion superconductors.[3] In this work they treat the superconducting and AFM order parameters on an equal footing so the two gap equations are coupled. They find that the AFM helps to stabilise some forms of superconductivity – specifically, *d*-wave superconductivity.

3.2.3 The Filling

The chemical potential, $\tilde{\mu}$, sets the filling for the normal state of each band through the relation

$$\begin{aligned} n &= \sum_{k\sigma} c^\dagger_{k\sigma} c_{k\sigma} \\ \langle n \rangle &= 2 \sum_{\boldsymbol{k}} f(\beta \varepsilon_{\boldsymbol{k}}) \\ &= \sum_{\boldsymbol{k}} \left(1 - \tanh\left(\tfrac{1}{2}\beta \varepsilon_{\boldsymbol{k}}\right)\right) \end{aligned} \tag{3.9}$$

where $f(x) \equiv (1 + e^x)^{-1}$ is the Fermi-Dirac distribution (with β the reciprocal temperature, $\beta \equiv 1/k_B T$) and the 2 is for the sum over spin ($\sigma = (\uparrow, \downarrow)$). For the superconducting state the filling is

[3] Heavy Fermion superconductors are metals that have an effective electron mass that can be hundreds of times the bare electron mass. They generally have critical temperatures on the order of one Kelvin.

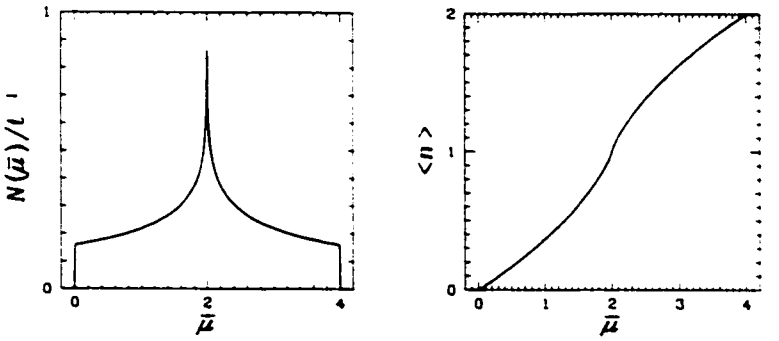

Figure 3.6: The density of states (DOS) for a tight binding band with only nearest neighbour hopping is shown on the left. On the right is the filling, $\langle n \rangle$ (note that the DOS is given by $d\langle n \rangle / d\mu$). There are van Hove singularities (vHS) at the top of the band ($\bar{\mu} = 4$) and bottom of the band ($\bar{\mu} = 0$) caused by the maxima and minima of the dispersion. There is another vHS at the middle of the band ($\bar{\mu} = 2$) which is caused by the saddle point at $(\pi, 0)$ (and symmetry related points) of the dispersion.

given by

$$\begin{aligned} n &= 2\sum_{k} |u_k|^2 \gamma^\dagger_{k,0}\gamma_{k,0} + |v_k|^2 \left(1 - \gamma^\dagger_{k,1}\gamma_{k,1}\right) \\ \langle n \rangle &= \sum_{k} \left(1 - \frac{\varepsilon_k}{E_k} \tanh\left(\tfrac{1}{2}\beta E_k\right)\right) \end{aligned} \tag{3.10}$$

in which Eq. 2.12 has been used to express the electron operators, c_k, in terms of the quasiparticle operators, $\gamma_{k,s}$, and Eq. 2.13 has been used for the coherence factors, u_k & v_k. Note that for $\Delta_k \to 0$ Eq. 3.10 reduces to Eq. 3.9.

On the right in Fig. 3.6 the variation of the filling, $\langle n \rangle$, with the (redefined) chemical potential, $\bar{\mu} \equiv 2 - 2t' - \frac{1}{2}\mu$, is plotted in the normal state for the Hubbard dispersion, Eq. 3.5; this curve is equivalent to an integrated density of states (shown on the left - see below). Note that the band is symmetric about half filling, $\langle n \rangle = 1$. There is a slight shift in this curve ($\sim 1\%$) in the superconducting state.

3.2.4 The Density of States – Van Hove Singularities

The density of states (DOS) is given by the derivative with respect to the chemical potential of the filling. In the normal state it is given by

$$\begin{aligned} N(\bar{\mu}) &\equiv \frac{d}{d\bar{\mu}} \langle n \rangle \\ &= \sum_{k} \tfrac{1}{2}\beta \mathrm{sech}^2\left(\tfrac{1}{2}\beta\varepsilon_k\right). \end{aligned} \tag{3.11}$$

At $T = 0$ this becomes a delta function

$$\begin{aligned} N(\bar{\mu}) &= 2\sum_{k} \delta(\varepsilon_k) \\ &= \lim_{\Gamma \to 0} \frac{2}{\pi} \sum_{k} \frac{\Gamma}{\varepsilon_k^2 + \Gamma^2} \end{aligned} \tag{3.12}$$

where we have approximated the delta function with a Lorentzian.

By changing the k-sum in Eq. 3.11 into energy and angular integrals

$$N(\bar{\mu}) = \frac{1}{(2\pi)^d} \int \frac{d\Omega_k}{4\pi} \int_0^\infty \frac{d\varepsilon_k}{|\nabla_k \varepsilon_k|} \left(\tfrac{1}{2}\beta \mathrm{sech}^2\left(\tfrac{1}{2}\beta\varepsilon_k\right)\right) \tag{3.13}$$

we can see that interesting feature of this type of dispersion is the presence of van Hove singularities, *i.e.* points in k-space where the Fermi velocity, $\nabla_k \varepsilon_k$, is zero, in the density of states. These appear at the top and bottom of the band at (π, π) and $(0, 0)$, respectively (*i.e.*, at the maxima and minima of ε_k) and at $(\pi, 0)$ and symmetry related points (*i.e.*, at a saddle points of ε_k). The van Hove singularities at the top and bottom of the band is responsible for the discontinuities in the density of states (DOS) which goes abruptly to zero. The van Hove singularities at the saddle points causes a logarithmic divergence in the DOS at $\bar{\mu} = 2$. If this divergence is near the Fermi energy it may cause a large enhancement of the part of the density of states that is important to superconductivity.[40]

On the left in Fig. 3.6 is the density of states for the Hubbard dispersion, Eq. 3.5. There are van Hove singularities (vHS) at the top of the band ($\bar{\mu} = 4$) and bottom of the band ($\bar{\mu} = 0$) caused by the maxima and minima of the dispersion. There is another vHS at the middle of the band ($\bar{\mu} = 2$) which is caused by the saddle point at $(\pi, 0)$ (and symmetry related points) of the dispersion.

In the superconducting state the equivalent expression is

$$\begin{aligned} N(\bar{\mu}) &\equiv \frac{d}{d\bar{\mu}} \langle n \rangle \\ &= \sum_{k} \tfrac{1}{2}\beta \mathrm{sech}^2\left(\tfrac{1}{2}\beta E_k\right). \end{aligned} \tag{3.14}$$

and there is a gap in the density of states at the Fermi surface. This gap in the density of states is discussed in §5.6.

Chapter 4

The Pairing and Other Interactions

In §2.2.1 an isotropic interaction is discussed which was originally introduced to describe conventional superconductors. By construction this isotropic interaction can only result in an isotropic order parameter (*i.e.* it has no spatial dependence), in order for a different symmetry of the order parameter to be possible the interaction must have some $\boldsymbol{k}$-space dependence. In this chapter such anisotropic interactions are introduced and the symmetries of the resulting order parameters are examined. Of particular interest are those interactions that result in an order parameter with d-wave symmetry, *i.e.* those with a $(\cos(k_x) - \cos(k_y))$ functional form, which is the order parameter symmetry most consistent with experimental results, in particular with the π-junction experiments.[41, 42, 43, 44, 45, 46]

In this chapter a specific model interaction, the spin-fluctuation model, is introduced that will be used for all subsequent calculations. There are two approximations used for this model: the FLEX approximation, discussed in §4.1, and the MMP approximation, discussed in §4.2. These model interactions, combined with the model dispersion of Ch. 3, will be used to solve the BCS and Eliashberg equations and these solutions are then used in subsequent chapters to calculate experimentally measurable properties. It is important to note that many of the calculated properties will depend upon the interaction only indirectly through the order parameter. Consequently, many of these properties do not provide direct support for these specific interactions as any interactions which yield a similar order parameter would give the same results and consequently our results should be interpreted with these caveats in mind.

4.1 The FLEX Approximation

The Fluctuation-Exchange (FLEX) approximation, introduced by Bickers and Scalapino [47] and implemented numerically by Pao and Bickers[48] and Lenck and Carbotte [49], assumes that the interaction in the Eliashberg equations is caused by charge and spin fluctuations. This

section makes use of a formalism which combines the frequency and temperature variables into one complex variable, the Matsubara frequency.

It is interesting to note that the main ideas of the FLEX model predate HTC and were originally introduced with the heavy Fermion materials in mind.[50] In the FLEX model the self-energy is given by (*cf.*Eq. 2.34)

$$\widehat{\Sigma}_{\boldsymbol{k},n} = -T\sum_{m}\sum_{\boldsymbol{q}}\left(V^{s}_{\boldsymbol{k}-\boldsymbol{q},n-m}\widehat{\tau}_0\widehat{G}_{\boldsymbol{q},m}\widehat{\tau}_0 + V^{c}_{\boldsymbol{k}-\boldsymbol{q},n-m}\widehat{\tau}_3\widehat{G}_{\boldsymbol{q},m}\widehat{\tau}_3\right) \tag{4.1}$$

where $V^{s}_{\boldsymbol{k},n}$ is the interaction due to the spin fluctuations and $V^{c}_{\boldsymbol{k},n}$ is that due to the charge fluctuations. This equation is a convolution of the fluctuations, $V^{s,c}_{\boldsymbol{k},n}$, and the Green's function, $\widehat{G}_{\boldsymbol{k},n}$. Since both functions are periodic in $\boldsymbol{k}$ the summation over $\boldsymbol{k}$ can be performed using Fourier transforms and the convolution theorem which results in a large saving in computational time. However, the sum over Matsubara frequencies is not periodic (although it does have a reflection symmetry) so this sum must still be performed explicitly (see §A.1.2 for a discussion of the Matsubara sums).

The $V^{s,c}_{\boldsymbol{k},n}$ are given by

$$\begin{aligned} V^{s}_{\boldsymbol{k},n} &= \frac{3}{2}U^2\chi^{s}_{\boldsymbol{k},n} \\ V^{c}_{\boldsymbol{k},n} &= \tfrac{1}{2}U^2\chi^{c}_{\boldsymbol{k},n} \end{aligned}$$

in which the $\chi^{s,c}_{\boldsymbol{k},n}$ are the spin and charge susceptibilities (see §4.1.2 for a discussion of these functions).

In a manner analogous to that for phonons (§2.6.1, p. 21) the self-energy from the FLEX approximation, Eq. 4.1, is to be equated with that given by the Eliashberg equations, Eq. 2.25, in order to solve for the fully interacting Green's functions, $\widehat{G}_{\boldsymbol{k},n}$. However, before doing so we will examine the renormalization functions and the susceptibilities in more detail.

4.1.1 The Renormalization Functions, $\phi_{\boldsymbol{k},n}$, $\xi_{\boldsymbol{k},n}$ and $Z_{\boldsymbol{k},n}$

Equating the real and imaginary parts of the diagonal expressions for the FLEX self-energy, Eq. 4.1, and the Eliashberg self-energy, Eq. 2.25, we obtain for the renormalization functions, $\xi_{\boldsymbol{k},n}$, $Z_{\boldsymbol{k},n}$ and $\phi_{\boldsymbol{k},n}$

$$\begin{aligned} \xi_{\boldsymbol{k},n} &= -T\sum_{n}\sum_{\boldsymbol{q}}(V^{s}_{\boldsymbol{k}-\boldsymbol{q},n-m} + V^{c}_{\boldsymbol{k}-\boldsymbol{q},n-m})\frac{\tilde{\varepsilon}_{\boldsymbol{q},m}}{\left|\widehat{G}^{-1}_{\boldsymbol{q},m}\right|} \\ \omega_n(1-Z_{\boldsymbol{k},n}) &= -T\sum_{n}\sum_{\boldsymbol{q}}(V^{s}_{\boldsymbol{k}-\boldsymbol{q},n-m} + V^{c}_{\boldsymbol{k}-\boldsymbol{q},n-m})\frac{\tilde{\omega}_{\boldsymbol{q},m}}{\left|\widehat{G}^{-1}_{\boldsymbol{q},m}\right|} \\ \phi_n &= -T\sum_{n}\sum_{\boldsymbol{q}}(V^{s}_{\boldsymbol{k}-\boldsymbol{q},n-m} - V^{c}_{\boldsymbol{k}-\boldsymbol{q},n-m})\frac{\phi_{\boldsymbol{q},m}}{\left|\widehat{G}^{-1}_{\boldsymbol{q},m}\right|}. \end{aligned} \tag{4.2}$$

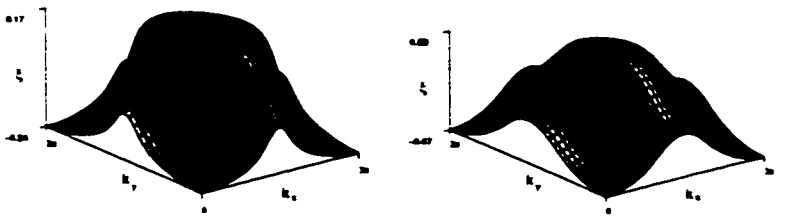

Figure 4.1: The Renormalization Function $\xi_{k,n}$ is shown for the lowest Matsubara frequency, $n = 0$, for two different dispersions, ε_k. On the left is that for $t' = 0$ and on the right is that for $t'/t = 0.45$.

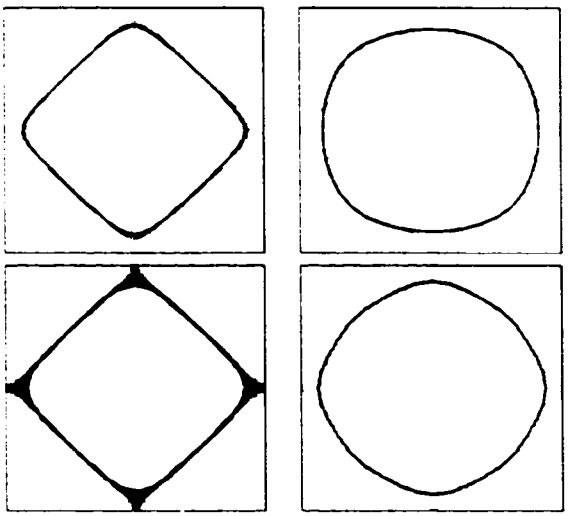

Figure 4.2: Shown is the contour of the Fermi surface, $\varepsilon_k = 0$, (top figures) and the renormalized Fermi surface, $\varepsilon_q + \xi_{q,m} = 0$, (bottom figures) in the 2D Brillouin zone for two different dispersions, ε_k. The shaded area represents that part of the dispersion that is within 1% of the bandwidth from the Fermi surface. Also shown is the magnetic Brillouin zone (dotted curve) which is perfectly connect by the AFM nesting vector, $Q \equiv (\pi, \pi)$. Note how the renormalized Fermi surface is closer to the magnetic Brillouin zone than the unrenormalized Fermi surface.

The Electron Dispersion Renormalization, $\xi_{k,n}$

The function $\xi_{k,n}$ corresponds to the renormalization of the electronic dispersion, ε_k. Its main effect is to slightly shift the Fermi surface as well as, perhaps, to change the curvature of the dispersion at the Fermi surface (and, hence, the effective mass).

In Fig. 4.1 representative samples of this function are shown for the lowest Matsubara frequency, $n = 0$, for two different dispersions, ε_k. On the left is that for $t' = 0$ and on the right is that for $t'/t = 0.45$. The effect of the $\xi_{k,n}$ is to shift the electronic dispersion, ε_k, and so shift the Fermi surface. It tends to shift the Fermi surface in such a manner so as to enhance the "nesting" of the Fermi surface. Shown in Fig. 4.2 is the contour of the unrenormalized Fermi surface (dashed curve), given by $\varepsilon_k = 0$ and the renormalized Fermi surface (solid curve), given

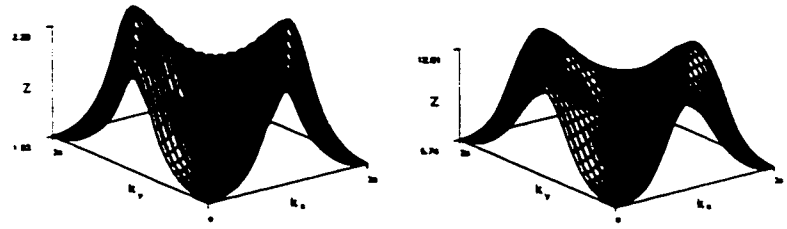

Figure 4.3: The Renormalization Function $Z_{k,n}$ is shown for the lowest Matsubara frequency, $n = 0$, for two different dispersions, ε_k.

by $\bar{\varepsilon}_{k,m} = \varepsilon_k + \xi_{k,m} = 0$. "Nesting" means that a large proportion of the Fermi surface can be connected to itself. In this case the nesting vector is given by $\boldsymbol{Q} = (\pi, \pi)$ - which is exactly where the spin-fluctuation interaction is peaked (see §4.1.2). The dotted curve is the magnetic Brillouin zone which is perfectly connect by the AFM nesting vector, $\boldsymbol{Q} = (\pi, \pi)$.

The Frequency Renormalization Function, $Z_{k,n}$

The function $(1 - Z_{k,n})$ corresponds to the renormalization of the electron mass similar to that which is seen in QED.

The Energy Gap Function, $\phi_{k,n}$

The energy gap function, $\phi_{k,n}$, is what defines superconductivity - it is zero above the critical temperature, T_c, and non-zero below T_c, growing to a saturated value as $T \to 0$.

4.1.2 The Spin and Charge Susceptibilities, $\chi^s_{k,n}$ and $\chi^c_{k,n}$

The spin and charge fluctuations, $\chi^s_{k,n}$ and $\chi^c_{k,n}$, respectively, are, in the RPA approximation, given by

$$\chi^s_{k,n} = \frac{\chi^s_{\circ k,n}}{1 - U\chi^s_{\circ k,n}} \tag{4.3}$$

$$\chi^c_{k,n} = \frac{\chi^c_{\circ k,n}}{1 + U\chi^c_{\circ k,n}} \tag{4.4}$$

In these expressions the $\chi^{s,c}_{\circ k,n}$ are the spin and charge susceptibilities, given by

$$\chi^s_{\circ k,n} = -T\sum_m \sum_q \mathrm{Tr}\left(\widehat{G}_{k+q,n+m}\widehat{\tau}_0\widehat{G}_{q,m}\widehat{\tau}_0\right) \tag{4.5}$$

$$\chi^c_{\circ k,n} = -T\sum_m \sum_q \mathrm{Tr}\left(\widehat{G}_{k+q,n+m}\widehat{\tau}_3\widehat{G}_{q,m}\widehat{\tau}_3\right) \tag{4.6}$$

where $\mathrm{Tr}(\widehat{x})$ indicates that a trace is to be taken of the resulting matrix. These equations are a convolution of the Green's function, $\widehat{G}_{k,n}$, with itself. As discussed above (§4.1) the k sum

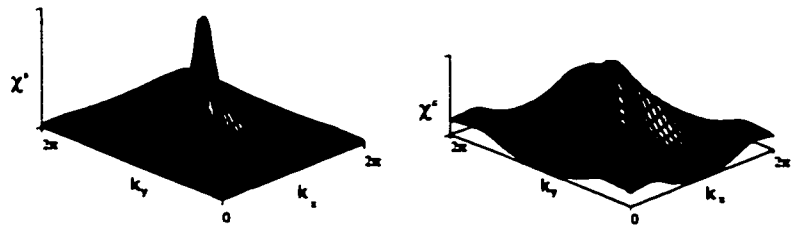

Figure 4.4: The spin and charge susceptibilities, $\chi^s_{k,n}$ and $\chi^c_{k,n}$, are shown for the lowest Matsubara frequency, $n = 0$, next nearest neighbour hopping of $0.0t$ and a filling of $\langle n \rangle = 0.88$.

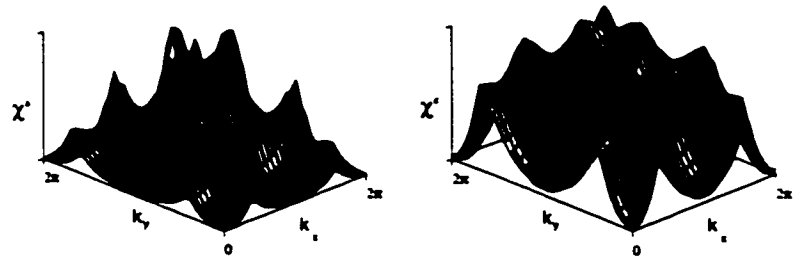

Figure 4.5: The spin and charge susceptibilities, $\chi^s_{k,n}$ and $\chi^c_{k,n}$, are shown for the lowest Matsubara frequency, $n = 0$, next nearest neighbour hopping of $0.45t$, and a filling of $\langle n \rangle = 0.88$.

can be performed using convolutions, but the Matsubara sums must be performed differently (see Appendix A.1.2 for a discussion of the Matsubara sums).

Expanding the Green's functions with the Pauli matrices and taking the trace we get

$$\chi^s_{o\,k,n} = -T \sum_m \sum_q \frac{\tilde{\varepsilon}_{k,n}\tilde{\varepsilon}_{k+q,n+m} - \tilde{\omega}_{k,n}\tilde{\omega}_{k+q,n+m} + \phi_{k,n}\phi_{k+q,n+m}}{\left|\widehat{G}^{-1}_{k,n}\right|\left|\widehat{G}^{-1}_{k+q,n+m}\right|} \tag{4.7}$$

$$\chi^c_{o\,k,n} = -T \sum_m \sum_q \frac{\tilde{\varepsilon}_{k+q,n+m}\tilde{\varepsilon}_{k,n} - \tilde{\omega}_{k,n}\tilde{\omega}_{k+q,n+m} - \phi_{k,n}\phi_{k+q,n+m}}{\left|\widehat{G}^{-1}_{k,n}\right|\left|\widehat{G}^{-1}_{k+q,n+m}\right|}, \tag{4.8}$$

which differ only in the sign of the last term in the numerator. In the normal state the energy gap function, $\phi_{k,n}$, is zero and the two susceptibilities are identical.

When the denominator of Eq. 4.3 becomes zero the spin susceptibility, $\chi^s_{k,n}$, becomes infinite and the antiferromagnetic (AFM) transition is reached. That the undoped cuprates (*i.e.* one electron per site) have an AFM ground state indicates that certain parameter regimes of this model are consistent with observations and also indicate that other regimes may be representative of the cuprate system.

In Figs. 4.4 and 4.5 the susceptibilities (given by Eqs. 4.3 and 4.4) are shown for two systems closer to half filling (*i.e.* one electron per site, $\langle n \rangle \sim 1$). In the first, Fig. 4.4, the spin and charge susceptibilities are shown for the Hubbard model (*i.e.* only nearest neighbour hopping) with an on-site Coulomb repulsion, U/t, of 3 at a temperature, T/t, of 0.05. One can see that due to

the proximity of the AFM instability the spin susceptibility, $\chi^s_{k,n}$, is very strongly peaked at the nesting vector, $Q \equiv (\pi, \pi)$, while the charge susceptibility, $\chi^c_{k,n}$, is less strongly peaked. Note that while both functions are peaked at the commensurate wave vector, $Q \equiv (\pi, \pi)$, that there is a large difference in the scales of the two functions - the spin susceptibility is several orders of magnitude larger that the charge susceptibility. This large difference is caused by the sign of the second term in the denominator of the spin susceptibility Eq. 4.3.

As an aside, the spin susceptibility is often calculated on the real axis using [51]

$$\begin{aligned}\chi^s_{\circ k}(\omega) = \sum_q \Bigg[& \frac{1}{2}\left(1 + \frac{\varepsilon_{q+k}\varepsilon_q + \Delta_{q+k}\Delta_q}{E_{q+k}E_q}\right)\frac{f(\beta E_{q+k}) - f(\beta E_q)}{\omega - E_{q+k} + E_q + i0^+} \\ & + \frac{1}{4}\left(1 - \frac{\varepsilon_{q+k}}{E_{q+k}} + \frac{\varepsilon_q}{E_q} - \frac{\varepsilon_{q+k}\varepsilon_q + \Delta_{q+k}\Delta_q}{E_{q+k}E_q}\right)\frac{1 - f(\beta E_{q+k}) - f(\beta E_q)}{\omega + E_{q+k} + E_q + i0^+} \\ & + \frac{1}{4}\left(1 + \frac{\varepsilon_{q+k}}{E_{q+k}} - \frac{\varepsilon_q}{E_q} - \frac{\varepsilon_{q+k}\varepsilon_q + \Delta_{q+k}\Delta_q}{E_{q+k}E_q}\right)\frac{f(\beta E_{q+k}) + f(\beta E_q) - 1}{\omega - E_{q+k} - E_q + i0^+}\Bigg] \quad (4.9)\end{aligned}$$

where $E_q = \sqrt{\varepsilon_q^2 + \Delta_q^2}$ is the quasi-particle energy and $f(x) \equiv (1 + e^x)^{-1}$ is the Fermi-Dirac distribution.

However, it is computationally much more efficient to use the imaginary axis formalism given by Eq.4.5 (*i.e.* it takes several seconds instead of several hours to compute) and, if the frequency dependence is required, to analytically continue the results.

4.1.3 The T_c Equation

The equation for the critical temperature, T_c, is Eq. 4.2, linearized in $\phi_{k,n}$. This process creates the eigen-value equation

$$\lambda\phi_{k,n} = -T\sum_m\sum_q (V^s_{k-q,n-m} - V^c_{k-q,n-m})\frac{\phi_{q,m}}{\left|\widehat{G}^{-1}_{q,m}\right|^{-1}_{\phi_{q,m}=0}} \quad (4.10)$$

in which the term $\left|\widehat{G}^{-1}_{q,m}\right|$, given by Eq. 2.33, is evaluated with $\phi_{q,m} = 0$, *i.e.* in the normal state,

$$\left|\widehat{G}^{-1}_{q,m}\right|_{\phi_{q,m}=0} \equiv -\tilde{\varepsilon}^2_{k,n} - \tilde{\omega}^2_{k,n}.$$

After solving for $\widehat{G}_{q,m}\Big|_{\phi_{q,m}=0}$ self-consistently in the normal state (*i.e.* for $\tilde{\varepsilon}_{k,n}$ and $\tilde{\omega}_{k,n}$) λ, the eigen value of Eq. 4.10, is found at different temperatures. As the temperature is lowered the eigen value increases, and at $T = T_c$, $\lambda = 1$. This process can be used to find the critical temperature, T_c, as a function of different parameters, *e.g.* the Coulomb interaction, U, or the filling, $\langle n \rangle$.

The sums over Matsubara frequencies are technically infinite, however the importance of the higher frequencies quickly decreases. Since these equations are solved numerically an arbitrary cutoff, denoted by C in units of energy, must be imposed on these sums. This cutoff must be large enough that the physics of the system described is not substantially changed but small enough to

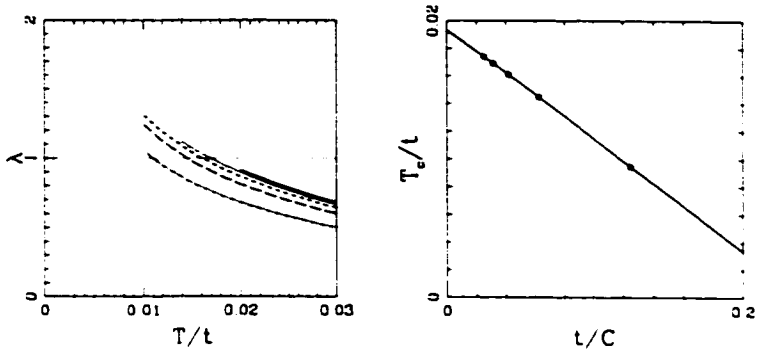

Figure 4.6: On the left is shown the eigen value of Eq. 4.10 as a function of reduced temperature, T/t, for a Coulomb interaction, $U/t = 6$, and several different cutoffs in the Matsubara sums. The cutoff ranges from $8t$, the bandwidth, for the lowest curve to $40t$, five times the bandwidth, for the top curve. The critical temperature corresponds to a eigen value $\lambda = 1$, and for this interaction occurs at $T/t \sim 0.016$. On the right is shown the critical temperature, T_c, as a function of one over the cutoff, t/C. These data vary linearly with the reciprocal cutoff and when extrapolated to zero (*i.e.*$C \to \infty$) provide an accurate estimate of the critical temperature, $T_c/t = 0.019$. The data points correspond to $C/t = 8, 16, 24, 32, 40$.

make the calculation tractable. In order to examine this issue the eigen values of Eq. 4.10 are examined for several different values of the cutoff, C, and the critical temperature, T_c, (given by an eigen value of one) is plotted as a function of the reciprocal cutoff.

Shown on the left in Fig. 4.6 is the eigen value, λ as a function of reduced temperature, T/t, for several different cutoffs, C/t, of the Matsubara frequencies. The bottom curve is for $C/t = 8$, the bandwidth, which gives a $T_c/t \sim 0.011$ and the top curve is for $C/t = 40$, five times the bandwidth, which gives a $T_c/t \sim 0.017$. On the right is shown the critical temperature, T_c, as a function of one over the cutoff, t/C. The extrapolation of $t/C \to 0$ (which corresponds to $C \to \infty$) gives a critical temperature of $T_c/t = 0.019$. Using a cutoff equal to the bandwidth underestimates the T_c by about 35%. However, since the computational time required increases with the square of the cutoff a compromise must be made between computational speed and the exactness of the results (*i.e.* the exact results is reached only in the limit $C \to \infty$). A reasonable compromise is to choose $C/t = 24$, three times the bandwidth which underestimates the critical temperature by approximately 15%.

In Fig. 4.7 we see the affect of temperature and the Coulomb repulsion itself on the critical Coulomb repulsion, U_c, *i.e.* that at which the denominator of $\chi^s_{k,n}$ vanishes (see Eq. 4.3). As the Coulomb repulsion is increased it seems to approach the critical value asymptotically (*i.e.* the critical value, U_c, increases with U). As the temperature is decreased for a given Coulomb repulsion, U, the critical value, U_c, is also approached. However the solid curve, which corresponds to $T/t = 0.01$ is below the superconducting transition temperature but was calculated in the normal state (*i.e.* $\phi_{k,n} = 0$). The other curves are for successively lower temperatures, decreasing in steps of 0.01.

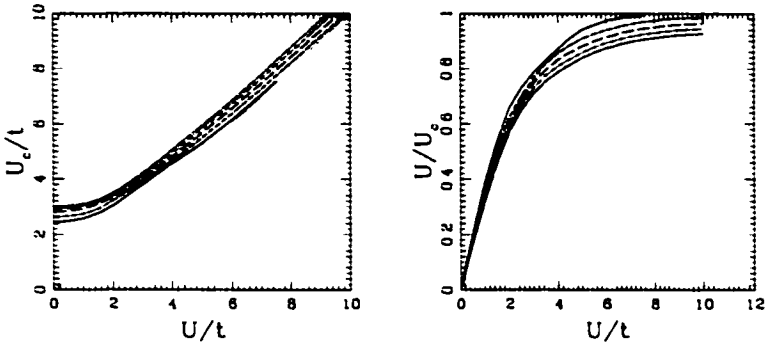

Figure 4.7: The Coulomb repulsion, U, divided by the critical Coulomb repulsion, U_c, as a function of the Coulomb repulsion, U, (in units of the nearest neighbour hoping integral, t) for the dispersion given by Eq. 3.5. As the Coulomb repulsion increases it approaches the critical Coulomb repulsion, U_c, asymptotically (*i.e.* $U/U_c \to 1$) and the Eliashberg equations become more difficult to solve numerically. Shown is the ratio U_c/U as a function of U for temperatures ranging from $0.05t$ (solid curve) to $0.01t$ (dotted curve) in steps of $0.02t$. As the temperature is decreased the critical Coulomb repulsion is approached more rapidly.

4.1.4 Reduction to BCS

The BCS approximation assumes that the diagonal parts of the self energy are zero and that only the zero frequency part of the interaction is important in the off-diagonal part of the self energy. In this approximation the diagonal part of the self energy in the FLEX approximation, Eq. 4.2, is given by

$$\phi_k = -T \sum_n \sum_q V^s_{k-q,n} \frac{\phi_q}{\varepsilon_q^2 + \phi_q^2 + \omega_n^2}$$

in which we have also dropped the charge fluctuation interaction term, $V^c_{k,n}$, as it is significantly smaller than the spin fluctuation term, $V^s_{k,n}$. Because the dispersion and order parameter, ε_k and ϕ_k, no longer have frequency dependencies, the Matsubara sum can be explicitly performed using the identity

$$\tanh\left(\frac{E}{2T}\right) = T \sum_n \frac{1}{E^2 + \omega_n^2} \tag{4.11}$$

(with $\omega_n \equiv (2n-1)\pi T$ the Matsubara frequencies) to yield

$$\phi_k = -\sum_q V^s_{k-q} \frac{\phi_q}{2E_q} \tanh\left(\tfrac{1}{2}\beta E_q\right)$$

with $E_k^2 \equiv \varepsilon_k^2 + \phi_k^2$ and $\beta^{-1} = k_B T$, which is precisely the BCS equation, Eq. 2.16, with the interaction given by the zero frequency part of the spin fluctuation interaction term of the FLEX approximation.

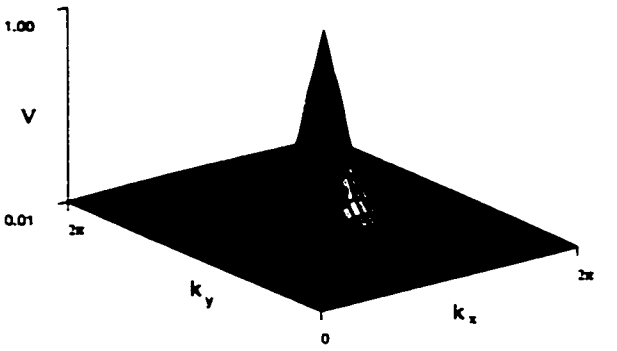

Figure 4.8: The MMP interaction, given by Eq. 4.12, as a function of $\boldsymbol{k}$ is shown as a stereographic projection in the first Brillouin zone.

4.2 The MMP Model

The MMP interaction[17] is a phenomenological fit to the spin susceptibility, $\chi^s_{\boldsymbol{k}}$. In the spin fluctuation scenario[50] the interaction is proportional to the spin susceptibility which is peaked at or near $\boldsymbol{Q} = (\pi, \pi)$. The purpose of the MMP interaction is to save having to calculate the susceptibility which is computationally expensive (see §4.1.2 for more details). The MMP interaction is given by the Lorentzian

$$V^{\mathrm{MMP}}_{\boldsymbol{k}} \equiv g^2 \frac{\chi_o}{1 + \xi_o^2 |\boldsymbol{k} - \boldsymbol{Q}|^2} \tag{4.12}$$

with ξ_o the magnetic coherence length, $\boldsymbol{Q} = (\pi, \pi)$ the AFM wave vector and $g^2\chi_o$ a phenomenological coupling constant which is adjusted so that the BCS equation has the desired critical temperature. In this work a magnetic coherence length of 2.5 unit cells (≈ 7Å) is used.

In Fig. 4.8 a stereographic projection of Eq. 4.12 is shown as a function of $\boldsymbol{k}$ in the first Brillouin zone. It is sharply peaked at $\boldsymbol{Q} = (\pi, \pi)$ and has a characteristic width given by the magnetic correlation length, ξ_o, and is very similar to Fig. 4.4.

Maly and Levin[52] have explored the consequences of the position in the Brillouin zone of the peak in the interaction (*i.e.* different values of $\boldsymbol{Q}$ in Eq. 4.12) on the symmetry of the order parameter with the lowest free energy. They find that a *d*-wave order parameter has the minimum free energy for an interaction peaked everywhere except for the corners of the Brillouin zone.

4.3 Impurities in HTS Materials

In superconductors the effects of magnetic and non-magnetic impurities are very different. Magnetic impurities act as pair breakers since the scattering of an electron changes its spin (and, hence, breaks the Cooper pair), while scattering from non-magnetic impurities does not change the spin of the electron. In this chapter the effects of non-magnetic impurities upon the critical

temperature, T_c, and the order parameter, $\phi_{k,n}$, are examined using a formalism that averages over the impurities.[53, 54] This method of averaging impurities is probably only valid for a reasonably high impurity content. For low levels of impurities, due to the short coherence length, the order parameter is able to "heal" itself between the impurity locations.[55, 56] In light of this one would expect that impurity levels below which the order parameter can heal ($\sim$ 1%) would have little effect upon the critical temperatures and the averaging of impurities performed using the formalism introduced below would not be entirely valid.

In HTS materials there are at least four distinct type of impurities: those caused by vacancies (*e.g.* the oxygen doping of YBCO), substitutional doping (*e.g.* the strontium in LSCO or nickel or zinc for copper) and structural defects (*e.g.* stacking faults, point defects and twin and grain boundaries).

It is the first and last types of doping that will be examined in this chapter since they are the two that directly effect the CuO_2 layer. There are two effects of these types of impurities. First, they act as scattering centres for electrons (the effect examined in this chapter) and second, they change the doping level of the HTS (which changes T_c in a known way). The other two types of impurities either effect the CuO_2 layer indirectly (substitutional doping can take place in the layers between the CuO_2 layers) or in a way that is beyond the scope of the analysis presented here (structural defects).

The two types of impurities that directly effect the CuO_2 layers are either vacancies on the oxygen site or substitution of zinc or nickel on the copper site. For materials with non-stoichiometric oxygen levels at optimal T_c (such as YBCO) it can be surmised that the main effect of the oxygen vacancies is to adjust the doping levels and that their effect as scattering centres is secondary. However, small amounts of zinc substituted for copper in the CuO_2 layer substantially reduce T_c while the equivalent amount of nickel has very little effect on T_c.[57, 58, 59] It is not clear if zinc acts as a magnetic impurity while nickel as a non-magnetic impurity but there is evidence from NMR experiments that nickel is preferentially substituted into the CuO chain layer [60] which shall be shown below (§6.3.1, p. 92) to have very little effect upon T_c.

4.3.1 Formalism

Impurities add a term to the self energy, $\widehat{\Sigma}_{k,n}$, of the form

$$\widehat{\Sigma}^{(I)}_{k,n} = n^{(I)}\widehat{T}_{k,n}$$

in which $n^{(I)}$ is the concentration of impurities of scattering strength $V_k^{(I)}$ and $\widehat{T}_{k,n}$ is the T-matrix.[61, 62] By taking the scattering to be momentum independent we get for the T-matrix [63]

$$\widehat{T}_n = \frac{-i\Omega_n\widehat{\tau}_0 + D_n\widehat{\tau}_1}{V_I^{-2} + \Omega_n^2 + D_n^2}$$

in which

$$D_n \equiv \sum_k \frac{\phi_{k,n}}{\tilde{\varepsilon}_k^2 + \tilde{\omega}_n^2 + |\phi_{k,n}|^2}, \tag{4.13}$$

$$\Omega_n \equiv \sum_k \frac{\tilde{\omega}_n}{\tilde{\varepsilon}_k^2 + \tilde{\omega}_n^2 + |\phi_{k,n}|^2}, \tag{4.14}$$

and the $\hat{\tau}_i$ are the Pauli matricies (Eq. 2.29).

The limit of very strong scattering, $V_I \to \infty$, is called the "unitary limit" and the weak scattering limit is called the "Born approximation."

4.3.2 Weak Coupling Limit

In the weak coupling limit there are no other contributions to the diagonal self-energy other than that due to the impurities. Performing the same procedure as in §2.6 we get in place of Eq. 2.35

$$\begin{aligned}
\tilde{\varepsilon}_{k,n} &= \varepsilon_k, \\
\tilde{\omega}_{k,n} &= \tilde{\omega}_n = \omega_n + n^{(I)} \frac{\Omega_n}{V_I^{-2} + \Omega_n^2 + |D_n|^2}, \\
\phi_{k,n} &= -T \sum_{k',n'} V_{k,k'} \frac{\phi_{k',n'}}{\tilde{\varepsilon}_{k'}^2 + \tilde{\omega}_{n'}^2 + |\phi_{k',n'}|^2} + n^{(I)} \frac{D_n}{V_I^{-2} + \Omega_n^2 + |D_n|^2}.
\end{aligned} \tag{4.15}$$

Because all of the frequency dependence of $\phi_{k,n}$ is contained in the last term of the last equation above, it can be rewritten as

$$\phi_{k,n} = -\sum_{k'} V_{k,k'} \chi_{k'}^p + f_n, \tag{4.16}$$

where

$$\chi_k^p \equiv T \sum_{n'} \frac{\phi_{k,n'}}{\tilde{\varepsilon}_k^2 + \tilde{\omega}_{n'}^2 + |\phi_{k,n'}|^2} \tag{4.17}$$

contains the k-space dependence of the order parameter and

$$f_n \equiv n^{(I)} \frac{D_n}{V_I^{-2} + \Omega_n^2 + |D_n|^2} \tag{4.18}$$

contains the frequency dependence which must be analytically continued to find $\phi_k(\omega)$, the order parameter as a function of real frequency.

The fact that in the weak coupling limit that the order parameter is separable into momentum and frequency parts greatly simplifies calculations.

4.3.3 Strong Coupling

In the strong coupling limit the simplification made in §4.3.2 can not be made and the Eliashberg equations, given by Eq. 2.23, becomes

$$\hat{G}_{k,n}^{-1} = \hat{G^o}_{k,n}^{-1} - \hat{\Sigma}_{k,n} - \hat{\Sigma}_{k,n}^{(I)}.$$

This limit is not examined in this work.

Chapter 5

Single Band Models

While this thesis is primarily concerned with multiband models the theoretical basis for the calculations performed is more easily presented for a single band model. In light of this, this chapter presents the formalism for each calculation and the subsequent chapter on multiband models only contain the changes to the formalisms presented here that are necessary for those calculations.

5.1 Single Band Model Dispersions

High temperature superconductors seem to all have a maximum critical temperature, T_c, at a filling of approximately $\langle n \rangle = 0.85$ (*i.e.* a doping of 15% away from the AFM parent compounds discussed in Ch. 3) with the possible exception of $YBa_2Cu_3O_{7-x}$ (The situation for $YBa_2Cu_3O_{7-x}$ is more complicated due to the chain structure of this material which is discussed in §5.1.2 and Ch. 6.). The hopping parameters, $t_{r-r'}$, of Eq. 3.4 are chosen so that the filling is correct and the Fermi surface is consistent with experimental results. Which parameters to actually use for the $t_{r-r'}$ to model different materials comes from both theory and experiment. Local density approximation (LDA) [31, 32, 33, 34, 35, 64, 65] and linear augmented-plane-wave (LAPW)[66] calculations provide a theoretical basis for the band structure, while angle resolved photoemission spectroscopy (ARPES) experiments [25, 26, 27, 28, 29, 30, 67, 68, 69, 70] help to provide the position of the Fermi surface in the Brillouin zone and the magnetic penetration depth at zero temperature provide information about the absolute magnitudes of the $t_{r-r'}$ (see §5.5.3). However, the details of the slope of the dispersion near the Fermi energy are also important, particularly the position of the saddle point in the dispersion.

In the remainder of this section several different model dispersions are examined. These model dispersions differ from the Hubbard dispersion shown in Fig. 3.4 in that the Fermi surface is closed about the (π, π) point (*i.e.* they are "hole" Fermi surfaces instead of "electron" Fermi surfaces). This is equivalent to noting that the van Hove singularity (vHS) is below the Fermi

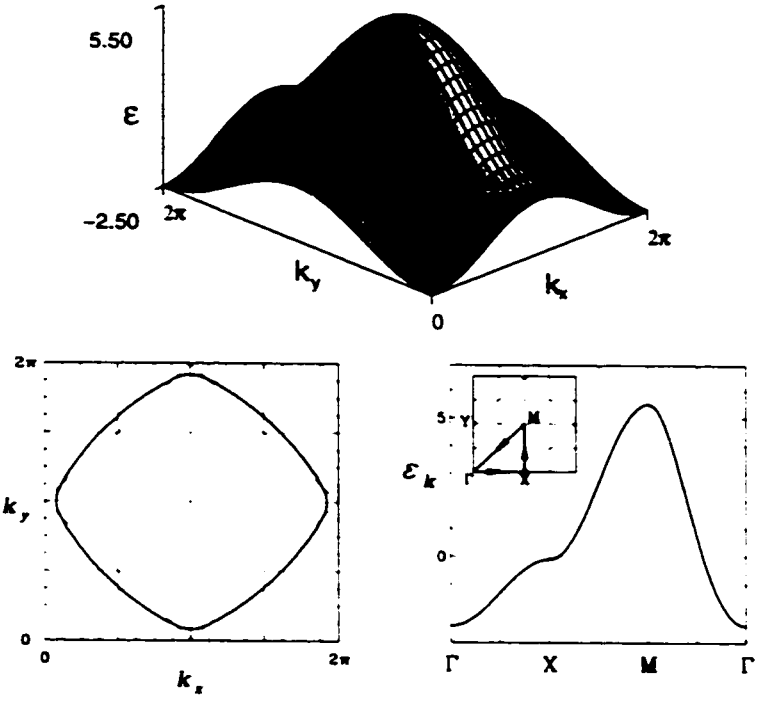

Figure 5.1: The dispersion relation for LSCO is modeled by Eq. 3.4 with $t' = 0.20$ and $\bar{\mu} = 2.50$. On the top is a stereographic projection of $\varepsilon_{\boldsymbol{k}}$ for the two dimensional Brillouin zone; the solid curve is the Fermi surface. Below on the left is the Fermi surface in the first Brillouin zone; the magnetic Brillouin zone, the diagonal dotted lines, are also shown for illustrative purposes (see text). Below on the right is $\varepsilon_{\boldsymbol{k}}$ along the $\Gamma X M \Gamma$ triangle in the Brillouin zone (inset).

energy.

5.1.1 $La_{2-x}Sr_xCuO_4$

$La_{2-x}Sr_xCuO_4$ (referred to hereafter as LSCO) was among the first HTS material discovered.[9] Despite its relatively low critical temperature ($\sim$ 30K) LSCO is still widely studied because it is one of the few HTS materials for which high quality, large ($\sim$ 5mm on a side) crystals can be made. The reason that large crystals can be made is due to its stiociometric doping. Large crystals are necessary for some experiments, especially neutron scattering.

In Fig. 5.1 is a dispersion relation with $t = 100$meV, $t' = 0.20$ and $\bar{\mu} = 1.25$ which is appropriate for modeling the CuO_2 layer of LSCO.[71] On the top is a stereographic projection of $\varepsilon_{\boldsymbol{k}}$ for the two dimensional Brillouin zone; the solid curve is the Fermi surface. Below on the left is the Fermi surface in the first Brillouin zone; the dotted lines are guides to the eye. On the right is $\varepsilon_{\boldsymbol{k}}$ along the ΓXMΓ triangle in the Brillouin zone (inset). Note that the dispersion has a maximum at the M point, $\boldsymbol{k} = (\pi, \pi)$, a minimum at the Γ point, $\boldsymbol{k} = (0, 0)$ and saddle points at the X and Y points, $\boldsymbol{k} = (\pm\pi, 0), (0, \pm\pi)$ (the saddle point appears as an inflection point at X on the lower right

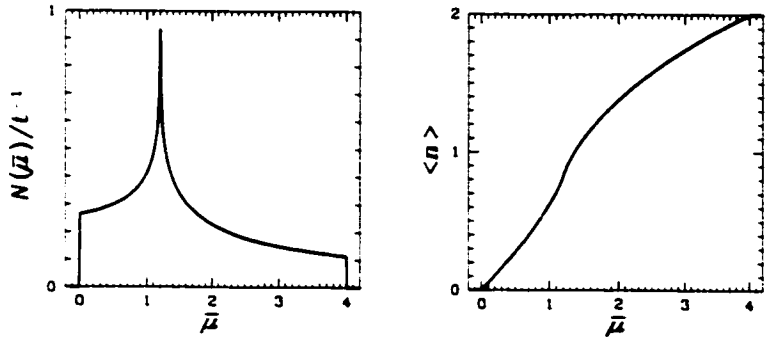

Figure 5.2: The density of states (DOS) for a tight binding band with next nearest neighbour hopping of $0.20t$ is shown on the left. On the right is the filling, $\langle n \rangle$. There are van Hove singularities (vHS) at the top of the band ($\bar{\mu} = 4$) and bottom of the band ($\bar{\mu} = 0$) caused by the maxima and minima of the dispersion. There is another vHS at the middle of the band ($\bar{\mu} = 2 - 4t' = 1.2$) which is caused by the saddle point at $(\pi, 0)$ (and symmetry related points) of the dispersion. The dotted lines correspond to a filling of $\langle n \rangle = 0.85$.

graph). The figures are similar to those in Fig. 3.4 but the saddle points at X and Y are much closer to the Fermi energy (*i.e.*, the inflection point at X in the lower right graph is closer to $\varepsilon_k = 0$).

On the right in Fig. 5.2 the variation of the filling, $\langle n \rangle$, with the (redefined) chemical potential, $\bar{\mu}$, is plotted in the normal state; this curve is equivalent to an integrated density of states. There is a slight shift in this curve ($\sim 1\%$) in the superconducting state. On the left is the DOS with the van Hove singularity shifted to $\bar{\mu} = 2 - 4t' = 1.2$. Note that the band is no longer symmetric about half filling, $\langle n \rangle = 1$, due to $t' \neq 0$. In the superconducting state a gap forms in the DOS at the Fermi energy (see §5.6). These and subsequent DOS and filling figures are calculated using Eqs. 3.9 & 3.11 at a temperature of $T = 0.005t$, which, for $t = 100$meV, corresponds to 4.2K.

LSCO is a single band material (*i.e.* it has only one CuO_2 layer per unit cell) and so it is not examined in subsequent chapters. It is presented here only for purposes of comparison.

5.1.2 $YBa_2Cu_3O_{7-x}$ and $Bi_2Sr_2CaCu_2O_{8+x}$

$YBa_2Cu_3O_{7-x}$ and $Bi_2Sr_2CaCu_2O_{8+x}$ (referred to hereafter as YBCO and BSCCO, respectively) are two of the most studied HTS materials. The high quality of YBCO materials particularly suits them for experiments which are sensitive to impurities such as penetration depth measurements. Furthermore, because the doping of YBCO can be varied by annealing them in an O_2 atmosphere, they are popular in the study of the effects of doping on HTS materials. The BSCCO materials, due to the van der Waals bonding between CaO layers, are easily cleaved to yield almost perfect surfaces. Such surfaces are particularly important for experiments which are local surface probes such as STM and ARPES.

In Fig. 5.3 is a dispersion relation with $t' = 0.45$ and $\bar{\mu} = 0.51$ which is appropriate for

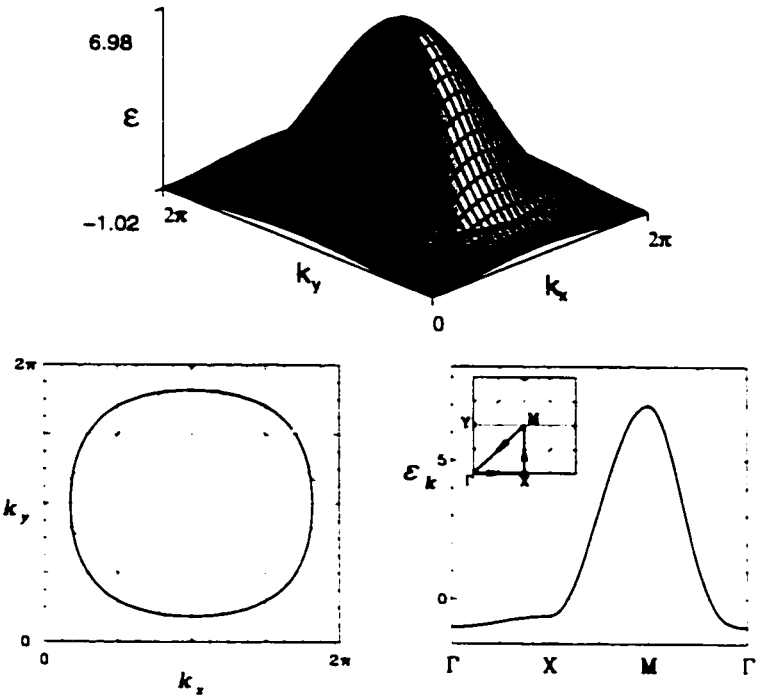

Figure 5.3: The dispersion relation for the CuO_2 layers in YBCO and BSCCO are modeled by Eq. 3.4 with $t' = 0.45$ and $\tilde{\mu} = 0.51$. On the top is a stereographic projection of ε_k for the two dimensional Brillouin zone; the solid curve is the Fermi surface. Below on the left is the Fermi surface in the first Brillouin zone and on the right is ε_k along a triangle in the Brillouin zone (inset).

modeling the CuO_2 layer of both $YBa_2Cu_3O_{7-x}$ and $Bi_2Sr_2CaCu_2O_{8+x}$.[72, 73, 74] In comparison with Fig. 5.1 the Fermi surface is much more rounded and the saddle point, while further from the Fermi energy, is much broader and flatter.

On the right in Fig. 5.4 the variation of the filling, $\langle n \rangle$, with the (redefined) chemical potential, $\tilde{\mu}$, is plotted in the normal state and on the left is the DOS with the van Hove singularity shifted to $\tilde{\mu} = 2 - 4t' = 0.2$. Note that the band is even more asymmetric than Fig. 5.2 and, due to the broader, flatter saddle point in the dispersion, that the vHS is significantly enhanced.

Orthorhombicity and YBCO

While the Fermi surface of the CuO_2 layers in YBCO and BSCCO are very similar, YBCO also has CuO chain layers present in its unit cell (see Fig. 3.3). The fact that there is a large a-b anisotropy in many of the properties of YBCO (*e.g.* the conductivity in the normal state and the magnetic penetration depth in the superconducting state) indicates that, even if the chain layers are not necessary to model the superconductivity in these materials, they are necessary to model specific properties that exhibit this large anisotropy. Furthermore, the presence of the chains makes it unclear precisely what the doping level of YBCO materials are. Here we assume that it is the

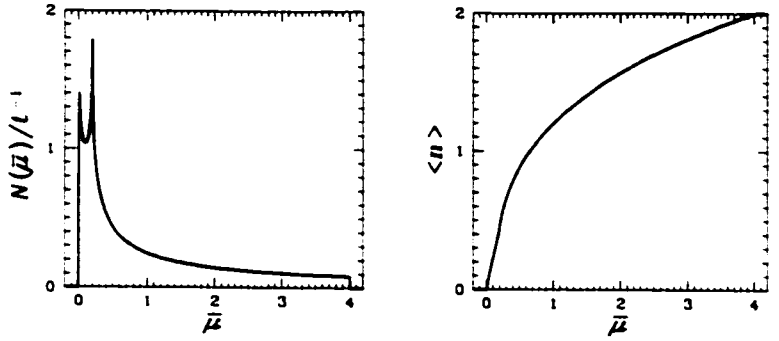

Figure 5.4: The density of states (DOS) for a tight binding band with only nearest neighbour hopping is shown on the left. On the right is the filling, $\langle n \rangle$ (note that the DOS is given by $d\langle n \rangle / d\mu$). There are van Hove singularities (vHS) at the top of the band ($\bar{\mu} = 4$) and bottom of the band ($\bar{\mu} = 0$) caused by the maxima and minima of the dispersion. There is another vHS at $\bar{\mu} = 2 - 4t' = 0.2$ which is caused by the saddle point at $(\pi, 0)$ (and symmetry related points) of the dispersion. The dotted lines correspond to a filling of $\langle n \rangle = 0.85$.

same as in other materials.

In the next chapter, Ch. 6, model dispersions appropriate for systems which contain multiple coupled CuO_2 (and CuO) layers are explored. In this section a simple method for including this anisotropy in a single band model is introduced. This method entails modifying the dispersion so that the a and b hopping integrals differ by introducing an anisotropy parameter, δ, to the dispersion of Eq. 3.6

$$\begin{aligned} \varepsilon_{\mathbf{k}} &= -2t\left((1-\delta)\cos(k_x) + (1+\delta)\cos(k_y) - 2t'\cos(k_x)\cos(k_y) - (2 - 2t' - \bar{\mu})\right) \\ &= -2t\left(\eta^s_{\mathbf{k}} - \delta\eta^d_{\mathbf{k}} - 2t'\cos(k_x)\cos(k_y) - (2 - 2t' - \bar{\mu})\right), \end{aligned} \tag{5.1}$$

with the $\eta^{s,d}_{\mathbf{k}}$ the basis functions defined in Eq. 2.22, which gives the dispersion an "$s - \delta d$" form.

In Fig. 5.5 this dispersion is plotted for the same parameters as in Fig. 5.3 with $\delta = 13\%$. On the top is a stereographic projection of $\varepsilon_{\mathbf{k}}$ for the two dimensional Brillouin zone; the solid curve is the Fermi surface. Below on the left is the Fermi surface in the first Brillouin zone and on the right is $\varepsilon_{\mathbf{k}}$ along a triangle in the Brillouin zone (inset). This value of the orthorhombic distortion, $\delta = 13\%$, accurately reproduces the a and b-axis zero temperature magnetic penetration depths for optimally doped YBCO (see §5.5.3) which directly reflects the hopping integrals in the a- and b-directions. It should be noted that, due to the asymmetry parameter, δ, the bandwidth of this orthorhombic dispersion is slightly larger than that in Figs. 5.1 and 5.3: the bottom of the band is now at $(\pm\pi, 0)$ and that the saddle points are at $(0, \pm\pi)$ and $(0, 0)$ (*i.e.* that the saddle point at Y and the minimum at Γ have exchanged places).

On the left in Fig. 5.6 is the density of states (DOS) for this tight binding band. There are van Hove singularities (vHS) at the top of the band ($\bar{\mu} = 4$) and bottom of the band ($\bar{\mu} = 0$) caused

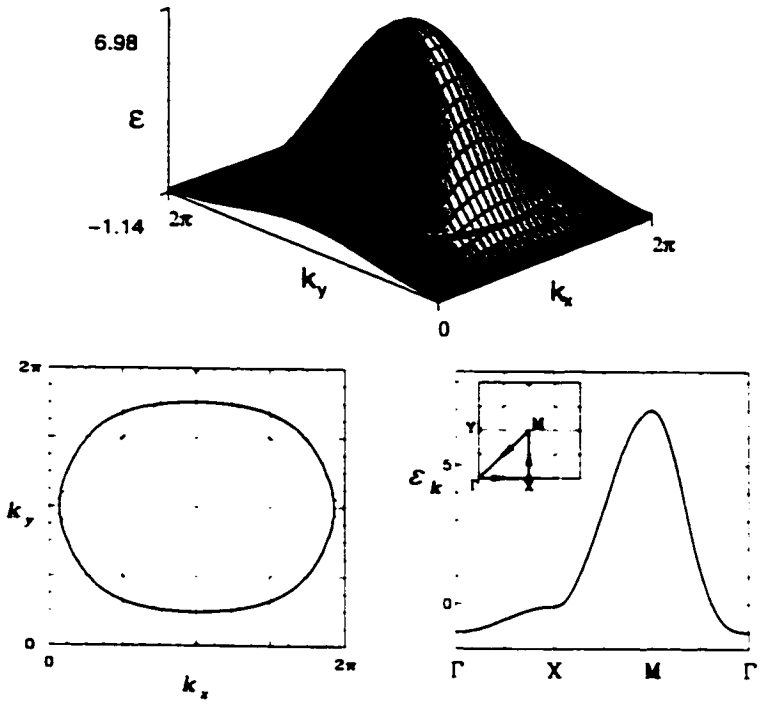

Figure 5.5: The orthorhombic dispersion relation for YBCO is modeled by Eq. 5.1 with $t' = 0.45$, $\bar{\mu} = 1.02$ and $\delta = 13\%$. On the top is a stereographic projection of ε_k for the two dimensional Brillouin zone: the solid curve is the Fermi surface. Below on the left is the Fermi surface in the first Brillouin zone and on the right is ε_k along a triangle in the Brillouin zone (inset).

by the maxima and minima of the dispersion. There is another pair of vHS at $\bar{\mu} = 2 - 4t' + 2\delta, 0$ which are caused by the saddle points at $(0, \pm\pi)$ and $(0,0)$ of the dispersion which, due to the orthorhombic distortion, are at different energies. On the right is the corresponding filling, $\langle n \rangle$, as a function of $\bar{\mu}$.

5.1.3 Three Dimensional Fermi Surface

For high temperature superconductors the hopping integrals, $t_{r-r'}$, are large within the CuO_2 plane and small out of plane (the hopping integral perpendicular to the CuO_2 planes is denoted by $t_\perp$). The Fermi surface is an undulating cylinder with its axis in the z-direction. In most of the calculations in this thesis the sums over k-space are taken as two dimensional even though the real system being modeled is three dimensional. This is a reasonable approximation since, due to the small dispersion in the k_z-direction, there is very little variation of most quantities in the k_z-direction and so the sum over k_z can be done assuming the summand is constant as a function of k_z. However, since we are dealing with a three dimensional system we can have long range order (which can only exist at $T = 0$ in two dimensions). However, in order to calculate c-axis properties

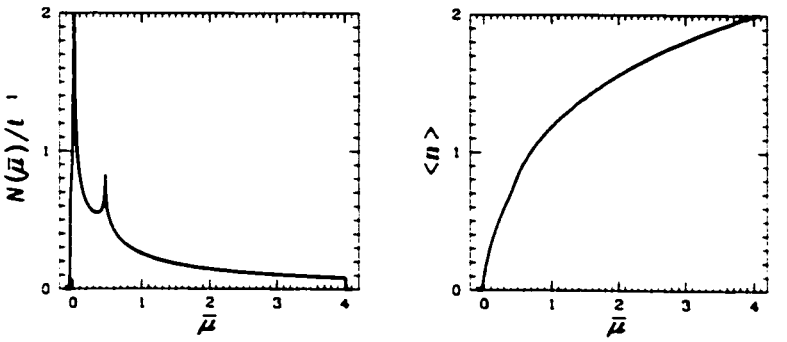

Figure 5.6: On the left is the density of states (DOS) for a tight binding band given by Eq. 5.1 with $\delta = 13\%$. On the right is the corresponding filling, $\langle n \rangle$. There are van Hove singularities (vHS) at the top of the band ($\bar{\mu} = 4$) and bottom of the band ($\bar{\mu} = -0.06$) caused by the maxima and minima of the dispersion. There is another pair of vHS ($\bar{\mu} = 2 - 4t' + 2\delta, 0$) which are caused by the saddle points at $(0,0)$ and $(0, \pm\pi)$ of the dispersion. The dotted lines correspond to a filling of $\langle n \rangle = 0.85$.

this k_z dispersion must be included.

The most straightforward way to include the k_z-dispersion is to assume that hopping from CuO_2 to CuO_2 plane is dealt with in a manner analogous to the derivation of Eq. 3.5 and introduces a term

$$-2t_\perp \cos(k_z c) \tag{5.2}$$

to the dispersion of Eq. 3.6 with $t_\perp$ being the hopping integral in the z-direction in units of t.

On the top left in Fig. 5.7 the Fermi surface is plotted in the k_x-k_y plane of the three dimensional Brillioun zone for the planes defined by $k_z = \{0, \pi/4, \pi/2, 3\pi/4, \pi\}$ using Eq. 5.2 in the dispersion of Fig. 5.3 with $t_\perp = 0.2$. In the middle, the Fermi surface is plotted in the k_x-k_z plane of the three dimensional Brillioun zone for the planes defined by $k_y = \{0, \pi/4, \pi/2, 3\pi/4, \pi\}$ (here there is no Fermi surface in the $k_y = 0$ plane). The solid curves are for $k_{y,z} = \pi/2$ and the solid curve in the k_x-k_y plane (top) is the same as that in Fig. 5.3. On the bottom is a stereographic projection of the three dimensional Fermi surface.

On the right in Fig. 5.7 the same Fermi surface contours and surfaces are plotted, but this time with $t_\perp = 0.4$ (here the innermost dashed curve is the Fermi surface in the $k_y = 0$ plane). For small $t_\perp$ the Fermi surface is a gently undulating cylinder (shown on the bottom left in Fig. 5.7) with its axis aligned along the k_z-direction and neglecting the k_z-dependence is reasonable. For a tetragonal system with $t_\perp > 0.3$ the Fermi surface intersects the Brillouin zone boundary and it is not so reasonable to neglect the k_z-dependence of the dispersion due to the topological change which can be seen most clearly in the two figures on the bottom of Fig. 5.7 - namely the "necks" that exist in the $k_y = 0$ and $k_x = 0$ planes only on the right.

In fact it is found, using the zero temperature c-axis magnetic penetration depth that

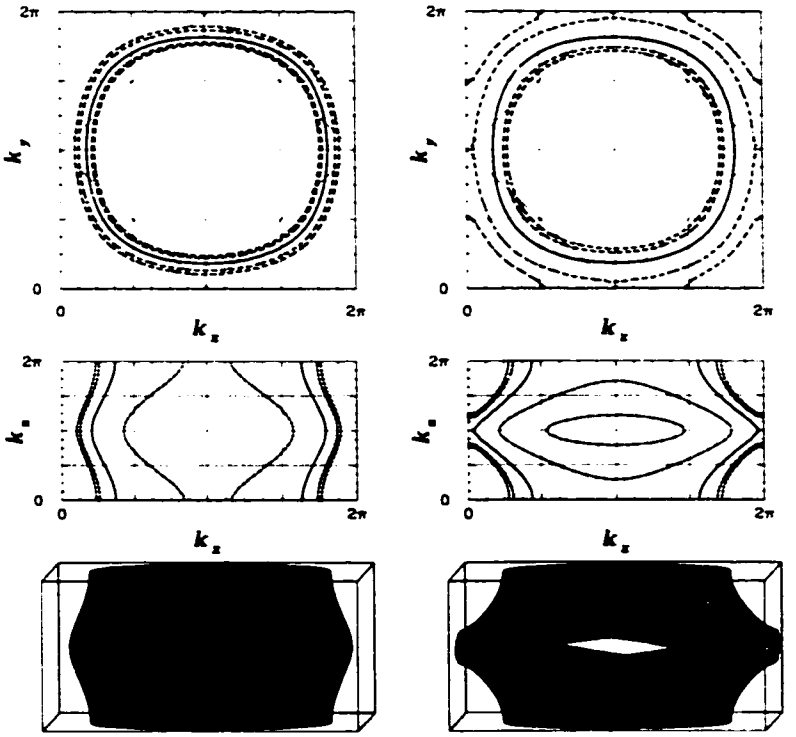

Figure 5.7: On the top left the Fermi surface is plotted in the k_x-k_y plane of the three dimensional Brillioun zone for the planes defined by $k_z = \{0, \pi/4, \pi/2, 3\pi/4, \pi\}$ using Eq. 5.2 in the dispersion with $t_\perp = 0.2$. In the middle the Fermi surface is plotted in the k_x-k_z plane of the three dimensional Brillioun zone for the planes defined by $k_y = \{0, \pi/4, \pi/2, 3\pi/4, \pi\}$ (here there is no Fermi surface in the $k_y = 0$ plane). The solid curves are for $k_{y,z} = \pi/2$. On the right the same Fermi surface contours are plotted, but this time with $t_\perp = 0.4$ (here the innermost dashed curve is the Fermi surface in the $k_y = 0$ plane). At the bottom are three dimensional depictions of the Fermi surfaces in the three dimensional Brillouin zone.

$t_\perp \sim 0.06$. This gives an undulation less than a third that shown on the left in Fig. 5.7 so that, in this case, neglect of the k_z-dependence is an excellent approximation. For an orthorhombic system (discussed below), however, even this small k_z-dependence causes the Fermi surface to intersect the Brillouin zone boundary. The effects of this topological change in the Fermi surface on the order parameter are investigated in §5.2 (a Fermi surface plot similar to those in Fig. 5.7 for this orthorhombic case is shown in Fig. 5.11 on p. 55) and upon the c-axis magnetic penetration depth are explored in §5.5.4.

Recent LDA calculations by O.K. Anderson *et al.*[75, 76] indicate that the transverse matrix element, $t_\perp$, is modulated by a momentum dependent factor in the a-b plane given by

$$-\tfrac{1}{2} t_\perp \left(\cos(k_x a) - \cos(k_y b)\right)^2 \cos(k_z c) \tag{5.3}$$

which is added to the dispersion of Eq. 5.14 with $t_\perp$ again being the hopping integral in the z-

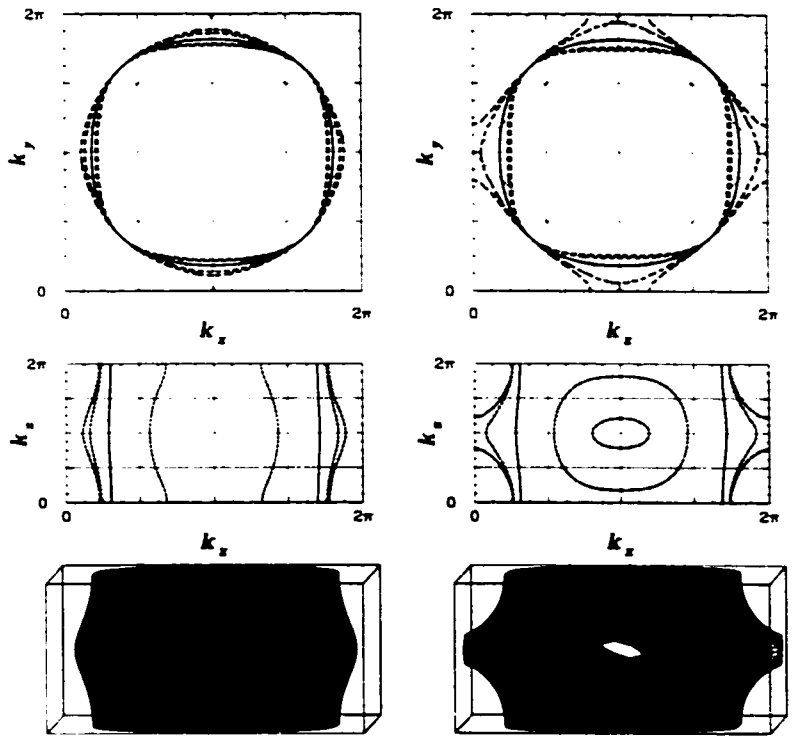

Figure 5.8: On the top left the Fermi surface is plotted in the k_x-k_y plane of the three dimensional Brillioun zone for the planes defined by $k_z = \{0, \pi/4, \pi/2, 3\pi/4, \pi\}$ using Eq. 5.3 in the dispersion with $t_\perp = 0.2$. In the middle the Fermi surface is plotted in the k_x-k_z plane of the three dimensional Brillioun zone for the planes defined by $k_y = \{0, \pi/4, \pi/2, 3\pi/4, \pi\}$ (here there is no Fermi surface in the $k_y = 0$ plane). The solid curves are for $k_{y,z} = \pi/2$. On the right the same Fermi surface contours are plotted, but this time with $t_\perp = 0.4$ (here the innermost dashed curve is the Fermi surface in the $k_y = 0$ plane). At the bottom are three dimensional depictions of the Fermi surfaces in the three dimensional Brillouin zone.

direction.

On the top left in Fig. 5.8 the Fermi surface is plotted in the k_x-k_y plane of the three dimensional Brillioun zone for the planes defined by $k_z = \{0, \pi/4, \pi/2, 3\pi/4, \pi\}$ using Eq. 5.3 in the dispersion of Fig. 5.3 with $t_\perp = 0.2$. In the middle the Fermi surface is plotted in the k_x-k_z plane of the three dimensional Brillioun zone for the planes defined by $k_y = \{0, \pi/4, \pi/2, 3\pi/4, \pi\}$ (here there is no Fermi surface in the $k_y = 0$ plane). The solid curves are for $k_{y,z} = \pi/2$ and the solid curve in the k_x-k_y plane (top) is the same as that in Fig. 5.3. On the right the same Fermi surface contours are plotted, but this time with $t_\perp = 0.4$. Here the innermost dashed curve is the Fermi surface in the $k_y = 0$ plane and, again, there are necks connecting adjacent Brillouin zones. Here, due to the nature of Eq. 5.3, there is no undulation of the Fermi surface along the diagonals of the k_x-k_y plane and this has a significant effect upon the c-axis transport properties because the k_z-dispersion is negligible near the gap nodes. This difference in the c-axis dispersion has a significant effect upon

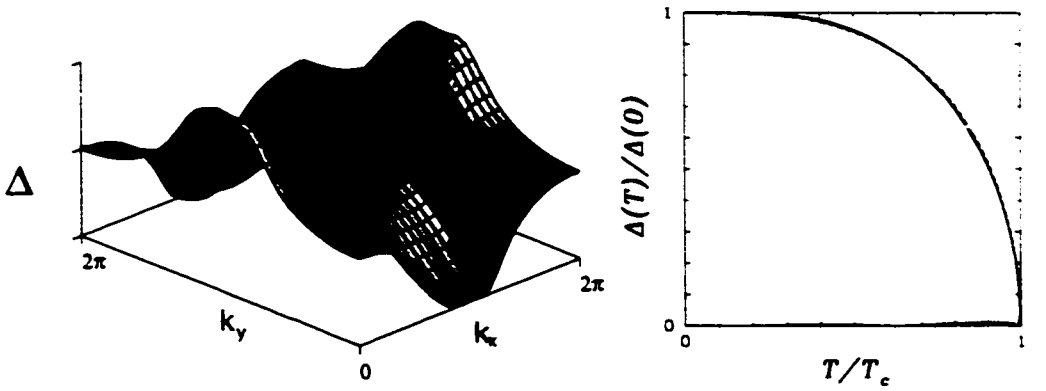

Figure 5.9: The gap due to an MMP interaction as a function of k is shown as a stereographic projection in the first Brillouin zone on the left. Although this function has a slightly different form to that shown in Fig. 2.5, because this gap has d-wave symmetry the gap nodes (dark lines) are along the diagonals of the Brillouin zone exactly as shown in lower right in Fig. 2.5. On the right is the temperature dependence of the gap (solid curve) found using the dispersion relation described in Fig. 5.3 on p. 47 with an MMP type interaction (Eq. 4.12 with $g^2\chi_o/t = 30.11$) which yields a $2\Delta/k_bT_c$ ratio of 4.55. Also shown for comparison is $h(T)$ (Eq. 2.21); note that the deviation of from the BCS solution (dotted curve) is different from that of the isotropic s-wave system (*cf.* Fig. 2.4).

the low temperature c-axis transport properties, especially the c-axis penetration depth (§5.5.4).

5.2 MMP Interaction

When the MMP interaction is used to solve the BCS equation a gap with d-wave symmetry results but it has a more complex form than the simple $\eta_k^d \equiv \cos(k_x) - \cos(k_y)$ discussed earlier. On the left in Fig. 5.9 the functional form of the gap near the critical temperature is shown. Because this gap has d-wave symmetry the gap nodes (dark lines) are along the diagonals of the Brillouin zone exactly as shown in lower right in Fig. 2.5. On the right is the temperature dependence of the magnitude of the gap (solid curve). The ratio $2\Delta^{(\max)}/k_BT_c$ is 4.55 with $\Delta^{(\max)}$ being the maximum value of the gap in the Brillouin zone at $T = 0$. This differs from the 3.53 of the BCS theory due to the different gap symmetry.[77, 78] In this single band tetragonal model the dispersion of Fig. 5.3 has been used and the coupling constant of the MMP interaction, Eq. 4.12, is $g^2\chi_o/t = 30.11$ which gives a critical temperature, T_c, of $0.12t$ which, for $t = 100$meV, corresponds to 100K. Also shown for comparison is $h(T)$, Eq. 2.21 (dashed curve); note that the deviation of from the BCS solution (dotted curve) is different from that of the isotropic s-wave system (*cf.* Fig. 2.4); a factor of 1.6 instead of 1.74 in Eq. 2.21 produces a result that more accurately reflects the BCS solution for a d-wave order parameter.

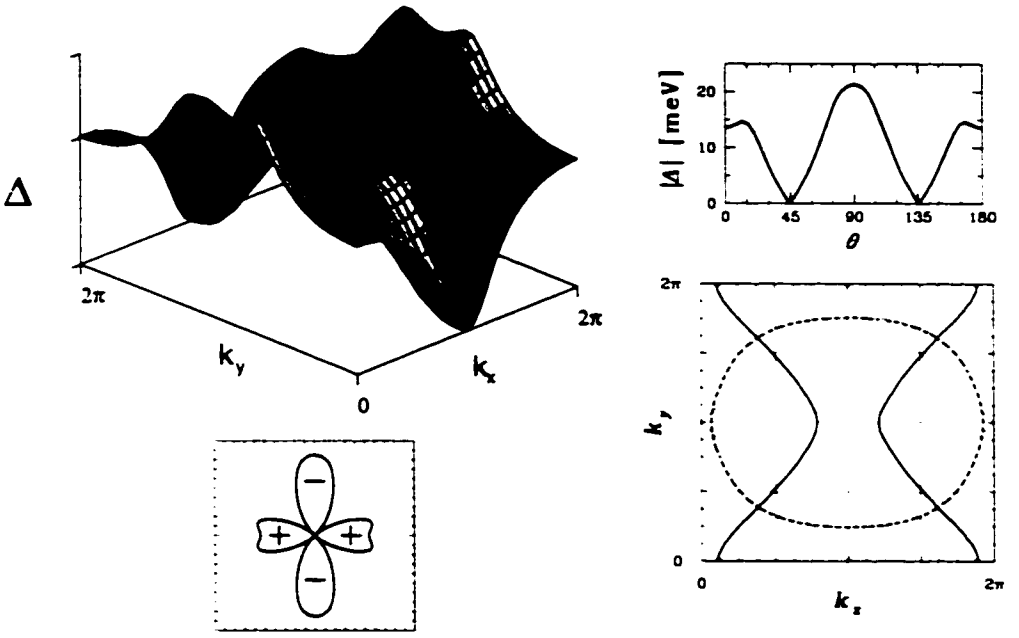

Figure 5.10: Four different representations of a d-wave order parameter, Δ_k, similar to those shown in Fig. 2.5. This order parameter is calculated using the orthorhombic system described in Fig. 5.5 on p. 49 and solving the BCS equation, Eq. 2.16, with an MMP type interaction (Eq. 4.12 with $g^2\chi_o/t = 29.30$). Note the significant asymmetry under rotations of 90°.

Orthorhombic System

When the single band orthorhombic system, used in §5.1.2 on p. 47 to model the dispersion of YBCO (Fig. 5.5), is used with the MMP interaction to solve the BCS equation the order parameter, due to the broken tetragonal symmetry, has an "$d - \delta s$" form given, for $\delta = 13\%$, roughly by

$$\begin{aligned} \Delta_k &= \Delta_o \left(-\tfrac{1}{2} + \cos(k_x) - \cos(k_y)\right) \\ &= \Delta_o \left(\eta_k^d - \tfrac{1}{2}\eta_k^o\right) \end{aligned}$$

in which the $\eta_k^{o,d}$ are the basis functions defined in Eq. 2.22. For comparison, the dispersion, Eq. 5.1, has an "$s - \delta d$" form. It is worth noting that the relatively small amount of asymmetry in the dispersion, 13%, produces a large amount of asymmetry in the order parameter, namely 50%, but that the gap nodes are only shifted by a small amount, $\approx 1°$.

An equivalent amount of asymmetry should perhaps be introduced to the interaction (*e.g.* the magnetic coherence, ξ_o, in Eq. 4.12 should be slightly different in the x and y-directions) but this added complication would change the results only in a minor way and so is not worthwhile.

On the bottom right in Fig. 5.10 is the Fermi surface (dashed curve) for an orthorhombic system (described in Fig. 5.5 on p. 49) and the gap node contour (solid curve) found by solving the BCS equation, Eq. 2.16, with an MMP type interaction (Eq. 4.12 with $g^2\chi_o/t = 29.30$). On the

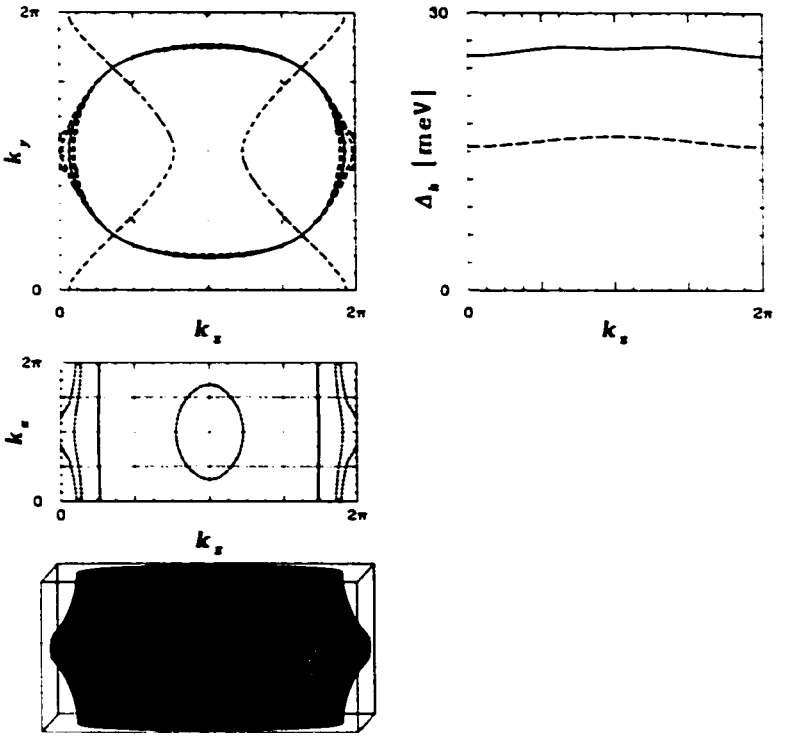

Figure 5.11: When the MMP interaction is modified to have a k_z-dependence (Eq. 5.4) the order parameter has ~5% variation along the k_z-direction with no shifting of the gap nodes. Plotted on the right is the order parameter for $\boldsymbol{k} = (\pi, 0)$ (solid line) and $\boldsymbol{k} = (0, \pi)$ (dashed line). Plotted on the left are the Fermi surface contours for $k_z = \{0, \pi/4, \pi/2, 3\pi/4, \pi\}$ (top) and $k_y = \{\pi/4, \pi/2, 3\pi/4, \pi\}$ (middle, there is no Fermi surface at $k_y = 0$) with the $\pi/2$ contours being the solid lines; also plotted on the top left are the gap nodes which do not vary with k_z. On the bottom is a stereographic projection of the three dimensional Fermi surface.

top left is a stereographic projection of the order parameter in the first Brillouin zone normalized so that $\sum_{\boldsymbol{k}} |\Delta_{\boldsymbol{k}}|^2 = 1$. On the top right is the magnitude of the order parameter around the Fermi surface and on the bottom left is the same quantity in a radial plot. Note the significant asymmetry under rotations of 90° which corresponds quite well to the "$d - \delta s$" form described above.

Three Dimensional System

If the MMP interaction given in Eq. 4.12 is used in a three dimensional system the order parameter will be almost identical to that of the corresponding two dimensional system (*i.e.* that with $t_\perp = 0$) because Eq. 4.12, as given, contains no k_z-dependence and so the order parameter will also have no k_z-dependence. In order to introduce a k_z-dependence to the order parameter the MMP interaction should be modified to

$$V_{\boldsymbol{k}}^{\mathrm{MMP}} \equiv g^2 \frac{\chi_o}{1 + \xi_x^2(k_x - \pi)^2 + \xi_y^2(k_y - \pi)^2 + \xi_z^2(k_z - \pi)^2} \tag{5.4}$$

with ξ_i the magnetic coherence length in the i-direction and $g^2\chi_o$ a phenomenological coupling constant which is adjusted so that the BCS equation has the desired critical temperature. When this interaction is used with $\xi = (2.5a, 2.5b, 2.5c)$ (with a, b and c the unit cell parameters) and the dispersion shown on the left in Fig. 5.11 (which is the same as that in Fig. 5.10, but with a small k_z-dependence added via Eq. 5.3 with $t_\perp = 0.06$) the order parameter varies in magnitude by ~5% in the k_z-direction. Plotted on the right in Fig. 5.11 is the order parameter for $\boldsymbol{k} = (\pi, 0)$ (solid line) and $\boldsymbol{k} = (0, \pi)$ (dashed line). For a smaller and more realistic ξ_z of 0.5c the order parameter varies by less than 2%. In light of this small effect, henceforth only Eq. 4.12 will be used for the MMP interaction since the added complexity of Eq. 5.4 would only change the results in a very minor way.

Using the three dimensional dispersions of §5.1.3, shown in Fig. 5.7, instead of the equivalent two dimensional dispersions when solving the BCS equation does not have a significant effect upon the order parameter. This validates the assertion made at the beginning of §5.1.3 that there is very little variation of most quantities in the k_z-direction and so the sum over k_z can be done assuming the summand is constant. The only exception to this is when a c-axis property is required (*e.g.* the c-axis magnetic penetration depth discussed in §5.5.4).

5.3 Impurities

Impurities are present in all HTS materials to some degree and it is only in the highest quality crystals that they can be neglected. In some crystals impurities are purposefully introduced in order to study their effects because the behaviour of s and d-wave superconductors in the presence of impurities can be radically different.

Tetragonal System

In Fig. 5.12 the effect of impurities upon the critical temperature of a single layer tetragonal system is shown for two different scattering strengths: the solid curve is for the unitary limit ($V_I \to \infty$) and the dashed curve is for the Born approximation ($V_I = 1t$). On the left is shown the effect of impurities for an isotropic s-wave system ($U_o = 1.3t$) and on the right is that for a d-wave system ($g^2\chi = 30.11t$).

That the isotropic system is much less affected by the presence of impurities than the d-wave system is a consequence of Anderson's Theorem [79] which shows how the detrimental effects upon T_c caused by the renormalization of ω_n is offset by the positive effect upon $\phi_{\boldsymbol{k},n}$. This theorem no longer holds for d-wave superconductors because D_n is zero (*i.e.* The sum over $\boldsymbol{k}$ in Eq. 4.13 is zero) and, hence, f_n is also zero.

The interaction strengths used ($g^2\chi = 30.11t$, $U_o = 1.3t$) is that which would result in a T_c of 100K in the absence of impurities. It is slightly lower than 100K (95.58K) due to the presence of the finite cutoff in the Matsubara sums – three times the bandwidth of $8t$ is used in these calculations.

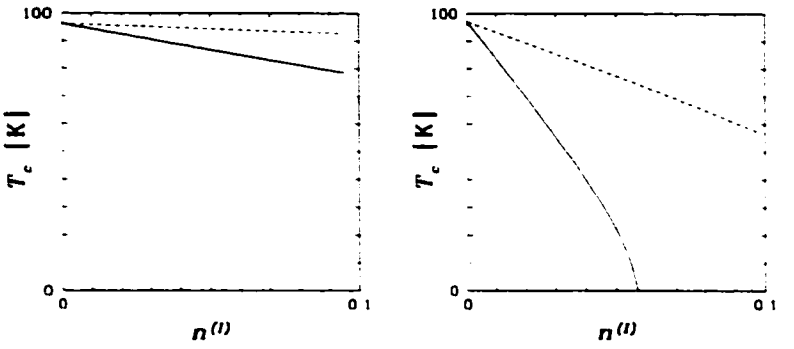

Figure 5.12: The critical temperature, T_c, as a function of impurities, $n^{(I)}$, for a single band tetragonal model. The solid curve is for the unitary limit ($V_I \to \infty$) and the dashed curve is for the Born approximation ($V_I = 1t$). On the left is shown the effect of impurities for an s-wave system ($U_o = 1.3t$) and on the right is that for a d-wave system ($g^2\chi = 30.11t$).

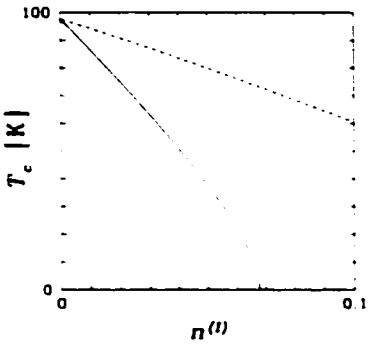

Figure 5.13: The critical temperature, T_c, as a function of impurities, $n^{(I)}$, for a single band orthorhombic model ($\delta = 13\%$). The solid curve is for the unitary limit ($V_I \to \infty$) and the dashed curve is for the Born approximation ($V_I = 1t$). Results are shown for a d-wave system ($g^2\chi = 29.30t$).

Orthorhombic System

In an orthorhombic system the order parameter will have a d+s admixture and the effects of impurities will be somewhere in between that of a pure s and a pure d-wave system and are shown in Fig. 5.13. Here the critical impurity concentration (*i.e.* that for which $T_c = 0$) in the unitary limit is 6.8%, compared to 5.7% for the tetragonal system. While Anderson's theorem [79] still doesn't hold, the detrimental effects upon T_c caused by the renormalization of ω_n is mitigated by the small positive effect upon $\phi_{k,n}$.

In Fig. 5.14 the order parameter, $\phi_k(\omega)$, for a single band orthorhombic model ($\delta = 13\%$) in the unitary limit ($V_I \to \infty$) with 2% impurities is shown for a d-wave system ($g^2\chi = 29.30t$) at $T = 10$K ($T_c = 74.8$K). On the left is the real (solid curve) and imaginary (dashed curve) parts of the analytic continuation, $f(\omega)$, of the frequency dependent part of the order parameter; the points

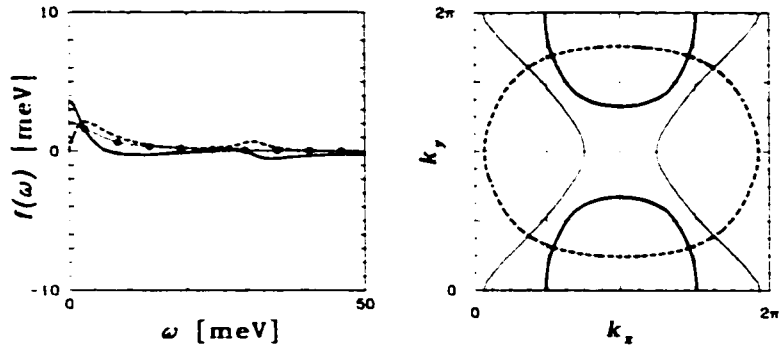

Figure 5.14: The order parameter, $\phi_{\mathbf{k}}(\omega)$, for a single band orthorhombic model ($\delta = 13\%$) in the unitary limit ($V_I \to \infty$) with 2% impurities. Results are shown for a d-wave system ($g^2\chi = 29.30t$) at $T = 10$K ($T_c = 74.8$K). On the left is shown the real (solid curve) and imaginary (dashed curve) parts of the analytic continuation, $f(\omega)$, of the frequency dependent part of the order parameter, f_n; the points are the f_n. On the right are shown the gap nodes in the first Brillouin zone of the $\mathbf{k}$-dependent part of the order parameter, $\Delta_{\mathbf{k}}$, (light solid curve) and the gap nodes of the analytic continuation of the order parameter, $\phi_{\mathbf{k}}(\omega)$, at $\omega = 0$ (dark solid curve) which is shifted due to the effect of $f(0)$. The Fermi surface (dashed curve) is also shown. The $\mathbf{k}$-dependent part of the order parameter, $\Delta_{\mathbf{k}}$, has a maximum value of 21.1meV and the frequency dependent part, $f(\omega)$, has a maximum value at zero frequency of 3.6meV.

plotted are the f_n. On the right are the gap nodes in the first Brillouin zone of the $\mathbf{k}$-dependent part of the order parameter, $\Delta_{\mathbf{k}}$, (light solid curve) and the gap nodes of the analytic continuation of the order parameter, $\phi_{\mathbf{k}}(\omega)$, at $\omega = 0$ (dark solid curve) which is shifted due to the effect of $f(0)$ (Note that at $\omega = 0$ the order parameter, $\phi_{\mathbf{k}}(\omega)$, is purely real.). The Fermi surface (dashed curve) is also shown. The $\mathbf{k}$-dependent part of the order parameter, $\Delta_{\mathbf{k}}$, has a maximum value of 21.1meV and the frequency dependent part, $f(\omega)$, has a zero frequency value of 3.6meV. A similar figure for the tetragonal system is not shown because $f(\omega)$ is zero and $\Delta_{\mathbf{k}}$ is a pure d-wave.

5.4 Optical Conductivity

Conductivity is probably the most important property of superconductors since it characterizes the electrical response of the system to an applied electromagnetic field and it is the electrical response of superconductors that makes them unique. Above the superconducting critical temperature conventional superconductors typically behave like metals with a conductivity having a Drude type frequency response given by the Lorentzian

$$\sigma(\omega) = \frac{ne^2\tau}{m^*(1 - \omega\tau)} \tag{5.5}$$

which is characterized by a scattering rate, τ. Below the critical temperature, however, the response changes to give a delta function at zero frequency (*i.e.* infinite DC conductivity) and a gap in the low frequency response of twice the width of the superconducting gap. Note that since the optical

range of frequencies are above the plasma frequency of HTS, HTS materials appear black (*i.e.* the index of refraction is almost pure imaginary in the visible range so all visible light is absorbed); the use of the term "optical" refers to the techniques used in the experiments rather than to the visible region of the electromagnetic spectrum.

Experiments measure the reflectivity [80] or, in some cases, the transmission of light as a function of frequency using different detectors for different frequency ranges. These results are extrapolated to zero and infinite frequency and, using Kramers-Kronig relations, are converted into a frequency dependent conductivity which can be compared with calculations. For the *c*-axis conductivity the situation is complicated by the presence of several phonons that are present in the frequency range of interest that are subtracted from the data prior to the Kramers-Kronig analysis.

High temperature superconductors are different in several respects from conventional superconductors. The main differences are that the normal state conductivity, instead of having a Drude-like form, seems to have a large background, and, even more striking, underdoped materials (and even some optimally doped materials [81, 82]) develop a gap, called the "pseudogap", at a temperature, T^*, above the superconducting critical temperature [80], the width of which seems to be temperature independent. The origin and nature of these features is controversial and several reviews have been written.[83, 84]

For underdoped materials something other than superconductivity is happening at T^* which appears to behave like a superconducting gap and has the size of the superconducting gap that does appear at T_c. Here, no attempt is made to explain the pseudo-gap other than to state that if some other order parameter involving the conduction electrons becomes non-zero at T^* it will enter the formalism given below in a way analogous to the superconducting order parameter

5.4.1 Formalism

The conductivity tensor, $\sigma_{ij}(\omega)$, characterizes the response of a system to an applied electric field, $E_j(\omega)$, (*i.e.* a current) through the relation

$$j_i(\omega) = \sum_j \sigma_{ij}(\omega) E_j(\omega)$$

although a suitable choice of coordinate system in most materials will render it diagonal, $\sigma_i(\omega) \equiv \sigma_{ij}(\omega)\delta_{ij}$. The conductivity is related to the complex dielectric constant by

$$\epsilon_i(\omega) = 1 + \frac{4\pi i \sigma_i(\omega)}{\omega}.$$

At optical frequencies $\omega\tau >> 1$ and, using Eq. 5.5, the real part of the dielectric constant is

$$\Re\epsilon_i(\omega) = 1 - \frac{4\pi n e^2}{m^* \omega^2}$$

and for $\omega^2 < 4\pi n e^2/m^*$ the index of refraction of the material, which is the square root of the dielectric constant, will be imaginary and electromagnetic radiation will not propagate in the material,

i.e. it will be reflected. The frequency at which this change in behaviour happens is known as the plasma frequency, $\omega_p^2 \equiv 4\pi ne^2/m^*$. Typical metals have a plasma frequency above the frequencies of visible light and so appear shiny or "metallic." HTC materials, in contrast, have a plasma frequency in the infra-red region of the spectrum, below the frequencies of visible light, and so appear black.

In any case, the dielectric constant is related to the reflectivity by

$$R_i(\omega) = \left| \frac{1 - \sqrt{\epsilon_i(\omega)}}{1 + \sqrt{\epsilon_i(\omega)}} \right|^2 \tag{5.6}$$

which is usually the quantity that is measured in experiments. Because both the dielectric constant and the conductivity are complex functions inverting Eq. 5.6 is non-trivial, requiring the use of Kramers-Kronig relations [85, 86] which give the relationship between the real and imaginary parts of the conductivity required by causality.

Theoretically, the conductivity tensor, $\sigma_k^{ij}(\omega)$, is related to the current-current response function, $K_k^{ij}(\omega)$, by the relation

$$\sigma_k^{ij}(\omega) = \frac{i}{4\pi\omega} K_k^{ij}(\omega). \tag{5.7}$$

and is both frequency and wave-vector dependent. Since we are interested in the optical conductivity (*i.e.* very small $\boldsymbol{k}$-vector) only the $\boldsymbol{k} = 0$ part of the conductivity tensor is of interest and henceforth the explicit $\boldsymbol{k}$-dependence is dropped.

The current-current response function consists of a paramagnetic and diamagnetic parts

$$K^{ij}(\omega) = K^{ij^{(p)}}(\omega) - K^{ij^{(d)}}(0),$$

in the normal state the diamagnetic part is unchanged and there is no response to a static field

$$K^{ij^{(N)}}(0) = K^{ij^{(pN)}}(0) - K^{ij^{(d)}}(0) = 0$$

so that we can write the conductivity tensor as

$$K^{ij}(\omega) = K^{ij^{(p)}}(\omega) - K^{ij^{(pN)}}(0). \tag{5.8}$$

The paramagnetic part of the current-current response function on the imaginary axis is given by [87]

$$K_m^{ij^{(p)}} = -4\pi e^2 T \sum_{k,n} \mathrm{Tr}\left(\gamma_k^i \widehat{G}_{k,n} \gamma_k^j \widehat{G}_{k,n+m}\right) \tag{5.9}$$

in which m is a Boson Matsubara frequency, $\gamma_k^i \equiv \partial\epsilon_k/\partial k_i$ is the vertex function and $\widehat{G}_{k,n}$ is the Green's function introduced in §2.6. Here we have neglected vertex corrections. Substituting Eq. 2.32 into the above we get

$$K_m^{ij^{(p)}} = 8\pi e^2 T \sum_{k,n} \frac{\partial\epsilon_k}{\partial k_i} \frac{\partial\epsilon_k}{\partial k_j} \frac{\epsilon_k^2 - \tilde{\omega}_{k,n}\tilde{\omega}_{k,n+m} + \phi_{k,n}\phi_{k,n+m}}{\left[\epsilon_k^2 + \tilde{\omega}_{k,n}^2 + |\phi_{k,n}|^2\right]\left[\epsilon_k^2 + \tilde{\omega}_{k,n+m}^2 + |\phi_{k,n+m}|^2\right]}. \tag{5.10}$$

The equivalent expression for the normal state, $K^{ij(pN)}(0)$, is found by substituting Eq. 4.11 into Eq. 5.9.

Since the current-current response function is calculated on the imaginary axis it must be analytically continued, $K^{ij}(i\omega_m \rightarrow \omega + i0^+)$, before it can be substituted into Eq. 5.8 to yield the optical conductivity

$$\sigma^{ij}(\omega) = -\frac{1}{4\pi\omega}\Im K^{ij(p)}(\omega) + \frac{i}{4\pi\omega}\Re\left[K^{ij(p)}(\omega) - K^{ij(pN)}(0)\right].$$

Note that since the current-current response function is dependent upon Boson Matsubara frequencies that $K^{ij(pN)}_{m=0} = K^{ij(pN)}(0)$.

5.4.2 Results

As well as the real and imaginary part of the conductivity, denoted by $\sigma_1(\omega)$ and $\sigma_2(\omega)$, respectively, a third quantity of interest is the frequency dependent scattering rate, $1/\tau^*(\omega) = \omega\sigma_1(\omega)/\sigma_2(\omega)$, which more clearly exhibits the effects of both temperature and frequency.

Shown on the left in Fig. 5.15 is the real part of the optical conductivity for an s (top) and d-wave (bottom) order parameter. The solid curve, calculated at $T = 100$K, is the normal state and shows the behaviour expected of Eq. 5.5: a Lorentzian. In the s-wave case the development of a gap equal to twice the superconducting gap as the temperature is lowered is clearly apparent while in the d-wave case, due to the nodes in the gap, no such gap structure is apparent, although the height of the peak at low frequency decreases. In fact, the area under $\sigma_1(\omega)$ obeys a sum rule and is equal to $\omega_p^2/8\pi$; the area that "disappears" as the temperature is lowered goes into the delta function at $\omega = 0$ (*i.e.*, in the superconducting state there is infinite DC conductivity).

In fact this sum rule is a useful check upon the analytic continuation of the electron-electron response function. The "missing" area is the superfluid density and is equal to $\omega\sigma_2(0)$, which does not rely upon the analytic continuation, and, with an appropriate change of units, is the magnetic penetration depth which is discussed in the next section.

In the middle in Fig. 5.15 is the imaginary part of the optical conductivity multiplied by ω for an s (top) and d-wave (bottom) order parameter. All curves clearly show the $\omega \rightarrow \infty$ asymptotic limit of ω_p^2 given by Eq. 5.5. Also, in the s-wave case there is a clear dip at a frequency of twice the superconducting gap frequency, $\sim$ 30meV, that is not present in the d-wave case. The zero frequency part is related to the magnetic penetration depth which is discussed in the next section.

Finally, on the right in Fig. 5.15 is the frequency dependent scattering rate, $1/\tau^*(\omega)$, which for both the s and d-wave cases clearly shows the optical gap opening as the temperature is lowered although in the d-wave case even at the lowest temperature the scattering is finite for finite frequencies due to the gap node.

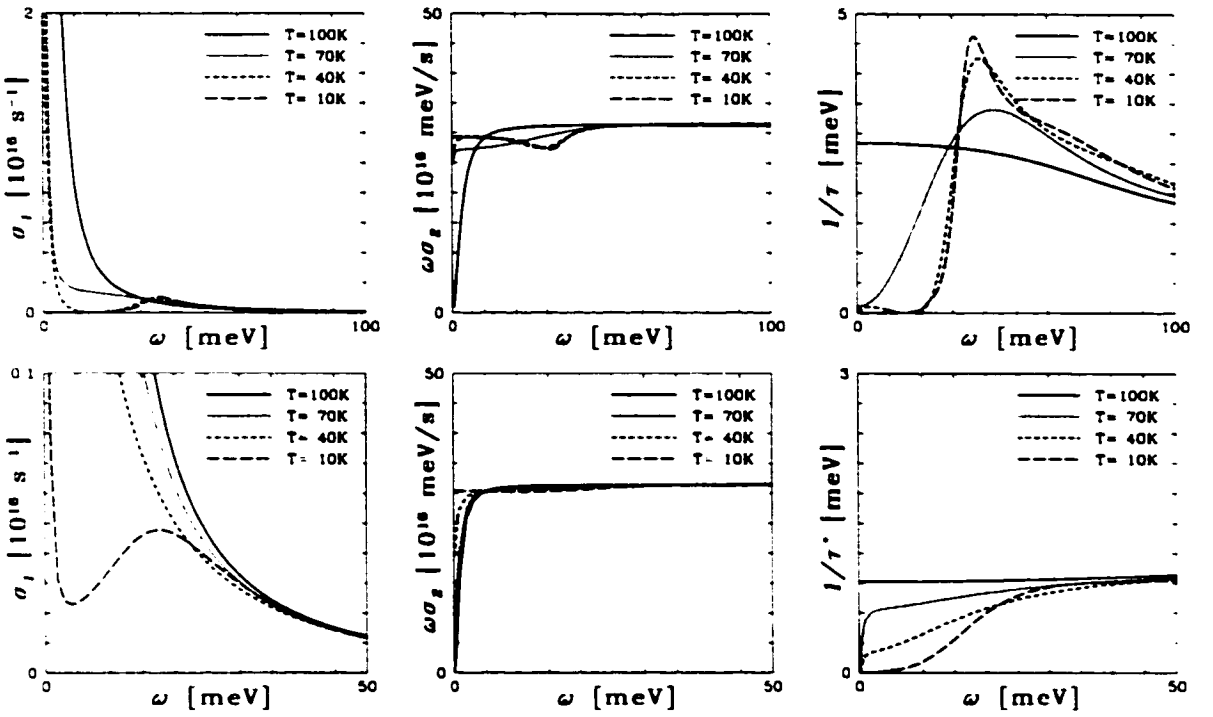

Figure 5.15: The optical conductivity for s (top) and d-wave (bottom) order parameters. On the left is the real part, $\sigma_1(\omega)$, in the middle is the imaginary part, $\sigma_2(\omega)$, and on the right is the scattering rate, $1/\tau^*(\omega) = \omega\sigma_1(\omega)/\sigma_2(\omega)$, calculated using Eq. 4.16 with the dispersion of Fig. 5.3 with 1% impurities in the Born approximation ($V_I = 1t$), yielding critical temperatures of 92.4 and 83.5K for the s and d-wave cases, respectively. For the s-wave case (top) an isotropic interaction was used with $V_{k,k'} = 1.3t$ and for the d-wave case (bottom) the MMP interaction given by Eq. 4.12 with $g^2\chi_o = 30.1t$ was used: both interactions give, for no impurities and $t = 100$meV, $T_c = 100$K.

5.5 The Penetration Depth

One of the most convincing tests for superconductivity is the Meissner effect: superconductors expel magnetic fields by setting up a diamagnetic current on the surface of the superconductor that creates a magnetic field inside the superconductor that is equal and opposite to the applied magnetic field.[2] An interesting side effect of this phenomena is that the superconductor levitates in the magnetic field. The magnetic field at the surface of the superconductor is equal to the applied field and, as a function of depth into the superconductor, decreases exponentially. The characteristic length of this exponential decrease in the magnetic field is know as the penetration depth and it is, along with the coherence length, one of the two characteristic length scales of superconductivity.

There is a significant difference in the temperature dependence of the penetration depth for s- and d-wave superconductors and, while early penetration depth measurements seemed to indicate that the order parameter was s-wave, subsequent measurements [88, 89] on high quality YBCO and

other crystals [90, 91, 92] have shown clear evidence of a d-wave order parameter.

Since the magnetic penetration depth is a measure of the superconductor's response to an electro-magnetic field it is related to the current-current response function introduced in §5.4. In fact, with an appropriate change of units, it is the zero frequency, zero $\boldsymbol{k}$-vector limit of the reciprocal square root of the current-current response function and, with an appropriate change of units, is given by

$$\lambda_{ij} = \lim_{\boldsymbol{k}\to 0}\lim_{\omega\to 0}\frac{\hbar c}{\sqrt{K_{\boldsymbol{k}}^{ij}(\omega)}}.$$

In this limit the current-current response function is real (*i.e.* it has no imaginary part) and its value calculated on the imaginary axis is the same as that which would be calculated on the real axis. This simplifies calculations since both the real and imaginary axis formalisms can be used and no analytic continuation is required.

5.5.1 Formalism

Using Eqs. 5.7 and 5.10 and setting $\boldsymbol{k}$ and ω equal to zero we get for the penetration depth [93, 94]

$$\lambda_{ij}^{-2} = \frac{8\pi e^2}{\hbar^2 c^2} T \sum_{\boldsymbol{k},n} \frac{\partial \tilde{\epsilon}_{\boldsymbol{k},n}}{\partial k_i}\frac{\partial \tilde{\epsilon}_{\boldsymbol{k},n}}{\partial k_j}\left[\frac{\tilde{\epsilon}_{\boldsymbol{k}}^2 + \phi_{\boldsymbol{k},n}^2 - \tilde{\omega}_{\boldsymbol{k},n}^2}{\left(\tilde{\epsilon}_{\boldsymbol{k}}^2 + \phi_{\boldsymbol{k},n}^2 + \tilde{\omega}_{\boldsymbol{k},n}^2\right)^2} - \frac{\tilde{\epsilon}_{\boldsymbol{k}}^2 - \tilde{\omega}_{\boldsymbol{k},n}^2}{\left(\tilde{\epsilon}_{\boldsymbol{k}}^2 + \tilde{\omega}_{\boldsymbol{k},n}^2\right)^2}\right] \tag{5.11}$$

where the constants c, $\hbar$ and e are the speed of light, Planck's constant and the electronic charge, respectively and the functions $\tilde{\epsilon}_{\boldsymbol{k},n}$, $\phi_{\boldsymbol{k},n}$ and $\tilde{\omega}_{\boldsymbol{k},n}$ are as previously defined in Eq. 4.15.

Weak Coupling

In the weak coupling limit $\tilde{\epsilon}_{\boldsymbol{k},n} = \epsilon_{\boldsymbol{k}}$, $\phi_{\boldsymbol{k},n} = \Delta_{\boldsymbol{k}}$ and $\tilde{\omega}_{\boldsymbol{k},n} = \omega_n$ and the Matsubara sum can be explicitly performed and the penetration depth can be simplified to

$$\lambda_{ij}^{-2} = \frac{8\pi e^2}{\hbar^2 c^2}\sum_{\boldsymbol{k}} \frac{\partial \epsilon_{\boldsymbol{k}}}{\partial k_i}\frac{\partial \epsilon_{\boldsymbol{k}}}{\partial k_j}\left(\frac{\partial f(\beta\epsilon_{\boldsymbol{k}})}{\partial \epsilon_{\boldsymbol{k}}} - \frac{\partial f(\beta E_{\boldsymbol{k}})}{\partial E_{\boldsymbol{k}}}\right) \tag{5.12}$$

where the constants c, $\hbar$ and e are the same as in Eq.5.11, $E_{\boldsymbol{k}} \equiv \sqrt{\epsilon_{\boldsymbol{k}}^2 + \Delta_{\boldsymbol{k}}^2}$ is the quasiparticle energy, $\beta = 1/k_B T$ is the reciprocal temperature and $f(x) \equiv (1 + e^x)^{-1}$ is the Fermi-Dirac distribution.

5.5.2 Measurements

Due to the large anisotropy in HTS materials the penetration depth of these materials must be treated as a tensor which is represented by λ_{ij}. By choosing the principle axes of the unit cell as the coordinate system this tensor is diagonal. The elements of this tensor can vary by more than an order of magnitude. In BSCCO, one of the most anisotropic materials, the ratio of the penetration

depth in the CuO_2 plane to that perpendicular to it is ~ 100; in YBCO, the most studied and best characterized material, the ratio is ~ 10. Because most of the single crystals of HTS materials are thin platlets the c-axis penetration depth is very difficult to measure and, for most materials at this time, has not been measured.

The in-plane penetration depth of YBCO,[80, 89, 88, 95] $HgBa_2Ca_2Cu_3O_{8+\delta}$ (HBCCO)[92], $Tl_2Ba_2CuO_{6+\delta}$[96] and BSCCO [90, 91] at optimum doping all have a low temperature linear behaviour that is distinct from the activated behaviour of conventional superconductors and is a characteristic of the presence of nodes in the gap, an essential feature of a d-wave order parameter. Other materials, such as LSCO and $Nd_{1.85}Ce_{0.15}CuO_4$ (NCCO), however, seem to have the activated behaviour expected of an s-wave superconductor; these materials are not of as high quality as those that exhibit the low temperature linear behaviour and, as we shall see (§5.5.3), this linear behaviour is destroyed by the presence of impurities.

The c-axis penetration depth of YBCO has been measured by Hardy *et al.*[88] and does not have the low temperature linear behaviour of the in-plane results but, instead, some higher power temperature dependence, possibly T^5 (see §5.5.4).

5.5.3 a-b Plane Penetration Depth

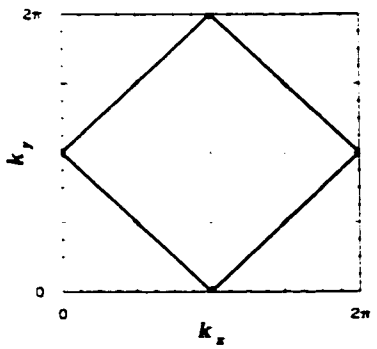

Figure 5.16: The square Fermi surface obtained with a nearest neighbour hopping tight binding dispersion at half filling, Eq. 5.14.

In the limit of zero temperature the second term in Eq. 5.12 is zero (the Fermi derivative becomes a delta function evaluated at the Fermi energy which, since it is gapped, yields zero) and partial integration can be performed on the $\boldsymbol{k}$-space integral of the remaining term to yield

$$\lambda_{ii}^{-2} = \frac{8\pi e^2}{\hbar^2 c^2} \sum_{\boldsymbol{k}} \frac{\partial^2 \varepsilon_{\boldsymbol{k}}}{\partial k_i^2} f(\beta \varepsilon_{\boldsymbol{k}}). \tag{5.13}$$

In the limit of low temperature the Fermi function in Eq. 5.13 can be considered a Heavyside or step function and for certain model dispersions the $\boldsymbol{k}$-space integral can be performed analytically. As an example we will take a two dimensional tight binding dispersion

$$\varepsilon_{\boldsymbol{k}} = -2t\left[\cos(k_x a) + \cos(k_y b) - (2 - \tilde{\mu})\right] \tag{5.14}$$

where a and b are the lattice parameters. With $\tilde{\mu} = 2$ (*i.e.* half filling) this gives the square Fermi

x	T_c [K]	$\lambda_a(0)$ Å	$\lambda_b(0)$ Å	$\lambda_c(0)$ Å
6.60	59	2100	1600	65 000
6.95	93.2	1600	1030	11 000
6.99	89	1600	800	11 000

Table 5.1: Table of penetration depths and critical temperatures as a function of doping reproduced from Hardy *et al.* [89]

surface shown in Fig. 5.16 for which the integral in Eq. 5.13 can be easily performed

$$\begin{aligned}\lambda_{xx}^{-2} &= 4\frac{8\pi e^2}{\hbar^2\bar{c}^2}\int_0^{2\pi/c}\frac{dk_z}{2\pi}\int_0^{\pi/b}\frac{dk_y}{2\pi}\int_0^{(\pi-k_y b)/a}\frac{dk_x}{2\pi}2ta^2\cos(k_x a)\\ &= 4\frac{8\pi e^2}{\hbar^2\bar{c}^2}\frac{8\pi ta^2}{8\pi^3 abc}\\ &= \frac{32e^2ta}{\hbar^2\pi\bar{c}^2bc}\end{aligned} \tag{5.15}$$

where we have replaced the speed of light with $\bar{c}$ in order to avoid confusion with the c-axis lattice parameter and the factor of four is because only one quarter of the Brillouin zone is integrated over. A similar expression for λ_{yy}^{-2} can be derived that is identical to Eq. 5.15 except that the lattice parameters a and b are interchanged.

This means that the zero temperature penetration depth in the CuO_2 plane can be used to estimate the electron hopping energy, t, in the plane

$$t_x = C/\lambda_x^2. \tag{5.16}$$

Taking two CuO_2 planes per unit cell and the lattice parameters for YBCO Eq. 5.15 gives $C = 1.46\text{meV}\cdot\mu\text{m}^2$.

Equation 5.15 is only valid for a system without impurities so it can only be used to estimate the hopping integrals for a system at optimal doping. Using the values of Hardy *et al.*[89] for the zero temperature penetration depths (see Table 5.1) at optimum doping ($x = 6.95$) yields values of 57meV and 138meV for the nearest neighbour hopping in the x- and y-directions respectively.

A different Fermi surface would change this result by a factor of order unity; when using these values for the hopping integrals the zero temperature penetration depth is found to differ only by a factor of ~20% when using the model dispersions of §5.1. In fact, for a Fermi surface similar to that in Fig. 5.16 the constant C will scale with $2 - n$, and Eq. 5.16 can be replaced with

$$t_x \approx (2-n)C/\lambda_x^2, \tag{5.17}$$

and the nearest neighbour hopping in the x- and y-directions become 65meV and 158meV, respectively.

The zero temperature values of the penetration depths presented in this chapter are found by fitting a cubic spline to the values which are calculated down to a low temperature (usually

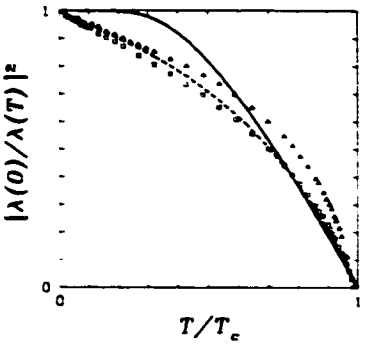

Figure 5.17: The penetration depth as a function of temperature is plotted for two different order parameter symmetries. The solid curve is for an isotropic s-wave order parameter and the dashed curve is for a d-wave order parameter, η_k^o and η_k^d of Eq. 2.22 respectively; the points are the a- (triangles) and b-axis (squares) penetration depth measurements of Hardy *et al.* [89].

2K) and extrapolating to zero degrees. This is done because the k-space integrals of Eqs. 5.11 become increasingly difficult at lower temperatures and the number of terms in the Matsubara sum in Eq. 5.12 becomes very large (and infinite at zero temperature).

While the zero temperature penetration depth is a normal state property (*i.e.* it does not depend upon the order parameter) the shape of its temperature dependence does depend upon the order parameter. In Fig. 5.17 the penetration depth as a function of temperature is plotted for two different order parameter symmetries. The solid curve is for an isotropic s-wave order parameter and the dashed curve is for a d-wave order parameter; the points are the a- (triangles) and b-axis (squares) penetration depth measurements of Hardy *et al.* [89] (which are representative of the YBCO, BSCCO and TBCO data). It is immediately apparent that there is a fundamental difference in the low temperature behaviour of the two curves: the s-wave order parameter leads to an activated behaviour (*i.e.* exponential) while the d-wave order parameter leads to a low temperature linear behaviour similar to that observed experimentally.

The curvature of the penetration depth's temperature dependence (or, in the case of an s-wave order parameter, where it deviates from a constant value) depends upon the magnitude of the order parameter. In Fig. 5.17 Eq. 5.12 is utilized with $\Delta_k(T) = 15h(T)\eta_k^i$ meV with $h(T)$ given by Eq. 2.21 and the momentum dependence given by η_k^d for the d-wave case (which gives a maximum value of 30meV in the Brillioun zone and slightly less on the Fermi surface) and $\eta_k^o = 1$ for the s-wave case (the η_k^i are defined in Eq. 2.22). The dispersion is that of Fig. 5.3 and $T_c = 100$K, which is suitable for modeling YBCO and yields an in-plane penetration depth of 1219Å; Eqs. 5.16 and 5.17 give penetration depths of 1209Å and 1288Å, 1% lower and 5% higher than calculated, respectively.

In Fig. 5.18 the penetration depth is plotted as a function of temperature for three different d-wave order parameters. The solid curve is for $\Delta_k(T) = 9h(T)\eta_k^d$, the short dashed curve is for $\Delta_k(T) = 15h(T)\eta_k^d$ and the long dashed curve is for $\Delta_k(T) = 20h(T)\eta_k^d$ with η_k^d given by Eq. 2.22

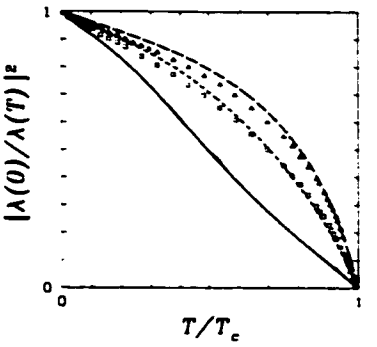

Figure 5.18: The penetration depth as a function of temperature is plotted as a function of temperature for three different d-wave order parameters. The solid curve is for $\Delta_k(T) = 9h(T)\eta_k^d$, the short dashed curve is for $\Delta_k(T) = 15h(T)\eta_k^d$ and the long dashed curve is for $\Delta_k(T) = 20h(T)\eta_k^d$ with $h(T)$ and η_k^d given by Eq. 2.21 and 2.22 respectively; the points are the a (triangles) and b-axis (squares) penetration depth measurements of Hardy *et al.* [89]. The light dotted straight line is a guide to the eye.

and $h(T)$ given by Eqs. 2.21; the points are the a (triangles) and b-axis (squares) penetration depth measurements of Hardy *et al.* [89]. The solid curve corresponds approximately to the BCS value for weak coupling d-wave superconductors, $2\Delta^{(\max)}/k_BT_c = 4.55$ (the value of 3.52 is for s-wave superconductors) and the light dotted straight line is a guide to the eye which shows how closely the penetration depth with this value for the order parameter approximates a straight line. The dashed curves, which seem to be the most consistent with the YBCO experimental data, correspond to $2\Delta^{(\max)}/k_BT_c$ of approximately 7 (short dashes) and 9 (long dashes) with the larger gap value in the a-direction (*i.e.* perpendicular to the chains). The in-plane penetration depths of BSCCO and TBCO are linear to even higher temperatures[91, 96] (about $0.9T_c$ and $0.95T_c$, respectively) and would correspond to values of $2\Delta^{(\max)}/k_BT_c$ closer to the BCS value.

This good agreement between experiment and theory for the temperature dependence and the zero temperature value of the penetration depth, $\lambda(T)$ and the zero temperature value of the gap is a consequence solely of a d-wave order parameter and reflects no underlying model.

Impurities

Using the solutions to the BCS equation in the presence of impurities (§5.3, p. 56) the effects of impurities on the magnetic penetration depth can be investigated using Eq. 5.11. On the left in Fig. 5.19 the penetration depth as a function of temperature for impurity levels, from top to bottom, of zero to four percent is plotted. In the presence of impurities the low temperature behaviour is parabolic (lower four curves) instead of linear, as is the case in the absence of impurities (top curve).

It is easy to see how the effect of impurities in the presence of experimental uncertainties

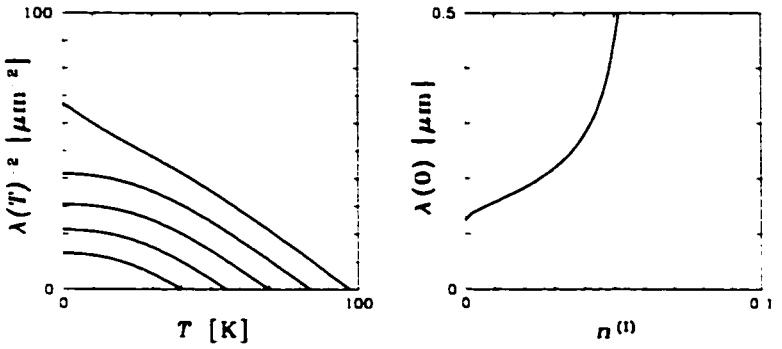

Figure 5.19: On the left is shown the penetration depth as a function of temperature for impurity levels, from top to bottom, of zero to four percent. In the presence of impurities the low temperature behaviour is parabolic (lower four curves) instead of linear, as is the case in the absence of impurities (top curve). On the right the zero temperature penetration depth as a function of impurity concentration is shown. At the critical impurity concentration, 5.7%, (*i.e.* that for which $T_c = 0$) the penetration depth is infinite.

could lead one to conclude that the penetration depth exhibits an activated (*i.e.* exponential) instead of parabolic behaviour.

As is to be expected in these weak coupling calculations the ratio $2\Delta^{(\max)}/k_B T_c$ is close to the BCS value (for zero impurities it is 4.55) and the zero impurity temperature dependence of the penetration depth (top curve) is very similar to the solid curve in Fig. 5.18 (*i.e.* it is almost linear). On the right in Fig. 5.19 the zero temperature penetration depth as a function of impurity concentration is plotted. At the critical impurity concentration, ~5.7%, (*i.e.* that for which $T_c = 0$) the penetration depth diverges .

Because of the different formalism used to calculate the penetration depth in the presence of impurities (Eq. 5.11 instead of Eq. 5.12) the zero temperature penetration depth and the critical temperature are slightly different, being 1219.52Å instead of 1219.13Å and 97K instead of 100K, respectively. These differences are caused by the finite cutoff in the Matsubara sum (Here, as elsewhere in this thesis, three times the bandwidth, $2N^{(\max)} + 1 = 24t$, is used.).

Orthorhombic System

There is a significant difference between the zero temperature penetration depths in the *a*- and *b*-directions in YBCO (see Table 5.1) that can be accounted for by including the effects of the CuO chains that are present in YBCO. A simple way to include this effect is to introduce an orthorhombicity to the dispersion [15, 97] (see §5.1.2, p. 47)

Using the solution of the BCS equation found with the orthorhombic system that is shown in Fig. 5.10 the absolute value of the penetration depth as a function of temperature for this orthorhombic system is calculated. The solid curve in Fig. 5.20 is for the *b*-axis and the dashed curve

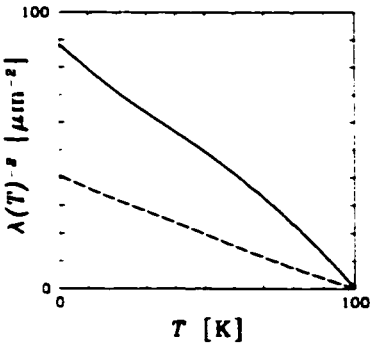

Figure 5.20: The absolute value of the penetration depth as a function of temperature for this orthorhombic system and solution described in §5.2. The solid curve is for the *b*-axis and the dashed curve is for *a*-axis.

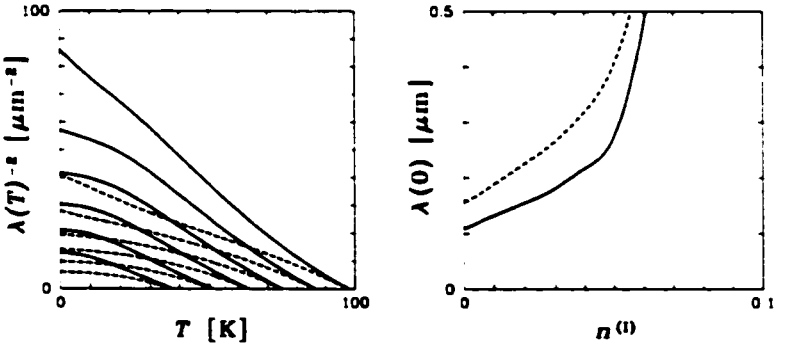

Figure 5.21: On the left is shown the penetration depth as a function of temperature for impurity levels, from top to bottom, of zero to five percent in the *a*- (dashed curves) and *b*-directions (solid curves). On the right is shown the zero temperature penetration depth as a function of impurity concentration in the *a*- (dashed curve) and *b*-directions (solid curve). At the critical impurity concentration, 6.8%, (*i.e.* that for which $T_c = 0$) the penetration depth is infinite.

is for *a*-axis. While the shape of these curves is what would be expected from solving the BCS equation (*i.e.* they are almost linear, *cf.* the short dashed curve in Fig. 5.18) the zero temperature values ($\lambda_x(0) = 1562$Å and $\lambda_y(0) = 1060$Å) are very close to those of Hardy *et al.* [89] for optimal doping (see Table 5.1), indicating that this dispersion is a good single band approximation for the dispersion of YBCO (*i.e.* The zero temperature values of the penetration depth only reflect the dispersion and not the order parameter.). That the curvature of the these penetration depth curves is dissimilar to the results of Hardy *et al.* is, as shown in Fig. 5.18, due to the low value of $2\Delta/k_BT_c$.

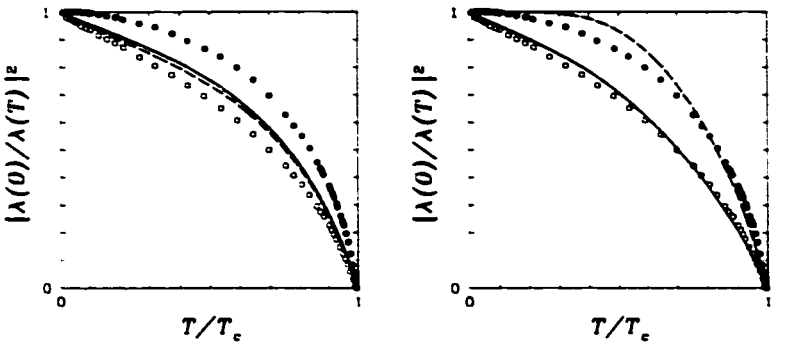

Figure 5.22: On the left the penetration depths corresponding to the dispersion on the left in Fig. 5.7 are plotted in the a (solid curve) and c-directions (dashed curve). On the right the same quantity is plotted but this time using the dispersion on the right in Fig. 5.7. Both use $\Delta_k(T) = 15h(T)\eta_k^d$ for the order parameter and $t_\perp = 0.05$. The points are the penetration depth measurements of Hardy *et al.*[89] of optimally doped YBCO for the a- (open points) and c-directions (solid points).

Impurities in an Orthorhombic System

On the left in Fig. 5.21 the absolute value of the reciprocal of the square of the penetration depth is plotted as a function of temperature for the a (dashed curves) and b-directions (solid curves) for impurity levels of zero (top curve) to five percent (bottom curve). The penetration depths for zero impurities differ slightly from those in Fig. 5.20 due to the finite cutoff in the Matsubara sum in Eq. 5.11 ($24t$ or three times the bandwidth in this case), although the zero temperature penetration depths differ by less than one percent (1078Å and 1562Å instead of 1064Å and 1567Å for the a and b-directions, respectively). For impurity levels of less than 2% the low temperature behaviour seems to remain linear rather than becoming quadratic, as is seen for higher impurity levels.

On the right in Fig. 5.21 the absolute value of the penetration depth is plotted as a function of impurity level in the a- (dashed curve) and b-directions (solid curve). The zero temperature penetration depth increases fairly linearly with impurity level until a level of approximately 5% when it starts to diverge rapidly, becoming infinite at a critical impurity level of 6.8%.

5.5.4 c-axis Penetration Depth

On the left in Fig. 5.22 the penetration depths, calculated using the solution on the left of Fig. 5.7 in §5.2 (*i.e.* a c-axis dispersion modulated by $\cos(k_z c)$, Eq. 5.2), are plotted for the a (solid curve) and c-directions (dashed curve). The points are the penetration depth measurements of Hardy *et al.* [89] of optimally doped YBCO for the a (open points) and c-directions (solid points). Note that only the zero temperature value and not the shape $\lambda_z(T)$ is affected by $t_\perp$, unlike the effect of t on $\lambda_z(T)$ and that in the c-axis case Eq. 5.15 does not provide an estimate of $t_\perp$.

While this dispersion reproduces quite well the zero temperature penetration depths (giving

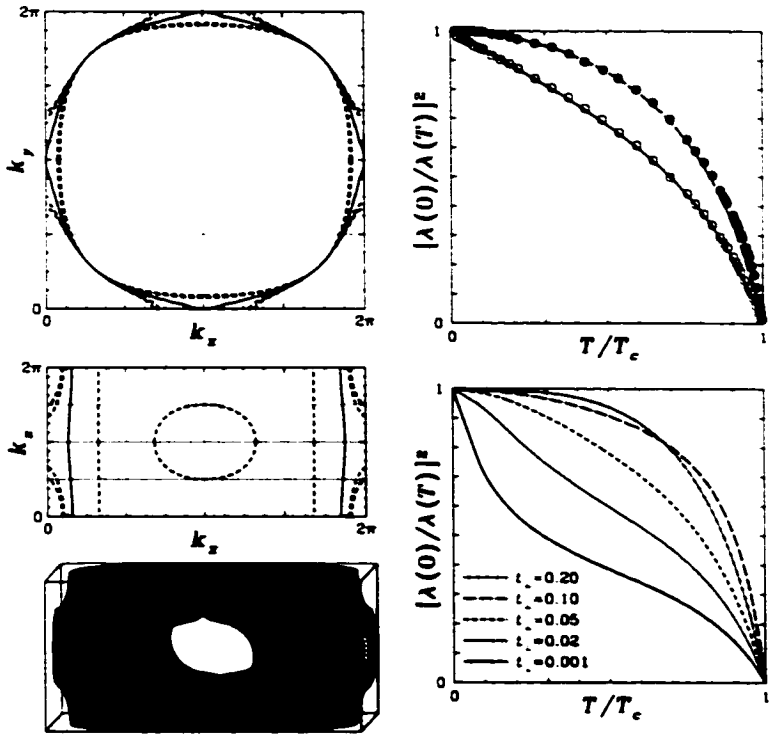

Figure 5.23: On the left is shown a dispersion the same as that on the right of Fig. 5.8 except that in this case $t_\perp = 0.08$ and $\bar{\mu} = 0.20$ which has moved the Fermi surface much closer to the Brillouin zone boundary. On the top right is penetration depths in the in-plane (solid curve) and c-directions (dashed curve) which is very similar to that measured of Hardy *et al.*[88] which are shown for the b (open circles) and c-directions (solid circles). On the bottom right is the c-axis penetration depth using the same dispersion relation but with several different values of $t_\perp$.

$\lambda_x = 1083$Å and $\lambda_z = 10\,942$Å, *cf.* Table 5.1 on p. 65), it is apparent that the term introduced into the dispersion, Eq. 5.2, does not reproduce the experimentally observed temperature dependence of the c-axis penetration depth (solid points in Fig. 5.22).

On the right in Fig. 5.22 penetration depths, calculated using the solution on the right of Fig. 5.8 in §5.2 (*i.e.* a c-axis dispersion modulated by $(\cos(k_x a) - \cos(k_y b))^2 \cos(k_z c)$, Eq. 5.3), are plotted for the a (solid curve) and c-directions (dashed curve); the points are the penetration depth measurements of Hardy *et al.* [89] of optimally doped YBCO for the a (open points) and c-directions (solid points).

In this case the c-axis penetration depth has what appears to be an activated behaviour similar to that seen for s-wave superconductors (*cf.* the solid curve in Fig. 5.17) due to there being no k_z dispersion along the diagonals of the two dimensional Brillioun zone (*i.e.* the k_z-dispersion does not in effect "see" the nodes in the gap). The low temperature behaviour is actually a T^5 dependence. [98]

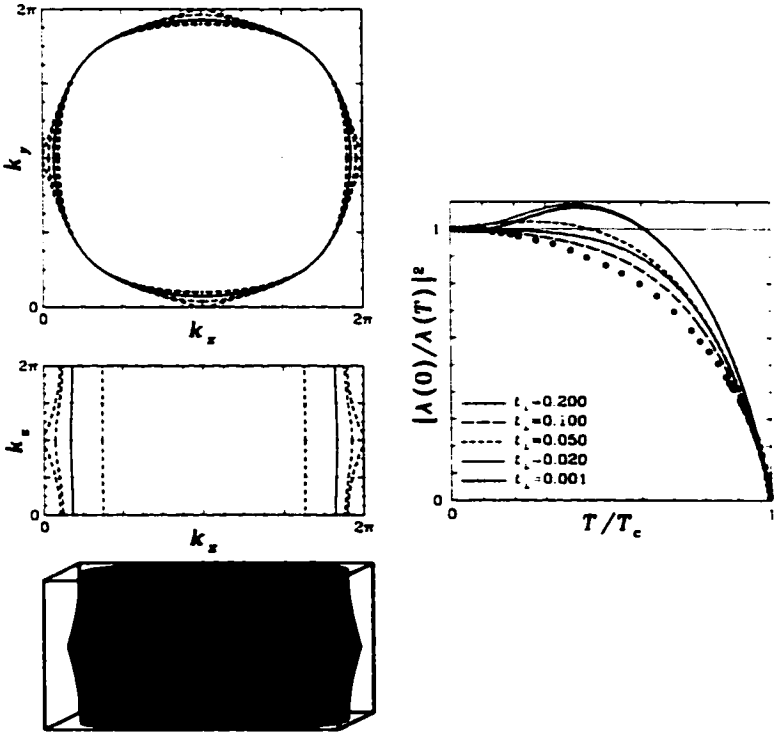

Figure 5.24: On the left is shown a dispersion the same as that on the right of Fig. 5.23 except that in this case $t_\perp = 0.05$ and $\bar{\mu} = 0.25$ which has moved the Fermi surface so that, for $t_\perp = 0.05$, it just touches the Brillouin zone boundary. On the right is the c-axis penetration depth for several different values of $t_\perp$.

It is apparent that neither of the c-axis dispersions of §5.1.3 (Eqs. 5.2 and 5.3) reproduce the c-axis penetration depth measurements of Hardy *et al.*.[89] However, if the dispersion is modified so that the Fermi surface is closer to the $k_z = 0$ and $k_y = 0$ boundaries of the Brillouin zone the low temperature slope of the c-axis penetration depth is very sensitive to the c-axis hopping parameter, $t_\perp$.

Shown on the left of Fig. 5.23 is a dispersion the same as that of Fig. 5.8 except that $t_\perp = 0.08$ and $\bar{\mu} = 0.20$ which has moved the Fermi surface so that for $k_z = \pi/2$ it intersects the Brillouin zone boundary (solid curve in the top left of Fig. 5.23). On the top right is the resulting penetration depth for the in-plane (solid curve) and c-directions (dashed curve) calculated using $\lambda_k(T) = 15h(T)\eta_k^d$. As can be clearly seen, this result very closely resembles the experimental results of Hardy *et al.*[88] which are shown for the b (open circles) and c-directions (solid circles). While this Fermi surface is not similar to that of HTS its proximity to the Brillouin zone boundary is similar to that expected for the chain Fermi surface of YBCO which is discussed in Ch. 6.

In the calculation of the penetration depth, Eq. 5.12, the Fermi derivative is sharply peaked at the Fermi energy with a width given by the thermal broadening, $k_B T$. When the Fermi surface

intersects the Brillouin zone boundary a large proportion of this peak, where the gap is the largest, is no longer included in the calculation of the penetration depth, giving a smaller effective $\Delta^{(max)}$. On the bottom right in Fig. 5.23 is the c-axis penetration depth calculated with several different c-axis hopping parameters, causing the low temperature slope to vary dramatically. This result, which is very sensitive to the choice of dispersion, along with those of Fig. 5.22 demonstrate the dependence of the temperature dependence of the c-axis penetration depth upon the details of the Fermi surface. For a c-axis dispersion given by Eqs. 5.2 the effect is less dramatic but is still present.

On the left in Fig. 5.24 is a dispersion the same as that of Fig. 5.23 except that $t_\perp = 0.05$ and $\bar{\mu} = 0.25$. In this case the Fermi surface just touches the Brillouin zone boundary at $k_z = \pi$. For values of $t_\perp$ less than 0.05 the Fermi surface is very near, but does not touch, the Brillouin zone boundary and the penetration depth, rather than decreasing monotonically with temperature, increases to a maximum before decreasing. This effect is caused by the vHS at $(\pi, 0)$ (and symmetry related points) – as the temperature increases the thermal broadening of the Fermi surface "sees" the vHS at a temperature, for small $t_\perp$, equal to the distance of the Fermi energy to the vHS. This effect is not seen for a c-axis dispersion given by Eqs. 5.2 because the effect of the gap node is much more pronounced.

Orthorhombic System

The dependence of the low temperature c-axis penetration depth upon the proximity of the Fermi surface to the Brillouin zone boundary and the c-axis dispersion is more interesting in the orthorhombic system discussed earlier (§5.1.2) because this dispersion is near the $k_z = 0$ Brillouin zone boundary without the manipulations used in Figs. 5.23 and 5.24. Shown in Fig. 5.25 is the c-axis penetration depth calculated using the dispersion of Fig. 5.5 with an orthorhombic distortion, δ, of 0.13 (top) and 0.155 (bottom) and with the c-axis dispersion of Eq. 5.2 (right) and Eq. 5.3 (left). For $\delta = 0.13$ (top graphs) the Fermi surface intersects the Brillouin zone boundary at $\boldsymbol{k} = (\pi, 0, \pi)$ (and symmetry related points) only for $t_\perp > 0.05$ and, for small $t_\perp$, the slopes of the low temperature penetration depth for the c-axis dispersion of Eq. 5.3 is significantly larger that those for larger $t_\perp$, rising to a maximum at $T/T_c \sim 0.4$ (top left) while for the c-axis dispersion of Eq. 5.2 there is very little change with $t_\perp$ (top right). For $\delta = 0.155$ (bottom graphs) the Fermi surface intersects the Brillouin zone boundary at $\boldsymbol{k} = (\pi, 0, \pi/2)$ (and symmetry related points) and, for small $t_\perp$, the slopes of the low temperature penetration depth is significantly less that those for larger $t_\perp$. In all cases the curves cease to change significantly for values of $t_\perp$ larger than 20 (although the absolute value of λ_c changes).

In Fig. 5.26 the variation of $1/\lambda_c(0)$ as a function of $t_\perp$ for two different in-plane dispersions, the tetragonal dispersion of Fig. 5.3 (dashed lines) and the orthorhombic dispersion of Fig. 5.5, and two different c-axis dispersions, those of Eq. 5.2 (gray curves) and Eq. 5.3 (black curves) are shown. The variation of $\lambda_c(0)$ is almost linear with $1/t_\perp$, unlike the case of the in-plane penetration depth

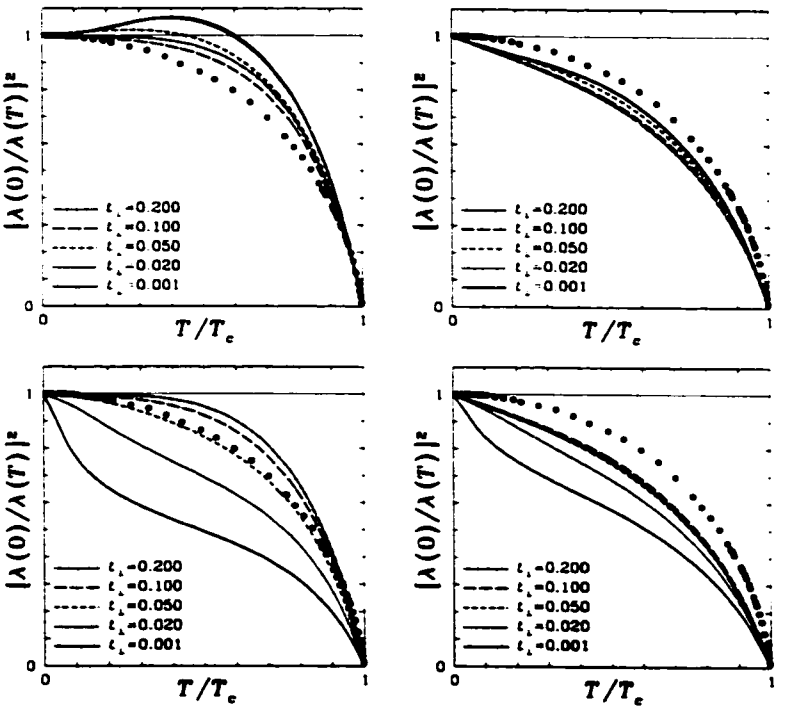

Figure 5.25: On the top c-axis penetration depth using the dispersion of Fig. 5.5 with a c-axis dispersion given by Eq. 5.2 (right) and Eq. 5.3 (left) is shown. For $t_\perp = 0.05$ the Fermi surface just touches the $k_z = 0$ Brillouin zone boundary. Below are the same calculations except that the orthorhombic distortion, δ, has been changed to 0.155 from 0.13 so that at $k_z = \pi/2$ the Fermi surface intersects the $k_z = 0$ Brillouin zone boundary. The points are the penetration depth measurements of Hardy *et al.* [89] for the c-direction.

which scales with $1/\sqrt{t}$.

It is interesting that although the analysis of Xiang and Wheatley[98] shows that the c-axis dispersion of Eq. 5.3 should give a T^5 temperature dependence to $1/\lambda_c^2(T)$ that in very specific cases, such as those which are shown in Figs. 5.23 and 5.24 and on the left in Fig. 5.25, that this behaviour is violated for small values of $t_\perp$, pushing $[\lambda(0)/\lambda(T)]^2$ above and below the expected curve, respectively. The reason that this is interesting is twofold, first because such small values of $t_\perp$ are necessary in order to yield the correct value for the zero temperature c-axis penetration depth and second, because of the proximity of the chain Fermi surface in YBCO to the Brillouin zone boundary at $(\pi, 0, \pi)$ (see Ch. 6).

5.6 STM Tunnel Junctions

Tunneling experiments using scanning, tunneling microscopes, STMs, provide insight into the density of states (DOS) of the material being studied. In these experiments the STM measures

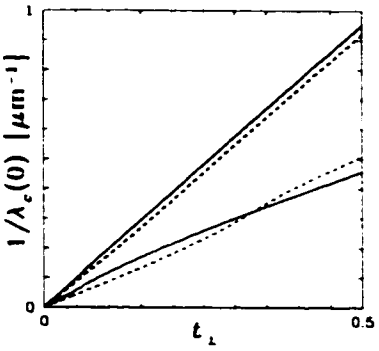

Figure 5.26: The variation of $1/\lambda_c(0)$ for the tetragonal dispersion of Fig. 5.3 (dashed lines) and the orthorhombic dispersion of Fig. 5.5 using the c-axis dispersions of Eq. 5.2 (gray curves) and Eq. 5.3 (black curves) is shown. The variation of $\lambda_c(0)$ is almost linear with $1/t_\perp$, unlike the case of the in-plane penetration depth which scales with $1/\sqrt{t}$.

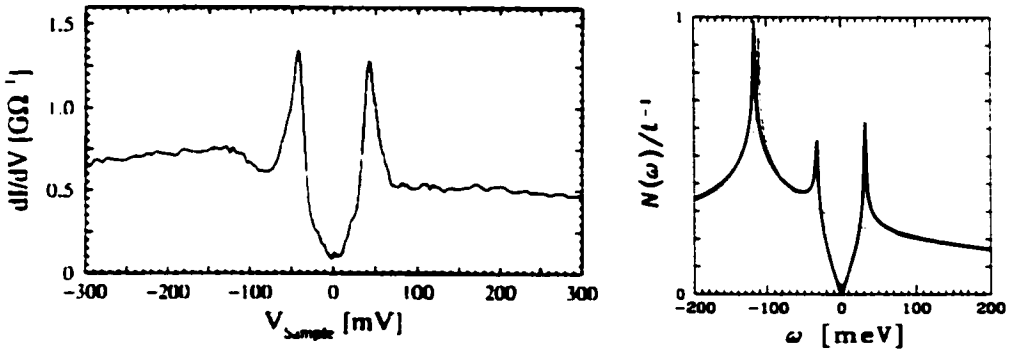

Figure 5.27: The figure on the left, taken from Ref. [100], shows a typical, high quality, STM tunneling conductance measurement. On the right is shown the DOS calculated using the dispersion similar to that of Fig. 5.3 and a d-wave order parameter using Eq. 2.20 (see text for the exact parameters). The dotted line is the normal state DOS.

the differential tunneling current through a superconductor-insulator-normal metal (SIN) junction as a function of voltage difference between the superconductor and the normal metal. The spectra obtained seem to be dependent upon the layer which is topmost but give spectra that are more-or-less consistent with a d-wave order parameter [99, 100] with some anomalies.

On the left in Fig. 5.27 a typical, high quality, STM tunneling conductance measurement at $T = 4.2$K is shown;[100] it has coherence peaks at $V \sim \pm 40$meV and becomes small or zero at $V = 0$. One of the anomalous features alluded to above is that the zero energy tunneling conductance is small but larger than would be expected for a high quality superconductor. A second feature is the dip in the conductance to the left of the left hand coherence peak, here at $V \sim -80$meV.

5.6.1 Formalism

The current through the SIN junction is given by Fermi's Golden Rule

$$I(\omega) = -4\pi e \sum_{k,k'} |T_{k,k'}|^2 \, \delta\left(\omega + E_k - \bar{\varepsilon}_{k'}\right) \left(f(\beta E_k) - f(\beta \bar{\varepsilon}_{k'})\right),$$

where $T_{k,k'}$ is the tunneling matrix element, $E_k = \sqrt{\varepsilon_k^2 + \Delta_k^2}$ is the quasi-particle dispersion of the superconductor, $\bar{\varepsilon}_{k'}$ is the dispersion of the normal metal and $f(x) \equiv (1 + e^x)^{-1}$ is the Fermi-Dirac distribution.

If we assume that the tunneling matrix element is constant, $T_{k,k'} \equiv T$, and that the density of states of the normal metal is a constant, N_o so that we can replace the sum over k' with $4\pi N_o \int d\bar{\varepsilon}$ we get for the tunneling current

$$\begin{aligned} I(\omega) &= -4\pi e |T|^2 N_o \int d\bar{\varepsilon} \sum_k \delta\left(\omega + E_k - \bar{\varepsilon}\right) \left(f(\beta E_k) - f(\beta \bar{\varepsilon})\right) \\ &= -4\pi e |T|^2 N_o \sum_k \left(f(\beta E_k) - f(\beta(\omega + E_k))\right). \end{aligned}$$

STM SIN tunneling experiments measure the conductance, $dI(\omega)/dV$, between the normal metal tip of the STM and the HTS material, separated by a small distance of vacuum which acts as an insulator. Using the above equation we get

$$\begin{aligned} \frac{dI(\omega)}{d\omega} &= 4\pi e |T|^2 N_o \sum_k \frac{d}{d\omega} f(\beta(\omega + E_k)) \\ &= GN(\omega) \end{aligned} \tag{5.18}$$

where $G \equiv 4\pi e |T|^2 N_o$ and the sum over k is the definition of the density of states from Eq. 3.11. When the superconductor is in the normal state (*i.e.* $T > T_c$) $N(\omega)$ is also, roughly, a constant (*i.e.* Ohm's Law holds) and a measurement of G is used to calibrate the experiment.

5.6.2 Results

The van Hove singularity (vHS) caused by the saddle points in the dispersion (see §3.2.4 on p. 31 for a description of its cause) has not been seen in tunneling experiments perhaps because these experiments do not solely measure the DOS but also measure the tunneling matrix element, $T_{k,k'}$.

This tunneling matrix element is, for analysis and scaling purposes, typically taken as a constant incorporated into the tunneling conductance when both electrodes are in the normal state, G. However, this matrix element is, in a more advanced treatment, k-dependent and most probably has the Fermi velocity, $\nabla_k \epsilon_k$, as a factor (since if the Fermi velocity is zero the tunneling current will be zero) and this would cancel the Fermi velocity in the denominator of the expression for the DOS, Eq. 3.13, which will eliminate the vHS from the tunneling conductance (This is equivalent to saying that while the electrons with zero Fermi velocity are present in the DOS they will not show

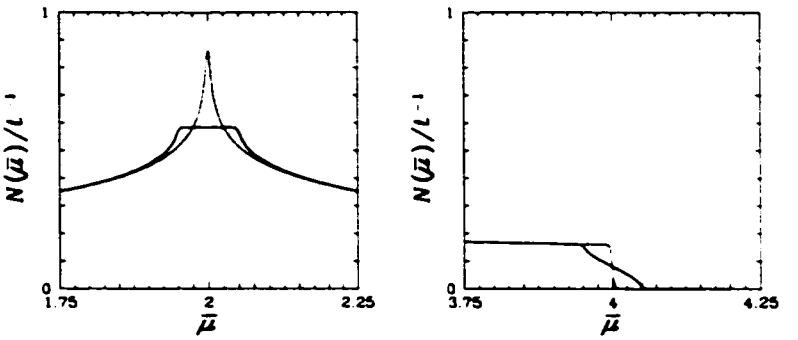

Figure 5.28: The sharp features of the DOS calculated with a two dimensional dispersion are no longer present when a three dimensional dispersion is used instead. Shown is the DOS at the middle (left) and top (right) of the band calculated using the dispersion of Fig. 3.6 with (solid curve) and without (dotted curve) the c-axis dispersion of Eq. 5.2; using Eq. 5.3 instead produces results that are not significantly different. For the calculation with the c-axis dispersion $t_\perp = 0.05$ and both curves were calculated at a temperature of $T = 0.005t$, which, for $t = 100$meV, corresponds to 4.2K.

up in tunneling measurements.). Note that the vHS is present in the normal state DOS of this as well as other two dimensional materials and it is not observed in the normal state STM tunneling conductance.

The tunneling matrix element may also have some weighting for those $\boldsymbol{k}$-vectors that point in the general direction of the STM's tip. These factors (*i.e.* those involved in the tunneling matrix element) may account for the zero bias anomaly (ZBA) observed in tunneling experiments. Another possible explanation is that it is caused by tunneling from another layer in these complex materials.

On the right in Fig. 5.27 is the DOS calculated at $T = 4.2$K using the dispersion of Eq. 3.6 with $t = 100$meV, $t' = 0.2$ and $\bar{\mu} = 1.75$ with a d-wave order parameter using Eq. 2.20 with a maximum gap in the Brillouin zone of 40meV calculated using Eq. 3.14. These parameters were chosen in order to show the relevant features clearly and are not necessarily representative of HTS materials. These features are the vHS at $\omega \sim -120$meV, the coherence peaks at $\omega \sim \pm 30$meV and the gap which closes at $\omega = 0$; these last two features are characteristics of a d-wave order parameter and the first feature is caused by the saddle points in the dispersion and is not seen in the tunneling experiments as discussed above. The dotted line is the normal state DOS which is shown for comparison.

A further argument for the non-appearance of the vHS in the STM tunneling experiments is that they are truncated in a three dimensional system. These singularities are characteristics of one and two dimensional systems and in STM tunneling measurements of one dimensional systems, such as carbon nanotubes,[101] they are observed. In light of the above discussion, for a one dimensional system the square of the Fermi velocity comes into the denominator of the DOS, and so it would not be completely canceled by the tunneling matrix element.

In Fig. 5.28 the DOS of Fig. 3.6 is plotted with a different horizontal scale (dotted curves) along with that calculated with the same dispersion but this time including the c-axis dispersion of Eq. 5.2 (solid curves). The sharp feature at the middle of the band (left) is truncated and the cutoffs at the top and bottom of the band (right) are extended, both with widths $2t_\perp$. Using Eq. 5.3 instead of Eq. 5.2 for the c-axis dispersion has very little effect upon this result. The curves are continuous because they are calculated at finite temperature, here at $T = 0.005t$, which, for $t = 100$meV, corresponds to 4.2K. Note that the c-axis dispersion has no effect upon the shape of either the gap or the coherence peaks.

The similarities and differences between theory and experiment are quite interesting. The lack of a vHS in the experimental measurements has been discussed above. The coherence peaks and the closing of the gap at $\omega = 0$ are similar enough to conclude that the experimental gap is a d-wave with the differences being that the coherence peaks are significantly wider than the theoretical calculation and that the DOS is not zero at zero frequency (a feature know as the zero bias anomaly, ZBA); these differences may, in fact, be related. If one postulates that there is a significant energy resolution in the experiment (*i.e.* electrons with energies close to but not at the STM bias voltage are also tunneling) both the width of the coherence peaks and the filling in of the DOS at $\omega = 0$ would be explained. The flat background and the dip to the left of the left hand coherence peak in the experimental results, however, are not present in the calculated DOS and are subject to intense speculation as a similar feature is also seen in ARPES experiments.

5.7 Josephson Tunneling

When two superconductors have a thin insulating layer in between them a Josephson current between the superconductors results and the system is called a "Josephson junction."[102] The variation of the current in a Josephson junctions as a function of the applied magnetic field are exploited in SQUIDs to yield some of the most sensitive and accurate measurements in physics. In fact, the "nail in the coffin" of the debate whether HTS are s or d-wave was hammered in by several experiments which showed the presence of a half flux quantum in "corner junctions." [41, 42, 43, 44, 103, 45, 46]

5.7.1 Formalism

The Josephson current through a superconductor-insulator-superconductor junction is given by the relation [53, 54]

$$J(T) = \frac{2\pi T}{RN^L(0)N^R(0)\pi^2} \times \sum_n \left[\left(\sum_k \frac{\Delta_k^L}{(\epsilon_k^L)^2 + (\Delta_k^L)^2 + (\omega_n)^2} \right) \left(\sum_{k'} \frac{\Delta_{k'}^R}{(\epsilon_{k'}^R)^2 + (\Delta_{k'}^R)^2 + (\omega_n)^2} \right) \right] \quad (5.19)$$

for incoherent tunnelling, where the superscript L(R) indicates on which side of the junction the dispersion and order parameter are on, the sum over $\omega_n = \pi T(2n-1)$ is for all Matsubara frequencies and R is the normal state resistance of the junction and $N^{L/R}(0)$ is the normal state DOS given by Eq. 3.14. If the tunnelling were coherent the matrix element (which is incorporated into R) would have a $\boldsymbol{k} - \boldsymbol{k}'$ dependence, and the sums over $\boldsymbol{k}$-space wouldn't be separable.

For two isotropic superconductors in which the order parameter can be taken as a constant and the dispersion varies as $|\boldsymbol{k}|^2$ the same manipulation used in Eq. 2.17 on p. 14 can be used to manipulate Eq. 5.19 into [104]

$$J(T) = \frac{2\pi T}{R} \sum_{n=0}^{\infty} \frac{\Delta^L}{\sqrt{\Delta^{L2} + \omega_n^2}} \frac{\Delta^R}{\sqrt{\Delta^{R2} + \omega_n^2}}. \tag{5.20}$$

At $T = 0$ this can be reduced to

$$J(0) = \frac{2\Delta^L \Delta^R}{R(\Delta^L + \Delta^R)} K\left(\left|\frac{\Delta^L - \Delta^R}{\Delta^L + \Delta^R}\right|\right), \tag{5.21}$$

where $K(x)$ is the complete elliptic integral. For two identical, isotropic superconductors ($\Delta^L = \Delta^R \equiv \Delta$) Eq. 5.20 can be reduced to

$$J(0) = \frac{\pi\Delta}{2R} \tanh\left(\frac{\Delta}{2k_B T}\right). \tag{5.22}$$

For a tunnel junction consisting of a conventional isotropic superconductor on one side and an HTS on the other side only one of the $\boldsymbol{k}$-sums of Eq. 5.19 can be explicitly performed and the resulting expression is

$$J(T) = \frac{2\pi T}{R} \sum_{n=0}^{\infty} \frac{\Delta^L(T)}{\sqrt{\Delta^L(T)^2 + \omega_n^2}} \sum_{\boldsymbol{k}'} \frac{\Delta^R_{\boldsymbol{k}'}}{(\varepsilon^R_{\boldsymbol{k}'})^2 + (\Delta^R_{\boldsymbol{k}'})^2 + (\omega_n)^2}. \tag{5.23}$$

5.7.2 Pb-YBCO c-axis Tunnelling Experiments

More recent Josephson tunneling experiments oriented the current in the direction of the c-axis of YBCO. The Josephson current that involves a superconductor of tetragonal symmetry in a pure d-wave state tunneling in the direction perpendicular to the planes should, to first order [105], be exactly zero since there would be equal positive and negative parts to the sum over $\boldsymbol{k}$ in Eq. 5.19. However, most high T_c superconductors are only approximately tetragonal (as discussed earlier) and the current observed will be a measure of the asymmetry of the Fermi surface (*i.e.* A d-wave superconductor with a 25% asymmetry yields a Josephson current that is approximately 25% of that of an s-wave superconductor).

In order to incorporate this important asymmetry into our single layer model (without which there would be no Josephson tunnelling) we use the dispersion relation of Eq. 5.1. These results for a single layer model are published in Ref. [106] and give an RJ product of order 1meV, similar to that seen in experiments.[107]

Chapter 6

Multiband Models

A common feature of HTC materials is that they all contain CuO_2 planes; however, there seems to be a strong correlation between the presence of adjacent CuO_2 layers and the superconducting critical temperature (see Table 6.1). The materials with higher critical temperatures tend to have multiple adjacent CuO_2 layers indicating that this may enhance the critical temperature. In this chapter different ways of modeling multiple Fermi surfaces are investigated; their effect upon the critical temperature are examined, and further properties are also investigated.

In this chapter the multiband models that are discussed are, to the most part, contained in three published papers. [109, 110, 110] The first of these papers [109] examines a two band model and its effects upon the DOS and magnetic penetration depth, the second [111] examines the effect upon the magnetic penetration of a three layer model in depth and the third and final paper [110] examines the effect of the two band model upon the c-axis Josephson tunneling.

While each of these papers is self contained, the preliminary sections outlining the dispersions and interactions used are discussed, respectively, in §6.1 and §6.2 below in order to both preserve the continuity of this chapter and to allow their elaboration. Some additional results are also presented in this chapter.

6.1 Model Dispersions

When there are multiple degenerate bands in a material they become hybridized. The single particle normal state band energies for a multilayer model can be written as an extension of Eq. 3.3 as

$$\mathcal{H} = \sum_{\boldsymbol{k},\alpha\beta} \varepsilon_{\boldsymbol{k},\alpha\beta} \left(c^{\dagger}_{\boldsymbol{k}\uparrow,\alpha} c_{\boldsymbol{k}\uparrow,\beta} + c^{\dagger}_{\boldsymbol{k}\downarrow,\beta} c_{\boldsymbol{k}\downarrow,\alpha} \right) \tag{6.1}$$

in which the greek indices enumerate the layers, the $c^{\dagger}_{\boldsymbol{k},\alpha}$ ($c_{\boldsymbol{k},\alpha}$) create (destroy) electrons of momentum $\boldsymbol{k}$ in layer α and the $\varepsilon_{\boldsymbol{k},\alpha\beta}$ are the electron dispersions.

Material	T_c [K]	Adjacent CuO_2 Layers	Tetragonal/ Orthorhombic
$HgBa_2Ca_2Cu_3O_{8+\delta}$	135	3	T
$HgBa_2CaCu_2O_{6+\delta}$	128	2	T
$TlBa_2Ca_2Cu_3O_{9+\delta}$	123	3	T
$Tl_2Ba_2Ca_3Cu_4O_{12}$	112	4	T
$TlBa_2Ca_3Cu_4O_{11}$	112	4	T
$(Sr,Ca)CuO_2$	110	∞	T
$TlBa_2Ca_4Cu_5O_{13}$	107	5	T
$Tl_2Ba_2Ca_4Cu_5O_{14}$	105	5	T
$HgBa_2Cu_1O_{4+\delta}$	98	1	T
$YBa_2Cu_3O_{7-\delta}$	92	2	O
$YBa_2Cu_4O_8$	80	2	O
$GaSr_2(Y,Ca)Cu_2O_7$	70	2	O
$(Sr,Ca)_5Cu_4O_{10}$	70	4	T
$Pb_2Sr_2YCu_3O_8$	70	2	O
$(La,Ba)_2CuO_4$	38	1	T
$(Nd,Sr,Ce)_2CuO_4$	35	1	T
$Pb_2(Sr,La)_2Cu_2O_6$	32	1	O
$(Nd,Ce)_2CuO_{4-\delta}$	24	1	T

Table 6.1: There seems to be a strong correlation between the presence of adjacent CuO_2 layers and the superconducting critical temperature (from [108]). The materials with higher T_c's tend to have multiple adjacent CuO_2 layers indicating that this enhances T_c.

If two Fermi surfaces cross and if electrons can cross from one to the other (ie, if they have the same symmetry) they become hybridized into odd and even Fermi surfaces that effectively "repel" each other. In order to see this we must go from the "layer" picture to the "band" picture by diagonalizing this Hamiltonian. In order to demonstrate this procedure a specific model of the $\varepsilon_{k,\alpha\beta}$ is required.

6.1.1 Two Band Models

The single particle normal state band energies for a two layer model can be written by explicitly expanding the sums over the greek indices of Eq. 6.1

$$\begin{aligned}\mathcal{H} &= \sum_k \varepsilon_{k,11}\left(c^\dagger_{k\uparrow,1}c_{k\uparrow,1}+c^\dagger_{k\downarrow,1}c_{k\downarrow,1}\right)+\sum_k \varepsilon_{k,22}\left(c^\dagger_{k\uparrow,2}c_{k\uparrow,2}+c^\dagger_{k\downarrow,2}c_{k\downarrow,2}\right)\\ &+\sum_k \varepsilon_{k,12}\left(c^\dagger_{k\uparrow,1}c_{k\uparrow,2}+c^\dagger_{k\downarrow,1}c_{k\downarrow,2}\right)+\sum_k \varepsilon_{k,21}\left(c^\dagger_{k\uparrow,2}c_{k\uparrow,1}+c^\dagger_{k\downarrow,2}c_{k\downarrow,1}\right)\end{aligned}$$

in which the $\varepsilon_{k,\alpha\beta}$ are the dispersions in and between the two bands. Note that, by symmetry, $\varepsilon_{k,21}=\varepsilon_{k,12}$. This Hamiltonian can be rewritten as

$$\mathcal{H}=\sum_{k\sigma}\Psi^\dagger_{k\sigma}\widehat{H}_k\Psi_{k\sigma}$$

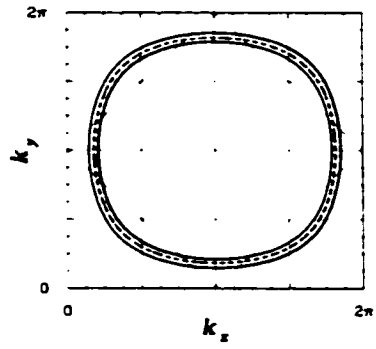

Figure 6.1: The Fermi surfaces for two identical layer dispersions (dashed curve) which model the bilayer present in BSCCO that have been hybridized by $t_\perp$ into odd and even bands (solid curves).

in which $\Psi^\dagger_{k\sigma} \equiv \left[c^\dagger_{k\sigma,1}\ c^\dagger_{k\sigma,2}\right]$ is a spinor, $\sigma = \{\uparrow,\downarrow\}$ and the Hamiltonian matrix, $\widehat{H}_k$, given by

$$\widehat{H}_k \equiv \begin{bmatrix} \varepsilon_{k,11} & \varepsilon_{k,12} \\ \varepsilon_{k,21} & \varepsilon_{k,22} \end{bmatrix}. \tag{6.2}$$

This Hamiltonian is easily diagonalized and has eigenvalues

$$\tilde{\varepsilon}_{k,o/e} = \left(\frac{\varepsilon_{k,11}+\varepsilon_{k,22}}{2}\right) \pm \sqrt{\left(\frac{\varepsilon_{k,11}-\varepsilon_{k,22}}{2}\right)^2 + \varepsilon_{k,12}\varepsilon_{k,21}} \tag{6.3}$$

which give the quasiparticles' dispersion (*i.e.* the band dispersion as opposed to the layer dispersion, $\varepsilon_{k,\alpha\beta}$) for the odd and even bands (o/e = +/−) and new quasiparticles given by the corresponding eigen vectors.[40, 111] These new quasiparticles act in the bands as opposed to the layers; for small $\varepsilon_{k,21}$ this is a small distinction – the band dispersions will not be significantly different from the layer dispersions.

BSCCO

In BSCCO there are two identical CuO_2 layers that are adjacent to each other and distant to other bilayers so that the dispersion within each layer is given by $\varepsilon_{k,11} = \varepsilon_{k,22} \equiv \varepsilon_k$ and the interlayer coupling is modeled in such a way that electrons can hop between two adjacent layers but not between bilayers by $\varepsilon_{k,12} = \varepsilon_{k,21} \equiv t_\perp$. This yields, from Eq. 6.3, the band dispersion $\tilde{\varepsilon}_{k,o/e} = \varepsilon_k \pm t_\perp$. The dispersion relation in each of the two CuO_2 layers is expected to be the same as for the CuO_2 layer in YBCO (Eq. 3.4, shown in Fig. 5.3). The effect of the hopping between the layers is to "push" the dispersions of the two layers apart (They effectively "cross" everywhere.). In Fig. 6.1 are the Fermi surfaces for two identical layer dispersions (dashed curve) which model the bilayer present in BSCCO that have been hybridized by $t_\perp/t = 0.2$ into odd and even bands (inner and outer solid curves, respectively).

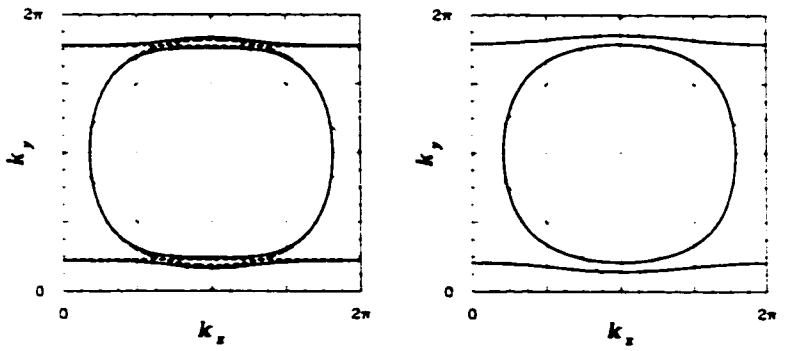

Figure 6.2: On the left are the Fermi surfaces for the chain and plane dispersions (dashed curve) which model the chain-plane bilayer present in YBCO that have been hybridized by $t_\perp$ into chain and plane-like bands (solid curves). In both cases $t_\perp/t = 0.20$.

It is unfortunate that this bilayer splitting is not seen in ARPES experiments,[68, 30, 69, 70] perhaps either due to ARPES being a surface probe (so that the symmetry required for the hybridization is not present) or because the splitting, $t_\perp$, is not large enough for the two Fermi surfaces to be distinguished; the latter is most likely the case since the actual $t_\perp$ is most likely much smaller than that shown in Fig. 6.1 so that the splitting between the Fermi surfaces is correspondingly small.

The situation is also complicated by the presence of an incommensurate CDW along the diagonal of the unit cell that is present in BSCCO. In light of these difficulties it is probably best to model BSCCO as a single CuO_2 layer with a unit cell dimension which is half that of the real unit cell (*i.e.* $c \to c/2$).

YBCO

Examined in this subsection are two ways of incorporating the chains that are present in the crystal structure of some materials (Of the compounds in Table 6.1 chains are present in $YBa_2Cu_3O_{7-\delta}$, $YBa_2Cu_4O_8$ and $GaSr_2(Y,Ca)Cu_2O_7$). In particular, the YBCO compounds have one or more CuO chain layers separating the pairs of adjacent CuO_2 layers (in the $GaSr_2(Y,Ca)Cu_2O_7$ compound the chains are composed of GaO). The presence of these CuO chains makes these materials have strongly anisotropic transport properties in the *a*- and *b*-directions (*e.g.* a factor of two difference in the conductivities in the *a*- and *b*-directions in $YBa_2Cu_3O_{6.95}$).

It is unfortunate that the most popular material among experimentalists is YBCO because of the complications brought about by the presence of CuO chains in this material. While the reasons for the choice of this material by experimentalists are valid (*i.e.* it is relatively easy to grow high quality crystals with a high critical temperature and the critical temperature is above the boiling point of liquid nitrogen) a consequence of this choice is that some of the best experimental results

are only available for this material. It is due to this consequence that the modeling of YBCO, with its attendant chain structure, is important.

The presence of the chains in YBCO can be modeled by allowing the electrons in the chain layer to only hop in the y-direction (*i.e.* the direction of the chains), which results in a chain dispersion given by

$$\varepsilon_{\mathbf{k}}^{(\mathrm{ch.})} = t^{(\mathrm{ch.})}\cos(k_y) - \mu^{(\mathrm{ch.})} \tag{6.4}$$

or equivalently, Eq. 5.1 can be used with $\delta = 1$, $t' = 0$ and $t^{(\mathrm{ch.})}$ half the value of that in the plane layer. Using Eq. 3.4 for the plane dispersion and hybridizing the two layer dispersions by way of Eq. 6.3 yields one of the quasiparticle dispersions examined in this subsection.

On the left in Fig. 6.2 are the Fermi surfaces for the chain and plane dispersions (dashed curves) which model the chain-plane bilayer present in YBCO that have been hybridized by $\varepsilon_{\mathbf{k},12} \equiv t_\perp$ into chain and plane-like bands (solid curves). This choice of $\varepsilon_{\mathbf{k},12}$ allows electrons to hop between adjacent chain and plane layers but not to other layers.

Using this method of hybridizing the layer dispersions to form the band dispersions is awkward when one is trying to reproduce the Fermi surfaces found experimentally. Since the details of the dispersion are less important that the shape of the Fermi surface, in this thesis the Fermi surfaces of YBCO are also modeled using a simpler scheme. Namely, using Eq. 5.1 for the two band dispersions with the plane band tetragonal dispersion in Fig. 5.3 and the chain band with the orthorhombic dispersion of Eq. 5.1 with $\delta = .09$ and $\mu = 0.4$. This procedure yields the Fermi surfaces shown on the right [109] in Fig. 6.2 which are much closer to those found experimentally.[69] The values of t for the two layers are chosen so that the zero temperature magnetic penetration depth in the a and b-directions are close to those found experimentally (given in Table 5.1 on p. 65).

6.1.2 Three Band Models

A three band system is treated analogously to the two band system, giving the Hamiltonian matrix

$$\widehat{H}_{\mathbf{k}} \equiv \begin{bmatrix} \varepsilon_{\mathbf{k},11} & \varepsilon_{\mathbf{k},12} & \varepsilon_{\mathbf{k},13} \\ \varepsilon_{\mathbf{k},21} & \varepsilon_{\mathbf{k},22} & \varepsilon_{\mathbf{k},23} \\ \varepsilon_{\mathbf{k},31} & \varepsilon_{\mathbf{k},32} & \varepsilon_{\mathbf{k},33} \end{bmatrix}. \tag{6.5}$$

The eigenvalues of this matrix are quite cumbersome and are, in fact, not required since some or all of the layers in HTC compounds are identical.

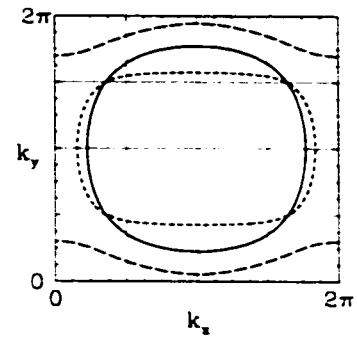

Figure 6.3: The three Fermi surfaces in the triplanar model of YBCO. The chain like band (dashed curve) is nearly one dimensional, the odd band Fermi surface has orthorhombic symmetry (dotted curve) due to its interaction with the chains and the even band (solid curve) remains tetragonal.

YBCO

The unit cell of YBCO has two CuO_2 plane layers separated by a CuO chain layer. This simplifies the matrix of Eq. 6.5, reducing it to[111]

$$\widehat{H}_{\boldsymbol{k}} = \begin{bmatrix} \varepsilon_{\boldsymbol{k},1} & t_{\boldsymbol{k},1} & t_{\boldsymbol{k},2} \\ t_{\boldsymbol{k},1} & \varepsilon_{\boldsymbol{k},2} & t_{\boldsymbol{k},1} \\ t_{\boldsymbol{k},2} & t_{\boldsymbol{k},1} & \varepsilon_{\boldsymbol{k},1} \end{bmatrix} \tag{6.6}$$

with $\varepsilon_{\boldsymbol{k},1}$ and $\varepsilon_{\boldsymbol{k},2}$ the CuO_2 plane and CuO chain layer dispersions respectively, $t_{\boldsymbol{k},1}$ the chain-plane hopping dispersion and $t_{\boldsymbol{k},2}$ the plane-plane hopping dispersion. This matrix can be easily diagonalized to give eigenvalues

$$\begin{aligned} \tilde{\varepsilon}_1 &= \varepsilon_1 - t_2 \\ \tilde{\varepsilon}_2 &= \tfrac{1}{2}(\varepsilon_1 + \varepsilon_2 + t_2) + \tfrac{1}{2}\sqrt{(\varepsilon_1 - \varepsilon_2)(\varepsilon_1 - \varepsilon_2 + 2t_2) + 8t_1^2 + t_2^2} \end{aligned}$$

and

$$\tilde{\varepsilon}_3 = \tfrac{1}{2}(\varepsilon_1 + \varepsilon_2 + t_2) - \tfrac{1}{2}\sqrt{(\varepsilon_1 - \varepsilon_2)(\varepsilon_1 - \varepsilon_2 + 2t_2) + 8t_1^2 + t_2^2}$$

in which the momentum index, $\boldsymbol{k}$, has been omitted for clarity. (The expressions given in Ref. [111], reproduced here in §6.5.2, are in error although those used in the calculations performed are, in fact, correct.)

Using Eq. 3.6 for $\varepsilon_{\boldsymbol{k},1}$ with the same parameters as in Fig. 5.3, Eq. 6.4 for $\varepsilon_{\boldsymbol{k},2}$ with $\mu/t = 1.2$ and only allowing hopping within the trilayer and not between different trilayers by taking $t_1 \equiv t_{\boldsymbol{k},1} = 30$ meV and $t_2 \equiv t_{\boldsymbol{k},2} = 15$ meV. The resulting band dispersions, $\tilde{\varepsilon}_{\boldsymbol{k},1}$, $\tilde{\varepsilon}_{\boldsymbol{k},2}$ and $\tilde{\varepsilon}_{\boldsymbol{k},3}$ are respectively the solid, dashed and dotted curves in Fig. 6.3. The chain like band (dashed curve) is nearly one dimensional, the odd band Fermi surface has orthorhombic symmetry (dotted curve) due to its interaction with the chains and the even band (solid curve) remains tetragonal.

In Fig. 6.3 are the Fermi surfaces for the chain (long dashed curves) and plane dispersions (solid and short dashed curves) which model the chain-plane trilayer present in YBCO that have been hybridized by $\varepsilon_{k,12} \equiv t_1$ and $\varepsilon_{k,13} \equiv t_2$ into chain and plane-like bands. This allows electrons to hop within a trilayer made up of two CuO_2 plane layers separated by a CuO plane layer but not to other layers.

6.2 Interaction

The most general way to introduce a pairing interaction to a multiband system is through the Hamiltonian

$$\begin{aligned} \mathcal{H} &= \sum_{k,\alpha\beta} \varepsilon_{k,\alpha\beta} \left(c^\dagger_{k\uparrow,\alpha\beta} c_{k\uparrow,\beta\alpha} + c^\dagger_{k\downarrow,\beta\alpha} c_{k\downarrow,\alpha\beta} \right) \\ &\quad - \sum_{k,q,\alpha\beta\gamma\delta} V_{k,q,\alpha\beta\gamma\delta} c^\dagger_{k\uparrow,\alpha} c^\dagger_{-k\downarrow,\beta} c_{q\uparrow,\gamma} c_{-q\downarrow,\delta}, \end{aligned} \tag{6.7}$$

where the greek indices enumerate the layers, the $c^\dagger_{k,\alpha}$ ($c_{k,\alpha}$) create (destroy) electrons of momentum k in layer α, $\varepsilon_{k,\alpha\beta}$ is the electron dispersion in layer α, and $V_{k,q,\alpha\beta\gamma\delta}$ is the generalized pairing interaction.

However, since it seems reasonable that the pairing acts in the bands and not the layers we can start from the band system in which the dispersions have already been diagonalized

$$\begin{aligned} \mathcal{H} &= \sum_{k,\alpha} \tilde{\varepsilon}_{k,\alpha} \left(c^\dagger_{k\uparrow,\alpha} c_{k\uparrow,\alpha} + c^\dagger_{k\downarrow,\alpha} c_{k\downarrow,\alpha} \right) \\ &\quad - \sum_{k,q,\alpha\beta\gamma\delta} V_{k,q,\alpha\beta\gamma\delta} c^\dagger_{k\uparrow,\alpha} c^\dagger_{-k\downarrow,\beta} c_{q\uparrow,\gamma} c_{-q\downarrow,\delta}, \end{aligned} \tag{6.8}$$

where the greek indices now enumerate the bands, the $c^\dagger_{k,\alpha}$ ($c_{k,\alpha}$) create (destroy) electrons of momentum k in band α, $\tilde{\varepsilon}_{k,\alpha\beta}$ is the electron dispersion in band α, and $V_{k,q,\alpha\beta\gamma\delta}$ is the pairing interaction. The case in which the pairing acts in the layers is studied by Atkinson.[40]

While the first sum in the above is very similar to that appearing in Eq. 6.7 it differs in that the $\tilde{\varepsilon}_{k,\alpha}$ are the band dispersions instead of the layer dispersions (*i.e.* they are the result of the diagonalization procedure in §6.1) and the electron creation and annihilation operators likewise operate in the bands instead of the layers. This distinction is made because of the assumptions that are made about the pairing interaction, namely that the pairing acts only in the bands.

Performing a mean field analysis similar to that in §2.4 we get

$$\mathcal{H} = \sum_{k,\alpha\beta} \Psi^\dagger_{k,\alpha} \hat{H}_{k,\alpha\beta} \Psi_{k,\beta}$$

where $\Psi^\dagger_{k,\alpha} \equiv \begin{bmatrix} c^\dagger_{k\uparrow,\alpha} & c_{-k\downarrow,\alpha} \end{bmatrix}$ is a Nambu spinor,

$$\hat{H}_{k,\alpha\beta} \equiv \begin{bmatrix} \tilde{\varepsilon}_{k,\alpha}\delta_{\alpha\beta} & \Delta_{k,\alpha\beta} \\ \Delta^\dagger_{k,\alpha\beta} & -\tilde{\varepsilon}_{k,\alpha}\delta_{\alpha\beta} \end{bmatrix}. \tag{6.9}$$

in which $\delta_{\alpha\beta}$ is a Kronecker delta function and

$$\Delta_{k,\alpha\beta} \equiv -\sum_{q,\alpha\beta\gamma\delta} V_{k,q,\alpha\beta\gamma\delta}\chi^{p}_{q,\gamma\delta} \tag{6.10}$$

with the pair susceptibility given by $\chi^{p}_{q,\gamma\delta} \equiv \langle c_{q\uparrow,\gamma}c_{-q\downarrow,\delta}\rangle$.

We now make the following assumption

$$V_{k,q,\alpha\gamma} \equiv V_{k,q,\alpha\alpha\gamma\gamma} = V_{k,q,\alpha\beta\gamma\delta}\delta_{\alpha\beta}\delta_{\gamma\delta}.$$

This means that there is only intraband pairing and no interband pairing (ie, $\Delta_{k,\alpha} \equiv \Delta_{k,\alpha\beta}\delta_{\alpha\beta}$ and $\chi_{q,\gamma} \equiv \chi_{q,\gamma\delta}\delta_{\alpha\beta}$ are both diagonal in the greek indices); this is a reasonable assumption because electrons near the Fermi surface in the different bands cannot have equal and opposite momenta. This Hamiltonian has the same form as that for a two band model studied by Chi [77] and is similar to that studied by others [77, 112, 113, 114] and is, as noted in [109], mathematically very similar to the system studied by Liu *et al.*.[52] Interlayer pairing has also been studied.[114, 115, 116]

With this assumption each of the elements of the Hamiltonian matrix is diagonal and so the Hamiltonian matrix can be diagonalized in the same manner as is §2.4 and has eigenvalues given by $E_{k,\alpha} = \pm\sqrt{\varepsilon^2_{k,\alpha} + \Delta^2_{k,\alpha}}$ and pair susceptibilities similar to Eq. 2.15. The resulting BCS equations are

$$\Delta_{k,\alpha} = -\sum_{q,\beta} V_{k,q,\alpha\beta}\chi^{p}_{q,\beta} \tag{6.11}$$

which are a set of coupled, non-linear integral equations which must be solved in a self-consistent manner.

There remains the choice of the $V_{k,q,\alpha\beta}$ and their relative magnitudes. In order not to complicate matters with an inordinate number of parameters all of the $V_{k,q,\alpha\beta}$ are taken to have the same functional form, namely Eq. 4.12, and to have the same coupling constant, $g^2\chi_o$. A ramification of this simplification is that all of the $\Delta_{k,\alpha}$ will have identical momentum and temperature dependencies.

However, the results of having different coupling constants for the different terms in the interaction matrix, $V_{k,q,\alpha\beta}$, have been investigated [109] and an interesting result is that, regardless of the sign, the off-diagonal term in the interaction matrix enhance the superconducting critical temperature.[77, 109, 117] It is easy to see that this is so in a two band system if one considers that the relative sign of the order parameters in the two bands can change to accommodate both attractive and repulsive off-diagonal interactions. For a larger number of bands the situation is more complex, with some of the off-diagonal terms possibly counteracting that of other off-diagonal terms, but there will be no net decrease in the superconducting critical temperature.

Bilayer Models

For a bilayer system the sum over the bands of the coupled BCS equations, Eq. 6.11, (*i.e.* $\alpha = 1, 2$) can be written explicitly as

$$\begin{aligned} \Delta_{k,1} &= -\sum_q V_{k,q,11}\chi^p_{q,1} + V_{k,q,12}\chi^p_{q,2} \\ \Delta_{k,2} &= -\sum_q V_{k,q,12}\chi^p_{q,1} + V_{k,q,22}\chi^p_{q,2} \end{aligned}$$

where we have taken $V_{k,q,12} = V_{k,q,21}$ although, in general, only $V_{k,q,12} = V^\dagger_{k,q,21}$ is required. Note that since the pair susceptibility changes sign with the corresponding order parameter we see that the above equation is unchanged by the substitution $\{\Delta_{k,2}, V_{k,q,12}\} \rightarrow \{-\Delta_{k,2}, -V_{kq,12}\}$ which means that the overall sign of $V_{kq,12}$ only affects the relative sign of the order parameters in the two bands and not their magnitudes. This is a reiteration of the above statement that the effect upon the critical temperature of having an interband interaction is independent of whether this interaction is attractive or repulsive, although some calculated properties (*e.g.* the *c*-axis Josephson tunneling current) still depend upon the relative sign of the interband interaction. If we had taken $V_{k,q,12}$ as complex the symmetry would be $\{\Delta_{k,2}, V_{k,q,12}\} \rightarrow \{\Delta_{k,2}e^{-i\phi}, V_{k,q,12}e^{i\phi}\}$ where $V_{k,q,12} = |V_{k,q,12}|e^{i\phi}$, and the relative phase of the order parameters in the two bands would no longer be ± 1. It is important to emphasize that any interband interaction, either attractive or repulsive, tends to enhance the critical temperature and that this is consistent with the observation that the critical temperature tends to be higher in materials with multiple adjacent CuO_2 layers.

By incorporating our choice of taking as identical the elements of the interaction matrix, $V_{k,q,\alpha\beta} \equiv V_{k,q}$, we get

$$\begin{aligned} \Delta_{k,1} &= -\sum_q V_{k,q}\left(\chi^p_{q,1} + \chi^p_{q,2}\right) \\ \Delta_{k,2} &= -\sum_q V_{k,q}\left(\chi^p_{q,1} + \chi^p_{q,2}\right) \end{aligned} \tag{6.12}$$

in which we can immediately see that the two order parameters are identical although the pair susceptibilities remain different. If we had chosen the off-diagonal terms of the interaction matrix to have the opposite sign of the diagonal terms the order parameters would have opposite signs but the same momentum dependencies.

BSCCO

Using the dispersions from §6.1.1 that were used to model BSCCO (shown in Fig. 6.1) and the MMP interaction, Eq. 4.12, we can solve the above coupled set of BCS equations. The resulting order parameter has, as expected, *d*-wave symmetry with nodes along the diagonals of the Brillouin zone. In Fig. 6.4 the effect of the interlayer hopping integral, $t_\perp/t$ upon the coupling constant,

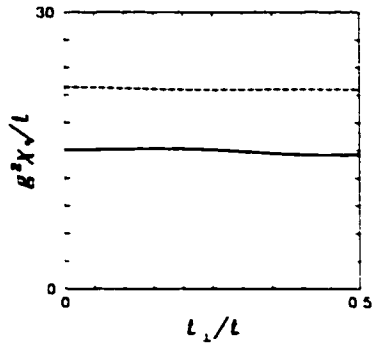

Figure 6.4: The effect of the interlayer hopping integral, $t_\perp/t$ upon the coupling constant, $g^2\chi_o/t$, required for a critical temperature of 100 K for BSCCO (solid line) and YBCO (dashed line) bilayers are shown. There is very little variation (< 5%) over the range of interest.

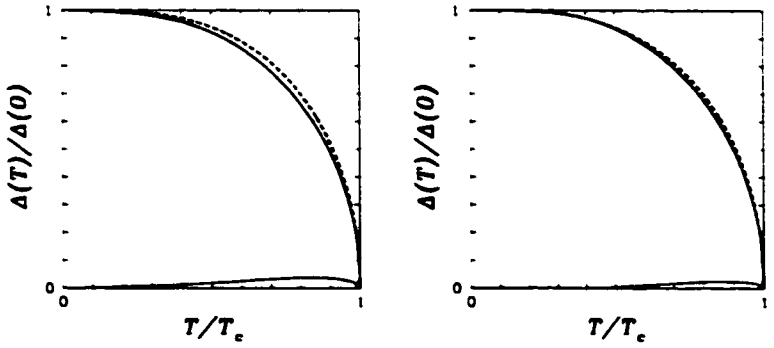

Figure 6.5: The temperature dependence of the order parameter as found by solving the BCS equation with an MMP interaction (solid curves) and that given by $h(T)$, Eq. 2.4, (dashed curves) for the two model YBCO dispersions shown in Fig. 6.2. The agreement between the two curves is quite good except near $T/T_c \sim 1$ where, $h(T)$ deviates from the BCS solution. This deviation is acceptable with the caveat that calculations of properties that rely upon the temperature derivative of the order parameter, such as the specific heat, will be incorrect if they use this function.

$g^2\chi_o/t$, required for a critical temperature of 100 K for a BSCCO bilayer is shown by the solid line. There is very little variation (< 5%) over the range of interest.

YBCO

In Fig. 6.5 the temperature dependence of the order parameter as found by solving the BCS equation with an MMP interaction (solid curves) and that given by $h(T)$, Eq. 2.4, (dashed curves) for the two model YBCO dispersions of §6.1.1 (shown in Fig. 6.6). The agreement between the two curves is again quite good except near $T/T_c \sim 1$. The gap nodes (dashed lines) of this solution are shown in Fig. 6.6. The Fermi surfaces of Fig. 6.2 are the solid lines reproduced here. While the gap nodes are superficially different in the centre of the Brillouin zone this reflects only the sign of the

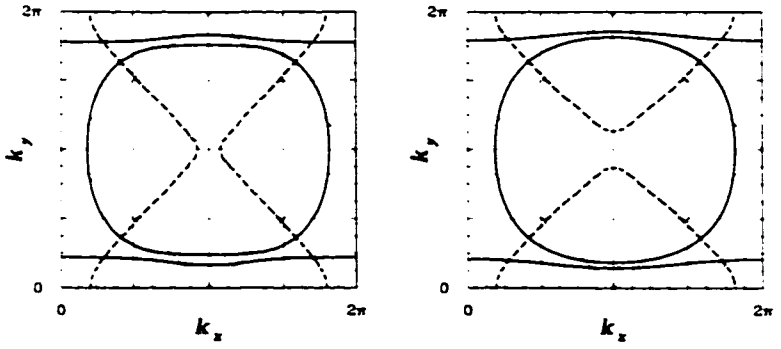

Figure 6.6: Solving the coupled BCS equations with the chain and plane dispersions of §6.1.1 (the Fermi surfaces of Fig. 6.2 are the solid lines reproduced here) yields the gap nodes (dashed lines) shown.

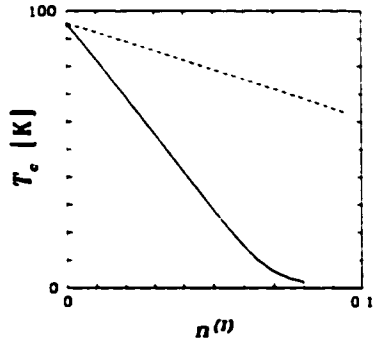

Figure 6.7: The critical temperature, T_c, as a function of impurities, $n^{(I)}$, for a plane-chain model. The solid curve is for the unitary limit ($V_I \to \infty$) and the dashed curve is for the Born approximation ($V_I = 1t$). Results are shown for a d-wave system ($g = 20.0t$).

order parameter at this point – it is the value of the order parameter along the Fermi surfaces that is important and this is very similar for the two different chain-plane dispersions shown.

In Fig. 6.4 the effect of the interlayer hopping integral, $t_\perp/t$ upon the coupling constant, $g^2\chi_o/t$, required for a critical temperature of 100 K for a YBCO bilayer is shown by the dashed line. There is even less variation ($< 1.5\%$) over the range of interest than in the BSCCO case.

6.3 Impurities

6.3.1 Chain-Plane Models

The effects of impurities in a chain-plane model, which models the Fermi surfaces of YBCO, is important because, while this is the most widely studied material, it is also potentially the one

with the most impurities in many experiments (only recently have crystals been obtained that are considered "perfect"). In order to compare theoretical calculations with experimental results it is important that impurities, which are present in most if not all experiments, are incorporated into the theoretical model. This is especially true for YBCO both because it is the most studied HTS material and because even poor quality crystals can have relatively high critical temperatures, even though some samples are also among the best HTS crystals available (see the end of this section, p. 92, for a discussion of why this material can have a lot of impurities and still have a high critical temperature).

In the chain-plane model studied here (see §6.1.1 for details of the dispersions used) the order parameter is more orthorhombic (*i.e.* the s component is larger) than the orthorhombic system examined above and, consequently, the critical impurity concentration is slightly larger ($\sim 8\%$). In Fig. 6.7 the critical temperature, T_c, as a function of impurities, $n^{(I)}$, for a plane-chain model is plotted. The solid curve is for the unitary limit ($V_I \to \infty$) and the dashed curve is for the Born approximation ($V_I = 1t$). Results are shown for a d-wave system with an interaction strength ($g = 20.0t$) which yields $T_c = 100$K for no impurities (Here $T_c = 95$K due to the finite cutoff in the Matsubara sums.)

The order parameter, $\phi_{\boldsymbol{k}}(\omega)$, for a chain-plane model in the unitary limit ($V_I \to \infty$) with 2% impurities for a d-wave system ($g = 20.1t$) at $T = 10$K ($T_c = 69.0$K) is plotted in Fig. 6.8. The top two figures are for the plane layer and the bottom two figures are for the chain layer. The curves are the same as in Fig. 5.14. The $\boldsymbol{k}$-dependent part of the order parameter, $\Delta_{\boldsymbol{k}}$, has a maximum value of 17.2 meV ($\Delta_{\boldsymbol{k}}$ is identical for the two layers) and the frequency dependent part, $f(\omega)$, has a zero frequency values of 0.040 and -3.22 meV on the plane and chain layers, respectively.

There are two interesting features of the $f(\omega)$: first, due to the repulsive interaction the $f(\omega)$ have opposite signs on each of the two layers and, second, $f(\omega)$ is much smaller on the plane layer than on the chain layer. This last feature is caused by the plane layer being very close to tetragonal (a tetragonal system would have $f(\omega) = 0$ – see the discussion in §5.3 on p. 56) since all of its orthorhombicity is caused by its coupling to the chain layer.

Finally, there is an interesting feature of $\phi_{\boldsymbol{k}}(0)$ on the chain layer, namely that the gap nodes no longer cross the Fermi surface – *i.e.* the gap along the chain Fermi surface has an anisotropic s-wave character while that along the plane Fermi surface still has a d-wave character (*i.e.* nodes and sign changes). For $n^{(I)} = 5\%$ ($T_c = 28.1$K) there is no longer a node in $\phi_{\boldsymbol{k}}(0)$ anywhere in the Brillouin zone on the chain layer and for $n^{(I)} = 6\%$ ($T_c = 15.0$K) the nodes are gone from the Brillouin zones of both layers. This disappearance of the gap nodes is caused both by the decrease in $\Delta_{\boldsymbol{k}}$ and the increase in $f(0)$ with increasing $n^{(I)}$.

Figure 6.9 shows the change in T_c as a function of impurities which are only in the chain layer (left) or plane layer (right) (*i.e.* there are no impurities in the other layer). The solid curve is for the unitary limit ($V_I \to \infty$) and the dashed curve is for the Born approximation ($V_I = 1t$). Results are shown for the same d-wave system ($g = 20.0t$) as Fig. 6.7.

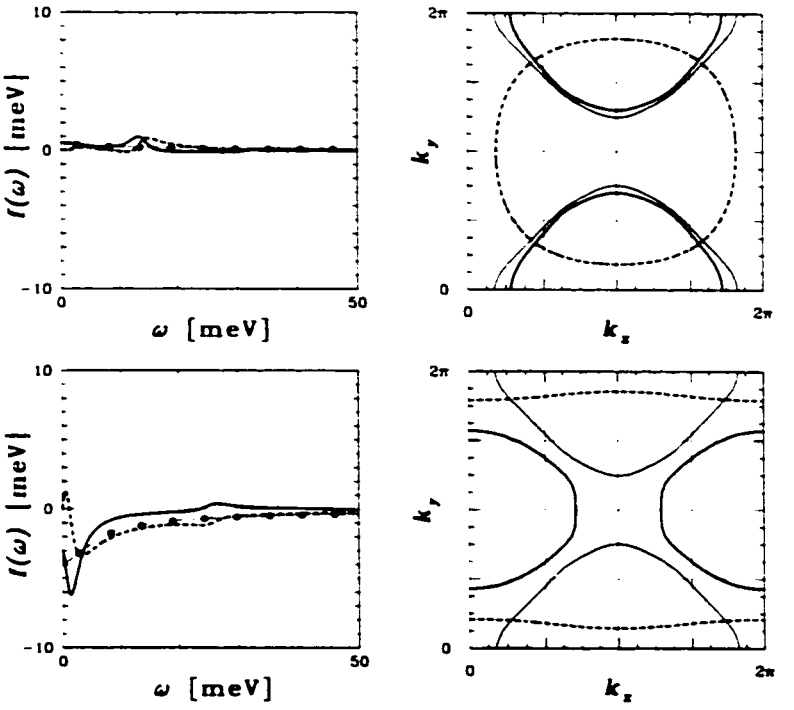

Figure 6.8: The order parameter, $\phi_k(\omega)$, for a chain-plane model in the unitary limit ($V_I \to \infty$) with 2% impurities for a d-wave system ($g = 20.1t$) at $T = 10$K ($T_c = 69.0$K). The top two figures are for the plane layer and the bottom two figures are for the chain layer. The curves are the same as in Fig. 5.14. The k-dependent part of the order parameter, Δ_k, has a maximum value of 17.2 meV and the frequency dependent part, $f(\omega)$, has a zero frequency values of 0.040 and -3.22 meV on the plane and chain layers, respectively.

The small variation of T_c with chain impurities, $n^{(I_c)}$, illustrates that, in this model, there can be a large amount of impurities in the chain layer without substantially affecting the critical temperature, T_c. In fact, these curves are not very different from those for an isotropic s-wave system (Fig. 5.12). This supports the view [118] that only systems with the very highest T_c's have intact chains since, in this model, impurities in the chains have little effect upon the critical temperature.

This is one of the important results of this research. If the oxygen vacancies are indeed in the chain layer then this could account for the factors that make YBCO both unique and widely studied; namely that it is relatively easy to make "dirty" YBCO crystals (*i.e.* with large amounts of impurities and defects) with high critical temperatures. There are two effects of these oxygen vacancies, first they provide the hole doping that is necessary for high critical temperatures (optimal doping is ~15%) and second, they provide a reservoir (*i.e.* the chains) for the impurities (*i.e.* the oxygen vacancies) that effects the critical temperature in a minimal way. These two effects, optimal doping and minimal impurity effects, can be balanced (with the former increasing and the latter decreasing the critical temperature) with the critical temperature only slightly lowered by the impurity

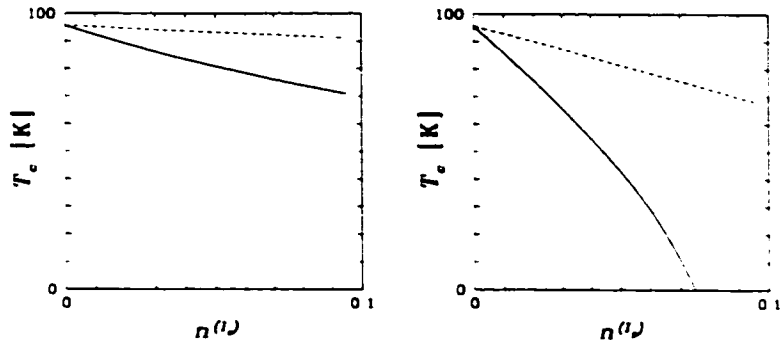

Figure 6.9: The critical temperature, T_c, as a function of impurities in only the chain layer (left) or only in the plane layer (right) for a plane-chain model. The solid curve is for the unitary limit ($V_I \to \infty$) and the dashed curve is for the Born approximation ($V_I = 1t$). Results are shown for a d-wave system ($g = 20.0t$). Note in particular that impurities in the chain layer behave as if the order parameter has s-wave symmetry (*cf.* Fig. 5.12) while impurities in the plane layer behave similar to the single band orthorhombic system (*cf.* Fig. 5.13).

effects. This is substantially different from other HTS materials in which the lowering of the critical temperature by the impurity effects of the doping is substantial due to the small or nonexistent s-component in the order parameter.

In fact, if one takes the view that there is a CuO_2 trilayer in YBCO in which half of the oxygen in one layer are missing, allowing the other two layers to be free of vacancies, the doping level is $1/6 = 17\%$, very close to optimal doping in other materials.

6.4 Optical Conductivity

The optical conductivity for a two layer system is the sum of the optical conductivities of each of the layers. This follows from the elementary rule for parallel conductors (The conductivity is the reciprocal of the resistivity.). The optical conductivity for a two layer BSCO model is not interesting: It is merely double that of the corresponding single layer system. In light of this only the optical conductivity of the YBCO system will be examined here.

6.4.1 YBCO

In Fig. 6.10 the optical conductivity for a chain-plane system with a $d+\delta s$-order parameter are shown for directions both perpendicular (top) and parallel to the chains (bottom). The only significant difference between the two directions being the relative magnitudes in the x (top) and y-directions (bottom). They are similar to those calculated for a single layer d-wave system, shown on the bottom in Fig. 5.15 except that the rise in $1/\tau^*$ with frequency is much more pronounced.

In Fig. 6.11 the optical conductivity for the same chain-plane system used in Fig. 6.10 is

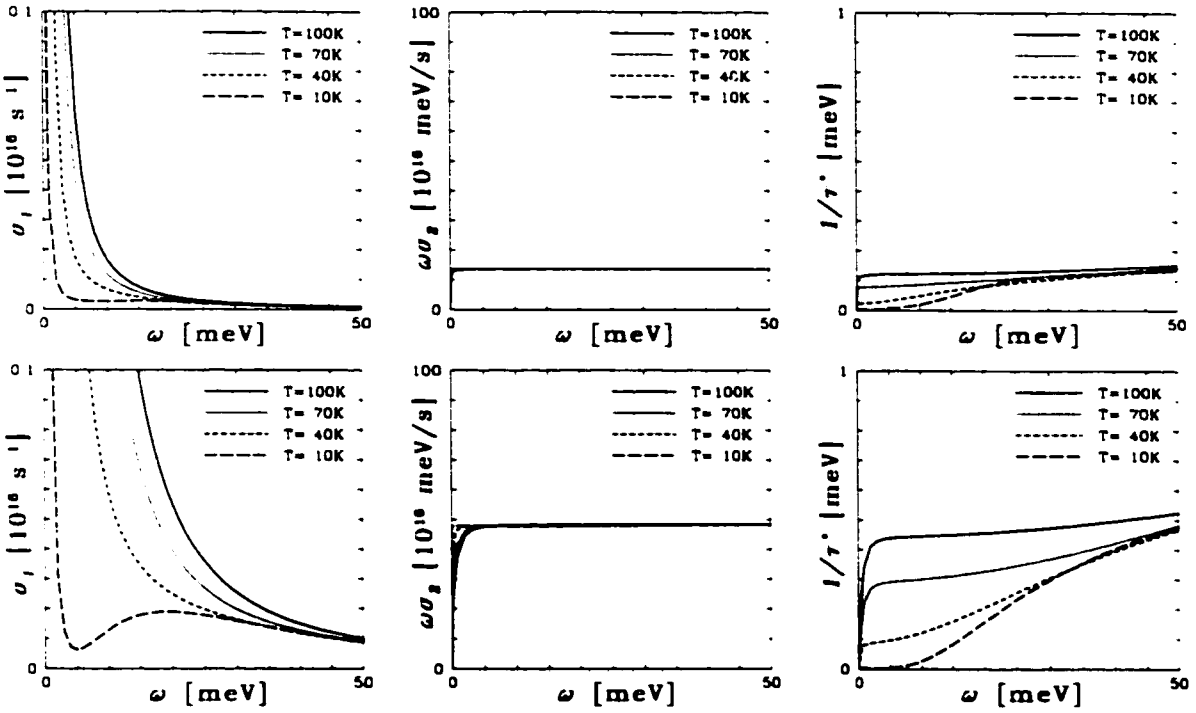

Figure 6.10: The optical conductivity for the x (top) and y-directions (bottom) at various temperatures. On the left is the real part, $\sigma_1(\omega)$, in the middle is the imaginary part, $\sigma_2(\omega)$, and on the right is the scattering rate, $1/\tau^*(\omega) = \omega\sigma_1(\omega)/\sigma_2(\omega)$, calculated using Eq. 4.16 with the dispersion on the left of Fig. 6.2 with 1% impurities in the chain layer and 0.1% in the plane layer in the Born approximation ($V_I = 1t$), yielding a critical temperature of 94.9K. The MMP interaction given by Eq. 4.12 with $g^2\chi_o = 20.18t$ was used; the interaction gives, for no impurities and $t = 100$meV, $T_c = 100$K.

plotted for $T = 10$K, this time for several different impurity levels in the chain layer. As the chain layer impurity level increases the conductivity curves evolve smoothly.

6.5 The Penetration Depth

6.5.1 Effects of Interlayer Interaction on the Superconducting State in $YBa_2Cu_3O_{7-\delta}$

This paper [109] examines the effect of the interaction between the chain and plane layers of YBCO upon the order parameter, the DOS, the magnetic penetration depth and the Knight shift. It shows, in detail, the diagonalization of the Hamiltonian of the two layer system and emphasizes that "any interlayer interaction, either attractive or repulsive, tends to enhance T_c and that this is consistent with the observation that T_c is higher in materials with multiple adjacent CuO layers."

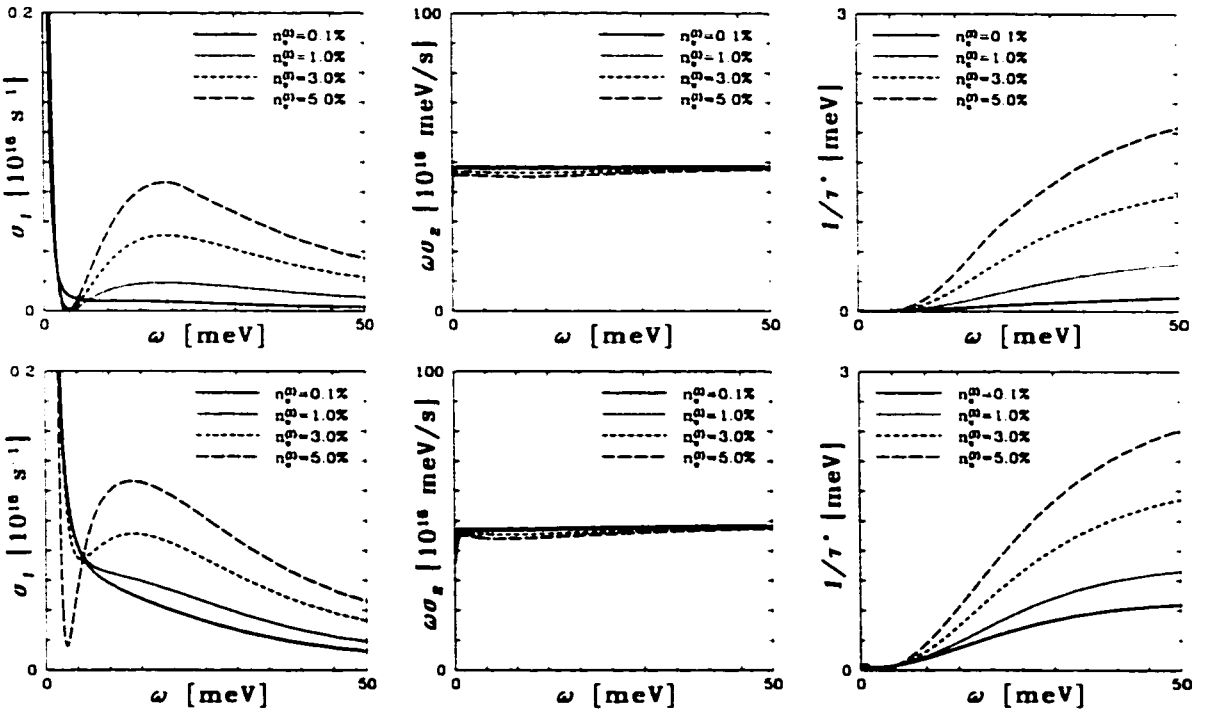

Figure 6.11: The optical conductivity in the y-direction for a chain-plane system with 0.1% (top) and 1.0% impurities in the plane layer (bottom) in the Born approximation ($V_I = 1t$) for various impurity levels in the chain layers at $T = 10$K. On the left is the real part, $\sigma_1(\omega)$, in the middle is the imaginary part, $\sigma_2(\omega)$, and on the right is the scattering rate, $1/\tau^*(\omega) = \omega\sigma_1(\omega)/\sigma_2(\omega)$, calculated using Eq. 4.16 with the dispersion on the left of Fig. 6.2. The MMP interaction given by Eq. 4.12 with $g^2\chi_o = 20.17t$ was used; this interaction gives, for no impurities and $t = 100$meV, $T_c = 100$K.

Note that the approximation given by Eq. 11 in this paper was not used in the calculations of the penetration depth in §6.5.3. Note that the dispersion also differs slightly. Finally, somewhere in the process of publishing this paper two of the panels of figure two were lost. The correct figure is reproduced here as figure 6.12.

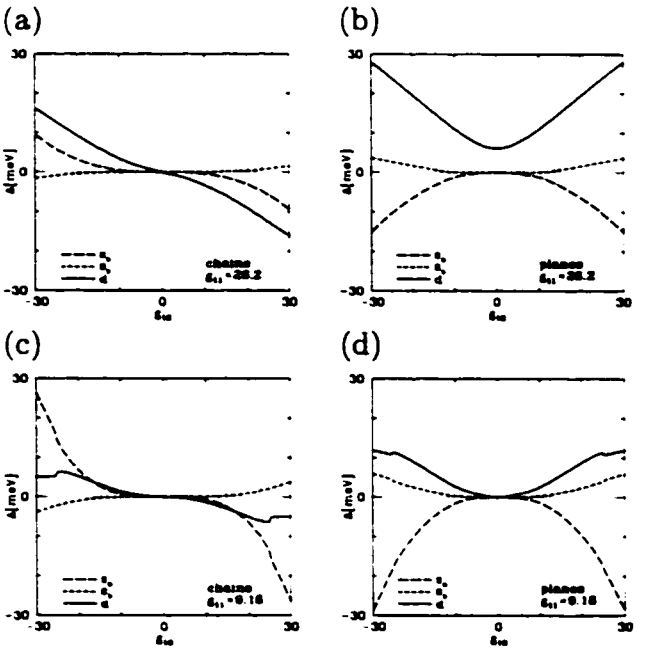

Figure 6.12: In the following published paper figure two has only half the number of panels that it should have. This figure has the correct number of panels.

PHYSICAL REVIEW B VOLUME 55, NUMBER 2 1 JANUARY 1997-II

Effects of interlayer interaction on the superconducting state in $YBa_2Cu_3O_{7-\delta}$

C. O'Donovan* and J. P. Carbotte
Department of Physics & Astronomy, McMaster University, Hamilton, Ontario, Canada L8S 4M1
(Received 2 January 1996)

For a two-layer system in a weak-coupling BCS formalism any interlayer interaction, regardless of its sign, enhances the critical temperature. The sign has an effect upon the relative phase of the order parameter in each of the two planes but not upon its magnitude. When one of the planes has a dispersion consistent with CuO chains and no intrinsic pairing interaction there is both an enhancement of the critical temperature and an $s+d$ mixing in both layers as the interlayer interaction is increased. The magnetic penetration depth, c-axis Josephson tunneling, density of states, and Knight shift are calculated for several sets of model parameters. [S0163-1829(97)05346-5]

I. INTRODUCTION

The search for the mechanism which causes superconductivity in the copper oxide materials is an ongoing effort which has yet to reach a consensus. One factor which any model should account for is that the critical temperature tends to be higher in systems with multiple adjacent CuO_2 layers, and even in systems, such as $YBa_2Cu_3O_{7-\delta}$ (YBCO), in which a CuO layer is adjacent to the CuO_2 layers, T_c seems to be enhanced.

It is generally believed that the superconducting condensate resides in the CuO_2 planes, although one interpretation of the observed large x-y anisotropy of the zero temperature magnetic penetration depth (a factor of ~ 1.6) in YBCO indicates that there is as much condensate in the CuO chains as in the CuO_2 planes (i.e., the condensate in the chains only contributes to the penetration depth for current in the direction parallel to the chains, i.e., the b direction).[1] Since it is believed that whatever mechanism is responsible for superconductivity in the copper oxides is intrinsic to the CuO_2 planes, some other mechanism for creating the superconducting condensate on the CuO chains is required.

In this paper we derive a Hamiltonian for a layered system and, making a simplifying assumption that there is no pairing between electrons which reside in different layers, derive a pair of coupled BCS equations for a system of two layers, each with possibly different dispersion and pairing interactions. In this model Cooper pairs can scatter between the layers so that, as in a two-band model,[2] even if there is no pairing interaction in one of the layers, there will still be a condensate in that layer due to the interlayer interaction.

Although we make a particular choice for the pairing interaction (which is motivated by the nearly antiferromagnetic Fermi liquid model which leads naturally to a d-wave gap for single CuO_2 planes[3]), a d-wave solution is also found for other types of nonisotropic pairing interactions.[4] One result of having gap nodes cross the Fermi surface is a low-temperature linear behavior of the magnetic penetration depth λ_{ii}^{-2}, as is observed in YBCO.[1,5–7] Here we only try to model the low-temperature behavior and relative magnitude[1] in the x and y directions of the magnetic penetration depth. The $T-T_c$ behavior is only reproduced for values of $2\Delta_{max}/T_c$ about 1.5 times higher[8] than the value of 4.4 found in the BCS weak-coupling approximation. In the two-layer model that we study here a higher value of $2\Delta_{max}/T_c$ is obtained which is closer to that observed in experiments such as angle-resolved photoemission spectroscopy (ARPES) (Ref. 9) or CITS (Ref. 10) that measure the absolute magnitude of the order parameter.

We find that the presence of the chains destroys the tetragonal symmetry of the CuO_2 planes and shifts the d-wave gap nodes in the CuO_2 plane off the diagonals in agreement with an earlier model.[11] In this case the gap contains an admixture of s- and d-wave symmetry. Calculations of the c-axis Josephson tunneling current show that the positive and negative parts of the order parameter do not cancel, as for d-wave pairing in a tetragonal system, and that the Josephson junction resistance-tunneling current products $RJ(T=0)$, are in the range of 0.1–3.0 meV, in agreement with the experiments of Sun *et al.*[12] We also calculate both the normal and superconducting density of states (DOS) for the CuO_2 planes and CuO chains separately since some surface probes, such as current-imaging tunneling spectroscopy (CITS),[10] can measure them separately. Finally the Knight shift is calculated separately for both the planes and the chains.

In Sec. II we introduce our Hamiltonian and derive a set of coupled BCS equations for planes and chains and other necessary formulas, particularly the expression for the magnetic penetration depth in this model. In Sec. III we present the the solutions of these BCS equations as well as the results of calculations of the magnetic penetration depth, electronic density of states, c-axis Josephson tunneling, and Knight shift. Section IV contains a short discussion and conclusion.

II. FORMALISM

In this section we will present a Hamiltonian in which multiple layers are coupled through the pairing interactions between adjacent layers. We will then make the assumption that there is no interlayer pairs (i.e., that each Cooper pair resides in only one of the layers) and that there is no single-particle interlayer hopping. The Hamiltonian of this special case is then diagonalized and coupled BCS equations derived. We then give expressions for the magnetic penetration

0163-1829/97/55(2)/1200(9)/$10.00

depth in this model, the Knight shift, the quasiparticle density of states, and the dc Josephson junction resistance-tunneling current product for a c-axis tunnel junction.

The general Hamiltonian is

$$H=\sum_{\mathbf{k},\alpha\beta}\varepsilon_{\mathbf{k},\alpha\beta}(a^{\dagger}_{\mathbf{k}\uparrow,\alpha}a_{\mathbf{k}\uparrow,\beta}+a^{\dagger}_{\mathbf{k}\downarrow,\beta}a_{\mathbf{k}\downarrow,\alpha})$$

$$-\frac{1}{\Omega}\sum_{\mathbf{k},\mathbf{q},\alpha\beta\gamma\delta}V_{\mathbf{k},\mathbf{q},\alpha\beta\gamma\delta}a^{\dagger}_{\mathbf{k}\uparrow,\alpha}a^{\dagger}_{-\mathbf{k}\downarrow,\beta}a_{\mathbf{q}\uparrow,\gamma}a_{-\mathbf{q}\downarrow,\delta}, \quad (1)$$

where the greek indices enumerate the layers, the $a^{\dagger}_{\mathbf{k},\alpha}$ ($a_{\mathbf{k},\alpha}$) create (destroy) electrons of momentum $\mathbf{k}$ in layer α ($\mathbf{k}$ is in units of a^{-1} where a is the lattice parameter), $\varepsilon_{\mathbf{k},\alpha\beta}$ is the electron dispersion, and $V_{\mathbf{k},\mathbf{q},\alpha\beta\gamma\delta}$ is the pairing interaction.

Performing a mean field analysis, we get

$$H=\sum_{\mathbf{k},\alpha\beta}\varepsilon_{\mathbf{k},\alpha\beta}(a^{\dagger}_{\mathbf{k}\uparrow,\alpha}a_{\mathbf{k}\uparrow,\beta}+a^{\dagger}_{\mathbf{k}\downarrow,\beta}a_{\mathbf{k}\downarrow,\alpha})$$

$$-\sum_{\mathbf{k},\alpha\beta}(\Delta_{\mathbf{k},\alpha\beta}a^{\dagger}_{\mathbf{k}\uparrow,\alpha}a^{\dagger}_{-\mathbf{k}\downarrow,\beta}+\text{H.c.})+C,$$

where C is a constant, H.c. indicates the Hermitian conjugate, $\Delta_{\mathbf{k},\alpha\beta}=\Omega^{-1}\Sigma\mathbf{q},\gamma\delta V_{\mathbf{k},\mathbf{q},\alpha\beta\gamma\delta}\chi_{\mathbf{q},\gamma\delta}$ are the order parameters, and $\chi_{\mathbf{q},\gamma\delta}=\langle a_{\mathbf{q}\uparrow,\gamma}a_{-\mathbf{q}\downarrow,\delta}\rangle$ are the pair susceptibilities.

Writing this in Nambu spinor notation, we get

$$H=\sum_{\mathbf{k},\alpha\beta}A^{\dagger}_{\mathbf{k},\alpha}\hat{H}_{\mathbf{k},\alpha\beta}A_{\mathbf{k},\beta},$$

where $A^{\dagger}_{\mathbf{k},\alpha}=[a^{\dagger}_{\mathbf{k}\uparrow,\alpha}\ a_{-\mathbf{k}\downarrow,\alpha}]$ and

$$\hat{H}_{\mathbf{k},\alpha\beta}=\begin{bmatrix}\varepsilon_{\mathbf{k},\alpha\beta} & \Delta_{\mathbf{k},\alpha\beta}\\ \Delta^{\dagger}_{\mathbf{k},\alpha\beta} & -\varepsilon_{\mathbf{k},\alpha\beta}\end{bmatrix}. \quad (2)$$

In this model the magnetic penetration depth is given by the expression[13]

$$\lambda_{ij}^{-2}=\frac{8\pi e^2}{\hbar^2c^2}\frac{1}{\Omega}\sum_{\mathbf{k},\alpha\beta}\hat{\gamma}^{(i)}_{\mathbf{k},\alpha\beta}\hat{\gamma}^{(j)}_{\mathbf{k},\beta\alpha}(\hat{G}_{\mathbf{k},\alpha\beta}|_{\Delta=0}-\hat{G}_{\mathbf{k},\alpha\beta}), \quad (3)$$

where

$$\hat{G}_{\mathbf{k},\alpha\beta}=\frac{\partial f(E_{\mathbf{k},\alpha})}{\partial E_{\mathbf{k},\alpha}}\delta_{\alpha\beta}+\frac{f(E_{\mathbf{k},\alpha})-f(E_{\mathbf{k},\beta})}{E_{\mathbf{k},\alpha}-E_{\mathbf{k},\beta}}(1-\delta_{\alpha\beta}),$$

$$\hat{\gamma}^{(i)}_{\mathbf{k},\alpha\beta}=\sum_{\gamma\delta}\hat{U}^{\dagger}_{\mathbf{k},\alpha\gamma}\frac{\partial\varepsilon_{\mathbf{k},\gamma\delta}}{\partial k_i}\hat{U}_{\mathbf{k},\delta\beta}.$$

$\pm E_{\mathbf{k},\alpha}$ are the eigenvalues of Eq. (2), $f(x)$ is the Fermi function, $\delta_{\alpha\beta}$ is a Kronecker delta, and $\hat{U}_{\mathbf{k},\alpha\beta}$ is the unitary matrix which diagonalizes Eq. (2). The quantities e, $\hbar$, and c are the electron charge, Planck's constant, and the speed of light, respectively.

We now make the following simplification: $V_{\mathbf{k},\mathbf{q},\alpha\gamma}=V_{\mathbf{k},\mathbf{q},\alpha\alpha\gamma\gamma}=V_{\mathbf{k},\mathbf{q},\alpha\beta\gamma\delta}\delta_{\alpha\beta}\delta_{\gamma\delta}$ and $\varepsilon_{\mathbf{k},\alpha}=\varepsilon_{\mathbf{k},\alpha\alpha}=\varepsilon_{\mathbf{k},\alpha\beta}\delta_{\alpha\beta}$. This means that there is only intralayer pairing and no interlayer pairing (i.e., $\Delta_{\mathbf{k},\alpha}=\Delta_{\mathbf{k},\alpha\beta}\delta_{\alpha\beta}$ and $\chi_{\mathbf{q},\gamma}=\chi_{\mathbf{q},\gamma\delta}\delta_{\alpha\beta}$ are both diagonal in the greek indices) and there is no single-particle interlayer hopping. This Hamiltonian has the same form as that for a two-band model studied by one of us[3] in an earlier publication and is similar to that studied by others.[14–16] Interlayer pairing[16–18] has also been studied.

The Hamiltonian has eigenvalues given by $E_{\mathbf{k},\alpha}=\pm\sqrt{\varepsilon^2_{\mathbf{k},\alpha}+\Delta^2_{\mathbf{k},\alpha}}$ and is diagonalized by the unitary matrix

$$\hat{U}_{\mathbf{k},\alpha}=\begin{bmatrix}u_{\mathbf{k},\alpha} & v_{\mathbf{k},\alpha}\\ -v_{\mathbf{k},\alpha} & u_{\mathbf{k},\alpha}\end{bmatrix}, \quad (4)$$

where

$$u_{\mathbf{k},\alpha}=\sqrt{\frac{1}{2}\left(1+\frac{\varepsilon_{\mathbf{k},\alpha}}{E_{\mathbf{k},\alpha}}\right)},$$

$$v_{\mathbf{k},\alpha}=\sqrt{\frac{1}{2}\left(1-\frac{\varepsilon_{\mathbf{k},\alpha}}{E_{\mathbf{k},\alpha}}\right)}$$

are the usual BCS coherence factors. Using this unitary transformation (4) we can evaluate the pair susceptibilities to get

$$\chi_{\mathbf{q},\alpha}=\langle a_{\mathbf{q}\uparrow,\alpha}a_{-\mathbf{q}\downarrow,\alpha}\rangle=\frac{\Delta_{\mathbf{q},\alpha}}{2E_{\mathbf{q},\alpha}}\tanh\left(\frac{E_{\mathbf{q},\alpha}}{2k_BT}\right), \quad (5)$$

where T is the temperature and k_B is Boltzmann's constant. Note that if we had included the interlayer pairing from Eq. (1) we would have susceptibilities of the form $\langle a_{\mathbf{q}\uparrow,\alpha}a_{-\mathbf{q}\downarrow,\beta}\rangle$ with $\alpha\neq\beta$ and both the eigenvalues and the unitary matrix (4) would be much more complicated.

For a bilayer system (i.e., $\alpha=1,2$) the BCS equations are

$$\Delta_{\mathbf{k},1}=\frac{1}{\Omega}\sum_{\mathbf{q}}(V_{\mathbf{k},\mathbf{q},11}\chi_{\mathbf{q},1}+V_{\mathbf{k},\mathbf{q},12}\chi_{\mathbf{q},2}),$$

$$\Delta_{\mathbf{k},2}=\frac{1}{\Omega}\sum_{\mathbf{q}}(V_{\mathbf{k},\mathbf{q},12}\chi_{\mathbf{q},1}+V_{\mathbf{k},\mathbf{q},22}\chi_{\mathbf{q},2}). \quad (6)$$

where we have taken $V_{\mathbf{k},\mathbf{q},12}=V_{\mathbf{k},\mathbf{q},21}$, although in general only $V_{\mathbf{k},\mathbf{q},12}=V^{\dagger}_{\mathbf{k},\mathbf{q},21}$ is required.

Noting that $\chi_{\mathbf{q},2}$ changes sign [see Eq. (5)] with $\Delta_{\mathbf{k},2}$ we see that this set of equations (6) is unchanged by the substitution $\{\Delta_{\mathbf{k},2},V_{\mathbf{k},\mathbf{q},12}\}\rightarrow\{-\Delta_{\mathbf{k},2},-V_{\mathbf{k},\mathbf{q},12}\}$ which means that the overall sign of $V_{\mathbf{k},\mathbf{q},12}$ only affects the relative sign of the order parameters in the two layers and not their magnitudes. This is interesting because it means that the effect on T_c of having an interlayer interaction is independent of whether this interaction is attractive or repulsive, although some calculated properties (e.g., c-axis Josephson tunneling current) still depend upon the relative sign of the interlayer interaction. *It is important to emphasize that any interlayer interaction, either attractive or repulsive, tends to enhance T_c and that this is consistent with the observation that T_c is higher in materials with multiple adjacent CuO layers.* This well known result can be easily shown by examining the coupled BCS equations (6) near $T\sim T_c$. In this limit we can write

$$\Delta_{\mathbf{k},\alpha}=\Delta_\alpha \eta_{\mathbf{k}}.$$

$$V_{\mathbf{k},\mathbf{q},\alpha\beta}=V_{\alpha\beta}\eta_{\mathbf{k}}\eta_{\mathbf{q}},$$

where Δ_α and $V_{\alpha\beta}$ are numbers and $\eta_{\mathbf{k}}$ is a normalized function which could be taken to be d wave and corresponds to the highest T_c. The coupled BCS equations (6) can then be written as

$$\Delta_1=\Delta_1 V_{11}\frac{1}{\Omega}\sum_{\mathbf{q}}\frac{(\eta_{\mathbf{q}})^2}{\varepsilon_{\mathbf{q},1}}\tanh\left(\frac{\varepsilon_{\mathbf{q},1}}{2k_BT_c}\right)+\Delta_2 V_{12}\frac{1}{\Omega}\sum_{\mathbf{q}}\frac{(\eta_{\mathbf{q}})^2}{\varepsilon_{\mathbf{q},2}}\tanh\left(\frac{\varepsilon_{\mathbf{q},2}}{2k_BT_c}\right). \tag{7a}$$

$$\Delta_2=\Delta_1 V_{12}\frac{1}{\Omega}\sum_{\mathbf{q}}\frac{(\eta_{\mathbf{q}})^2}{\varepsilon_{\mathbf{q},1}}\tanh\left(\frac{\varepsilon_{\mathbf{q},1}}{2k_BT_c}\right)+\Delta_2 V_{22}\frac{1}{\Omega}\sum_{\mathbf{q}}\frac{(\eta_{\mathbf{q}})^2}{\varepsilon_{\mathbf{q},2}}\tanh\left(\frac{\varepsilon_{\mathbf{q},2}}{2k_BT_c}\right). \tag{7b}$$

We now assume that Δ_1 is the dominant superconducting channel when $V_{12}=V_{21}=0$ and obtain, assuming an infinite band with cutoff ω_C.

$$\Delta_1=(\Delta_1\lambda_{11}+\Delta_2\lambda_{12})\ln\left(\frac{1.13\omega_C}{T_c}\right). \tag{8a}$$

$$\Delta_2=(\Delta_1\lambda_{21}+\Delta_2\lambda_{22})\ln\left(\frac{1.13\omega_C}{T_c}\right). \tag{8b}$$

where $\lambda_{ij}=V_{ij}\times$ the density of electronic states at the Fermi surface. Substitution of Eq. (8b) into Eq. (8a) leads to a quadratic in $\ln(1.13\omega_C/T_c)$ with the solution

$$T_c=1.13e^{1/\tilde{\lambda}}, \tag{9}$$

with

$$\tilde{\lambda}=\frac{1}{2}[\lambda_{11}+\lambda_{22}+\sqrt{(\lambda_{11}-\lambda_{22})^2+4\lambda_{12}\lambda_{21}}]. \tag{10}$$

This result is well known and is given by Eq. (6.3) on p. 105 of Ref. 23. It is also found as Eq. (40) of Chi and Carbotte.[3] We note that λ_{12}, whatever its sign, increases $\tilde{\lambda}$ and so increases T_c.

If we had taken $V_{\mathbf{k},\mathbf{q},12}$ as complex, the symmetry would be $\{\Delta_2, V_{\mathbf{k},\mathbf{q},12}\}\rightarrow\{\Delta_2 e^{-i\phi}, V_{\mathbf{k},\mathbf{q},12}e^{i\phi}\}$ where $V_{\mathbf{k},\mathbf{q},12}=|V_{\mathbf{k},\mathbf{q},12}|e^{i\phi}$, and the relative phase between the layers would no longer be ± 1.

We note that by performing the unitary transformation $\hat{S}^\dagger\hat{H}\hat{S}$ where

$$\hat{S}=\frac{1}{\sqrt{2}}\begin{bmatrix}1&1&0&0\\1&-1&0&0\\0&0&1&1\\0&0&1&-1\end{bmatrix},$$

and making the substitutions $V_{11}=V_{22}=V_\parallel+V_\perp$, $V_{12}=V_\parallel-V_\perp$, $\varepsilon_1=\varepsilon+t$, and $\varepsilon_2=\varepsilon-t$ we obtain both the Hamiltonian and BCS equations used by Liu *et al.*[19] Our work differs from theirs in that we allow both the dispersion and the interaction to be different in the two layers. This is important not only because we are able to model systems such as YBCO in which there are CuO_2 planes and CuO chains, but also because the order parameter in each of the layers may differ in sign even in two identical layers.[16] Other workers have studied models in which the electrons in the pairs reside in different layers[17] (i.e., in which only $\chi_{\mathbf{k},12}$ is nonzero) as well as models in which there is no intralayer interaction[16,18] (i.e., in which only $V_{\mathbf{k},\mathbf{q},12}$ is nonzero).

After solving the set of coupled BCS equations (6) at $T=0$ using a fast Fourier transform (FFT) technique[4,11,20] we approximate the order parameters $\Delta_{\mathbf{k},1}$ and $\Delta_{\mathbf{k},2}$ with

$$\Delta_{\mathbf{k},\alpha}=(\Delta_\alpha^{(s_0)}\eta_{\mathbf{k}}^{(s_0)}+\Delta_\alpha^{(s_2)}\eta_{\mathbf{k}}^{(s_2)}+\Delta_\alpha^{(d)}\eta_{\mathbf{k}}^{(d)})\tanh(1.74\sqrt{T_c/T-1}), \tag{11}$$

where the $\eta_{\mathbf{k}}^{(\cdot)}$ are the three lowest harmonics given by

$$\eta_{\mathbf{k}}^{(s_0)}=1,$$

$$\eta_{\mathbf{k}}^{(s_2)}=\cos(k_x)+\cos(k_y),$$

$$\eta_{\mathbf{k}}^{(d)}=\cos(k_x)-\cos(k_y),$$

and the $\Delta_\alpha^{(\cdot)}$ are their amplitudes. The amplitudes of the higher harmonics are all very much smaller in magnitude and the gap nodes and the maximum magnitude of the gap, which are the most important features of the order parameter, are essentially unchanged by this approximation. We also calculate the magnetic penetration depth which in this system, since the $\tilde{\gamma}_{\mathbf{k},\alpha\beta}^{(l)}$ are diagonal in the greek indices, is given by the simplified expression

$$\lambda_{ij}^{-2}=\frac{4\pi e^2}{\hbar^2c^2}\frac{1}{\Omega}\sum_{\mathbf{k},\alpha}\frac{\partial\varepsilon_{\mathbf{k},\alpha}}{\partial k_i}\frac{\partial\varepsilon_{\mathbf{k},\alpha}}{\partial k_j}\left(\frac{\partial f(\varepsilon_{\mathbf{k},\alpha})}{\partial\varepsilon_{\mathbf{k},\alpha}}-\frac{\partial f(E_{\mathbf{k},\alpha})}{\partial E_{\mathbf{k},\alpha}}\right). \tag{12}$$

which is the usual expression[20] summed over the layers.

The curvature of the penetration depth curve, $\lambda_{ii}^{-2}(T)$ (and also its low-temperature slope), is governed by the ratio $2\Delta_{max}/T_c$, where Δ_{max} is the maximum value of the order parameter in the first Brillouin zone, and is close to a straight line for the d-wave BCS value of $2\Delta_{max}/T_c=4.4$. The presence of the interlayer interaction increases this ratio and makes the $\lambda_{ii}^{-2}(T)$ curve have a downward curvature. Experimental measurements of both the ratio $2\Delta_{max}/T_c$ (Refs. 10 and 21) as well as the penetration depth in high quality crystals of both YBCO (Ref. 1) and BSCO (Ref. 22) indicate that this ratio is quite high in the HTC (high-T_c) materials — on the order of 6 or 7.

Other quantities calculated are the Knight shift which is given by

$$K(T) \propto \frac{1}{\Omega}\sum_{\mathbf{k}} \frac{\partial f(E_{\mathbf{k}})}{\partial E_{\mathbf{k}}}. \quad (13)$$

the normal state electronic DOS which is given by

$$N(\omega) = \frac{1}{\Omega}\sum_{\mathbf{k}} \delta(\varepsilon_{\mathbf{k}} - \omega) = \lim_{\Gamma \to 0} \frac{1}{\pi\Omega}\sum_{\mathbf{k}} \frac{\Gamma}{(\varepsilon_{\mathbf{k}} - \omega)^2 + \Gamma^2}. \quad (14)$$

the superconducting electronic DOS which is given by

$$N(\omega) = \frac{1}{\Omega}\sum_{\mathbf{k}} \delta(E_{\mathbf{k}} - \omega) = \lim_{\Gamma \to 0} \frac{1}{\pi\Omega}\sum_{\mathbf{k}} \frac{\Gamma}{(E_{\mathbf{k}} - \omega)^2 + \Gamma^2}. \quad (15)$$

and the c-axis Josephson junction resistance-tunneling current product $RJ(T)$ through a superconductor-insulator-superconductor junction for incoherent c-axis tunneling is given by the relation:[24]

$$RJ(T) = \frac{2\pi T}{N^L(0)N^R(0)\pi^2}\sum_{n} A^L(\omega_n)A^R(\omega_n). \quad (16)$$

where

$$A^{L(R)}(\omega_n) = \frac{1}{\Omega}\sum_{\mathbf{k}} \frac{\Delta_{\mathbf{k}}^{L(R)}}{(\varepsilon_{\mathbf{k}}^{L(R)})^2 + (\Delta_{\mathbf{k}}^{L(R)})^2 + (\omega_n)^2}.$$

in which the superscript $L(R)$ indicates on which side of the junction the dispersion and order parameter are on, the sum over $\omega_n = \pi T(2n-1)$ is for all Matsubara frequencies, R is the resistance of the junction, and $N^{L(R)}(0)$ is the normal state electronic DOS given by Eq. (14). If the tunneling were coherent, the matrix element (which is incorporated into R) would have a $(\mathbf{k}-\mathbf{k}')$ dependence, and the sums over $\mathbf{k}$ space would not be separable.

III. RESULTS

In this section we make an explicit choice for the dispersions and interactions and then present the results of our numerical solutions to the coupled BCS equations (6) as well as the results of our calculations of the magnetic penetration depth, densities of states, Knight shift, and Josephson current. As we wish to model YBCO we will want to account for both the CuO_2 planes as well as the CuO chains. Further, we will assume that we do not have a pairing interaction in the chains, but only in the planes as well as an interlayer interaction. This means that all of the order parameter in the chains is due to the interlayer interaction. We note that although our solution technique[4] allows the order parameters to be complex and to have a relative phase between layers we find that in the models studied here, to within an overall phase, the order parameters are all real with a relative phase of ± 1.

For the dispersions, $\varepsilon_{\mathbf{k},\alpha}$, we use

$$\varepsilon_{\mathbf{k},\alpha} = -2t_\alpha[(1+\epsilon_\alpha)\cos(k_x) + \cos(k_y) - 2B_\alpha\cos(k_x)\cos(k_y) - (2 - 2B_\alpha - \mu_\alpha)]. \quad (17)$$

where the parameters $\{t_\alpha, \epsilon_\alpha, B_\alpha, \mu_\alpha\}$ are chosen so that the Fermi surface and bandwidth are close approximations to those observed experimentally[25] (see Fig. 1). In order to model YBCO we chose $\{100, 0.0, 0.45, 0.51\}$ for the planes and $\{-50, -0.9, 0.1.2\}$ for the chains. In both dispersions t_α, which sets the overall energy scale, is in units of meV. For the interactions, $V_{\mathbf{k},\mathbf{q},\alpha\beta}$, we chose the form of Millis *et al.*[2] (MMP form)

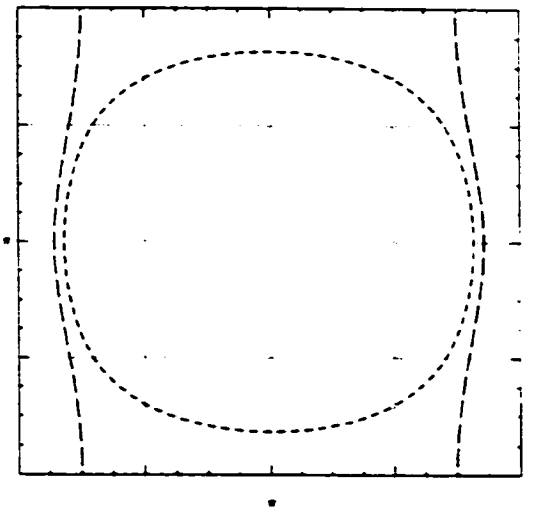

FIG. 1. Model of YBCO Fermi surfaces for chains (long dashed curve) and planes (closed short dashed curve) in the first Brillouin zone. The (π,π) point is at the center of the figure. For the chains the parameters $\{t_\alpha, \epsilon_\alpha, B_\alpha, \mu_\alpha\}$ in Eq. (17) are $\{-50, -0.9, 0, 1.2\}$ and for the planes they are $\{100, 0, 0.45, 0.51\}$.

$$V_{\mathbf{k},\mathbf{q},\alpha\beta} = g_{\alpha\beta}\frac{-\chi_0}{1 + \xi_0^2|\mathbf{k} - \mathbf{q} - \mathbf{Q}|^2}.$$

where χ_0 is a constant that sets the scale of the susceptibility, ξ_0 is the magnetic coherence length, $\mathbf{Q} = (\pi,\pi)$ is the commensurate nesting vector, and $g_{\alpha\beta}$ is the coupling to the conduction electrons, the size of which can be fixed to get a desired value of the critical temperature and can be considered to contain χ_0. The remaining parameter ξ_0, is given in Ref. 2 and will not be varied in this work. In this paper we set $g_{22} = 0$; i.e., there is no intrinsic pairing in the chains. This means that any superconductivity in the chains is induced by the interlayer interaction g_{12}, since we have set the hopping between layers to zero. The effect of an interlayer hopping has been extensively studied in works by Atkinson and Carbotte[13] as well as others.[14,15,17–19]

We solve the coupled BCS equations (6) using a FFT technique.[4] In Fig. 2 we plot the lowest three Fourier components (11) of the zero-temperature order parameter as a function of the interlayer interaction (higher Fourier components are all much smaller in magnitude) for two different intralayer interactions (upper and lower frames) in the planes (left frames) and chains (right frames). The values plotted in Fig. 2 are the amplitudes $\Delta_\alpha^{(s_0)}$, $\Delta_\alpha^{(s_2)}$, and $\Delta_\alpha^{(d)}$ given by Eq.

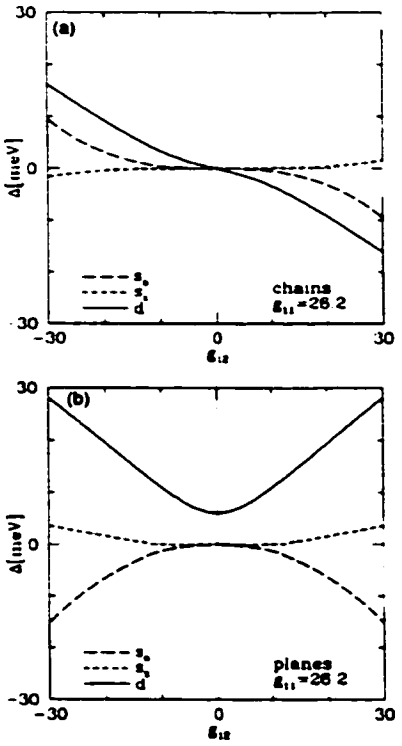

FIG. 2. Calculation of the zero-temperature order parameters as a function of the interlayer interaction g_{12} for two fixed values of the intralayer interaction g_{11} (upper and lower frames) presented for the planes (right frames) and chains (left frames) separately. In all frames the solid curve is the d-wave component of the order parameter, the short dashed curve is the extended s-wave component, and the long dashed curve is the isotropic s-wave component. In the upper frames $g_{11}=26.2$ and for $g_{12}=10$, $T_c=100$ K. At $g_{12}=0$ the order parameter is zero in the chains and is pure d wave in the planes. As the interlayer interaction is increased the order parameter becomes present in the chains and there is a mixing of s-wave components. In the lower frames $g_{11}=9.18$ and for $g_{12}=20$, $T_c=100$ K. At $g_{12}=0$ the order parameter is zero in both the chains and the planes. As the interlayer interaction is increased the order parameter becomes present in both the chains and planes and there is a mixing of s-wave components with the isotropic s-wave component eventually becoming dominant. The feature at $g_{12}\sim 25$ occurs when the gap node leaves the Brillouin zone. As discussed in the text there is a $g_{12}\leftrightarrow -g_{12}$ symmetry. Both g_{11} and g_{12} are in units of t_1; g_{22}, the coupling in the chains, is set equal to zero.

(11) with $\alpha=1$ for the plane layers (right frames) and $\alpha=2$ for the chain layers (left frames). For the orthorhombic system studied here all three of these harmonics belong to the same irreducible representation of the crystal point group except for $g_{12}=0$ when the tetragonal CuO_2 layer is decoupled from the orthorhombic CuO layer. Recent CITS measurements[26] show that the gap has a magnitude of ~ 20 meV in the chains and ~ 30 meV in the planes which would indicate that g_{12} is large.

For the first choice of intralayer interaction (upper frames), $g_{11}=26.2$, and there is no order parameter in the chains when there is no interlayer interaction (i.e., $g_{12}=0$) and the order parameter in the planes is pure d wave. As the interlayer interaction is increased from zero, s-wave components appear in the planes and all three components appear in the chains. This "$s+d$ mixing" is caused by the breaking of the tetragonal symmetry upon the introduction of the chains; there is no relative phase between the s- and d-wave components within either the planes or chains but there can be a relative phase between the order parameter in the planes and chains. In the range of g_{12} explored here the d-wave component in the plane remains dominant but for sufficiently strong interlayer interaction the isotropic s-wave component eventually dominates[27] (i.e., the gap nodes disappear). For interaction parameters $\{g_{11},g_{12},g_{22}\}=\{26.2,10,0\}$ the critical temperature is 100 K and the maximum value of the gap in the Brillouin zone is 27.5 meV in the planes and 8.0 meV in the chains, while the maximum values on the Fermi surfaces are approximately 22 and 7 meV, respectively. The ratio $2\Delta_{max}/T_c$ is 6.4 in the planes and 1.9 in the chains.

For the second choice of intralayer interaction (lower frames), $g_{11}=9.18$, there is no order parameter in either the chains or the planes when there is no interlayer interaction (i.e., $g_{12}=0$). As the interlayer interaction is increased d-wave and then s-wave components of the order parameter appear in both the planes and chains. Again, there is no relative phase between the s- and d-wave components within either the planes or chains but there can be a relative phase between the order parameter in the planes and chains. In the range of g_{12} explored here, the d-wave component is dominant. At approximately $g_{12}=15$ the gap nodes no longer cross the Fermi surface in the chains; the feature at $g_{12}\sim 25$ coincides with the gap nodes leaving the Brillouin zone and the isotropic s wave becoming dominant. For interaction parameters $\{g_{11},g_{12},g_{22}\}=\{9.18,20,0\}$ the critical temperature is again 100 K and the maximum value of the gap in the Brillouin zone is now 32.8 meV in the planes and 20.1 meV in the chains, while the maximum values on the Fermi surfaces are approximately 27 and 17 meV, respectively. The ratio $2\Delta_{max}/T_c$ is 7.6 in the planes and 4.7 in the chains.

Note that for $g_{12}>0$ all of the s-wave components of the order parameters in both the planes and chains have the same relative sign and the d-wave components have opposite signs, while for $g_{12}<0$ all of the relative signs are reversed but that the magnitudes of the components are insensitive to the sign of g_{12} as noted after Eq. (6).

In Fig. 3 we plot the density of states (DOS) for the planes (left frames) and chains (right frames) calculated using the lowest three harmonics (11) of the solution to the BCS equations (6) with two sets of interaction parameters. The dotted curves are the normal state DOS (NSDOS) and the solid curves are the superconducting DOS (SCDOS). The insets show the Fermi surface (dashed curves) and gap nodes (solid curves) in the first Brillouin zone [with (π,π) at the center]. The peak in the NSDOS (dotted curves) is the van Hove singularity located at $2t_\alpha(2-\mu_\alpha-4B_\alpha\pm\epsilon_\alpha)$ which is at -62 meV in the plane layers (left frames) and at 10 and -170 meV in the chain layers (right frames). They are caused by the saddle points in the electron dispersions,

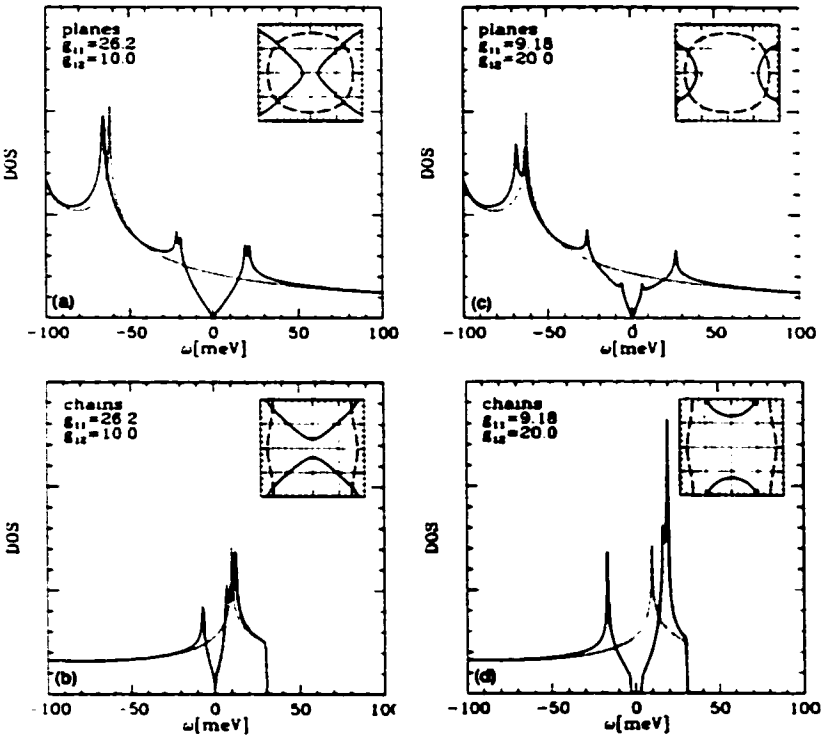

FIG. 3. Calculation of the superconducting (solid curves) and normal (dotted curves) density of states (DOS) for two sets of interaction parameters $g_{\alpha\beta}$ (upper and lower frames) presented separately for the planes (left frames) and chains (right frames). Some experiments are surface probes and may probe either the planes or chains independently. The insets show the Fermi surface (dashed curve) and gap nodes (solid curve) in the planes and chains for the two different parameter choices in the first Brillouin zone with (π,π) at the center. In the upper frames, (a) and (b), we have chosen $\{g_{11},g_{12},g_{22}\}=\{26.2,10.0\}$ which gives $T_c=100$ K. In the lower frames, (c) and (d), we have chosen $\{g_{11},g_{12},g_{22}\}=\{9.18,20.0\}$ which also gives $T_c=100$ K. Note that for the second parameter choice the gap nodes do not cross the Fermi surface in the chains [frame (d), inset] and that the DOS is gapped. The c-axis Josephson resistance-tunneling current product for a YBCO-Pb junction for a pure d-wave order parameter is zero due to the equal parts of the order parameter with opposite signs. Here this is not the case (insets) and the c-axis Josephson resistance-tunneling currents product for a YBCO-Pb junction are (a) ± 0.18 meV, (b) 2.35 meV, (c) ± 0.25 meV, and (d) 2.17 meV. The relative sign is due to the relative sign of the s-wave components of the order parameter (i.e., the only part which contributes).

$\varepsilon_{k,\sigma}$, at $(0,\pm\pi)$ and $(\pm\pi,0)$. These van Hove singularities are shifted by the presence of the superconducting order parameter (solid curves) by an amount that depends upon the value of the order parameter at the saddle points;[28] in frame (c) these values are very different and the van Hove singularity is split, and in frame (a) these values are almost the same and no splitting is evident.

An interesting feature is that the low-energy behavior ($\omega\sim 0$) of the SCDOS is governed by the *smallest* local *maxima* of the gap on the Fermi surface when the gap nodes cross the Fermi surface and by the *minima* of the gap on the Fermi surface when there are no gap nodes which cross the Fermi surface. In Fig. 4 the magnitude of the gap along the Fermi surface is plotted. In Figs. 4(a)–4(c) one can see that there are two different local maxima of the gap on the Fermi surface and these maxima are (to first order[28]) manifested as twin peaks in the SCDOS [Figs. 3(a)–3(c)]; these peaks are distinct from the van Hove singularities which are also present in the normal DOS (dotted curves in Fig. 3) and which are slightly shifted in the superconducting state.[28] In frame (a) of Fig. 4 the local maxima of the gap on the Fermi surface are 16 and 18 meV, in (b) they are 1 and 7 meV, and in (c) they are 25 and 3 meV. In (d) one can see that there are no gap nodes which cross the Fermi surface; the maximum and minimum values of the gap on the Fermi surface are 17 and 4 meV, respectively. In Fig. 3(d) the finite gap in the SCDOS corresponds to the minimum of the gap on the Fermi surface and the peak to the maximum.

The Josephson junction resistance-tunneling current product $RJ(T=0)$ for a c-axis YBCO-Pb junction, given by Eq. (16) with Δ_k^L and ε_k^L appropriate for Pb,[11] is ± 0.25 and ± 2.2 meV for the planes and 2.2 meV and 3.4 meV for the chains for the two choices of $g_{\alpha\beta}$ made, in agreement with earlier calculations.[11] The relative sign is due to the relative sign of the s-wave components (i.e., the only part which contributes) of the order parameters. The actual c-axis Jo-

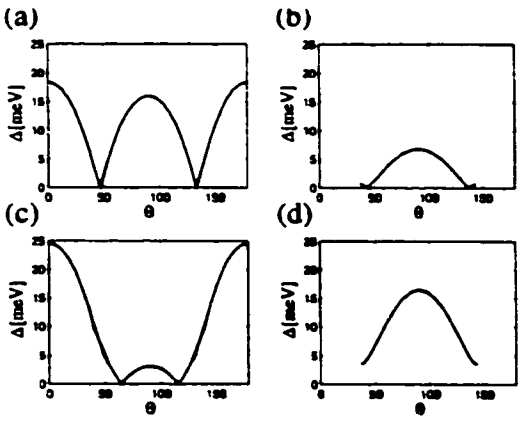

FIG. 4. The magnitude of the gap on the Fermi surface as a function of angle for the four cases of Figs. 2 and 3. The angle θ is measured from the center or (π,π) point of the Brillouin zone with the y axis (i.e., the vertical in the insets of Fig. 3) corresponding to $\theta=0$. Frames (b) and (d) do not span all angles due to the Fermi surface not being closed in the chain layer. For the first choice of interaction parameters, $\{g_{11},g_{12},g_{22}\}=\{26.2,10.0\}$, the ratio $2\Delta_{max(FS)}/T_c$, where $\Delta_{max(FS)}$ is the maximum value of the gap on the Fermi surface, is 4.3 and 1.6 for the planes and chain, respectively; for the second, $\{g_{11},g_{12},g_{22}\}=\{9.18,20.0\}$, they are 5.7 and 3.8.

sephson junction resistance-tunneling current product $RJ(T)$ for a junction made with untwinned YBCO would be some weighted average of the plane and chain c-axis tunneling currents depending upon the relative abundance of chains and planes in the top layer of the YBCO. For a twinned sample with both twins equally abundant there would be zero net tunneling current, although there is evidence that for single crystals of YBCO there can be up to a 5:1 ratio in the relative abundance of the two twin orientations.[29] We note that due to the different magnitudes of the order parameters in the two layers the model presented here is consistent with the observed π shifts in corner junctions[30–33] for both attractive and repulsive interlayer interactions g_{12}.

In Fig. 5 we have plotted the magnetic penetration depth (left frames) and the Knight shift (right frames) calculated with the lowest three harmonics (11) of the solutions of the BCS equations (6) for the two choices of interaction parameters. In the penetration depth frames (left) the solid curve is for the x direction (along the chains) and the dashed curve is for the y direction (perpendicular to the chains). The dotted curve is $1-(T/T_c)^2$ and is plotted for comparison. The ratio $\lambda_{yy}/\lambda_{xx}$ at zero temperature is 1.37 for both interaction parameter choices since the zero-temperature penetration depth is a normal state property [i.e., the second term in Eq. (12) does not contribute at zero temperature]. The zero-temperature penetration depth is largely governed by the bandwidth [i.e., $4t_a(2-\epsilon_a)$] — the larger the bandwidth, the larger the zero-temperature penetration depth.

As pointed out above, the curvature of the penetration depth curve, $\lambda_{ii}^{-2}(T)$, is largely governed by the ratio $2\Delta_{max}/T_c$ and is a straight line for the d-wave BCS value of 4.4. The presence of the chain layer and the interlayer interaction increases this ratio in the plane layer but it remains low in the chain layer due to the absence of an interaction in this layer. It is this lower value that makes $\lambda_{yy}^{-2}(T)$ (along the chains) have upward curvature (solid curves).

One can see [Figs. 5(a) and 5(c)] that the in-plane penetration depth perpendicular to the chains (dashed curve) closely resembles that observed experimentally in high quality crystals,[1,22] and is largely determined by the presence of gap nodes crossing the Fermi surface, which cause the low-temperature linear behavior, and the ratio $2\Delta_{max}/T_c$ which, for values above ~ 4.4, make the curve of $\lambda_{ii}^{-2}(T)$ have downward curvature. The penetration depth along the chains (solid curves), however, has an overall upward curvature due to the low values of $2\Delta_{max}/T_c$ in the chains. It is the component of the penetration depth due to the chains that makes the overall $\lambda_{yy}^{-2}(T)$ have downward curvature. The component of the penetration depth due to the chains perpendicular to the chains does not contribute significantly to the overall penetration depth in this direction, λ_{yy}^{-2} is due almost entirely to the CuO_2 layers. For a single plane model[20] we would have $\{g_{11},g_{12},g_{22}\}=\{30,0,0\}$, $2\Delta_{max}/T_c$ would be 4.5, and the penetration depth would closely resemble the straight line $1-(T/T_c)$.[20]

The Knight shift [Figs. 5(b) and 5(d)], which is calculated independently for the planes (solid curves) and chains (dashed curves), has a low-temperature power law behavior when the gap nodes cross the Fermi surface (planes, both figures and chains in the upper figure) and an exponential behavior when the gap is finite over all the Fermi surface (chains, lower figure). When these quantities are measured[4] the distinction between a power law and exponential behavior rests upon the choice zero and so is not a reliable indicator of the presence of gap nodes on the Fermi surface.

IV. CONCLUSION AND DISCUSSION

We have derived a general expression for the Hamiltonian in a multilayer system and then made a simplification and have explicitly diagonalized the Hamiltonian. A set of two coupled BCS equations is then derived for this simplified system which is subsequently solved numerically by a FFT technique. This technique, unlike others,[18,16] makes no assumptions about the functional form (and hence the symmetry) of the order parameter in either layer or any relationship between the order parameters in the different layers.

Using the three lowest harmonics (11) of the solutions found for the coupled BCS equations (6) the magnetic penetration depth (12), normal and superconducting density of states (14) and (15), Knight shift (13), and c-axis Josephson resistance-tunneling current products (16) were calculated.

Our choice of electron dispersion relations was made so as to approximate the YBCO system in which there are layers consisting of CuO_2 planes as well as layers which contain CuO chains. Our choice of interactions was made so that there is a pairing interaction in the CuO_2 layer as well as an interlayer interaction, but no pairing interaction in the CuO layer.

The solution of the BCS equations is predominately of a d-wave character, but because the tetragonal symmetry is broken by the presence of the chains, there is some mixture

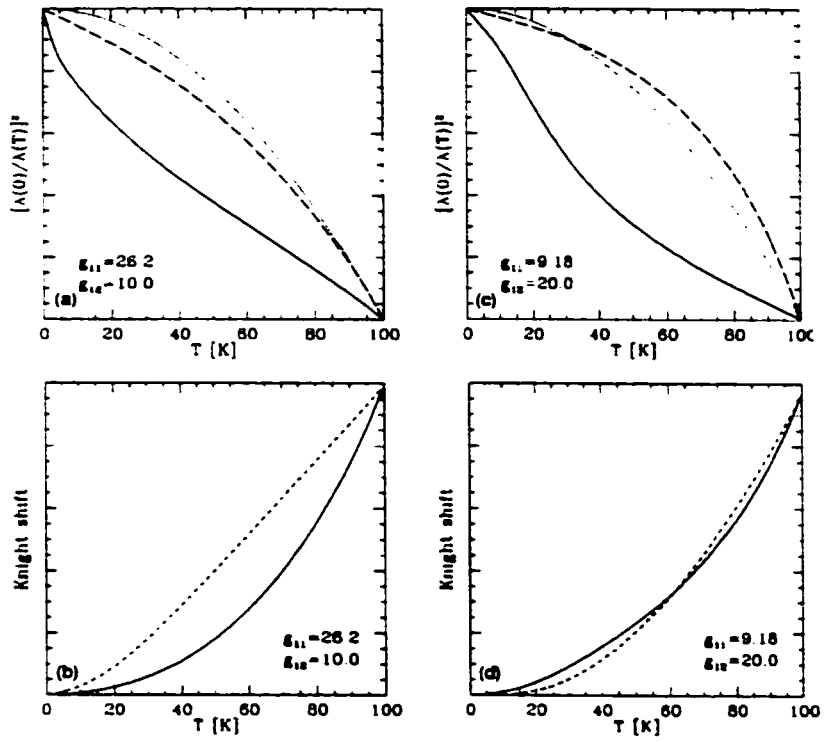

FIG. 5. Calculations of the magnetic penetration depth (left frames) and the Knight shift (right frames) for the two sets of interaction parameters. Frames (a) and (c) show the magnetic penetration depth along (solid curve) and perpendicular (dashed curve) to the CuO chains. The dotted curve is $1-(T/T_c)^2$ and is shown for comparison. The chains, due to their Fermi surface, do not contribute appreciably to the penetration depth perpendicular to the chains (dashed curves). The ratio $(\lambda_{yy}/\lambda_{xx})^2$ is 1.37 for both sets of parameters since this is a normal state property. Frames (b) and (d) show the Knight shift in the planes (solid curves) and chains (dashed curves); due to the crossing of the gap nodes and the Fermi surface in the chains in (b), the Knight shift in the chain is a power law at low temperature, while due to the finite gap in (d), the Knight shift in the chain is exponential at low temperature.

of s-wave order parameter with no relative phase between the components, although the relative sign of the order parameter in the planes and chains may be ± 1. Further, we find that due to a symmetry in the set of coupled BCS equations derived, the sign of the interlayer interaction affects only the relative sign of the order parameter in the two layers and not their absolute magnitudes (although some properties could be affected by this relative sign). We also find that any interlayer interaction strongly enhances the zero-temperature order parameter and, hence, the critical temperature. This is consistent with the observation that T_c is higher in materials with multiple adjacent CuO_2 layers.

Furthermore, we find that the presence of gap nodes in only one of the layers is enough to produce a low-temperature linear behavior for the penetration depth, although if the minimum gap in the chains is too large, the $\lambda_{xx}^{-2}(T)$ and $\lambda_{yy}^{-2}(T)$ curves can cross. Our calculation of the magnetic penetration depth gives a form that is similar to that measured experimentally perpendicular to the chains, but not along the chains due to the small value of $2\Delta_{max}/T_c$ in the chains. This leads us to speculate that there may be intrinsic pairing in the CuO chains of the same order as in the CuO_2 planes since the $2\Delta_{max}/T_c$ ratios must both be large (6 – 7) for the low-temperature slope of the $\lambda_{ii}^{-2}(T)$ curves to be approximately equal as is observed in experiments.[1,22] This would tend to support the simple single-band orthorhombic model previously proposed by us.[1,20]

Our calculation of the superconducting density of states indicates that a surface probe may measure very different results depending upon whether the top layer is CuO chains or CuO_2 planes. Depending upon the interlayer pairing strength the CuO chain layer may have a very narrow "d-wave"-type gap or a finite "isotropic s-wave"-type gap.

Our calculation of the c-axis Josephson resistance-tunneling current products $RJ(T=0)$ for a YBCO-Pb junction for several choices of $g_{\alpha\beta}$ ranges from 0.18 to 0.50 meV for the planes and from 2.35 to 3.06 meV for the chains, with possibly a relative sign between the chain and plane layers due to the relative sign of the s-wave components of the order parameters. The actual c-axis Josephson resistance-tunneling current product for a junction made with untwinned YBCO would be some weighted average of the plane and chain results depending upon the relative abundance of chains and planes in the top layer of the YBCO. For a twinned sample with both twins equally abundant there would be zero net tunneling current although there is evidence that for single crystals of YBCO there can be up to a 5:1 ratio in the relative abundance of the two twin orientations.[29]

ACKNOWLEDGMENTS

This research was supported in part by the Natural Sciences and Engineering Research Council of Canada (NSERC) and by the Canadian Institute for Advanced Research (CIAR). We would like to thank W. A. Atkinson and A. M. Westgate for discussions and insights.

*Electronic address: odonovan@mcmaster.ca

[1] D.N. Basov, R. Liang, D.A. Bonn, W.N. Hardy, B. Dabrowski, M. Quijada, D.B. Tanner, J.P. Rice, D.M. Ginsberg, and T. Timusk, Phys. Rev. Lett. 74, 598 (1995).
[2] A.J. Millis, H. Monien, and D. Pines, Phys. Rev. B 42, 167 (1990).
[3] H. Chi and J.P. Carbotte, Physica C 169, 55 (1990).
[4] C. O'Donovan and J.P. Carbotte, Physica C 252, 87 (1995).
[5] D.A. Bonn, P. Dosanjh, R. Liang, and W.N. Hardy, Phys. Rev. Lett. 68, 2390 (1992).
[6] W.N. Hardy *et al.*, Phys. Rev. Lett. 70, 3999 (1993).
[7] D.A. Bonn, S. Kamal, K. Zhang, R. Liang, D.J. Baar, E. Klein, and W.N. Hardy, Phys. Rev. B 50, 4051 (1994).
[8] N. Bulut and D.J. Scalapino, Phys. Rev. B 45, 2371 (1992).
[9] H. Ding *et al.*, Phys. Rev. Lett. 50, 1333 (1994).
[10] H.L. Edwards, J.T. Markert, and A.L. de Lozanne, Phys. Rev. Lett. 69, 2967 (1992).
[11] C. O'Donovan, D. Branch, J.P. Carbotte, and J. Preston, Phys. Rev. B 51, 6588 (1995).
[12] A.G. Sun *et al.*, Phys. Rev. Lett. 72, 2267 (1994).
[13] W.A. Atkinson and J.P. Carbotte, Phys. Rev. B 52, 10 601 (1995).
[14] R.A. Klemm and S.H. Liu, Physica C 191, 383 (1992).
[15] S.H. Liu and R.A. Klemm, Phys. Rev. B 45, 415 (1992).
[16] R. Combescot and X. Leyronas, Phys. Rev. Lett. 75, 3732 (1995).
[17] S. Kettemann and K.B. Efetov, Phys. Rev. B 46, 8515 (1992).
[18] T. Xiang and J.M. Wheatley, Phys. Rev. Lett. 76, 134 (1996).
[19] D.Z. Liu, K. Levin, and J. Maly, Phys. Rev. B 51, 8680 (1995).
[20] C. O'Donovan and J.P. Carbotte, Phys. Rev. B 52, 4568 (1995).
[21] I. Maggio-Aprile, Ch. Renner, A. Erb, E. Walker, and O. Fischer, Phys. Rev. Lett. 75, 2754 (1995).
[22] T. Jacobs, S. Sridhar, Qiang Li, G.D. Gu, and N. Koshizuka, Phys. Rev. Lett. 75, 4516 (1995).
[23] V.Z. Kresin, H. Morawitz, and S.A. Wolf, *Mechanisms of Conventional and High T_c Superconductivity* (Oxford University Press, New York, 1993).
[24] V. Ambegaokar and A. Baratoff, Phys. Rev. Lett. 10, 486 (1963); 11, 104 (1964).
[25] K. Gofron, J.C. Campuzano, A.A. Abrikosov, M. Lindroos, A. Bansil, H. Ding, D. Koelling, and B. Dabrowski, Phys. Rev. Lett. 73, 3302 (1994).
[26] H.L. Edwards, D.J. Derro, A.L. Barr, J.T. Markert, and A.L. de Lozanne, Phys. Rev. Lett. 75, 1387 (1992).
[27] A.I. Liechtenstein, I.I. Mazin, and O.K. Andersen, Phys. Rev. Lett. 74, 2303 (1995).
[28] C. Zhou and H.J. Schulz, Phys. Rev. B 45, 7397 (1992).
[29] B. Gaulin (private communication).
[30] D.A. Wollman, D.J. Van Harlingen, W.C. Lee, D.M. Ginsberg, and A.J. Leggett, Phys. Rev. Lett. 71, 2134 (1993).
[31] D.A. Brawner and H.R. Ott, Phys. Rev. B 50, 6530 (1994).
[32] C.C. Tsuei *et al.*, Phys. Rev. Lett. 73, 593 (1994).
[33] A. Mathai, Y. Gim, R.C. Black, A. Amar, and F.C. Wellstood, Phys. Rev. Lett. 74, 4523 (1995).

6.5.2 Triplanar Model for the Gap and Penetration Depth in $YBa_2Cu_3O_7$

In this paper, Ref. [111], the order parameter and penetration depths for several choices of interactions are calculated. A triplanar model similar to what is actually present in YBCO was used in the hope that this would capture the anisotropy that is present in the penetration depth measurements. By using dispersion relations appropriate for the three layers of YBCO the zero temperature penetration depth in the x- and y-directions was accurately modeled and, for some interaction parameters, the temperature dependence of the penetration depth was much closer to the experimental results than was the case in the two plane model.

PHYSICAL REVIEW B VOLUME 55, NUMBER 13 1 APRIL 1997-I

Triplanar model for the gap and penetration depth in $YBa_2Cu_3O_7$

C. O'Donovan* and J. P. Carbotte
Department of Physics & Astronomy, McMaster University, Hamilton, Ontario, Canada L8S 4M1
(Received 11 October 1996)

$YBaCuO_7$ is a trilayer material with a unit cell consisting of a CuO_2 bilayer with a CuO plane of chains in between. Starting with a model of isolated planes coupled through a transverse matrix element, we consider the possibility of intra- as well as interplane pairing within a nearly antiferromagnetic Fermi-liquid model. Solutions of a set of three coupled BCS equations for the gap exhibit orthorhombic symmetry with s- as well as d-wave contributions. The temperature dependence and a-b in-plane anisotropy of the resulting penetration depth is discussed and compared with experiment. [S0163-1829(97)06110-9]

I. INTRODUCTION

Within the unit cell of $YBa_2Cu_3O_7$, (YBCO), there are two CuO_2 planes and a single set of CuO chains oriented along the b axis. The chains break the tetragonal symmetry of the system and make it orthorhombic. The role of the chains is not yet fully understood but it is clear that they lead to a large in-plane anisotropy in various properties such as the value of the zero temperature penetration depth and the dc conductivity, etc.[1-7] For example, in optimally doped $YBa_2Cu_3O_{6.95}$, the penetration depth along the a axis at $T=0$ is $\lambda_a(0)\sim 1600$ Å while that along the b axis is $\lambda_b(0)\sim 1030$ Å.[2] At 300 K the ratio of the dc resistivities ρ_b/ρ_a is larger than a factor of 2. These large anisotropies would not exist in a purely tetragonal system. The role of the chains in YBCO has been investigated before using a two-plane model[8] as well as a plane-chain model.[9,10] While these calculations have given us considerable insight, such a model is not fully realistic. Here we want to explicitly introduce the trilayer nature of the system. We start with a pair of isolated CuO_2 planes and a set of chains (CuO plane). They are assumed to be coupled through a transverse matrix element, t_1, between the chain and each of the planes and t_2 between the two planes. A set of three coupled BCS equations are used to describe the pairing with intra- as well as interband coupling. For the pairing potential, we use the form of the magnetic susceptibility introduced in the phenomenological nearly antiferromagnetic Fermi-liquid model of Millis, Monien, and Pines[11] (MMP) which we multiply by a dimensionless parameter $g_{\alpha\beta}$ which allows us to vary at will the strength of the diagonal (in-plane) and off-diagonal (interplane) couplings. Here the indices $\alpha\beta$ range over the three subbands. Numerical solutions of these equations using a fast-Fourier-transform technique give solutions which are an admixture of d, s_0, and s symmetry. For the tetragonal crystal-point group, these three symmetries would belong to two different irreducible representations and would, in general, not mix. But because of the existence of the chains, the system possesses reduced symmetry although, in most cases considered, nodes remain on the Fermi surface and the linear low-temperature variation of the penetration depth remains. In Sec. II, we give the formalism. Solutions of the gap equations are discussed in Sec. III along with results for the penetration depth. A brief conclusion is included in Sec. IV.

II. FORMALISM

Consider a three-plane per unit-cell system with energies $\varepsilon_{\mathbf{k},\alpha}$. Here $\alpha=1,2,3$ is an index that enumerates the three planes; two CuO_2 which are identical to each other and one CuO plane consisting of chains oriented along the b direction. The momentum index $\mathbf{k}$ is restricted to the two-dimensional CuO_2 Brillouin zone which has tetragonal symmetry. A tight-binding model will be used to describe these isolated planes of the form:[12-14]

$$\varepsilon_{\mathbf{k},\alpha}=-2t_\alpha[(1+\epsilon_\alpha)\cos(k_x)+(1-\epsilon_\alpha)\cos(k_y) -2B_\alpha\cos(k_x)\cos(k_y)-(2-2B_\alpha-\mu_\alpha)]. \quad (1)$$

where t_α is the first-neighbor hopping parameter, ϵ_α an orthorhombic distortion which can be used to describe the chains, B_α is the second-neighbor hopping in units of t_α, the k_i are in units of reciprocal-lattice vectors, and μ_α is related to the chemical potential and determines the filling. Here it will be treated as a parameter. In what follows, the t_α's will be taken to be the same for simplicity and denoted by t_0. The three-dimensional nature of the system is introduced through transverse matrix elements, t_1, between the CuO_2 planes and the CuO chains and t_2 directly between the CuO_2 bilayer. This changes the energies $\varepsilon_{\mathbf{k},\alpha}$ to band energies $\bar{\varepsilon}_{\mathbf{k},\alpha}$ which we then use in the BCS gap equations assuming singlet pairing between equal and opposite momentum pairs. Including intraband (on diagonal) as well as interband (off diagonal) pairing through the two-body potential $V_{\mathbf{k},\mathbf{k}',\alpha\beta}$, which describes scattering from $\mathbf{k}$ to $\mathbf{k}'$ with α and β band indices, the gap in the αth band $\Delta_{\mathbf{k},\alpha}$ satisfies the BCS equations:[10]

$$\Delta_{\mathbf{k},\alpha}=\frac{1}{\Omega}\sum_{\mathbf{k}',\beta}V_{\mathbf{k},\mathbf{k}',\alpha\beta}\frac{\Delta_{\mathbf{k}',\alpha}}{2E_{\mathbf{k}',\alpha}}\tanh\left(\frac{E_{\mathbf{k}',\alpha}}{2k_BT}\right). \quad (2)$$

In Eq. (2), Ω is the crystal volume, k_B is Boltzmann's constant, T is temperature, and

$$E_{\mathbf{k},\alpha}=\sqrt{\bar{\varepsilon}^2_{\mathbf{k},\alpha}+\Delta^2_{\mathbf{k},\alpha}} \quad (3)$$

0163-1829/97/55(13)/8520(9)/$10.00

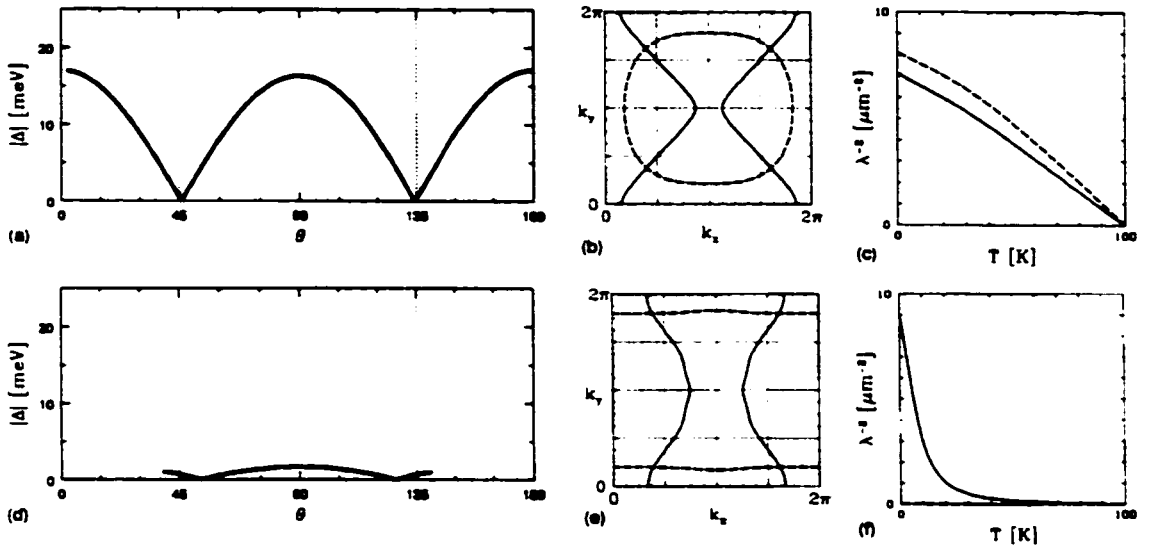

FIG. 1. (a) and (d) are the absolute value of gap as a function of angle θ measured clockwise from the k_x axis along the Fermi surface for the CuO_2 plane and CuO chains, respectively. (b) and (e) are Fermi-surface contours (dashed line) and gap zeros (solid line), while (c) and (f) are the contributions to the inverse square of the penetration depth $\lambda^{-2}(T)$ as a function of temperature along a (dashed curve) and b direction (solid curve). Note that the chains (d), (e), and (f) contribute almost exclusively to the b direction. The same pairing was included in chains and plane [Eq. 13)] yet note the very small energy scale for the gap in the chains (d) as compared to the gap in the plane (a). This is due to the quasi-one-dimensional nature of the chain Fermi surface. Note also that the low-energy scale in the chains leads to the sharp drop in penetration depth in b direction with increasing temperature seen in (f).

are the quasiparticle energies of the αth band in the superconducting state. The single-particle normal-state band energies for a two layer model come from the Hamiltonian:

$$H=\begin{bmatrix} \varepsilon_1 & t_1 \\ t_1 & \varepsilon_2 \end{bmatrix} \tag{4}$$

with eigenvalues

$$\bar{\varepsilon}_{1,2}=\left(\frac{\varepsilon_1+\varepsilon_2}{2}\right)\pm\sqrt{\left(\frac{\varepsilon_1-\varepsilon_2}{2}\right)^2+t_1^2}. \tag{5}$$

and for the three-layer model come from the Hamiltonian

$$H=\begin{bmatrix} \varepsilon_1 & t_1 & t_2 \\ t_1 & \varepsilon_2 & t_1 \\ t_2 & t_1 & \varepsilon_1 \end{bmatrix} \tag{6}$$

with eigenvalues

$$\bar{\varepsilon}_1=\varepsilon_1-t_2$$

$$\bar{\varepsilon}_2=\frac{\varepsilon_1+\varepsilon_2+t_2}{2}+\frac{1}{2}\sqrt{(\varepsilon_1-\varepsilon_2)^2+t_2(2\varepsilon_1-2\varepsilon_2+t_2)+8t_1^2}$$

and

$$\bar{\varepsilon}_3=\frac{\varepsilon_1+\varepsilon_2+t_2}{2}-\frac{1}{2}\sqrt{(\varepsilon_1-\varepsilon_2)^2+t_2(2\varepsilon_1-2\varepsilon_2+t_2)+8t_1^2}$$

which are, respectively, the solid, dashed, and dotted curves in Fig. 5.

The set of three coupled equations (2) for the gap's $\Delta_{\mathbf{k},\alpha}$ in the αth band ($\alpha=1,2,3$) are explicit once the pairing potentials $V_{\mathbf{k},\mathbf{k}',\alpha\beta}$ are specified. Different models could be used. Here for simplicity and to be specific, we will assume that the superconducting condensation proceeds through the spin susceptibility $\chi_{\mathbf{k},\mathbf{k}'}$ which for the nearly antiferromagnetic Fermi liquid is peaked at the commensurate wave vector (π,π) at the corner of the Brillouin zone. So as not to introduce new parameters, here we will use the form of $\chi_{\mathbf{k},\mathbf{k}'}$ introduced through a fit to NMR data by Millis, Monien, and Pines (MMP).[11] Their susceptibility and consequent pairing potential has the form:

$$V_{\mathbf{k},\mathbf{k}',\alpha\beta}=g_{\alpha\beta}\frac{-t_0}{1+\xi_0^2|\mathbf{k}-\mathbf{k}'-\mathbf{Q}|^2}. \tag{7}$$

where the scale on $V_{\mathbf{k},\mathbf{k}',\alpha\beta}$ has been set by t_0 for convenience and $g_{\alpha\beta}$ are dimensionless parameters that determine the overall size of the pairing as well as the relative amount of diagonal ($\alpha=\beta$) and off-diagonal ($\alpha\neq\beta$) coupling desired. In all our calculations, the relative sizes of the $g_{\alpha\beta}$ will be chosen at will with absolute value adjusted to get a critical temperature of 100 K typical for the oxide superconductors. The other parameters in Eq. (7) are also specified and fixed at values given by MMP. $\xi_0=2.5$ Å is the magnetic coherence length and Q is the commensurate wave vector (π,π) in the two-dimensional CuO_2 Brillouin zone.

In writing down the set of equations (2), we have assumed that the coherence length transverse to the planes is short so that the gap can have different values in the different bands $\bar{\varepsilon}_{\mathbf{k},\alpha}$. The model still allows for a single gap, applicable to

all three planes, to exist. The appropriate limit is $g_{\alpha\beta}$ independent of α and β in which case $\Delta_{\mathbf{k},\alpha}$ on the left-hand side of Eq. (2) is clearly independent of α and a single gap parameter describes the entire system.

Numerical solution of the set of equations (2) using fast-Fourier transforms makes no assumption on the symmetry of the resulting gap parameters $\Delta_{\mathbf{k},\alpha}$ as a function of momentum $\mathbf{k}$ in the two-dimensional Brillouin zone. In our work, we find that these solutions consist of a mixture of $d_{x^2-y^2}$, s_0, and $s_{x^2+y^2}$ symmetries with higher harmonics as well as the more familiar lowest ones which are

$$s_0 \sim \eta_{\mathbf{k}}^{(s_0)} = 1, \tag{8a}$$

$$s_{x^2+y^2} \sim \eta_{\mathbf{k}}^{(s_x)} = \cos(k_x) + \cos(k_y), \tag{8b}$$

$$d_{x^2-y^2} \sim \eta_{\mathbf{k}}^{(d)} = \cos(k_x) - \cos(k_y). \tag{8c}$$

We are now ready to present results including the temperature dependence of the penetration depth $\lambda(T)$ for various model parameters. To obtain the penetration depths, we have adopted the following approximate procedure. The lowest harmonics represented by Eqs. (8a) to (8c) are projected out of our numerical solutions and these are used in all further calculations. This neglects higher harmonic contributions but is an adequate procedure since we are mainly interested in qualitative results and trends. In any case, our model for the pairing interaction (7) is simplified and is not believed to be accurate. We use a BCS approach while it is necessary to go to an Eliashberg formulation to get quantitative results. This goes beyond the scope of this work.

For completeness, the approximate formula for the penetration depth employed here is

$$\lambda_{ij}^{-2} = \frac{4\pi e^2}{c^2} \frac{1}{\Omega} \sum_{\mathbf{k},\alpha} v_{\alpha,i} v_{\alpha,j} \left(\frac{\partial f(\tilde{\varepsilon}_{\mathbf{k},\alpha})}{\partial \tilde{\varepsilon}_{\mathbf{k},\alpha}} - \frac{\partial f(E_{\mathbf{k},\alpha})}{\partial E_{\mathbf{k},\alpha}} \right), \tag{9}$$

where the constant c is the speed of light, $v_{\alpha,i}$ is the ith component of the electron velocity in the αth band

$$v_{\alpha,i} = \frac{1}{\hbar} \frac{\partial \tilde{\varepsilon}_{\mathbf{k},\alpha}}{\partial k_i}, \tag{10}$$

and $f(x)$ is the Fermi-Dirac distribution given by

$$f(x) = (e^{\tilde{\varepsilon}_{\mathbf{k},\alpha}/k_B T} + 1)^{-1}. \tag{11}$$

We are now in a position to present results.

III. RESULTS

Before presenting results for the trilayer model, it is instructive to consider a bilayer consisting of a CuO_2 plane with tetragonal symmetry and a set of CuO chains directed along the b axis which has lower orthorhombic symmetry. This difference in symmetry has a drastic effect on the solution of the BCS gap equation. To illustrate this, we take a model band structure

$$\{t_0, \epsilon_\alpha, B_\alpha, \mu_\alpha\} = \begin{Bmatrix} 50.0 & 0.0 & 0.45 & 0.51 \\ 50.0 & 1.0 & 0.00 & 1.2 \end{Bmatrix} \tag{12}$$

with t_0 in meV and the other parameters are dimensionless. We also consider the pairing potential to be of the MMP type and of equal magnitude in both chains and plane. So as to have a single critical temperature, we also include a smaller off-diagonal pairing $g_{\alpha\beta} \neq 0$ for $\alpha \neq \beta$. Specifically, we take

$$g_{\alpha\beta} = \begin{bmatrix} 38.75 & 1.0 \\ 1.0 & 38.75 \end{bmatrix}. \tag{13}$$

Solutions of the BCS equations using fast-Fourier transforms give an admixture of s_0, $s_{x^2+y^2}$, and $d_{x^2-y^2}$ which all belong to the same irreducible representation for an orthorhombic system. The gap amplitudes are

$$\Delta_{\mathbf{k},\alpha} = \begin{bmatrix} -0.196 & -0.467 & 9.482 \\ -0.644 & -0.182 & 1.482 \end{bmatrix} \begin{bmatrix} \eta_{\mathbf{k}}^{(s_0)} \\ \eta_{\mathbf{k}}^{(s_x)} \\ \eta_{\mathbf{k}}^{(d)} \end{bmatrix}, \tag{14}$$

with the $\eta_{\mathbf{k}}^{(\cdot)}$ as given in Eqs. (8a)–(8c). We note that in the CuO_2 plane, the $d_{x^2-y^2}$ component is dominant with a small admixture of s_0 and $s_{x^2+y^2}$ having the opposite sign (out of phase by π). Although the same MMP interaction as used in the CuO_2 planes has been assumed to also apply on the CuO chains, the very different symmetry of the quasi-one-dimensional Fermi surface has led to a gap on the chains which is smaller by an order of magnitude. The $d_{x^2-y^2}$ component has the same phase as it has in the planes but it is now not much larger than its s_0 and $s_{x^2+y^2}$ parts. In Fig. 1(b) (middle upper frame) and (e) (middle lower frame), we show the CuO_2 and CuO Fermi surfaces (dashed lines), respectively, as well as the contour of gap zeros (solid lines). In Fig. 1(b), the Fermi surface has tetragonal symmetry but the gap zeros have nevertheless moved off the main diagonals (solid curve) because of the admixture into the mainly $d_{x^2-y^2}$ gap function of s_0 and $s_{x^2+y^2}$ components. As these are negative in Eq. (14), the zeros cross the Fermi surface at an angle (θ) measured clockwise from the negative k_y axis

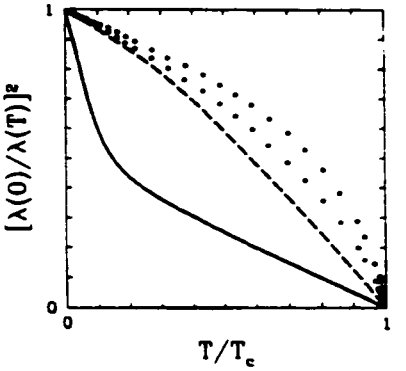

FIG. 2. Total contribution to the a (dashed) and b directions (solid) as a function of temperature to the inverse square of the penetration depth normalized to its zero-temperature value. The dots are experimental values (Ref. 1) with the b direction falling below the a direction. The b direction theoretical curve is much too steep at low temperature because of the small energy scale for the chain gap.

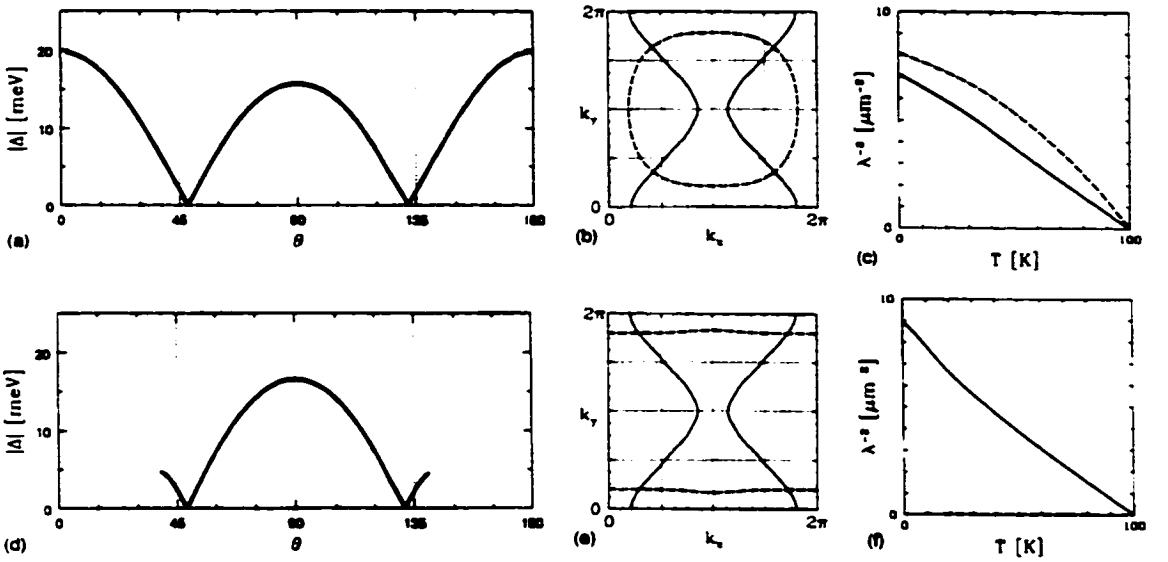

FIG. 3. (a), (b), and (c) apply to the CuO_2 planes while (d), (e), and (f) apply to the CuO chains with a nearly one-dimensional Fermi surface. The pairing interaction is assumed to be the same on chains and planes and off diagonal so that a single gap results. (b) and (e) give the Fermi-surface contours (dashed curve) and the gap zeros (solid curves) which are the same in both frames but different from pure d wave which would be lines on the main diagonals in the Brillouin zone. (a) and (d) give the absolute value of the gap as a function of angle θ along the Fermi surface measured clockwise from the k_x axis. (c) and (f) give partial contributions to the inverse square of the penetration depth as a function of temperature along a direction (dashed) and b direction (solid). Note that the zeros in the gap are not at 45° and 135° as they would be in pure d wave [Fig. (a) and (d)].

which is slightly larger than 45°. This is seen more clearly in Fig. 1(a) where we show the absolute value of the gap on the Fermi surface as a function of θ for the plane. Note that the gap does not display full tetragonal symmetry in that the zeros are displaced from 45° and 135° and that the gap at 90° is smaller than it is at 0° and 180°.

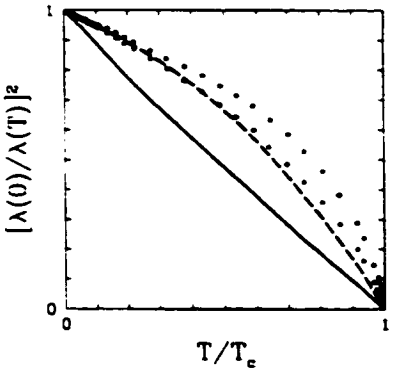

FIG. 4. Total contribution to the a (dashed) and b directions (solid) as a function of temperature to the inverse square of the penetration depth normalized to its zero-temperature value. The dots are experimental values (Ref. 1) with the b direction falling below the a direction. The agreement is good and the value of $\lambda_a/\lambda_b \approx 1.4$ is also in reasonable but not exact agreement with experiment.

For the chain case, the gap zeros [solid curves in Fig. 1(e)] are displaced much more off the main diagonals and as illustrated in Fig. 1(d) the value of the absolute value of the gap as a function of θ along the quasi-one-dimensional chain Fermi surface is very small. Note that this is a result of the orthorhombicity (i.e., geometry of the Fermi surface) of the chain Fermi surface as the pairing potential has been assumed to have the same size and form in the chains as in the tetragonal planes. For the given value of pairing interaction, the gap ratio $2\Delta_{max}/T_c$ is 3.86 in the plane while it has been reduced to 0.47 in the chains. Finally, it is important to note that in Fig. 1(d), the gap on the Fermi surface starts at a finite

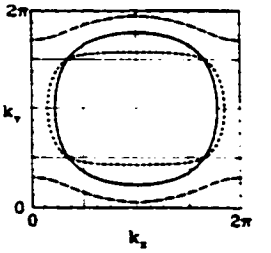

FIG. 5. The three Fermi surfaces in the triplanar model of YBCO. The chainlike band (dashed curve) is nearly one dimensional, the odd-band Fermi surface has orthorhombic symmetry (dotted curve) due to its interaction with the chains and the even band (solid curve) remains tetragonal.

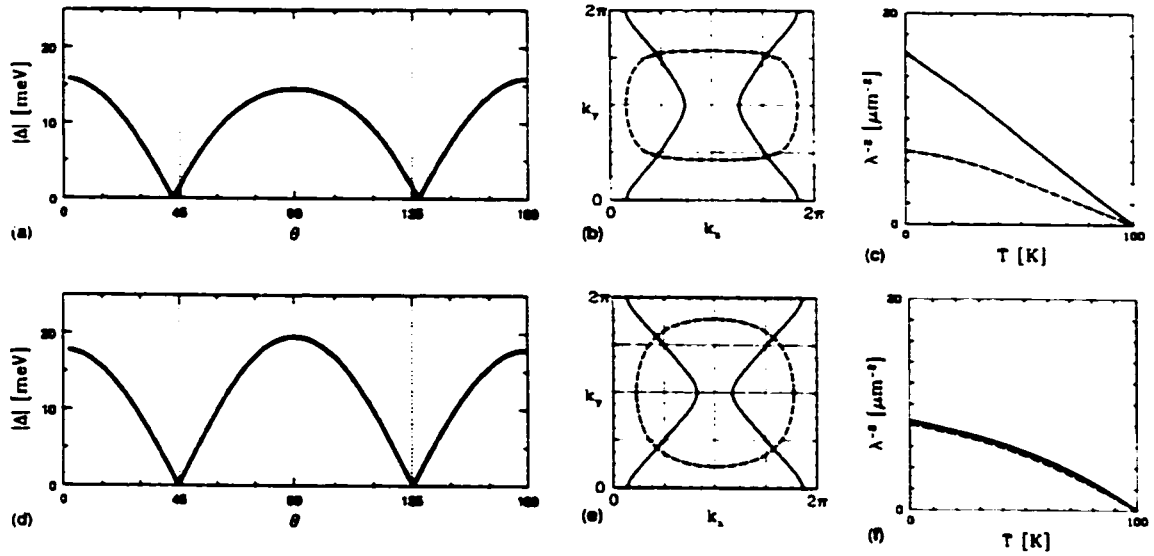

FIG. 6. Results for the triplanar model illustrated in Fig. 5 assuming no pairing diagonal or off diagonal on the chains which then remain normal. (a), (b), and (c) apply to the odd-band (orthorhombic symmetry) while (d), (e), and (f) apply to the even-band (tetragonal symmetry). (a) and (d) illustrate the absolute value of the gap along the Fermi surface as a function of angle θ measured clockwise from the k_x axis. These curves do not have full tetragonal symmetry and the zeros are displaced somewhat from the ideal $d_{x^2-y^2}$ case which would be at 45° and 135°. (b) and (e) give the Fermi surface (dashed line) and gap nodes (solid line) for odd and even plane (tetragonal), respectively. (c) and (f) give partial contributions to the inverse square of the penetration depth as a function of temperature for the a (dashed) and b (solid) directions. Note that the odd (orthorhombic) band gives a contribution to the b direction which is about twice its contribution to the a direction, while the even band (tetragonal) gives nearly the same contribution in both directions. In the model, the ratio $\lambda_a/\lambda_b \approx 1.3$.

value of θ reflecting the geometry of the nearly linear chain Fermi surface. The very small energy scale exhibited by the gap in the chains leads directly to a very steep slope in the resulting b-axis penetration depth as seen in the solid curve of Fig. 1(f). The contribution of the chains to the a-axis penetration depth is by contrast (dashed line) very small. This is quite different from the contribution of the plane to the penetration depth illustrated in Fig. 1(c). In this case, the nearly tetragonal symmetry of the Fermi surface leads to very similar contributions for the temperature dependence of the a- (dashed) and b- (solid) direction penetration depth. The small differences between these two curves as to absolute value of $\lambda^{-2}(0)$ at zero temperature is due to the orthorhombic symmetry of the dispersion [Eq. (1)]. Unfortunately, these small differences are not measured directly in an experiment which probes the sum of contributions from chains and planes, i.e., Fig. 1(f) and 1(c). This sum is shown in Fig. 2 where it is compared with experiment[1] (circles). The agreement is poor although the order of the zero-temperature slopes is correct, i.e., it is steeper in the chain direction (b direction). The large discrepancy can be traced directly to the small energy scale found in the chains in this model and we can conclude that the data favors a gap which is of the same magnitude in the chains as it is in the planes. Finally, we note that $\lambda_a/\lambda_b \approx 1.4$ in our calculation, which is reasonably close to (but not exactly) the measured value.

It is easy to modify our model so that chains and planes have the same gap value. A single gap results for $\Delta_{k,\sigma}$ inde-

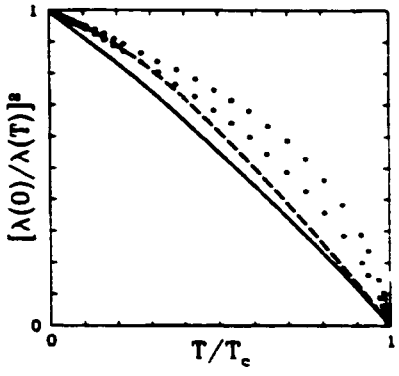

FIG. 7. Total contributions to the inverse square of the penetration depth normalized to its zero-temperature value as a function of temperature. The solid curve is for the b direction and the dashed for the a direction. The dots are the experimental data (Ref. 1) with the b-direction curve below the a-direction curve. Results are for the trilayer model of Figs. 5 and 6 in which it is assumed that there is no pairing on the chains on or off diagonal so they remain normal and do not contribute directly to the condensate.

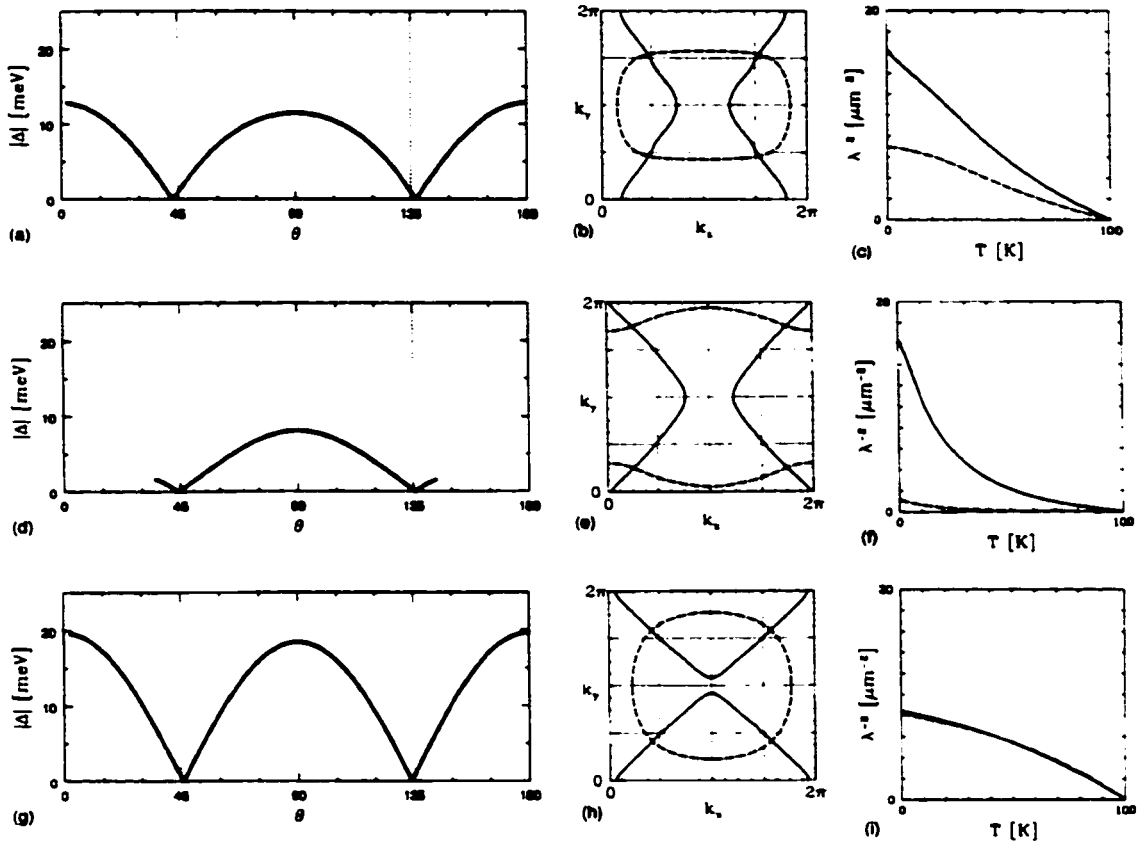

FIG. 8. Results for a triplanar model with some off-diagonal pairing on the chains but with $g_{22}=0$, i.e., no direct pairing in the chains themselves. The chains become superconducting but with a small gap amplitude. Top frames apply to the odd (orthorhombic) CuO_2 band, the middle three to the chain (CuO) band and the lower three frames to the even (tetragonal) CuO_2 band. (a), (d), and (g) give the absolute value of the gap as a function of angle θ along the Fermi surface measured clockwise from the k_x axis. Note the lack of tetragonal symmetry in the gap and the shift off 45° and 135° of the gap nodes. (b), (e), and (h) give the Fermi surface (dashed curve) and gap zero contours (solid curve). The odd CuO_2 plane band is orthorhombic as are the chains, while the even CuO_2 band Fermi surface retains tetragonal symmetry. Contributions to the inverse square of the penetration depth as a function of temperature are given in (c), (f), and (i) for the a direction (dashed) and b direction (solid). The odd orthorhombic band contributes almost twice as much to the b as to the a direction, while the even tetragonal band makes almost equal contributions. The chains contribute mainly in the b direction.

pendent of α if all diagonal and off-diagonal elements of the pairing potential are taken to have the same value, i.e., $g_{\alpha\beta}=$ const for any α and β. In Fig. 3, we illustrate results obtained with the same band parameters as used in our previous model but now with $g_{\alpha\beta}=24.7$ for all α and β in which case a single gap results which has the form:

$$\Delta_{\mathbf{k}}=[-1.83 \quad -0.288 \quad 10.09]\begin{bmatrix}\eta_{\mathbf{k}}^{(s_0)}\\ \eta_{\mathbf{k}}^{(s_{x^2-y^2})}\\ \eta_{\mathbf{k}}^{(d)}\end{bmatrix}. \qquad (15)$$

This gap has mainly d-wave character with a small admixture of s_0 and $s_{x^2-y^2}$ so that the gap zeros (solid curve) in Fig. 3(b) and 1(e) have moved off the main diagonal as in the previous example. Now these zero contours are the same in both chains and planes. The absolute value of the gap (on the Fermi surface) as a function of θ are shown in Fig. 3(a) and 3(d) for plane and chain, respectively, and the maximum value of $2\Delta/k_BT_c$ is 4.5 in the planes and 3.76 in the chains, much more comparable in value than was the case in the first model considered. It is to be noted that over the entire Brillouin zone the gaps in the planes and chains are not different but, of course, the Fermi-surface geometry is totally different in these two cases. In particular, we note that on the Fermi surface the gap in the chains starts at a finite angle θ near 45° and that there is no Fermi surface at small values of θ.

The smaller value of the maximum gap found in the

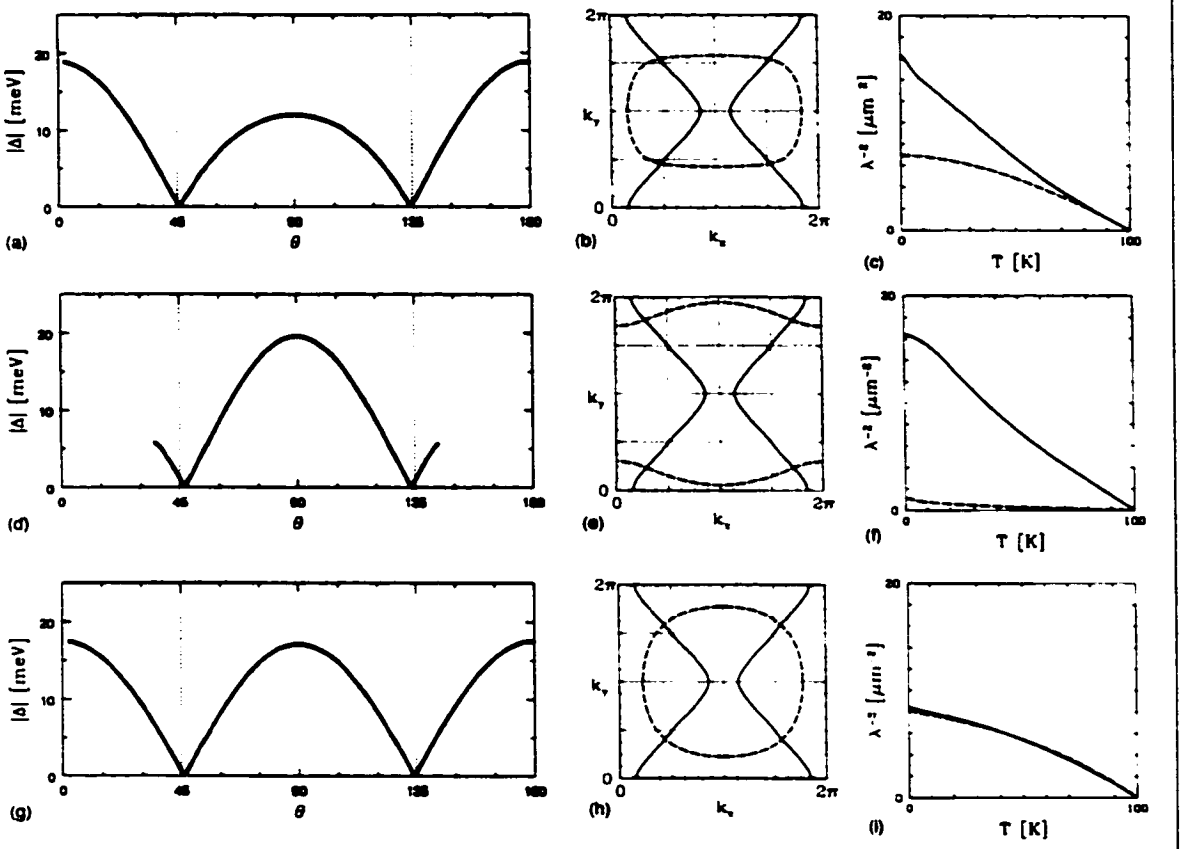

FIG. 9. Results for a trilayer model with pairing interaction having the same value on and off diagonal, i.e., $g_{\alpha\beta}$=constant for all α and β. This assumption ensures that a single gap applies to both the CuO_2 planes and the CuO chain. The three upper frames apply to the odd CuO_2 orthorhombic band, the middle three to the CuO chain band and the lower three to the even CuO_2 (tetragonal) band. (a), (d), and (g) gives the gap on the Fermi surface as a function of angle θ measured clockwise from the k_x axis. Note the lack of tetragonal symmetry and the "missing parts" in the chain case which reflects the geometry of the quasi one dimensional Fermi surface. (b), (e), and (h) give the Fermi contours (dashed line) for the odd CuO_2 (orthorhombic) band, chainlike CuO band, and even CuO_2 (tetragonal) band. The solid curves are the gap zero contours and are the same in all three figures. (c), (f), and (i) give the contributions to the inverse square of the penetration depth as a function of temperature for the a direction (dashed) and the b direction (solid). Note that the odd orthorhombic band contributes almost twice as much to the b as it does to the a direction in contrast to the even (tetragonal) band which makes nearly equal contributions. The chains contribute mainly to the b direction. In this model part of the a-b asymmetry in the penetration depth comes from the orthorhombic nature of the *even* plane Fermi surface of frame (b).

chains as opposed to the planes will lead to a steeper slope of the low-temperature dependence of the inverse square of the penetration depth in the chain direction as seen in Fig. 4 where we compare with experiments. While theory predicts somewhat steeper slopes, qualitative agreement with experiment is obtained in this simple model.

We turn next to results obtained for the trilayer model with CuO_2 planes on both sides of a CuO chain plane. The transverse coupling between CuO_2 and CuO plane is denoted by t_1 and t_2 is a direct transverse coupling between the two CuO_2 planes of the same unit cell. For $\{t_0, t_1, t_2\}=\{50,30,15\}$ in meV the resulting Fermi surfaces obtained from Eq. (6) are shown in Fig. 5, where

$$\{t_0 \quad \epsilon_\alpha \quad B_\alpha \quad \mu_\alpha\}=\begin{Bmatrix} 50.0 & 0.0 & 0.45 & 0.51 \\ 50.0 & 1.0 & 0.0 & 1.2 \\ 50.0 & 0.0 & 0.45 & 0.51 \end{Bmatrix}, \quad (16)$$

with t_0 in meV. The chain Fermi surface, denoted by the dashed line, is quasi-one dimensional and has only orthorhombic symmetry. The two CuO_2 plane Fermi surfaces are shown as dotted (odd) and solid (even) curves. Only the even-band Fermi surface has tetragonal symmetry, while the odd band is flatter along k_x than it is along k_y. This orthorhombicity will lead to different a- and b-direction contributions to the penetration depth from the CuO_2 planes themselves and this will now be described.

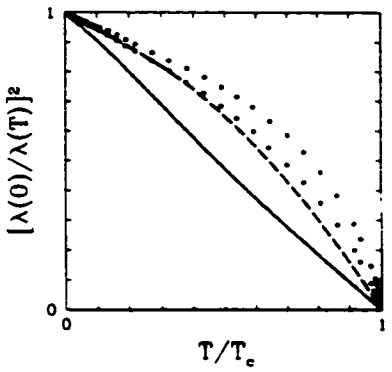

FIG. 10. Total contributions to the inverse square of the penetration depth normalized to its zero-temperature value as a function of temperature. The solid curve applies to the b direction and dashed to the a direction. The dots are experimental data (Ref. 1) with the b direction falling below a direction. The model is that of Fig. 9 with pairing interaction assumed constant (i.e., $g_{\alpha\beta}=$const) independent of α and β which leads to a single gap for all three planes in the primitive cell. This does not imply that it has $d_{x^2-y^2}$ symmetry because the bands do not have tetragonal symmetry and the gap contains an admixture of s_0 and $s_{x^2+y^2}$ although it is still dominantly $d_{x^2-y^2}$.

A first set of results that is instructive is illustrated in Fig. 6. The chains are assumed not to contribute directly to the penetration depth but only provide an agency whereby the CuO_2 plane acquires orthorhombic symmetry. This is accomplished easily if no pairing is assumed to act on the chains be it diagonal or off diagonal. That is, we take for the pairing potential the matrix:

$$g_{\alpha\beta}=\begin{bmatrix} 36.8 & 0.0 & 15.0 \\ 0.0 & 0.0 & 0.0 \\ 15.0 & 0.0 & 36.8 \end{bmatrix}. \tag{17}$$

What is critical in Eq. (17) is that the second row is all zero so the chains remain normal by arrangement. In this case, we obtain a gap of the form:

$$\Delta_{\mathbf{k},\sigma}=\begin{bmatrix} 1.81 & -1.46 & 9.96 \\ 0.0 & 0.0 & 0.0 \\ 0.59 & -0.80 & 10.88 \end{bmatrix}\begin{bmatrix} \eta_{\mathbf{k}}^{(s_0)} \\ \eta_{\mathbf{k}}^{(s_z)} \\ \eta_{\mathbf{k}}^{(d)} \end{bmatrix}. \tag{18}$$

The gap on even (top row) and odd (bottom row) band is mainly d-wave like with s components an order of magnitude smaller. The contours of gap zeros are illustrated as the solid curves in Figs. 6(b) and 6(e) for odd and even bands, respectively. The Fermi contour is the dashed curve in each case. The absolute value of the gap ($|\Delta|$) as a function of angle θ along the Fermi surface are given in Figs. 5(a) and 5(d) for odd and even band, respectively. In both cases, the gap zeros occur slightly before $\theta=45°$ and beyond 135° so that the gap does not have tetragonal symmetry even in the even band with a tetragonal Fermi surface. Also, the maximum gap on the Fermi surface is not quite the same in the two bands and is $2\Delta/k_BT_c=4.5$ and 3.69 for even and odd cases, respectively. While these values are not very different, the contributions of even and odd bands to the a- and b-direction penetration depths are very different. The odd band with orthorhombic Fermi surface gives a factor of 2 difference in the value of the square of the zero-temperature penetration depth as shown in Fig. 6(c). The solid curve applies along the b direction and the dashed curve along the a direction. For the even Fermi surface, which has tetragonal symmetry, the situation is very different as illustrated in Fig. 6(f) where it is seen that solid (along the b direction) and dashed curve (along a direction) are nearly the same (the slight difference is due to the difference in the a and b lattice parameters). Finally, in Fig. 7, we compare results for the a- (dashed) and b-direction (solid) penetration depth with experimental results. Again the curves are correctly ordered as to value of slope at zero temperature and the agreement is qualitative. It is as good as that shown in Fig. 4, although the physics of the two cases is quite different. In Fig. 7, the chains are normal by assumption and do not contribute directly to the condensate density in the a or b directions. The in-plane anisotropy is due mainly to the odd-band Fermi surface which has been made orthorhombic through its coupling to the chains and much less importantly to the s admixture in the gap function. Thus, we are dealing mainly with a band-structure effect which dominates and overwhelms any gap symmetry effects.

As a second illustration of a triplanar model, we show in Fig. 8 results for model parameters chosen so that the chains also become superconducting but by virtue of off-diagonal coupling and not because there is intrinsic pairing in the chains themselves. That is g_{22} is assumed to be zero. Specifically, we assume

$$g_{\alpha\beta}=\begin{bmatrix} 44.4 & 10.0 & 0.0 \\ 10.0 & 0.0 & 10.0 \\ 0.0 & 10.0 & 44.4 \end{bmatrix}, \tag{19}$$

while the band parameters remain the same as in the previous cases. In Figs. 8(b), 8(e), and 8(h), we show, respectively, odd, chain, and even-band Fermi surface as the dashed curves and contours of gap zeros are the solid curves. The gap solution is

$$\Delta_{\mathbf{k},\sigma}=\begin{bmatrix} 1.21 & -1.35 & 7.77 \\ 0.65 & -0.34 & 3.79 \\ -0.59 & 0.15 & 11.17 \end{bmatrix}\begin{bmatrix} \eta_{\mathbf{k}}^{(s_0)} \\ \eta_{\mathbf{k}}^{(s_z)} \\ \eta_{\mathbf{k}}^{(d)} \end{bmatrix}. \tag{20}$$

The absolute values of the gaps as a function of angle θ along odd, chain, and even Fermi surface are shown in Figs. 8(a), 8(d), and 8(g). Because no pairing was assumed to act in the chains, the gap is smallest in frame 8(d) with maximum $2\Delta/k_BT_c$ equal to 1.88 as opposed to 4.58 and 2.98 for even and odd band, respectively. Frames (c), (f), and (i) show that the odd orthorhombic band makes a very different contribution to the b-direction (solid curve) penetration depth than to the a-direction; the difference in zero-temperature value being of order 2. The differences are even more pronounced in the case of the chains which contribute very little to the a direction (dashed curve), while the even

tetragonal Fermi surface makes an almost equal contribution to the a and b directions. Because of the small energy scale present on the chains, which can be traced to the assumption $g_{22}=0$, i.e., zero pairing on the chains, this model will not lead to good agreement with experiment. To achieve this, a final model is considered with the same single gap for both CuO_2 planes and for the chains. If we take all $g_{\alpha\beta}=\text{const}=18.4$, we obtain a single gap

$$\Delta_{\mathbf{k}}=[-0.363 \quad -0.502 \quad 10.14]\begin{bmatrix}\eta_{\mathbf{k}}^{(s_0)}\\ \eta_{\mathbf{k}}^{(s_2)}\\ \eta_{\mathbf{k}}^{(d)}\end{bmatrix}. \quad (21)$$

Detailed results are illustrated in the nine frames of Fig. 9. In Figs. 9(b), 9(e), and 9(h), the gap zeros are all the same (solid curves) yet because the Fermi contours (dashed curves) are different, the gap as a function of angle along the Fermi surfaces are different as shown in Figs. 9(a), 9(d), and 9(g) for odd, chain, and even Fermi surfaces, respectively. The maxima in $2\Delta/k_BT_c$ are, respectively, 4.39, 4.55, and 4.07. Resulting contributions to the a- (dashed) and b- (solid) direction penetration depth are found in Figs. 9(c), 9(f), and 9(i). The odd orthorhombic Fermi surface again contributes about twice as much to the b and to a directions at low temperature, while the even one contributes equally. The chains mainly contribute to the b direction. The sum of all contributions are shown in Fig. 10 and compared with experiment. The agreement is satisfactory with the a-direction curve (dashed) above the b direction (solid) as observed. The ratio λ_a/λ_b was ~ 1.6 in the calculations, close to the observed value.

IV. CONCLUSIONS

We have presented results of calculations for the temperature dependence of the in-plane penetration depth in a trilayer model of $YBa_2Cu_3O_7$ which includes two CuO_2 planes and a set of CuO chains oriented along the b direction. Transverse hopping matrix elements couple the three planes together leading to three coupled bands in which the gap parameters is an admixture of $d_{x^2-y^2}$, $s_{x^2+y^2}$, and s_0 symmetries. While the s- and d-symmetry types belong to two different irreducible representations of the tetragonal crystal-point group, they belong to the same representation in the orthorhombic case which is the case we are dealing with here because of the presence of the chains. Nevertheless, it is found that the penetration depth remains linear in temperature at low temperature as a result of nodes in the gap crossing the Fermi contours. To compare with experiment, the ratio of λ_a/λ_b was kept near the observed value in all our calculations. With this constraint, it was found that the observed normalized temperature variation of the penetration depth in the a and b directions is difficult to understand in models where no intraplane pairing is introduced in the chains even if a large amount of interplane pairing is considered. The most natural explanation of the data is obtained when the pairing interaction is assumed not to depend significantly on the subband and is taken to be independent of α and β, i.e., $V_{\mathbf{k},\mathbf{k}',\alpha\beta}=V_{\mathbf{k},\mathbf{k}'}$. Also the zero-temperature anisotropy in $\lambda_{a,b}$ can be traced to the orthrhombicity of the band structure which resides in the chains and hybridized planes.

ACKNOWLEDGMENTS

Work supported in part by the Canadian Institute for Advanced Research (CIAR) and the Natural Sciences and Engineering Research Council of Canada (NSERC). We have benefited from conversations with W. Atkinson.

*Electronic address: odonovan@mcmaster.ca

[1] D.N. Basov, R. Liang, D.A. Bonn, W.N. Hardy, B. Dabrowski, M. Quijada, D.B. Tanner, J.P. Rice, D.M. Ginsberg, and T. Timusk, Phys. Rev. Lett. 74, 598 (1995).

[2] K. Zhang, D.A. Bonn, S. Kamal, R. Liang, D.J. Baar, W.N. Hardy, D. Basov, and T. Timusk, Phys. Rev. Lett. 73, 2484 (1994).

[3] D.A. Bonn, S. Kamal, K. Zhang, R. Liang, and W.N. Hardy, J. Phys. Chem. Solids 56, 1941 (1995).

[4] T.A. Friedmann, M.W. Fabin, J. Giapintzakis, J.P. Rice, and D.M. Ginsberg, Phys. Rev. B 42, 6217 (1990).

[5] Y. Iye, in *Physical Properties of High Temperature Superconductors*, edited by D.M. Ginsberg (World Scientific, Singapore, 1992), Vol. III, p. 285.

[6] R. Gagnon, C. Lupien, and L. Taillefer, Phys. Rev. B 50, 3458 (1994).

[7] K. Takenaka, K. Mizuhashi, H. Takagi, and S. Uchida, Phys. Rev. B 50, 6534 (1994).

[8] W.A. Atkinson and J.P. Carbotte, Phys. Rev. B 51, 1161 (1995); 51, 16 371 (1995).

[9] W.A. Atkinson and J.P. Carbotte, Phys. Rev. B 52, 6894 (1995); 52, 10 601 (1995).

[10] C. O'Donovan and J.P. Carbotte, Phys. Rev. B 55, 1200 (1997).

[11] A.J. Millis, H. Monien, and D. Pines, Phys. Rev. B 42, 167 (1990).

[12] C. O'Donovan and J.P. Carbotte, Phys. Rev. B 52, 4548 (1995).

[13] C. O'Donovan, D. Branch, J.P. Carbotte, and J. Preston, Phys. Rev. 51, 6588 (1995).

[14] C. O'Donovan and J.P. Carbotte, Physica C 252, 87 (1995).

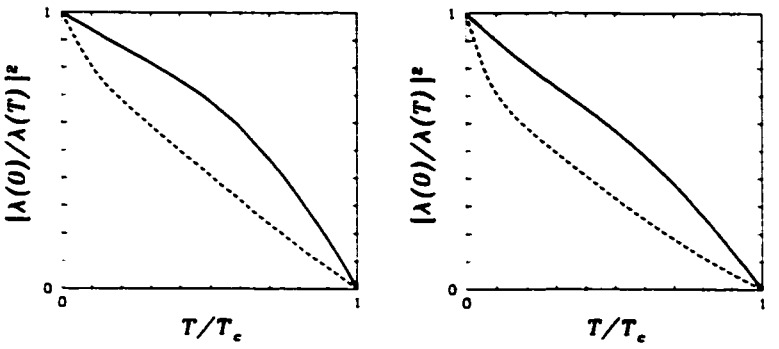

Figure 6.13: The magnetic penetration depths as a function of temperature found using the solutions of the BCS equation with chain-plane model dispersions of §6.2 (shown in Fig. 6.6 on p. 90) are shown. The sharp upturn in the penetration depth in the *b*-direction (dashed curves) is due to the small energy scale that is present in the gap on the chain Fermi surface.

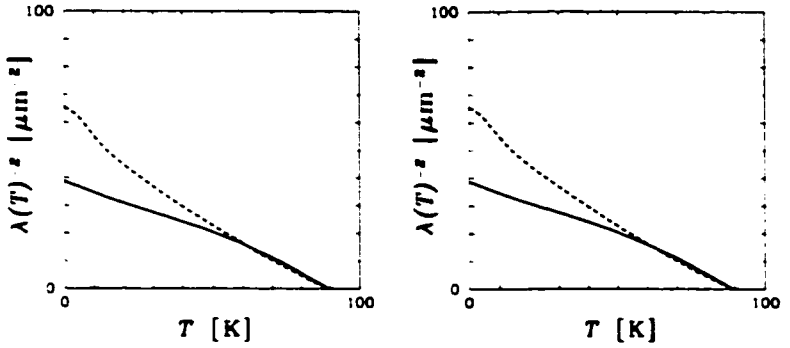

Figure 6.14: The magnetic penetration depths as a function of temperature found using the solutions of the BCS equation with chain-plane model dispersions of §6.2 with 2% impurities in the chain layer are shown. The sharp upturn of the penetration depth in the *b*-direction present in Fig. 6.13 has been substantially attenuated.

6.5.3 The Penetration Depth with Impurities

Chain-Plane Models

The magnetic penetration depths as a function of temperature found using the solutions of the BCS equation with chain-plane model dispersions of §6.2 (shown in Fig. 6.6) are shown in Fig. 6.13. The sharp upturn in the penetration depth in the *b*-direction (dashed curves) is due to the small energy scale that is present in the gap on the chain Fermi surface.

Due to the judicious choice of the hopping parameters in the chain and plane layers the zero temperature penetration depths are close to those observed by Hardy *et al.* [89]; for the hybridyzed model (shown on the left) the values in the *a* and *b*-directions are 1855 Å and 968 Å, for the second model (right) they are, respectively, 1603 Å and 1045 Å.

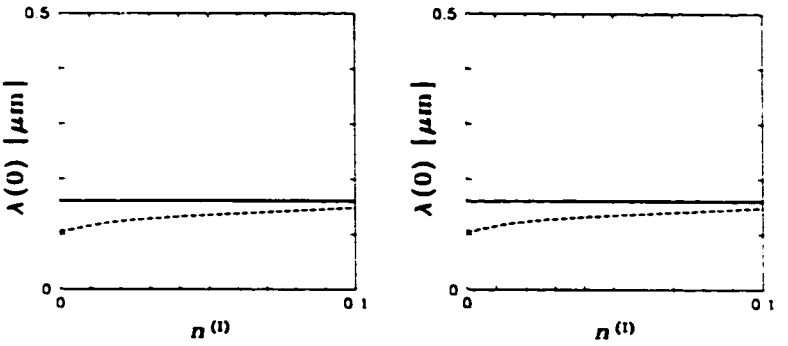

Figure 6.15: The zero temperature magnetic penetration depths as a function of impurities found using the solutions of the BCS equation with chain-plane model dispersions of §6.2 with impurities only in the chain layer are shown.

The sharp upturn in the penetration depth in the *b*-direction, which is a direct consequence of a *d*-wave order parameter in the chain-like band, is not present in the data of Hardy *et al.* [89] and it is difficult to reconcile the two results. By introducing impurities to the chain layer this sharp upturn is significantly rounded. Shown in Fig. 6.14 is the magnetic penetration depths as a function of temperature found using the solutions of the BCS equation with chain-plane model dispersions of §6.2 with 2% impurities in the chain layer.

As noted in §6.3.1 impurities in the chain layer do not substantially effect the critical temperature (89 K instead of 95 K) and, from Fig. 6.14, neither does it have a large effect upon the zero temperature penetration depths which for 2% impurities are 1605 Å and 1234 Å for the *a* and *b*-directions, respectively. Shown in Fig. 6.15 is the zero temperature magnetic penetration depths as a function of impurities found using the solutions of the BCS equation with chain-plane model dispersions of §6.2 with impurities only in the chain layer. As can be seen there is almost no change to the penetration depth perpendicular to the chains (solid curve) while the penetration depth parallel to the chains (dashed curve) slowly increases.

6.6 Josephson Tunneling

6.6.1 *c*-axis Josephson Tunneling in Twinned and Untwinned YBCO-Pb Junctions

This paper [110] examines the rôle played by twins in an ostensibly untwinned YBCO crystal in the Josephson tunneling current. Early experiments on highly twinned films [107] seemed to indicate that there existed a *c*-axis tunneling current, in contradiction to the predictions of *d*-wave theory. We argue that the assumption that the abundance of the two twin orientations are equally abundant is not necessarily true. We also show that the effect of the chain layer upon the plan layer

leads to a large breaking of the tetragonal symmetry and, consequently, a significant c-axis tunneling current.

PHYSICAL REVIEW B VOLUME 55, NUMBER 14 1 APRIL 1997-II

c-axis Josephson tunneling in twinned and untwinned YBCO-Pb Junctions

C. O'Donovan,* M. D. Lumsden, B. D. Gaulin, and J. P. Carbotte
Department of Physics & Astronomy, McMaster University Hamilton, Ontario, Canada L8S 4M1
(Received 17 July 1996)

Within a microscopic two-band model of planes and chains with a pairing potential in the planes and off-diagonal pairing between planes and chains we find that the chains make the largest contribution to the Josephson tunneling current and that through them the d-wave part of the gap contributes to the current. This is contrary to the usual assumption that the d-wave part of the gap does not contribute to the c-axis Josephson current for incoherent tunneling into an s-wave superconductor and for a d-wave orthorhombic superconductor with a small s-wave component to its gap only the s-component contributes. It has been further argued that the effect of twins, in $YBa_2Cu_3O_{7-\delta}$ (YBCO) would lead to cancellation between pairs of twins, and so the observation of a current in c-axis YBCO-Pb experiments is evidence against a d-wave-type order parameter. We argue that there is evidence that the two twin orientations are not necessarily equally abundant in call cases. [S0163-1829(97)02813-0]

I. INTRODUCTION

The symmetry of the order parameter in the cuprates is the subject of much current debate. While several experimental techniques such as angle-resolved photoemission spectroscopy[1–4] and current imaging tunnelling spectroscopy (CITS) (Refs. 5 and 6) probe the magnitude of the superconducting order-parameter, Josephson tunneling is, perhaps, the only observable phenomena which directly probes the phase of the superconducting order parameter as well as, indirectly, its magnitude.

The focus of the debate has been upon whether the order parameter has s-wave (even under a 90° rotation) or d-wave (odd under a 90° rotation) symmetry. Since most experiments are performed upon orthorhombic materials in which the s- and d-wave symmetries belong to the same irreducible representation there is no clear distinction between them and, rather than the symmetry of the order parameter, the discussion should focus on whether there are nodes present in the order parameter which cross the Fermi surface.

Although the s- and d-wave representations of the tetragonal systems mix freely in orthorhombic systems we can still speak of the "s" and "d" parts of the order parameter if what we mean are, respectively, the parts which are odd and even under a 90° rotation. It would, however, be highly unusual for one of these components to be present in an orthorhombic superconductor without the other being present as well. Further, if the odd, or d, part is dominant then nodes which cross the Fermi surface will be present in the order parameter [what we call a $(d+\epsilon s)$-wave order parameter], while if the even, or s, part is dominant the nodes, if they are present, will not cross the Fermi surface [what we call an $(s+\epsilon d)$-wave order parameter]. It is possible for an order parameter that is even under a 90° rotation (i.e., s wave) to have nodes but we consider this situation unlikely and we will not examine this possibility here.

Several corner junction YBCO-Pb tunneling experiments[7–9] are cited as strong evidence for the order parameter in YBCO having d-wave type symmetry. Other tunneling experiments which contain only YBCO in a bi- and tricrystal rings[10–12] also give strong indications of order parameters with d-wave type symmetry. Both of these types of experiments have the plane of the junctions perpendicular to the a-b plane—what we refer to as "edge junction" experiments. It is the observation of π phase shifts in the corner junctions and half flux quanta in the ring experiments that is the strong evidence for the order parameter in YBCO having d-wave type symmetry.[13] Note that for the observation of π phase shifts there is no difference between a d-wave order parameter and a $(d+\epsilon s)$-wave order parameter.

The results of these edge junction experiments are independent of the presence of twins in these materials.[14] This indicates that the order parameter is phase locked across the twin boundaries, although calculations indicate[15,16] that the magnitudes (as well as the relative magnitudes and perhaps the relative phase as well) of the d and s may change in the twin boundary. Although this phase locking is not unexpected it may have other consequences.

There is a second class of YBCO-Pb tunneling experiments in which the plane of the junction is parallel to the a-b plane—what we refer to as "c-axis junction" experiments.[17,18] The presence of a current in these experiments is cited as evidence against a d-wave order parameter in the literature[16,19] as well as articles for more general physics audiences.[20] In fact, due to the orthorhombic symmetry of these materials the order parameter will have $(d+\epsilon s)$-wave symmetry and a c-axis tunneling current of reduced magnitude is expected in untwinned materials.[21,22] The current is *not* just due to the ϵs part of the order parameter but is also caused by the d part of the order parameter due to the orthorhombicity of the Fermi surface, a fact that appears not to be widely appreciated. Here we use a plane-chain double layer model[22] in which each set of electrons has its own Fermi surface in the two-dimensional CuO_2 Brillouin zone.

While there is quite a large variation in the maximum resistance-tunneling current product, I_cR_N, observed in these c-axis tunneling experiments, I_cR_N in the untwinned

0163-1829/97/55(14)/9088(6)/$10.00

samples is, on average, about twice that in the twinned samples.[24] The argument that a finite c-axis YBCO-Pb tunneling current is evidence against a d-wave order parameter is based upon the intuitive assumption that over the junction area, the relative abundance of each orthorhombic twin domain will be roughly equal and any orthorhombicity in a phase-locked order parameter will average out. The view that, over any macroscopic region in the crystal, the relative volume fraction occupied by each of the orthorhombic twin domains must be approximately equal, is prevalent in the literature,[16,20] and is used as a simplifying assumption for some calculations.

The issue of the microstructure of coexisting twin domains is sufficiently important to these arguments that we have carried out a high-resolution x-ray-scattering study of a particular twinned $YBa_2Cu_3O_{6.93}$ single crystal, for the purpose of investigating whether such averaging out of the orthorhombicity on macroscopic length scales in fact necessarily occurs in real samples. These results show the volume fractions occupied by the two twin domains to be quite different over macroscopic dimensions in the sample studied. While it does not follow that this particular morphology is present in the "heavily twinned" YBCO crystals employed in the c-axis tunnel junctions mentioned above, these results clearly demonstrate that the widely accepted view of the orthorhombic twin domains occurring in roughly equal populations, is not correct. As will be discussed, this experiment, which measures the relative abundance of the two twins by comparing the intensities and line shapes of the (200) and (020) diffraction peaks from each twin, indicates that over the whole sample, one of the two twins is 2–3 times more abundant than the other.

If the ratio of the two possible twin orientations is $n:m$ and if the current-resistance product, $I_cR_N(T=0)$, is $I_cR_N^{(o)}$ for an untwinned junction then for the twinned sample the current should be:

$$I_cR_N^{(\text{twin})}=\left|\frac{n-m}{n+m}\right|I_cR_N^{(o)}. \tag{1}$$

This is consistent with the experimental observation of Sun *et al.*[24] in which the Josephson tunneling current in untwinned c-axis YBCO-Pb is about double that observed in twinned junctions if the ratio of twins is approximately 3:1.

In Sec. II we present a BCS formalism for a model system in which a tetragonal CuO_2 plane layer is coupled to an orthorhombic CuO chain layer and give the equation for the resistance-tunneling current product, I_cR_N. In Sec. III we present the results of some representative calculations as well as some experimental results on the relative abundances of the two twin orientations. In Sec. IV we make some concluding statements.

II. FORMALISM

For a bilayer system (i.e., $\alpha=1,2$) the coupled BCS equations are[22]

$$\Delta_{\mathbf{k},1}=\frac{1}{\Omega}\sum_{\mathbf{q}}\left(V_{\mathbf{k},\mathbf{q},11}\chi_{\mathbf{q},1}+V_{\mathbf{k},\mathbf{q},12}\chi_{\mathbf{q},2}\right),$$

$$\Delta_{\mathbf{k},2}=\frac{1}{\Omega}\sum_{\mathbf{q}}\left(V_{\mathbf{k},\mathbf{q},12}\chi_{\mathbf{q},1}+V_{\mathbf{k},\mathbf{q},22}\chi_{\mathbf{q},2}\right). \tag{2}$$

where we have taken $V_{\mathbf{k},\mathbf{q},12}=V_{\mathbf{k},\mathbf{q},21}$ and

$$\chi_{\mathbf{q},\alpha}\equiv\langle a_{\mathbf{q}\uparrow,\alpha}a_{-\mathbf{q}\downarrow,\alpha}\rangle=\frac{\Delta_{\mathbf{q},\alpha}}{2E_{\mathbf{q},\alpha}}\tanh\left(\frac{E_{\mathbf{q},\alpha}}{2k_BT}\right),$$

is the pair susceptibility, with

$$E_{\mathbf{k},\alpha}=\sqrt{\varepsilon_{\mathbf{k},\alpha}^2+\Delta_{\mathbf{k},\alpha}^2},$$

where $\varepsilon_{\mathbf{k},\alpha}$ are the band energies in the normal state. Note that we have taken $\langle a_{\mathbf{q}\uparrow,1}a_{-\mathbf{q}\downarrow,2}\rangle=0$, i.e., there is no pairing between electrons in different planes. This assumption seems reasonable since a $\{\mathbf{k}\uparrow,-\mathbf{k}\downarrow\}$ Cooper pair could not both be on the Fermi surfaces of two layers simultaneously, although other workers[23] do not make this assumption.

We note that this set of equations (2) is invariant under substitution $\{\Delta_{\mathbf{k},2},V_{\mathbf{k},\mathbf{q},12}\}\rightarrow\{-\Delta_{\mathbf{k},2},-V_{\mathbf{k},\mathbf{q},12}\}$ which means that the overall sign of $V_{\mathbf{k},\mathbf{q},12}$ only affects the relative sign of the order parameters in the two layers and not their magnitudes. This is interesting because it means that the effect on T_c of having an interlayer interaction is independent of whether this interaction is attractive or repulsive, although the c-axis Josephson tunneling current still depends upon the relative sign of the interlayer interaction.

The c-axis Josephson-junction resistance-tunneling current product, $I_cR_N(T)$, through a superconductor-insulator-superconductor junction for incoherent c-axis tunneling is given by the relation[27]

$$I_cR_N(T)=\frac{2\pi T}{N^{(\text{Pb})}(0)N^{(\text{YBCO})}(0)\pi^2}\times\sum_{n}A^{(\text{Pb})}(\omega_n)A^{(\text{YBCO})}(\omega_n), \tag{3}$$

where

$$A^{(\cdot)}(\omega_n)\equiv\frac{1}{\Omega}\sum_{\mathbf{k}}\frac{\Delta_{\mathbf{k}}^{(\cdot)}}{(\varepsilon_{\mathbf{k}}^{(\cdot)})^2+(\Delta_{\mathbf{k}}^{(\cdot)})^2+(\omega_n)^2}. \tag{4}$$

in which the superscript $(\cdot)$ indicates on which side of the junction the dispersion and order parameter are on, the sum over $\omega_n=\pi T(2n-1)$ is for all Matsubara frequencies, R is the resistance of the junction, and $N^{(\cdot)}(0)$ is the normal-state electronic density-of-states DOS given by

$$N^{(\cdot)}(\omega)=\frac{1}{\Omega}\sum_{\mathbf{k}}\delta(\varepsilon_{\mathbf{k}}^{(\cdot)}-\omega)=\lim_{\Gamma\rightarrow0}\frac{1}{\pi\Omega}\sum_{\mathbf{k}}\frac{\Gamma}{(\varepsilon_{\mathbf{k}}^{(\cdot)}-\omega)^2+\Gamma^2}. \tag{5}$$

Since the DOS and $\Delta_{\mathbf{k}}^{(\text{Pb})}$ for lead are constant the sum in Eq. (4) can be performed and $A^{(\text{Pb})}(\omega_n)$ is given by[26]

$$A^{(\text{Pb})}(\omega_n)=\frac{\Delta^{(\text{Pb})}}{\sqrt{(\Delta^{(\text{Pb})})^2+(\omega_n)^2}}.$$

If the tunneling were coherent the matrix element (which is incorporated into R) would have a $(\mathbf{k}-\mathbf{k}')$ dependence, and the sums over k space would not be separable.

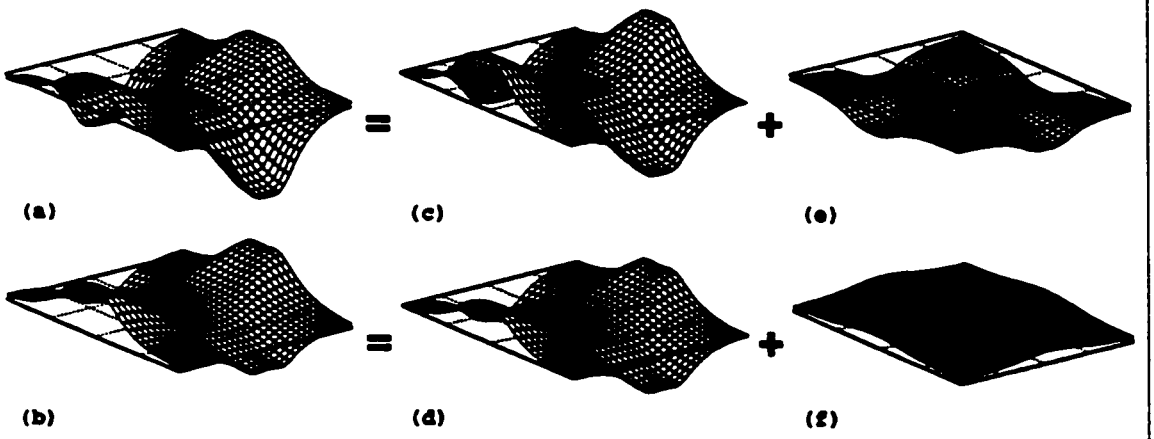

FIG. 1. The order parameter in the first Brillouin zone for (a) the plane layers and (b) the chain layers. Beside are the projections of the d components, (c) and (d), and the s components, (e) and (f). The vertical scale in all frames is the same. Note that the relative phase of the d components in the two layers are the same, while that of the s components are opposite; this is caused by the interlayer interaction, $V_{k,q,12}$, being negative (i.e., repulsive).

III. RESULTS

We use the same band structure as in our previous work on the penetration depth of a coupled chain-plane bilayer[22] in which we assume tetragonal symmetry for the electron dispersion in the CuO_2 plane with first- and second-neighbor hopping, while the chains are quasi-one-dimensional (1D) with very different hopping probabilities in the x and y directions (the chains are along the y direction). For the pairing potential, $V_{k,q,\alpha\beta}$, which appears in the coupled BCS equations (2) and which determines the superconductivity, we use a nearly antiferromagnetic Fermi-liquid model with magnetic susceptibility of the phenomenological form given by Millis, Monien, and Pines:[27]

$$V_{k,q,\alpha\beta}=g_{\alpha\beta}\frac{-\chi_o}{1+\xi_o^2|k-q-Q|^2},$$

where ξ_o is the magnetic coherence length and Q is the commensurate vector (π,π) in the 2D Brillouin zone. Our results are not specific to this interaction—any interaction which would result in a d-wave order parameter in the CuO_2 plane layer will give a $(d+\epsilon s)$-wave order parameter when the CuO_2 planes are coupled to the CuO chain layers.

No pairing interaction is assumed to act directly in the chain band, i.e., $g_{22}=0$, so that the superconductivity in the chains is entirely due to the $g_{12}=g_{21}\neq 0$. This parameter (g_{12}) is fixed to get a critical temperature value of 100 K for a chosen value of the in-plane pairing, g_{11}. In Fig. 1, we show results for the gap value $\Delta_{k,1}$ in the planes [Fig. 1(a)] and for $\Delta_{k,2}$ in the chains [Fig. 1(b)] as a function of k in the first Brillouin zone. The order parameters result from a numerical solution of equations (2). For the runs shown in Fig. 1, $\{g_{11},g_{12},g_{22}\}=\{26.2,10,0\}$ and $T_c=100$ K.

On the right-hand side of Fig. 1, we have decomposed the order parameters into d-wave (c) and (d) and s-wave (e) and (f) components for the plane and chain, respectively. While the main component is certainly the d-wave part, the s-wave admixture is, nevertheless, significant in magnitude in both the chain and plane bands.

A useful representation of these gap results is to show the contours of gap zeros on the same plot as the Fermi surface. This is presented in the series of frames shown in Fig. 2. The top frames apply to the plane while the bottom frames apply to the chains. In all cases, (a), (c), (e) for the planes and (b), (d), (f) for the chains, the same Fermi surface (dashed curves) was used. By choice, the Fermi contours have tetragonal symmetry in the top figure, while the chain Fermi surface is a quasistraight line along k_x as is expected for chains along the y direction in configuration space. The pictures are for three different values of pairing potential. The first set of two frames (a) and (b) are for $\{g_{11},g_{12},g_{22}\}=\{29.9,5,0\}$, i.e., very little coupling between chains and planes (off-diagonal g_{12} small). In this case, the gap in the plane is nearly pure d wave as is also the induced gap in the chains. The zero gap contours are given by the solid line and would be the main diagonals in a pure d-wave system. As the coupling g_{12} is increased $\{g_{11},g_{12},g_{22}\}=\{26.2,10,0\}$, a significant s-wave component gets mixed into both solutions and the gap nodes move off the main diagonals of the Brillouin zone (This is the solution that is plotted in Fig. 1). The gap nodes still cross the Fermi surfaces in both chains and planes. As the coupling is further increased to $\{g_{11},g_{12},g_{22}\}=\{9.18,20,0\}$, Figs. 2(e) and 2(d), the gap nodes move far off the diagonal and for the chains they no longer cross the Fermi surface so that there is a finite minimum value of the gap on this sheet of the Fermi surface.

Calculation of the product of Josephson current times resistivity given in Eq. (3) for a YBCO-I-Pb tunnel junction gives for the intermediate case $\{g_{11},g_{12},g_{22}\}=\{26.2,10,0\}$ the tunneling current, $I_cR_N(T=0)$, is 0.2–0.3 meV for the

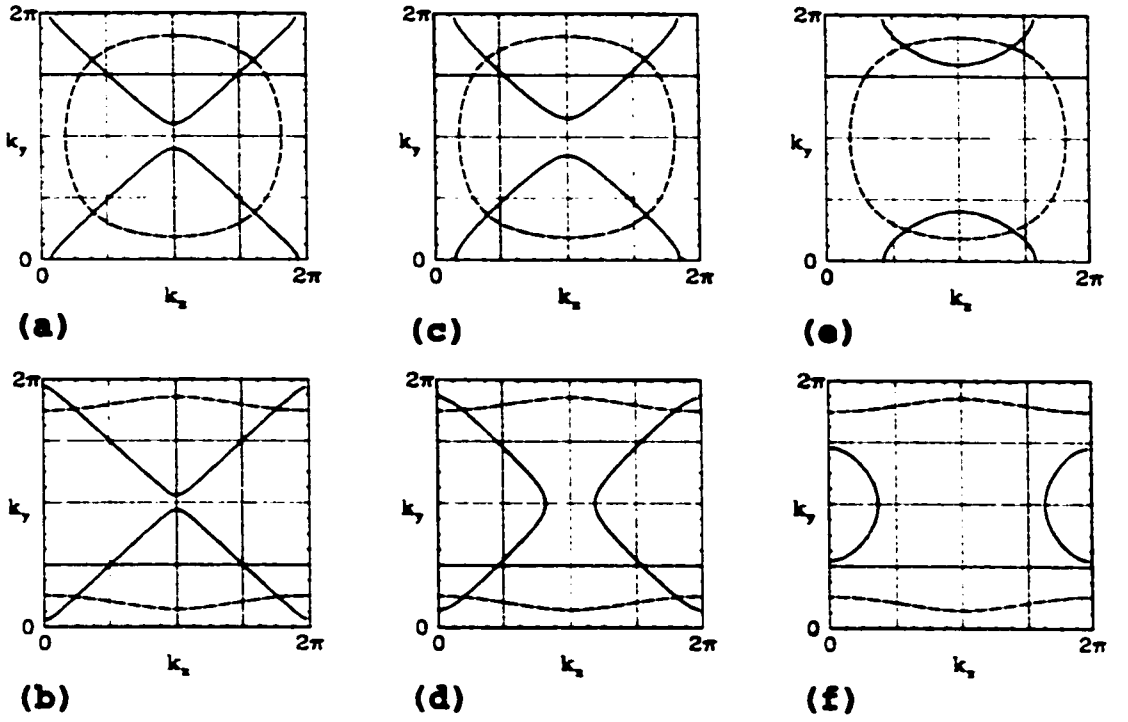

FIG. 2. The Fermi surface (dashed curves) and gap nodes (solid curves) for a CuO_2 plane layer (top frames) and a CuO chain layer (bottom frames) for three different interlayer interaction strengths (left, middle, and right frames). As the strength of the interlayer interaction, g_{12}, is increased (left to right frames) the proportion of the s component in both layers increases. If the interlayer interaction were further increased the gap nodes would leave the Brillouin zone altogether and the order parameter would become s like. Note that the Fermi surface in the CuO_2 plane layer is tetragonal but that the gap node is orthorhombic.

plane layers and $\pm$(2-3) meV for the chain layers. The relative sign depends upon whether the interlayer interaction, g_{12}, is attractive or repulsive. These values for chain and plane tunneling current, I_cR_N, are upper and lower bounds and note that the expected value should be somewhere in between since the $I_cR_N(T=0)$ values are dependent upon the amount of tunnel junction area which is covering the uppermost chain or plane layer.

The order of magnitude difference obtained between plane and chain layer for the $I_cR_N(T=0)$ product is understood as follows. For a given Matsubara frequency, ω_n in Eq. (4), the contribution to the sum over $\mathbf{k}$, which ranges over the entire Brillouin zone, is strongly peaked about the Fermi surface because the denominator in Eq. (4) becomes smallest in this case. This is seen clearly in Fig. 3 where we show the integrand of Eq. (4), again for the intermediate case, as a function of $\mathbf{k}$ in the first Brillouin zone for planes (a) and chains (b), respectively, for a particular Matsubara frequency, $\omega_n=50$ meV. It is clear that in the plane layer the positive and negative parts largely cancel each other. They would, in fact, give exactly zero if the gap had pure d-wave symmetry. The situation for the chains is completely different because the Fermi surface now does not have tetragonal symmetry and even if the gap was pure d wave there would not be a large degree of cancellation between the positive and negative regions. *Thus, we note the important result that the main part of the Josephson current coming from the chains is due to the d-wave part of the gap function and would still be large if we did not account for the s-wave admixture. Thus, in an experiment on an untwinned single crystal of YBCO the Josephson current coming from the chain part of the Fermi surface is sampling mainly the d-wave part of the gap and therefore, such experiments do not reflect directly the s-wave admixture.*

It has been argued that for twinned samples, the c-axis Josephson current will cancel because of the cancellation between a and b twins.[24] This argument would apply equally well to our work, since we should then average over pictures as shown in Fig. 3(b) with opposite phases (a and b twins). However, we do not expect twins to be present in equal numbers, and the expected cancellation will not occur.

The issue of the morphology of the orthorhombic twin domains in YBCO and whether such domains must occur in equal volume fraction over macroscopic dimensions is sufficiently important to this study that high-resolution x-ray-scattering measurements on a small single crystal of twinned

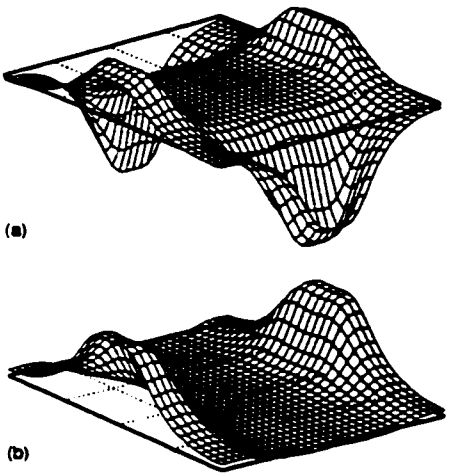

FIG. 3. The k-space integrand of $A^{(YBCO)}(\omega_n)$ [see Eq. 3] for (a) the CuO_2 plane layer and (b) the CuO chain layer. In the plane layer the positive and negative parts mostly cancel and the resulting current is small, while in the chain layer only a very small amount of the integrand, $A^{(YBCO)}(\omega_n)$, is negative and the resulting current is large. This effect is due to the different Fermi surfaces in the two layers.

$YBa_2Cu_3O_{6.93}$ were carried out for the purpose of investigating its twin structure. Measurements were made with an 18-kW rotating anode x-ray source and a double-axis diffractometer using a perfect Ge(111) monochromator with sufficient resolution to cleanly separate Cu $K\alpha 1$ from Cu $K\alpha 2$ radiation. Full details will be reported separately.[25]

The crystal under study was grown by the UBC group and had approximate dimensions of $1\times1\times0.03$ mm^3, with the c-axis oriented along the thin dimension. The crystal was sufficiently thin that scattering within the orthorhombic basal plane [such as (2,0,0) and (0,2,0)] could be performed in transmission geometry and such measurements thus probe the bulk of the crystal. Representative longitudinal scans of the (2,0,0) and (0,2,0) Bragg peaks are shown for both twin domains in Fig. 4. As is clear from this figure, one twin domain has a peak intensity which is more than an order of magnitude stronger than the other. This leads naturally to an interpretation of the twin structure in the crystal in terms of a majority and a minority domain. Also, as would be expected in this scenario, the minority phase line shape is very noticeably broader than that of the majority phase, whose line shape appears to be approximately resolution limited. This is shown in the inset to Fig. 4, where the same data is plotted on a linear intensity axis, and has been scaled so that the peak intensity of the two domains coincide.

The majority and minority phase domain distribution in this crystal was found to be inhomogeneous. X-ray-scattering measurements were performed with a very narrow ($\sim$0.05 mm) incident beam to allow measurements which probe different regions of the crystal. The twin structure was investigated as the sample was translated through the narrow beam along the majority phase a axis. This investigation yielded results which ranged from completely untwinned on one extreme edge of the crystal to an approximate 1:1 ratio of the volume fraction of majority to minority domains on the other edge. Interior regions of the crystal yielded some intermediate value of this ratio. We estimate the average ratio of the volume fraction occupied by the majority and minority twin domains for the entire sample to be about 2–3 to 1. While these measurements reveal a complex inhomogeneous morphology to the twin structure, it is certainly clear that macroscopic regions of the crystal exist in which one domain predominates over the other.

IV. CONCLUSIONS

For c-axis incoherent YBCO-I-Pb Josephson tunneling junctions, the d-wave component of the gap parameter can contribute very significantly because of the orthorhombic nature of the chain Fermi surface which emphasizes the contributions to the Josephson current from those parts of the Brillouin zone along the Fermi surface. The s component of the gap in the chains and planes will also contribute but this may be less important so that such experiments on untwinned

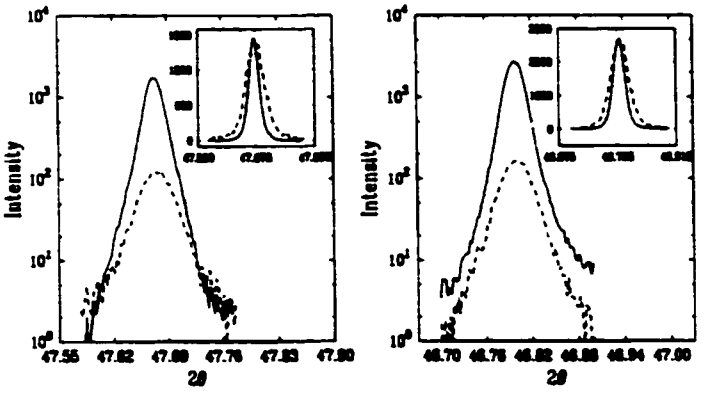

FIG. 4. Representative longitudinal x-ray scattering scans through the (2,0,0) and (0,2,0) Bragg peaks of the $YBa_2Cu_3O_{6.93}$ single crystal are shown on a logarithmic scale. It is clear that the peak intensity of the majority phase twin domains are at least an order of magnitude stronger than that of the corresponding minority phase domain. The inset shows the same data, but now on a linear intensity axis, and scaled so that the peak intensities for the two domains coincide. The Bragg features of the minority twin domains are clearly much broader than those of the majority phase domains.

samples do not probe directly the s-wave admixture of a predominantly d-wave gap function.

The observation of a c-axis tunneling current in the experiments of Sun *et al.*[17,28] and Tanaka *et al.*[18] on twinned samples can only be understood within our theory if we do not have equal numbers of a and b twins. Experimental evidence is presented that in some cases twins will not be equally abundant.

ACKNOWLEDGMENTS

Research supported in part by the Natural Sciences and Engineering Research Council of Canada (NSERC), the Ontario Centre for Materials Research (OCMR) and by the Canadian Institute for Advanced Research (CIAR). We would like to thank Bob Goodings for discussions and insights and D. Bonn for providing the crystal.

*Electronic address: odonovan@mcmaster.ca

[1] C. G. Olson *et al.*, Science **245**, 731 (1989).
[2] Z. X. Shen *et al.*, Phys. Rev. Lett. **70**, 1553 (1993).
[3] H. Ding *et al.*, Phys. Rev. B **50**, 1333 (1994).
[4] H. Ding, J. C. Campuzano, A. F. Bellman, T. Yokoya, M. R. Norman, M. Randeria, T. Takahashi, H. Katayama-Yoshida, T. Mochiku, K. Kadowaki, and G. Jennings, Phys. Rev. Lett. **74**, 2784 (1995).
[5] H. L. Edwards, J. T. Markert, and A. L. de Lozanne, Phys. Rev. Lett. **69**, 2967 (1992).
[6] H. L. Edwards, D. J. Derro, A. L. Barr, J. T. Markert, and A. L. de Lozanne, Phys. Rev. Lett. **75**, 1387 (1995).
[7] A. Mathai, Y. Gim, R. C. Black, A. Amar, and F. C. Wellstood, Phys. Rev. Lett. **74**, 4523 (1995).
[8] D. A. Brawner and H. R. Ott, Phys. Rev. B **50**, 6530 (1994).
[9] D. A. Wollman, D. J. Van Harlingen, W. C. Lee, D. M. Ginsberg, and A. J. Leggett, Phys. Rev. Lett. **71**, 2134 (1993).
[10] C. C. Tsuei *et al.*, Phys. Rev. Lett. **73**, 593 (1994).
[11] J. R. Kirtley, C. C. Tsuei, J. Z. Sun, C. C. Chi, Lock See Yu-Jahnes, A. Gupta, M. Rupp, and M. B. Ketchen, Nature (London) **373**, 225 (1995).
[12] C. C. Tsuei *et al.*, Science **271**, 329 (1996).
[13] Half flux quanta have also been recently found in tricrystal ring experiments performed on Hg compounds which have tetragonal symmetry. See C. C. Tsuei *et al.*, Science **271**, 329 (1996).
[14] A. Mathai (private communication).
[15] A. Beardsal (private communication).
[16] M. Sigrist, K. Kuboki, P. A. Lee, A. J. Millis, and T. M. Rice, Phys. Rev. B **53**, 2835 (1996).
[17] A. G. Sun, D. A. Gajewki, M. B. Maple, and R. C. Dynes, Phys. Rev. Lett. **261**, 237 (1993).
[18] R. Kleiner *et al.*, Phys. Rev. Lett. **76**, 2161 (1993).
[19] D. J. Van Harlingen, Rev. Mod. Phys. **67**, 515 (1995).
[20] B. G. Levi, Physics Today **49** (1), 19 (1996).
[21] C. O'Donovan, D. Branch, J. P. Carbotte, and J. Preston, Phys. Rev. B **51**, 6588 (1995).
[22] C. O'Donovan and J. P. Carbotte, Phys. Rev. B **55**, 1200 (1997).
[23] Kazuhiro Kuboki and Patrick Lee, J. Phys. Soc. Jpn. **64**, 3179 (1995).
[24] R. C. Dynes (private communication).
[25] M. D. Lumsden and B. D. Gaulin (unpublished).
[26] V. Ambegaokar and A. Baratoff, Phys. Rev. Lett. **10**, 486 (1963); **11**, 104 (1964).
[27] A. J. Millis, H. Monien, and D. Pines, Phys. Rev. B **42**, 167 (1990).
[28] A. G. Sun, A. Truscott, A. S. Katz, R. C. Dynes, B. W. Veal, and C. Gu, Phys. Rev. B **54**, 6734 (1996).

Figure 6.16: The DOS in the trilayer model of Fig. 9 of §6.5.2 calculated with $V_{\mathbf{k},\mathbf{q},\alpha\beta} = V_{\mathbf{k},\mathbf{q}}$, i.e., the interaction within and between the bands being the same.

6.7 STM Tunnel Junctions

The DOS for a two band plane-chain system is reported in Ref. [109], included here starting on p. 102.

For a three band system, shown in Fig. 6.16, the DOS has even more detail due to the number of coherence peaks and van Hove singularities present. This DOS corresponds to the order parameter shown in Fig. 9 of the paper included in §6.5.2 and has coherence peaks, which are more clearly seen for $\omega > 0$, at $\omega \approx 6, 20$meV due the chain layer (see Fig. 9a in §6.5.2) and at $\omega \approx 14, 17, 18$meV due to the plane layers. The extra peaks for $\omega < 0$ are van Hove singularities.

It is interesting that the experimental STM tunneling measurements , Fig. 5.27, most closely resemble those calculated using a single band system. This would seem to indicate that for STM tunneling there are only electrons coming from one layer.

Chapter 7

Conclusions

This thesis has examined some of the ramifications of having multiple conducting bands in HTC materials, with special emphasis on YBCO and its problematical chain layer. Several different band structures have been examined and the effect of impurities upon the order parameter as well as several electronic properties have been calculated, including the optical conductivity, the magnetic penetration depth, the density of states and the Josephson current.

While the interactions discussed in Ch. 4 were used for the subsequent calculations presented in Ch. 5 & 6, in most cases the details of the interaction were unimportant: Any interaction that resulted in a d-wave order parameter would have given much the same results. It is perhaps an unfortunate consequence of BCS theory that it provides very little insight into the interaction that gives rise to the Cooper pairing. So far there is no equivalent for the HTS materials to the tunneling inversion process that has been so successful for the conventional superconductors.

A significant part of the work in Ch. 6 has been included as three previously published papers, but some of the calculations, particularly the optical conductivity and the c-axis penetration depth, are presented here for the first time.

It is hoped that future work calculating both the AFM and SC order parameters utilizing the same interaction for different fillings, alluded to in Ch. 3, will yield a phase diagram similar to Fig. 3.1. This would provide much stronger, albeit indirect, evidence for the spin-fluctuation type interactions used in this work.

The main conclusion of this work is that, even if the spin-fluctuation model is not the correct explanation for HTS, the details of the band structure can have significant effects upon the electronic properties of these unusual, and potentially technologically important, materials.

Appendix A

Computer Algorithms

A.1 Convolutions

The convolutions required in the calculation of the self energy, $\widehat{\Sigma}_{k,n}$, (*e.g.* Eqs. 2.34, 4.1) and susceptibilities, $\chi_{k,n}$, (*e.g.* Eqs. 4.6 and 4.6), given by equations of the form (dropping the spinors for clarity)

$$\begin{aligned} \Sigma_{k,n} &= -T\sum_{m}\sum_{q} V_{k-q,n-m}G_{q,m} \\ \chi_{k,n} &= -T\sum_{m}\sum_{q} G_{k+q,n+m}G_{q,m}, \end{aligned} \tag{A.1}$$

are performed in a slightly different manner. In both the reciprocal space sums (*i.e.* the Σ_k) are performed with Fourier transforms and the Matsubara sums (*i.e.* the Σ_n) are performed explicitly.

A.1.1 Reciprocal Space Sums

The reciprocal space sums are performed using the convolution theorem

$$\begin{aligned} \Sigma_k &= \sum_{q} V_{k-q}G_q \\ &= \mathcal{F}_k^{-1}\left[\mathcal{F}_r\left[V_k\right]\cdot\mathcal{F}_r\left[G_k\right]\right], \end{aligned}$$

where "$\cdot$" indicates a dot product, and the $\mathcal{F}$ are the Fourier transform operators defined by

$$\begin{aligned} \mathcal{F}_k^{-1}[x_r] &\equiv \frac{1}{\sqrt{N}}\sum_{r} e^{-ik\cdot r}x_r \\ \mathcal{F}_r[x_k] &\equiv \frac{1}{\sqrt{N}}\sum_{k} e^{ik\cdot r}x_k \end{aligned}$$

with $\mathcal{N}$ the number of terms in the k-sum. These transforms are implemented with a fast Fourier transforms (FFT) algorithm.[119] The assumption of FFTs that the function being transformed is periodic is very convenient since all of the functions are indeed periodic in the Brillouin zone.

Since all functions have inversion symmetry (*i.e.* $x_k = x_{-k}$) the two different types of convolutions in Eq. A.1 can be treated the same. This is not true for the Matsubara sums.

A.1.2 Matsubara Sums

The matsubara sums are defined for Fermionic frequencies, $\omega_n \equiv (2n+1)\pi T$, and Bosonic frequencies, $\nu_n \equiv 2n\pi T$, with $n = -\infty ... 0 ... + \infty$. Obviously, the Matsubara sums are not periodic in n so they can not be implemented with FFTs and the sums have to be performed explicitly and with care.

The first approximation is that imposing a cutoff does not change the results significantly so long as the cutoff is large enough. For most of the work in this thesis a cutoff of $\omega_N = 24t$ (which is three times the bandwidth) has been used. This limits the Matsubara indices on the functions to the range $-N ... 0 ... (N-1)$. The two types of sums can then be written as

$$\begin{aligned} \Sigma_n &= -T \sum_{m=-N}^{N-n-1} V_{n-m} G_m \\ \chi_n &= -T \sum_{m=-N+n+1}^{N-1} G_{n+m} G_m \end{aligned} \tag{A.2}$$

where the unusual limits on the sums ensure that the indices on V_{n-m} and G_{n+m} stay within the range $-N ... 0 ... (N-1)$

All functions are either symmetric or antisymmetric in ω_n so that only the positive n values need to be stored. This does, however, impose the condition that the above sums must be manipulated so that only the positive m are needed.

Convolution of Two Fermionic Functions

Using the fact that for Fermionic Matsubara frequencies, $\omega_{-n} = -\omega_{n-1}$ for $n > 0$ we can perform the following manipulations so that only positive Matsubara frequencies are used

$$\begin{aligned}
\chi_n &= -T\sum_{m=-N}^{N-n-1} G(\omega_{n+m})G(\omega_m) \\
&= -T\sum_{m=-N}^{-n-1} G(\omega_{n+m})G(\omega_m) - T\sum_{m=-n}^{-1} G(\omega_{n+m})G(\omega_m) - T\sum_{m=0}^{N-n-1} G(\omega_{n+m})G(\omega_m) \\
&= -T\sum_{m=n+1}^{N} G(\omega_{n-m})G(\omega_{-m}) - T\sum_{m=1}^{n} G(\omega_{n-m})G(\omega_{-m}) - T\sum_{m=0}^{N-n-1} G(\omega_{n+m})G(\omega_m) \\
&= -T\sum_{m=n+1}^{N} G(\omega_{-|m-n|})G(\omega_{-m}) - T\sum_{m=1}^{n} G(\omega_{|n-m|})G(\omega_{-m}) - T\sum_{m=0}^{N-n-1} G(\omega_{n+m})G(\omega_m) \\
&= -T\sum_{m=n+1}^{N} G(-\omega_{m-n-1})G(-\omega_{m-1}) - T\sum_{m=1}^{n} G(\omega_{n-m})G(-\omega_{m-1}) - T\sum_{m=0}^{N-n-1} G(\omega_{n+m})G(\omega_m) \\
&= -T\sum_{m=n}^{N-1} G(-\omega_{m-n})G(-\omega_m) - T\sum_{m=0}^{n-1} G(\omega_{n-m-1})G(-\omega_m) - T\sum_{m=0}^{N-n-1} G(\omega_{n+m})G(\omega_m). \quad \text{(A.3)}
\end{aligned}$$

Note that for the imaginary component of the diagonal part of $\widehat{G}_{k,n}$ is odd in ω_n so the second term in Eq. A.3 will have to be treated differently from the rest.

Convolution of Fermionic and Bosonic Functions

Using the fact that for Bosonic Matsubara frequencies, $\nu_{-n} = \nu_n$ for $n > 0$ we can perform a similar manipulations so that only positive Matsubara frequencies are used

$$\begin{aligned}
\Sigma_n &= -T\sum_{m=-N+n+1}^{N-1} V(\nu_{n-m})G(\omega_m) \\
&= -T\sum_{m=0}^{N-n-1} V(\nu_{n+m-1})G(-\omega_m) - T\sum_{m=0}^{n} V(\nu_{n-m})G(\omega_m) - T\sum_{m=n+1}^{N-1} V(\nu_{m-n})G(\omega_m)
\end{aligned} \quad \text{(A.4)}$$

Note that in this case it is the first term in Eq. A.4 that will that will cause the imaginary component of the diagonal part of $\widehat{G}_{k,n}$ to have to be treated differently.

Bibliography

[1] H. Onnes, Commun. Phys. Lab **124c**, (1911).

[2] W. Meissner, Ges. Kältenindustr **34**, 197 (1927).

[3] F. London and H. London, Proc. R. Soc. A **149**, 71 (1935).

[4] V. Ginzburg and L. Landau, Zh. Eksp. Teor. Fiz. **20**, 1064 (1950).

[5] J. Bardeen, L. N. Cooper, and J. R. Schrieffer, Phys. Rev. **108**, 1175 (1957).

[6] G. Eliashberg, Zh. Eksp. Teor. Fiz **38**, 966 (1960).

[7] G. Eliashberg, Sov. Phys. JETP **11**, 696 (1960).

[8] J. P. Carbotte, Rev. Mod. Phys. **62**, 1027 (1990).

[9] J. G. Bednorz and K. A. Müller, Z. Phys. B **64**, 189 (1986).

[10] H. Frölich, Phys. Rev. **79**, 845 (1950).

[11] L. Cooper, Phys. Rev. **104**, 1189 (1956).

[12] N. Bogolyubov, Nuovo Cimento **7**, 794 (1958).

[13] N. Bogolyubov and S. Tyablikov, Sov. Phys.-Doklady **4**, 604 (1959).

[14] C. O'Donovan and J. Carbotte, Physica C **252**, 87 (1995).

[15] C. O'Donovan, M.Sc. thesis, McMaster University, Hamilton, Ont., Canada, 1993.

[16] M. Graf, A. Balatsky, and J. Sauls, Phys. Rev. **B 61**, 3255 (2000).

[17] A. Millis, H. Monien, and D. Pines, Phys. Rev. **B 42**, 167 (1990).

[18] G. Green, *An Essay on the Application of Mathematical Analysis to the Theories of Electricity and Magnetism* (T. Wheelhouse, Notingham, 1828).

[19] P. Allen and B. Mitrovič, in *Solid State Physics*, edited by H. Ehrenreich (Academic Press, New York, 1982), Vol. 37.

[20] W. McMillan and J. Rowell, in ***Superconductivity***, edited by R. Parks (Decker, New York, 1969), ch. 13.

[21] E. Fradkin, ***Field Theories of Condensed Matter Systems*** (Addison-Wesley, Reading, MA, 1991).

[22] B. Minor, Ph.D. dissertation, McMaster University, Hamilton, Ont., Canada, 1996.

[23] E. Dagotto, Phys. Rev. Lett. **70**, 682 (1993).

[24] E. Dagotto, Phys. Rev. **B48**, 4002 (1993).

[25] Z. Shen *et al.*, J. Phys. Chem. Solids **54**, 1169 (1993).

[26] P. Aebi *et al.*, Phys. Rev. Lett. **72**, 2757 (1994).

[27] B. Wells *et al.*, Phys. Rev. Lett. **65**, 3056 (1990).

[28] Z. Shen *et al.*, Phys. Rev. Lett. **70**, 1553 (1993).

[29] Y. Hwu *et al.*, Phys. Rev. Lett. **67**, 2573 (1991).

[30] R. Kelley, J. Ma, G. Margaritondo, and M. Onellion, Phys. Rev. Lett. **71**, 4051 (1993).

[31] D. J. Singh, Phys. Rev. **B 50**, 4106 (1994).

[32] A. Freeman, J. Yu, and C. Fu, Phys. Rev. **B 36**, 7111 (1987).

[33] H. Krakauer and W. E. Pickett, Phys. Rev. Lett. **60**, 1665 (1988).

[34] M. S. Hybertsen and L. Mattheiss, Phys. Rev. Lett. **60**, 1661 (1988).

[35] J. Yu, S. Massidda, and A. Freeman, Phys. Rev. Lett. **60**, 1661 (1988).

[36] A. Overhauser and A. Arrott, Phys. Rev. Lett. **4**, 226 (1960).

[37] W. Lomer, Proc. Phys. Soc. **80**, 489 (1962).

[38] D. R. Penn, Phys. Rev. **142**, 350 (1966).

[39] M. Kato and K. Mashida, Phys. Rev. **B 37**, 1510 (1988).

[40] W. Atkinson, Ph.D. dissertation, McMaster University, Hamilton, Ont., Canada, 1995.

[41] D. A. Wollman *et al.*, Phys. Rev. Lett. **71**, 2134 (1993).

[42] D. A. Wollman, D. J. V. Harlingen, J. Giapintzakis, and D. M. Ginsberg, Phys. Rev. Lett. **74**, 797 (1995).

[43] C. C. Tsuei *et al.*, Phys. Rev. Lett. **73**, 593 (1994).

[44] D. A. Brawner and H. R. Ott, Phys. Rev. **B 50**, 6530 (1994).

[45] A. Mathai *et al.*, J. Supercond **8**, 491 (1995).

[46] P. Chaudhari and S. Y. Lin, Phys. Rev. Lett. **72**, 1084 (1994).

[47] N. Bickers and D. Scalapino, Ann. Phys. **193**, 206 (1989).

[48] C.-H. Pao and N. Bickers, Phys. Rev. **B 51**, 16310 (1995).

[49] S. Lenck, J. Carbotte, and R. Dynes, Phys. Rev. **B 50**, 10149 (1994).

[50] D. Scalapino, E. L. Jr., and J. Hirsh, Phys. Rev. **B 34**, 8190 (1986).

[51] N. Bulut and D. J. Scalapino, Phys. Rev. B **45**, 2371 (1992).

[52] D. Liu, K. Levin, and J. Maly, Phys. Rev. **B 51**, 8680 (1995).

[53] V. Ambegaokar and A. Baratoff, Phys. Rev. Lett. **10**, 486 (1963).

[54] V. Ambegaokar and A. Baratoff, Phys. Rev. Lett. **11**, 104 (1964).

[55] D. Feder, Ph.D. dissertation, McMaster University, Hamilton, Ont., Canada, 1996.

[56] I. McDonald, M.Sc. thesis, McMaster University, Hamilton, Ont., Canada, 1996.

[57] K. Ishida *et al.*, Physica C **179**, 29 (1991).

[58] K. Ishida *et al.*, Physica C **185-189**, 1115 (1991).

[59] K. Ishida *et al.*, J. Phys. Soc. Jpn **62**, 2803 (1993).

[60] D. J. Payne, M. Chandrasekhar, and H. Chandrasekhar, Solid State Comm. **98**, 971 (1996).

[61] P. Hirshfeld, D. Volhardt, and P. W olfe, Solid State Comm. **59**, 111 (1986).

[62] P. Hirshfeld, P. W olfe, and D. Einzel, Phys. Rev. **B 37**, 83 (1988).

[63] P. Arberg, Ph.D. dissertation, McMaster University, Hamilton, Ont., Canada, 1995.

[64] W. Pickett, R. Cohen, and H. Krakauer, Phys. Rev. B **42**, 8764 (1990).

[65] W. Pickett, H. Krakauer, R. Cohen, and D. J. Singh, Science **255**, 46 (1992).

[66] L. Mattheiss and D. Hamann, Phys. Rev. **B 40**, 2217 (1989).

[67] R. Kelley, J. Ma, B. Margaritondo, and M. Onellion, Phys. Rev. Lett. **71**, 4051 (1993).

[68] J. Ma, C. Quitmann, R. Kelly, G. M. H. Berger, and M. Onellion, Science **267**, 862 (1995).

[69] K. Gofron, J. Campuzano, A. Abrikosov, M. Lindroos, A. Bansil, H. Ding, D. Koelling, and B. Dabrowski, Phys. Rev. Lett. **73**, 3302 (1994).

[70] A. Abrikosov, J. Campuzano, and K. Gofron, Physica C **214**, 73 (1993).

[71] H. Krakauer and W. Pickett, Phys. Rev. Lett. **60**, 7967 (1988).

[72] M. S. Golden, S. V. Borisenko, S. Legner, T. Pichler, C. Duerr, M. Knupfer, J. Fink, G. Yang, S. Abell, G. Reichardt, R. Mueller, and C. Janowitz, xxx.lanl.gov **cond-mat**, 9912332 (1999).

[73] S. V. Borisenko, M. S. Golden, S. Legner, T. Pichler, C.Duerr, M.Knupfer, J. Fink, G.Yang, S. Abell, and H.Berger, xxx.lanl.gov **cond-mat**, 9912289 (1999).

[74] S. Legner, S. V. Borisenko, C. Duerr, T. Pichler, M. Knupfer, M. S. Golden, J. Fink, G. Yang, S. Abell, H. Berger, R. Mueller, C. Janowitz, and G. Reichardt, xxx.lanl.gov **cond-mat**, 0002302 (2000).

[75] O. Anderson *et al.*, Phys. Rev. **B 49**, 4145 (1994).

[76] O. Anderson *et al.*, J. Phys. Chem. Solids **56**, 1573 (1995).

[77] H. Chi and J. Carbotte, Physica C **169**, 55 (1990).

[78] C. Jiang and J. P. Carbotte, Phys. Rev. B **48**, 4231 (1993).

[79] P. Anderson, J. Phys. Chem. Solids **11**, 26 (1959).

[80] D. Basov, R. Liang, D. Bonn, W. Hardy, B. Dabrowski, M. Quijada, D. Tanner, J. Rice, D. Ginsberg, and T. Timusk, Phys. Rev. Lett. **74**, 598 (1995).

[81] T. Startseva *et al.*, Phys. Rev. Lett. **81**, 2747 (1998).

[82] T. Startseva *et al.*, Physica C **321**, 135 (1999).

[83] A. Puchkov, D. Basov, and T. Timusk, J. Phys., Cond. Matt. **8**, 10049 (1996).

[84] T. Timusk and B. Statt, Rep. Prog. Phys. **62**, 61 (1999).

[85] T. Timusk and D. Tanner, in *Physical Properties of High Temperature Superconductors I*, edited by D. M. Ginsberg (World Scientific, New Jersey, 1989), p. 339.

[86] D. Tanner and T. Timusk, in *Physical Properties of High Temperature Superconductors III*, edited by D. M. Ginsberg (World Scientific, New Jersey, 1992), p. 363.

[87] S. Nam, Phys. Rev. **156**, 470 (1967).

[88] W. N. Hardy *et al.*, Phys. Rev. Lett. **70**, 3999 (1993).

[89] W. Hardy, S. Kamal, R. Liang, D. Bonn, C. Homes, D. Basov, and T. Timusk, Houston Workshop preprint .

[90] O. Waldmann, F. Steinmeyer, P. M uller, J. Neumeier, F. Régi, H. Savary, and J. Schneck, Phys. Rev. **B 53**, 11825 (1996).

[91] S.-F. Lee *et al.*, Phys. Rev. Lett. **77**, 75 (1996).

[92] C. Panagopoulos *et al.*, Phys. Rev. **B 53**, R2999 (1996).

[93] P. Arberg, M. Mansor, and J. Carbotte, J. Phys. Chem. Solids **54**, 1461 (1993).

[94] P. Arberg, M. Mansor, and J. Carbotte, Solid State Comm. **86**, 671 (1993).

[95] C. Homes, T. Timusk, D. A. Bonn, R. Liang, and W. N. Hardy, Physica C **254**, 265 (1995).

[96] Broun *et al.*, Phys. Rev. Lett. **77**, 735 (1996).

[97] C. O'Donovan and J. Carbotte, Phys. Rev. **B 52**, 4548 (1995).

[98] T. Xiang and J. Wheatley, Phys. Rev. Lett. **77**, 4632 (1996).

[99] K. Kitazawa, Science **271**, 313 (1996).

[100] O. Fischer, C. Renner, and I. Maggio-Aprile, in *The Gap Symmetry and Fluctuations in High-T_c Superconductors*, edited by J. Bok (Plenum Press, New York, 1998), p. 487.

[101] C. Dekker, Physics Today **52**, 22 (1999).

[102] B. D. Josephson, Phys. Lett. **1**, 251 (1962).

[103] J. H. Miller, Jr., *et al.*, Phys. Rev. Lett. **74**, 2347 (1995).

[104] G. Kido *et al.*, in *Advances in Superconductivity III*, edited by H. Kajimura and H. Hayakawa (Springer-Verlag, Tokyo, 1991).

[105] Y. Tanaka, Phys. Rev. Lett. **72**, 3871 (1994).

[106] C. O'Donovan, D. Branch, J. Carbotte, and J. Preston, Phys. Rev. **B 51**, 6588 (1995).

[107] A. G. Sun, D. A. Gajewski, M. B. Maple, and R. C. Dynes, Phys. Rev. Lett. **72**, 2267 (1994).

[108] H. Shaked *et al.*, *Crystal Structures of the High-T_c Superconducting Copper-Oxides* (Elsevier Science B.V., Amsterdam, 1994).

[109] C. O'Donovan and J. Carbotte, Phys. Rev. **B 55**, 1200 (1997).

[110] C. O'Donovan and J. Carbotte, Phys. Rev. **B 55**, 9088 (1997).

[111] C. O'Donovan and J. Carbotte, Phys. Rev. **B 55**, 8520 (1997).

[112] R. Klemm and S. Liu, Physica C **191**, 383 (1992).

[113] S. Liu and R. Klemm, Phys. Rev. **B 45**, 415 (1992).

[114] R. Combescot and X. Leyronas, Phys. Rev. Lett. **75**, 3732 (1995).

[115] S. Kettemann and K. B. Efetov, Phys. Rev. B **46**, 8515 (1992).

[116] T. Xiang and J. Wheatley, Phys. Rev. Lett. **76**, 134 (1996).

[117] V. Kresin, H. Morawitz, and S. Wolf, *Mechanisms of Conventional and High T_c Superconductivity* (Oxford University Press, New York, 1993).

[118] W. Hardy, Private communication (1997).

[119] W. H. Press, S. A. Teukolsky, W. T. Vettering, and B. P. Flannery, *Numerical Recipes* (University of Cambridge, Cambridge, 1992).